

AFFIDAVIT

I declare that I have authored this thesis independently, that I have not used other than the declared sources/resources, and that I have explicitly indicated all material which has been quoted either literally or by content from the sources used. The text document uploaded to TUGRAZonline is identical to the present doctoral thesis.

Date

Signature

Acknowledgments

I owe great thank to my supervisor Scott Kieffer, who introduced me to this beautiful, hidden geologic jewel within the heart of the Himalayan mountain range. His fascination and enthusiasm for this special place caught on me right away and I was captured by its enchanting nature and character. I am grateful for his immense support to perform my research and his efforts keeping me motivated with his ideas and visions over the years. His comments and remarks on the manuscript were highly appreciated. Many thanks go to my external advisors Prof. Kuroschi Thuro and Clark Fenton for their thorough revision of the manuscript and valuable comments.

I thank my loving wife Sarah and my little son Aeneas, who were able to cheer me up when things did not work out as planned. I also thank my parents for their unconditional support and patience and believe in me during my studies.

Special thanks go to the warm people of Spiti and Dangkhar, who made my field trips an unforgettable memory and experience. Thank you, Parul Gupta, Manik Raj Pandit, Sunil Kumar and Vaneet Rana for your hospitality, countless hours of great entertainment, inspiring conversations and laughs during my stay at your Monastery Guest House and for introducing me to other parts of Spiti. Thanks to the kitchen staff for their excellent culinary supply. Thanks to Georg Nussbaumer for accompanying me on the trip to India and his assistance in the field.

Finally, my thank goes to all the members of the Institute of Applied Geosciences at TU Graz, especially to Albrecht Leis for performing stable isotope analyses, and Annie Pendl and Evelyn Reiterer who assisted me in all paperwork and administrative issues.

Preface

In 2011, a team of scientists from TU Graz first visited the Spiti Valley (Tibetan: *piti = middle province*), a sparsely inhabited remote high mountain desert in the Indian Himalayas, which is also referred to as “Little Tibet”. Traditional Tibetan culture is still preserved in large parts of this region with numerous Buddhist Monasteries (*Gompas*). The *Save Dangkhar Project* initiated by the Swiss entrepreneur Markus Weisskopf was an initiative related to one of these monasteries. It was to develop a remediation strategy for the over 1000-year old Buddhist Dangkhar monastery resting on top of a conspicuous brecciated cliff (Fig.1) overlooking parts of the Spiti Valley and Pin Valley. It was that unique nature of the rocks that formed this cliff and the overall characteristics of the slope around Dangkhar (*Dang = cliff, ridge; khar = citadel, fort; “citadel on a cliff”*) that caught my advisor’s attention, who was at that time part of the *Save Dangkhar* project. Considerations regarding the geologic origin of the brecciated foundation rock (Fig.1) led to initial observations and interpretations of massive landslide features, which may have eluded prior detection due to its remote geographical location and enormous dimensions. Time constraints did not allow further field investigation of the site at that time. Hence, it was decided to develop this project to investigate the geologic history, geomorphologic features and processes of this unique site. It serves as a case study to help understanding the nature, timing, mechanisms and causes of extremely large-scale landslides. Performing field work in the fascinating geologic environment of the Himalayas and the people living there was a memorable experience. Calling Dangkhar my home for several months during field work, one quickly becomes a part of the friendly and hospitable local community interested in your research activities. Living with the local people and Buddhist monks during my site visit was a lifetime experience in a professional and spiritual way.



Fig.1 The 1000-year-old Dangkhar Monastery and village situated on top of a carbonate breccia (photograph taken by Samuel Bourne in 1866; © Victoria & Albert Museum, London, Museum No. 53.093)

...Dankar itself is perched upon a projecting ledge of conglomerate limestone, rising out of the valley in steep indurated masses, which the erosion of time has filed into slender spires and the percolation of snow eaten away at their bases till they present a groupe of turrets and ravines almost deceiving the senses by the effect of natural agents. These lofty piles have a compact solidity which resists the hammer. Their sides are often scooped into places of abode, and the natural excavations are taken possession of by monks and a vagrant priesthood, who detaching themselves from the rest of the world like the Druids of old, are to be seen peeping out from their isolated niches....

J.G. Gerard, 1833

(Oldest description of the rock formations of Dangkhar)

EXECUTIVE SUMMARY (extended abstract)

The Spiti Valley in northern India hosts the newly discovered and previously undescribed Dangkhar Landslide. It is one of the five largest continental landslides on Earth with an area of approximately 54 km² and an estimated volume of 15 to 20 km³. The landslide occurred in a remote, high mountain desert in the Tethys Himalayas, sculpted by fluvio-, para- and periglacial processes, at an altitude between 3400 and 5600 m. It provides an exceptional opportunity to study the landslide structure, mechanism, geochronology and deformation history. The properties of this mass movement are considered in a broad context, including geological, geomorphological, tectonic, and climatic aspects. A wide range of techniques, such as high resolution satellite imagery and digital elevation data, detailed geological and geomorphological mapping and sampling for laboratory analysis, and geotechnical evaluation, have been used to provide insight to the landslide characteristics.

Geological mapping reveals structures and the extent of the Dangkhar Landslide, of bedrock and quaternary deposits, as well as the general geometry that favored the development of the landslide at this particular location. Block theory confirmed the favorable setting conditioned by the valley geometry in order to form a removable block. Geomorphologic investigations revealed large-scale lineaments as the result of slope tectonic structures typical of extremely large landslides. Relationships between erosional and depositional glacial features and the landslide lineaments provide insights on the relative motion stages. With the aid of rock glacier deposits of different generations, which are preserved on the Dangkhar Landslide, it has been able to reconstruct stages of landslide activity. Radiocarbon dating specifies the evolution of the mass movement and allows establishing a timeframe for the Dangkhar Landslide activity. The investigations indicate that during the Holocene and late Pleistocene, large parts of the landslide moved in a slow and coherent manner, as the glaciers began to retreat. This manifested itself in recurring, episodic, slow movement patterns, resulting in an interplay of glacial and landslide deposits and structures. Parts of the landslide mass were mobilized by glacial meltwater action as debris flows and cemented into a breccia under fresh water influence as indicated by stable hydrogen and oxygen isotope analyzes of the breccia deposits.

KURZFASSUNG

Das Spiti-Tal in Nordindien beherbergt den neu entdeckten und bisher unbeschriebenen Dangkhar-Erdrutsch. Es handelt sich hierbei um einen der fünf größten Erdrutsche der Erde mit einer Fläche von ca. 54 km² und einem geschätzten Volumen von 15 bis 20 km³. Der Erdrutsch ereignete sich in einer abgelegenen Hochgebirgswüste im Tethys-Himalaya, die durch fluvio-, para- und periglaziale Prozesse in einer Höhe zwischen 3400 und 5600 m geprägt ist. Diese Region bietet eine außergewöhnliche Gelegenheit, die Struktur, den Mechanismus, die Geochronologie und die Deformationsgeschichte dieses Erdrutsches zu untersuchen. Die Eigenschaften dieser Massenbewegung werden in einem breiten Kontext betrachtet, einschließlich geologischer, geomorphologischer, tektonischer und klimatischer Aspekte. Eine breite Palette von Techniken, wie hochauflösende Satellitenbilder und digitale Höhendaten, detaillierte geologische und geomorphologische Kartierungen und Probenahmen für Laboranalysen sowie geotechnische Auswertungen, wurden angewendet, um Einblicke in die Eigenschaften der Massenbewegung zu erhalten.

Die geologische Kartierung offenbarte die Strukturen und das Ausmaß des Dangkhar-Erdrutsches sowie jene des Grundgebirges und der quaternären Ablagerungen, aber auch die generelle Geometrie, die die Entwicklung des Erdrutsches an genau dieser Stelle begünstigte. Die Blocktheorie bestätigte die günstigen Rahmenbedingungen, die durch die Talgeometrie bedingt ist, um einen entfernbar Block zu bilden. Geomorphologische Untersuchungen ergaben großmaßstäbliche Lineamente, die das Ergebnis von hangtektonischen Aktivitäten sind und für extrem große Erdrutsche typisch sind. Die Beziehungen zwischen glazialen Erosions- und Ablagerungsstrukturen und den Lineamenten liefern Einblicke in die relativen Bewegungsstadien. Mit Hilfe von Blockgletschervorkommen verschiedener Generationen, die auf dem Dangkhar-Erdrutsch erhalten sind, ist es gelungen, die einzelnen Stadien der Erdrutschaktivität zu rekonstruieren. Radiokarbondatierungen spezifizieren die Entwicklung der Massenbewegung und ermöglichen die Festlegung eines Zeitrahmens für die Aktivität des Dangkhar-Erdrutsches. Die Untersuchungen zeigen, dass sich während des Holozäns und des späten Pleistozäns große Teile des Erdrutsches langsam und kohärent bewegten, als die Gletscher sich zurückziehen begannen. Dies manifestierte sich in wiederkehrenden, episodischen, langsamen Bewegungsmustern, die zu einem Wechselspiel aus glazialen und erdrutschbedingten Ablagerungen und Strukturen führten. Teile der Erdrutschmasse wurden durch Schmelzwassereinwirkung als Schuttströme mobilisiert und unter Frischwassereinfluss in Form einer Brekzie zementiert, wie stabile Wasserstoff- und Sauerstoffisotopenanalysen der Brekzien anzeigen.

TABLE OF CONTENTS

Acknowledgments.....	i
Preface	ii
EXECUTIVE SUMMARY (extended abstract)	iv
KURZFASSUNG	v
1 INTRODUCTION	1
1.1 Purpose and scope	1
1.2 Previous geologic investigations in Spiti – a historic review.....	4
2 BACKGROUND.....	8
2.1 Characteristics of non-catastrophic extremely large landslides.....	8
2.2 Landslide geochronology	13
3 REGIONAL CONDITIONS.....	16
3.1 The Himalayan orogen	16
3.1.1 Indus Tsangpo Suture Zone (ITSZ) and Transhimalaya	16
3.1.2 Tethys (Tibetan) Himalaya and Higher Himalaya	17
3.1.3 Lesser Himalaya	18
3.1.4 Subhimalaya	18
3.2 The Spiti Valley	20
3.2.1 Geologic and geomorphologic conditions	20
3.2.2 Regional seismotectonics and landsliding	22
3.2.3 Climate	28
3.2.4 Paleoclimate.....	29
4 THE DANGKHAR LANDSLIDE	39
4.1 Investigative methods	39
4.2 Results and findings	41
4.2.1 Dangkhar Landslide geomorphology	41
4.2.2 Dangkhar Landslide hydrology.....	54
4.2.3 Geologic units and structure.....	57
4.2.4 Extent and dimensions of the Dangkhar Landslide	67
4.2.5 Dangkhar Landslide volume estimates	70
4.2.6 Dangkhar carbonate breccia deposits	78

4.2.7	Laboratory testing.....	83
4.2.7.1	Solids – Mineralogy, microscopy and cathodoluminescence	83
4.2.7.2	Stable isotope data of solids (Delta ¹⁸ O, Delta ¹³ C).....	86
4.2.7.3	Stable isotope data of liquids (Delta ¹⁸ O, Delta ² H).....	87
4.2.7.4	Radiocarbon sampling and dating.....	90
4.2.8	Formation and evolution of the Dangkhari carbonate breccia	95
4.2.9	Geochronology and evolution of the Dangkhari Landslide	100
4.2.10	Geotechnical evaluation	106
4.2.10.1	Block Theory	106
4.2.10.2	Triggering mechanism	109
4.2.11	Style of deformation and classification	112
5	SUMMARY AND CONCLUSION.....	116
	REFERENCES.....	121
	APPENDIX	

LIST OF FIGURES

Fig.I: The 1000-year-old Dangkhar Monastery situated on top of a carbonate breccia.....	1
Fig. 1.1 Panorama of the Dangkhar Landslide (#GP www.gigapan.com/gigapans/178308)	3
Fig. 1.2 Location map of the Spiti Valley (modified after Draganits 2004)	4
Fig. 1.3 Study area around the Ancient Dangkhar Monastery looking upstream the Spiti Valley.....	5
Fig. 1.4 Early geologic sketches of the Dangkhar area by Griesbach (1891). a) Geological cross section of the Spiti Valley near Dangkhar (8 – Ganmachidam Formation, 9 – Kuling Group, 10 & 11 – Mikin Formation, 12 – Kaga to Rongtong Formation, 13 – Alaror & Rangrik Formation, 14 & 15 – Kioto Group; formation names updated after Bhargava (2008). b) Sketch of the Dangkhar and Mane area looking northwest, upstream the Spiti Valley	7
Fig. 2.1 Laserscan model of the Stupfarri Landslide (modified after Weißflog et al. 2010)....	10
Fig. 2.2 Slope tectonic features of extremely large landslides. a) Landslide deformation structures. b) characteristic morphostructures of extremely large, non-catastrophic landslides (after Jaboyedoff et al. 2013; Agliardi et al. 2001)	11
Fig. 2.3 Different mechanisms of large-scale slow rock slope deformations reported in literature. (a), (b), (c), (f) Bois et al. (2008); (d) Mahr (1977); (e), (g), (h), (i) Ambrosi and Crosta (2006); (j) Agliardi et al. (2001); (k), (l) Hutchinson (1988); (m), (n) Zischinsky (1966); (o), (p), (t) Chigira (1992); (q), (r) Nemcok (1972); (s) Agliardi et al. (2009b); (u), (v), (w) Kieffer (1998). Compiled by Agliardi et al. (2012), for detailed references see there	12
Fig. 2.4 Dating methods applied in landslide studies. TT OSL/OSL = (Thermally Transferred/ Optically Stimulated Luminescence, TL = Thermoluminescence, CRE = Cosmic Ray Exposure, AMS = Accelerator Mass Spectrometry; modified after Pánek 2014).....	15
Fig. 3.1 Evolution of the Himalayan orogen. a & b) The Indian subcontinent approaches Asia closing the Tethys ocean basin. c) Present day situation of the Himalaya with extensive development of thrusting, nape stacking and subsequent emplacement of marine deposits at high elevations (modified after Lutgens et al. 2012).....	17
Fig. 3.2 Tectonic map of the central and northwestern Himalayan Mountain Belt. Block diagram cross section A – A' is shown in Fig.3.3 (modified after DiPietro and Pogue 2004)..	19

- Fig. 3.3** Schematic block diagram cross section through the northwestern Himalaya region illustrating the main structural components of the Himalayan Mountain Belt. The study area in Spiti is situated within the Tethys Himalaya. For abbreviations see text and Fig 3.2 (modified and compiled after Steck 2003; DiPietro and Pogue 2004; Hornung et al. 2007; Thöni et al. 2012; Wiesmayr and Grasemann 2002)20
- Fig. 3.4** Location map of the study area. a) Geographic location of the study area within Himachal Pradesh, India. b) The Spiti Valley with its major rivers and villages. c) Simplified tectonic map of the Himalaya (modified after Neumayer et al. 2004)22
- Fig. 3.5** Seismotectonic map of the study area and surrounding regions (compiled after Bhargava 1990; Bhargava and Bassi 1998; Bookhagen et al. 2005; Hintersberger et al. 2010; Anoop et al. 2012). CF – Chandra Fault, KCF – Kaurik-Chango Fault, KNF – Karcham Normal Fault, LPF – Leo Pargil Fault, MPF – More Plain Fault, SF – Sarchu Fault, SFC – Syarma Fault Complex, SVF – Spiti Valley Fault, TMF – Tso Morari Fault. Moment tensors shown for major large earthquakes (KEQ – Kinnaur Earthquake). Landslide details are listed in Tab. 3.2.....24
- Fig. 3.6** Earthquake hazard map of Himachal Pradesh (Vulnerability Atlas of HP). The study area falls under Zone IV of the Vulnerability Atlas of India, which corresponds to zone VIII of the MSK scale, rating the region as a high damage risk zone (after SEEDS 2009)25
- Fig. 3.7** Landslide hazard map of Himachal Pradesh. The study area around Dangkhar village is situated in the high hazard zone shown in green (after SEEDS 2009)27
- Fig. 3.8** Climatic characteristics of the study area (modified after Scherler et al. 2010)29
- Fig. 3.9** Monsoon systems in the Himalaya acting during the Holocene and present times. ELA = Modern Equilibrium Line Altitudes (compiled after Yao et al. 2012; Rawat et al. 2015)29
- Fig. 3.10** Contemporary glaciation and river network of the Lahaul, Spiti and Zaskar regions. Important glaciers are labelled in light blue. Locations investigated in previous studies are labelled together with names of valleys and river basins referred to in the text for comparison. Lahaul and Spiti district boundaries are approximate (modified after NRSC 2013)30
- Fig. 3.11** Extent, duration and names of glacial stages in the Lahaul Region and Zaskar Range. Age in thousand years (ka). For locations of study sites see Fig. 3.10. (modified after Hedrick et al. 2011)31

- Fig. 3.12** Distribution of glacierized areas during the Last Glacial Maximum (LGM) for the Himalayan Tibetan region. Shi's map is considered the most likely reconstruction of the last major Himalayan glaciation (after Shi 1992 in Owen and Dortch 2014).....32
- Fig. 3.13** Schematic valley evolution during and after the Chandra glacial stage. a) Valley glacier expansion during the Chandra glacial stage. b) Post-valley glacier morphology and river incision. Grey patches mark deposits of later glaciations (i.e. Batal stage moraine) in the already incised valley (modified after Taylor and Mitchell 2000).....33
- Fig. 3.14** The Manirang area. a) Location of the Manirang area (bold dashed circle), located southeast of the study area. b) Manirang glacier recession reconstructed from historic reports of Theobald (1862), Bourne (1870), Griesbach (1891) and satellite imagery acquired in 2016 (Google Earth Pro).....37
- Fig. 3.15** Glacier situation in the Manerang area from the LIA to 2016. a) Photograph near Sopona camp site by Bourne (1870) looking upstream the upper Spiti Valley. Note moraine ridge (red line) in front of image.....38
- Fig. 4.1** Topographic map of the study area; inset images: GeoMapApp (Ryan et al. 2009)..42
- Fig. 4.2:** Topographic profiles of the study area. Locations of profiles shown in Fig. 4.143
- Fig. 4.3** Geomorphologic map of the Dangkhar Landslide44
- Fig. 4.4** Characteristic gentle, hummocky topography of the Dangkhar landslide southwest of Mt. Chokula. Note prominent bedrock outcrop around the peak of Mt. Chokula45
- Fig. 4.5** DEM representations of the study area depicting various geomorphic features. a) Hillshade map (illumination from 270° azimuth). b) Hillshade map – 2x vertically exaggerated. c) Slope inclination map. d) Slope orientation map46
- Fig. 4.6** Hypsometric histogram of the Dangkhar hillslope (1 m intervals) and statistical parameter of the DEM used for the histogram (sd = standard deviation, H_i = hypsometric integral; for hypsometric curve see appendix).....47
- Fig. 4.7** Satellite photointerpretive lineament map of the study area. Alignment of lineaments within the Dangkhar Landslide and the Mane Landslides are shown in rose diagrams (top right and bottom left corner, respectively). Note valley parallel alignment of the lineaments. Yellow star marks viewpoint of Fig.4.8c towards the southeast.....49

- Fig. 4.8** Major geomorphologic features of the Dangkhar Landslide. a) Parallel array of lineaments on the mid-slope bench downhill from the Dangkhar Lake b) Satellite image of lineaments downhill from the Dangkhar Lake. c) Field photograph of the lineaments shown in (a) expressed as ridges and trenches. d) Ridge and trench formed in the upper part of the Dangkhar Landslide deposit. e) Cross section of lineaments in an ephemera stream channel exposing counterscarps (red lines indicate slip surfaces active during toppling)50
- Fig. 4.9** Characteristic Dangkhar Landslide slope features; secondary landslides, lineaments and scarps51
- Fig. 4.10** Permafrost zonation (after Gruber 2012) on the Dangkhar Landslide. Ridgeline of Mt. Chokula shown for orientation52
- Fig. 4.11** Rock glaciers near Mt. Chokula. a) Satellite image of the rock glacier generations and lineaments. Note how rock glacier generations get more subdued from first to third generation. b) Mapped rock glacier generations and lineaments showing their cross cutting relation (yellow star marks location of field photograph shown in c. c) Field photograph of third rock glacier generation overriding a lineament (dotted where concealed).....53
- Fig. 4.12** Surface water distribution of the Dangkhar hillslope (image source: NRSC 2016) ..55
- Fig. 4.13** Fluvial processes on the Dangkhar Landslide. a) Fresh debris flows triggered after a heavy thunderstorm event during the night from July 21st to 22nd, 2015. Dissected fans overlying Mane paleolake sediments (pale yellow deposits) Dashed rectangle shows location of features shown in b). GigaPan panorama was taken at Siluk the day after the thunderstorm event #GP www.gigapan.com/gigapans/178319 (Snapshots: Debris flows). b) Field photograph after the debris flow events. Dashed line marks contact between the Mane paleolake sediments and the deposits of the dissected fan56
- Fig. 4.14** Geologic map of the Dangkhar Landslide. Geologic units as in Tab.4.160
- Fig. 4.15** Geologic cross sections through the study area and stereographic plot of syncline limbs. Upper hemisphere projection is used to be consistent with orientations of cross section and map view (geologic units as in Fig. 4.14).....61
- Fig. 4.16** Overview of the study area.....62

- Fig. 4.17** Characteristic Dangkhar Landslide structures. a) Carbonate breccia patches near the slope toe area. b) Exposed bedrock units in the Lingti Valley. c) Transition zone from bedrock to debris and carbonate breccia (#GP <http://www.gigapan.com/gigapans/178308> Snapshot: Transition Zone). d) Southern part of the Dangkhar Landslide showing bedrock blocks within the debris. e) Folded strata within the Dangkhar Landslide 63
- Fig. 4.18** Rafted block within the Dangkhar Landslide debris incorporating the Rama and Chomule Formations..... 64
- Fig. 4.19** Active tectonics within the study area..... 65
- Fig. 4.20** The Mane Landslide seen from the Dangkhar hillslope. White arrows indicate direction of sliding (#GP www.gigapan.com/gigapans/178300)..... 66
- Fig. 4.21** Boundary between the Dangkhar and the Mane Landslide debris. Note difference in color of the two deposits in the image in bottom right corner..... 66
- Fig. 4.22** The Dangkhar Landslide. a) 3D digital elevation model of the Dangkhar Landslide outlining the major geomorphic features. b) Schematic cross section with 2D landslide dimensions. Morphometric details are also listed in Tab. 4.2 68
- Fig. 4.23** Areal extent of the Dangkhar Landslide deposit (40.44 km²) and the Mane landslide deposit (16.90 km²). Image and data source: ArcGIS Explorer Online 69
- Fig. 4.24** Average End-Area method illustrated for the Dangkhar Landslide. Areas of cross sections (A_{A-A'} to A_{D-D'}) are highlighted with hachures; red line indicates location of inferred basal slip surface. For abbreviations see equation 5.1..... 72
- Fig. 4.25** Dangkhar Landslide volume estimate using TIN difference modelling. Modelled volume lies above the basal slip surface (blue) and below the present day surface (green) . 73
- Fig. 4.26** 3D-visualizations of the Dangkhar Landslide. a) View of the modelled Dangkhar Landslide. b) Modelled Dangkhar Landslide (left) and corresponding field photograph (right). Red dot-dashed line delineates approximate location of the basal slip surface 74
- Fig. 4.27** Dangkhar Landslide volume estimate obtained by the Cut and Fill operation. Black plane represents the outlined areal extent of the Dangkhar Landslide..... 75

- Fig. 4.28** a) View upstream the Spiti River highlighting the distribution of the carbonate breccia deposits along the U-shaped Spiti Valley flanks (Image: Google Earth Pro). a) Polished bedrock surface near Siluk on the right Spiti River bank. Blue arrow indicates flow direction of Spiti River and of former glacier ice #GP www.gigapan.com/gigapans/178298 (Snapshot: Polished bedrock surface). 79
- Fig. 4.29** Carbonate breccia around Dangkhar. Black solid line marks the contact between different layers. White dashed lines indicate stratification pattern. 79
- Fig. 4.30** Characteristics of the carbonate breccia. a) Dangkhar carbonate breccia section at the Ancient Dangkhar Monastery with the inferred origin of the breccia layers. b) Wet sediment deformation structures. c) Sketch of breccia highlighting inclined, crudely stratification. d) Profile exposing different layers of the carbonate breccia (inferred origin is given in parentheses). Note normal faulting (red line) and loading structures (white arrow) in crudely stratified layer. e) Schematic sketch of characteristics of wet sediment deformation structures (after Pickering 1987). Details can be explored at #GP www.gigapan.com/gigapans/178298..... 81
- Fig. 4.31** Carbonate breccia of Sichling and Mane. a) Cemented carbonate breccia deposits uphill from Sichling overlain by a pale yellow layer lake sediments and stratified sand and gravel. b) Mane breccia along the right side of the Spiti River (#GP www.gigapan.com/gigapans/178685) 82
- Fig. 4.32** Dangkhar carbonate breccia. a & b) Hand specimen of the carbonate breccia. c & d) Thin section photograph of the carbonate breccia showing clasts and calcite spar cement. e) Cathodoluminescence image of the carbonate breccia: split grains and displaced pre-breccia veins (small arrows) and sense of displacement (large arrows). f) Intra clast void space filled with drusy, equant, mosaic burial cement and dogtooth cement. Note zoning of crystals. ... 85
- Fig. 4.33** Stable isotope data of carbon and oxygen of the carbonate breccia cements and host rocks (clasts). Dashed arrow indicates evolutionary trend of isotope composition from host rock to cements 87
- Fig. 4.34** Local Meteoric Water Line (Dangkhar MWL) constructed from stable isotopes of Dangkhar surface waters. WHMWL (Kumar et al. 2010); GMWL (Craig 1961)..... 88
- Fig. 4.35** 3D plot of Local Dangkhar MWL. Blue line in XY plane represents the DMWL shown in Fig. 4.34. The altitudinal information of the water samples (W1 to W8) is projected in the z-direction. 89
- Fig. 4.36** Altitude versus stable isotope values of Dangkhar water samples 89

Fig. 4.37 VSMOW normalized stable oxygen isotope data of the carbonate breccia (host rock clasts and cements) and Dangkhar waters	90
Fig. 4.38 Locations selected for organic sample drilling.....	91
Fig. 4.39 Dangkhar borehole logs	93
Fig. 4.40 ^{14}C age plot for sample BH6_55. Black line = reference curve; green shaded area = one sigma range; yellow shaded area = two sigma range.....	94
Fig. 4.41 Distribution and mechanism of carbonate breccia formation. a) Google Earth Pro satellite image and topographic profile through Dangkhar highlighting locations of carbonate breccia deposits and inferred Spiti Valley paleo-glacier. White box indicates location of polished bedrock surface (after Kaspar et al. 2019). b) Conceptual model of debris accumulation against a valley glacier at elevated levels of valley flanks during deglaciation. c) Debris accumulation after deglaciation near the valley floor (after Iturrizaga 1999)	97
Fig. 4.42 Characteristics of the deposits of the Phuktal and Ancient Dangkhar Monastery. a) The Phuktal Monastery surrounded by the lithified deposits above the Tsarap River (image: Flickr). b) Ancient Dangkhar Monastery situated on top of breccia deposits above the Spiti River. c) Detailed view of massive lithified deposits at Phuktal (image by Shakti; Wikipedia.org). d) Ancient Dangkhar Monastery located atop a massive breccia spur. e) Detailed view of an apron of inclined stratified layers of the carbonate breccia at Dangkhar	98
Fig. 4.43 Fitting of clasts versus groundmass (clast + cement ratio) as tool for identifying the origin of breccia types (after Füchtbauer and Richter 1983)	99
Fig. 4.44 Satellite image of the Dangkhar Landslide with the different features of glacial stages (image: Bing Maps) and tentative temporal framework.....	101
Fig. 4.45 Hypothesized evolution of the Dangkhar Landslide through time. Abbreviations: Ki = Kioto Gr., AlRa = Alaror and Rangrik Fm., Ro = Rongtong Fm., Ram = Rama Fm., Cho = Chomule Fm., Ka = Kaga Fm., Mi = Mikin Fm, GLOF = Glacial Lake Outburst Flood	104

Fig. 4.46 Summary chart of the evolution of the Dangkhari Landslide in a broader regional context. Color bars correspond to glacial stages in Fig. 4.44 and Fig. 4.45. Total, episodic activity of the Dangkhari Landslide between the solid black dots. Dangkhari Landslide activity stages refer to stage numbers of Fig. 4.45 (modified and compiled after Srivastava et al. 2013; Anoop et al. 2012; Dortch et al. 2009; Bhattacharyya et al. 2006; Chauhan et al. 2000) 105

Fig. 4.47 Block Theory analysis setup. a) Map of the free surfaces and location of schematic cross section (dash-dotted line) shown in b (image: Google Earth Pro). b) Cross section with outlined wedge bound by bi-planar planes 1 and 2 and the free surface 1..... 107

Fig. 4.48 Block Theory analysis for the Dangkhari Landslide. a) Removability plot of block 00; b) Failure mode of block 00 (Single digit indicates planar sliding on respective plane, i.e. Plane 1) 108

Fig. 4.49 Shape of identified removable block pyramid 00 111 (the first two digits relate to planes 1 and 2, digits three to five relate to the three free surfaces). Block schematically placed in the setting between the Spiti and Lingti Valley representing the sliding body of the Dangkhari Landslide..... 109

Fig. 4.50 Static factor of safety versus yield acceleration for the Dangkhari Landslide..... 110

Fig. 4.51 Magnitude and type of rock strength degradation cycles (rock mass fatigue) at different geologic time scales. Blue bar indicates approximate state of the Dangkhari Landslide. Note strong strength degradation due to glacial activity (modified after Eberhardt et al. 2016) 112

Fig. 4.52 Relationship between elevation, latitude and permafrost/ rock glacier distribution to determine slope settings favorable for large landslides such as sagging (modified after Hutchinson 2006). Bracket indicates approximate altitude and latitude range of the Dangkhari Landslide from toe to crown 115

Fig. 5.1 Schematic Dangkhari Landslide block diagram with the identified characteristic features. General landslide layout modified after Dikau et al. (2006). Not to scale..... 118

Fig. 5.2 The Dangkhari Landslide (location map: GeoMapApp; Ryan et al. 2009) 119

LIST OF TABLES

Tab. 2.1 Landslide activity states and estimated age based on geomorphologic conditions . 14	14
Tab. 3.1 Seismic characterization of the study area. Fault abbreviations as in Fig. 3.5. Earthquakes are assumed to occur within ruptured fault segments of the respective faults, which are considered to be about one third of the total fault length (Wells and Coppersmith 1994; Shanker and Shubham 2018)..... 24	24
Tab. 3.2 List of Quaternary river damming giant (> 0.5 km ³) landslides in the Spiti-Satluj River region. The Holocene Lingti Landslide (B; #GP www.gigapan.com/gigapans/178309) and Sichling/Mane (C) Landslide are partly located within the study area. Name of blocked river is given in parentheses next to the name of the landslide. (N.D. = not dated; after Bookhagen et al. 2005) 26	26
Tab. 4.1 Lithostratigraphic sequence of the Tethys Himalaya within the study area. For the formations of the Lilang Supergroup the equivalent historic formation names of Hayden (1904) are given in italics in parentheses (modified after Bhargava 2008; Fuchs 1982 and references therein) 59	59
Tab. 4.2 Morphometric characteristics of the Dangkhar Landslide (after WP/WLI 1990; Varnes 1978). Subscripts “d” and “r” indicate properties attributed to the displaced material and the surface of rupture, respectively 70	70
Tab. 4.3 Summary of Dangkhar Landslide volume estimates 77	77
Tab. 4.4 Mineralogical compositions of selected rocks (Tr. = traces) 84	84
Tab. 4.5 Stable isotope data of carbon and oxygen of the carbonate breccia cements. Oxygen isotope data are referred to VPDB standard and converted VSMOW standard..... 86	86
Tab. 4.6 Stable oxygen and hydrogen isotope data of Dangkhar waters 88	88
Tab. 4.7 Borehole details. Sample labelling: <i>BoreholeNo_depth of sample in centimeters</i> . Sample names in bold indicate samples submitted for ¹⁴ C AMS dating 92	92
Tab. 4.8 Orientation data of the planes and free surfaces used in the Block Theory analysis 107	107
Tab. 5.1 Dangkhar Landslide fact sheet..... 120	120

The paradox of our age

*We have bigger houses but smaller families;
more conveniences, but less time;
We have more degrees, but less sense;
more knowledge, but less judgement;
more experts, but more problems;
more medicines, but less healthiness;
We've been all the way to the moon and back,
but have trouble crossing the street to meet
the new neighbour.
We build more computers to hold more
information to produce more copies than ever,
but have less communication;
We have become long on quantity,
but short on quality.
These are times of fast foods
but slow digestion;
Tall men but short character;
Steep profits but shallow relationships.
It's a time when there is much in the window,
but nothing in the room.*

- His Holiness the 14th Dalai Lama -

1 INTRODUCTION

1.1 Purpose and scope

Records of extremely large landslides are comparably rare and are usually not related to contemporary landslide activity, representing relict or just episodically active remnants of postglacial times (Agliardi et al. 2001). The Dangkhari Landslide is an extremely large landslide located in a remote, paraglacial, high mountain desert environment at elevations between 3400 m to 5600 m within the Spiti Valley, Himachal Pradesh, India (Fig. 1.1, Kieffer and Kaspar 2013). It is amongst of the five largest continental landslides on earth, covering an area of approximately 54 km² with an estimated volume of 15 – 20 km³. It has been over a century since a landslide of such magnitude has been first documented. The Dangkhari Landslide so far has eluded documentation due to its remote location, valley-scale extent and poor accessibility. The evolution of extremely large landslides and their activity is still discussed and until recent times this landslide type was commonly considered to be a relic from the last ice age (Agliardi et al. 2012). Even though extremely large landslides are a rare events, their study is critical. Monitoring of infrastructure affected by such landslides in alpine regions has proven their significance in recent times (Ambrosi and Crosta 2006) and attempts have been made to assess the hazard potential of such landslides for hazard map integration (Willerich et al. 2009). They can impact infrastructural facilities such as tunnels, roads, and dams in the long term, but also favor the development of secondary landslides, for example, debris flows and rock falls (Soldati 2013).

The thesis serves as a case study contributing to better understand extremely large landslides. Through systematic studies of the Dangkhari Landslide, significant insight has been obtained in regard to its structure, mechanism, deformation characteristics and geochronology. The landslide characteristics are considered in a broad context including geologic, geomorphic, geomechanic, tectonic and climatic aspects. Techniques such as evaluation of high resolution satellite images and digital elevation data, detailed geologic and geomorphic field mapping and sampling for laboratory analysis together with a geomechanic analysis are performed to provide insight on key aspects of the landslide.

So far, existing geologic maps illustrated the study area as a large “blank” spot of about 40 km² (e.g. Bhargava and Bassi 1998), usually mapped as undifferentiated Quaternary deposits and diamictons of glacio-fluvial origin. Thorough field mapping revealed the structure and nature of the local bedrock and Quaternary geology and is supported by evaluation of remote sensing data and laboratory analyses. The geologic and geomorphologic field observations are used to establish a geologic model of the study area serving as a base for geomechanical

considerations employing block theory (Goodman and Shi 1985). Geochronologic data refine the temporal framework of the Dangkhar Landslide activity.

This thesis includes five chapters starting with an introduction of the purpose and scope of this study. Chapter two provides an overview of the thematic background pointing out the current state of research and knowledge regarding extremely large landslides. The third chapter contains key background data on geology, geomorphology, tectonics, previous landslide activity and climatic conditions of the northwestern Himalaya and the Spiti Valley. The fourth chapter comprises details on the Dangkhar Landslide including the description of the methodology and the data collection. The investigative findings regarding its geologic, geomorphologic, tectonic, hydrologic, climatic setting, but also geochronologic implications and geotechnical evaluation using Block Theory (Goodman and Shi 1985) are presented. The data are presented in a comprehensive framework reconstructing the evolution of the Dangkhar Landslide through and a classification of the landslide is performed addressing its evolution, structural setting, potential trigger, and type and style of deformation. The final chapter summarizes the results and findings and its implications in a broader context. Throughout the text, hyperlinks leading to GigaPan panoramas are inserted allowing an interactive inspection of the presented features. The links are indicated by *#GP* followed by the internet address.



Fig. 1.1 Panorama of the Dangkhar Landslide (#GP www.gigapan.com/gigapans/178308)

1.2 Previous geologic investigations in Spiti – a historic review

The earliest scientific expeditions to the Spiti Valley (Fig. 1.2) date back to the 1820s, providing insight on the landscape and geology of the Spiti Valley and the study area around Dangkhari (Fig. 1.3). The first geologic descriptions of the Dangkhari area by A. Gerard date back to 1827. He termed the terrain around Dangkhari a *rugged projection of gravel*. A few years later, J.G. Gerard (1833) provided a geological description of the conspicuously looking cliff of Dangkhari. He named the rock formation on which the Ancient Dangkhari Monastery is located an *indurated mass of limestone conglomerate, which erosion has shaped into hard spires, turrets and ravines*.

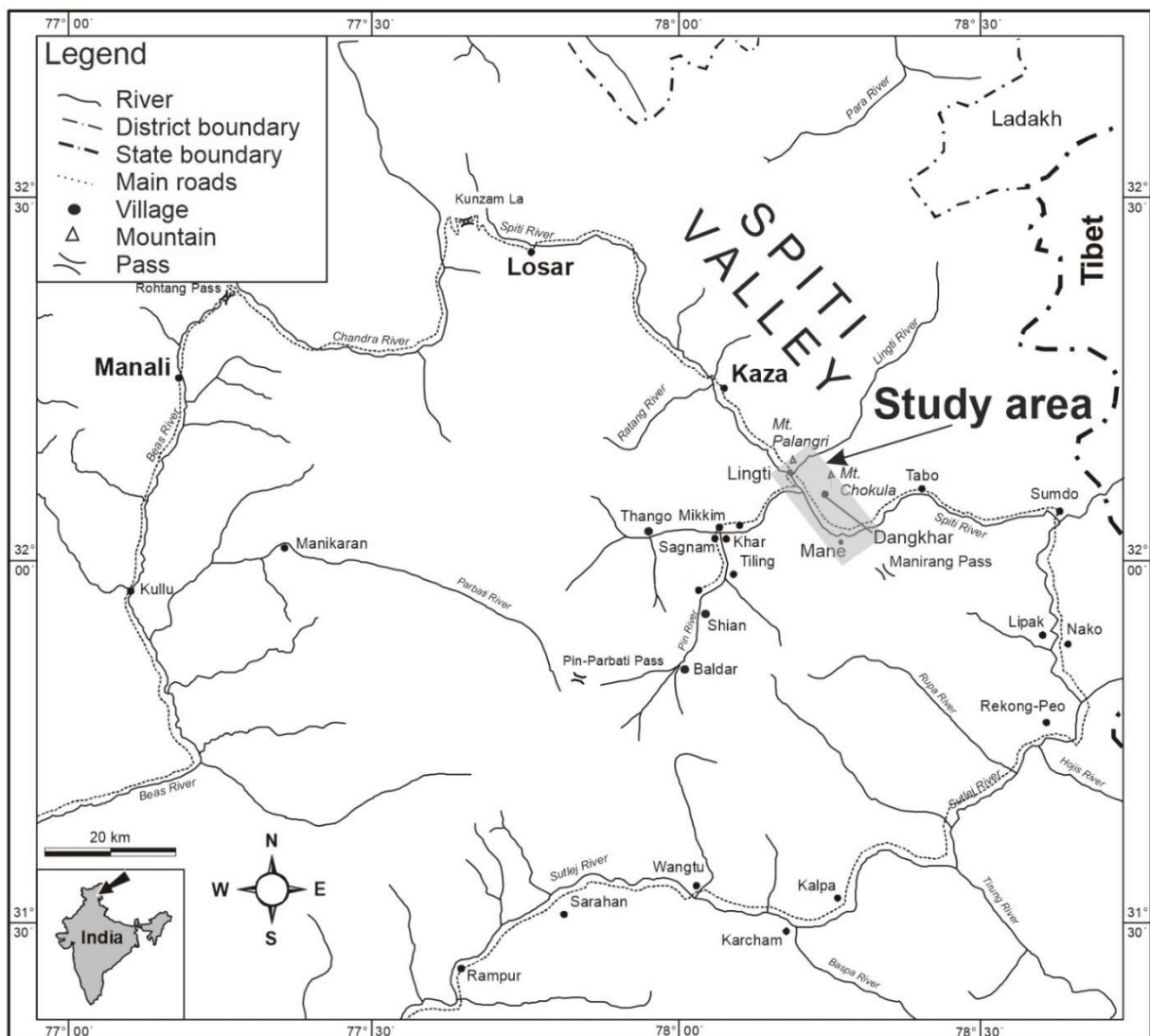


Fig. 1.2 Location map of the Spiti Valley (modified after Draganits 2004)

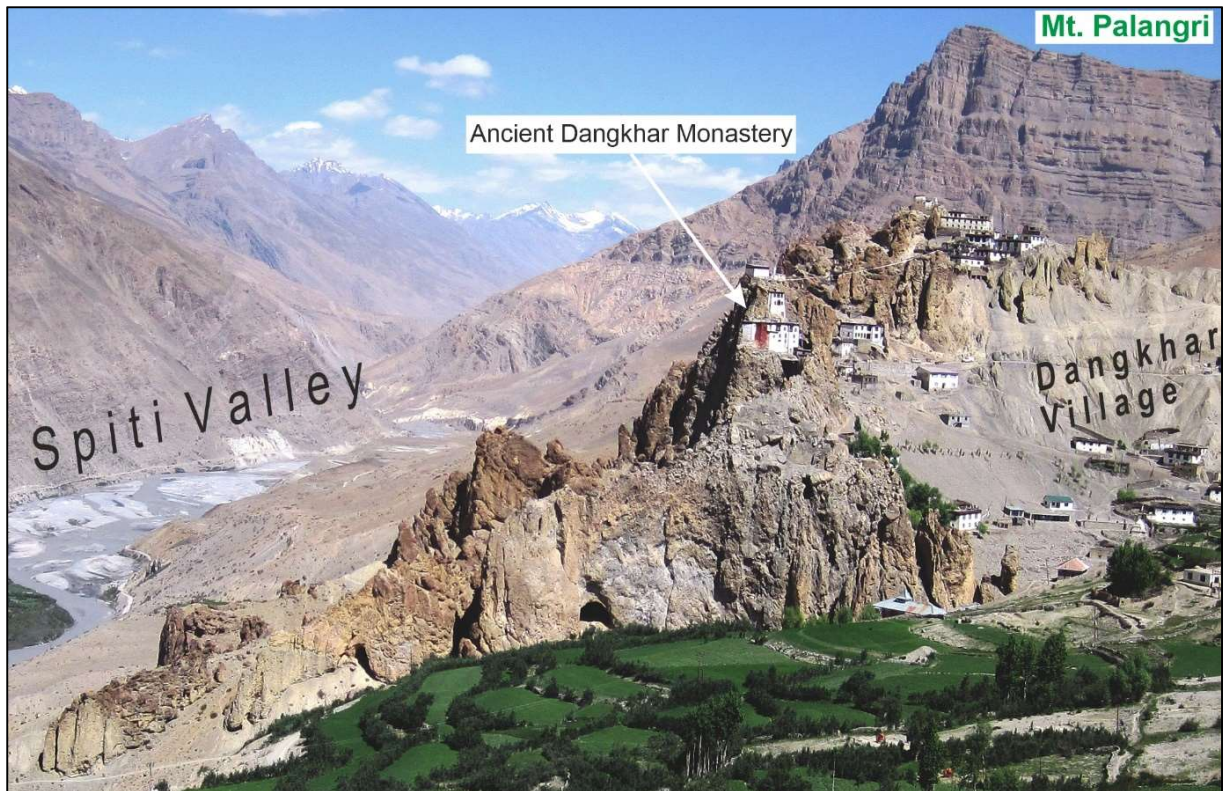


Fig. 1.3 Study area around the Ancient Dangkhar Monastery looking upstream the Spiti Valley

Hutton visited Dangkhar in 1840 that he reports to be *sitting on ragged spires on a spur, or offshoot of time worn rocks towards the river*. Moorcroft and Trebeck (1841), who already visited Dangkhar in 1820, mention the gently sloping landscape around the Dangkhar Lake for the first time, but no explanation of its origin is provided.

Another expedition to the area was later done by Thomson (1852) describing the alluvial deposits of the Spiti Valley in great detail. Arriving at Dangkhar he describes the rocks as an *elevated patch of alluvium resting high above the valley floor and extending even further uphill from the village*. Moreover, he recognized the position of the deposits to rest on the bedrock (*ancient rock*) not reaching down to the Spiti River.

Similar descriptions are provided by Theobald (1862), who also noticed the vast occurrence of terraces and talus in the Spiti Valley, which locally is cemented by percolation of water. He sees Dangkhar resting on a *heterogeneous mass of consolidated debris, worn into pinnacles with honey-combed cavities*.

Egerton (1864) describes Dangkhar to be *situated on a bluff of conglomerate limestone* and outlines how Spiti is especially of geological interest. When Harcourt (1871) visited Spiti, he described the position of Dangkhar to be on a *huge clayey promontory*.

Four years later, Wilson (1875) provides the oldest descriptions debris deposits around Mane naming them soft alluvial strata with steep ravines, worn into towers and all kinds of shapes.

He compares them to the deposits around Dangkhar calling them [...] *an immense ridge of soft strata which descends towards the river, but breaks off with a sudden fall [...]*.

The Austrian geologist Stoliczka (1866) was among the earliest researchers to conduct comprehensive and systematic geological studies in the Spiti area for the Geological Survey of India. He states for the first time, that the breccia deposits of Dangkhar could be related to a mass movement:

“Calcareous waters have occasionally with their solutions cemented these accumulations to a perfectly hard rock, as is to be found in places round Drangkhar. This town is built on ground which seems to be an immense slip of the western portion of the adjoining mountain. It seems to have resulted from the combined action of the flowing water below and probably great masses of snow above.”

McMahon (1879) was the first to notice and describe a synclinal bedrock structure stretching from Dangkhar beyond Mt. Palangri (Fig. 1.4a). He is also one of the first researchers to intensely deal with the glaciation history of the area and states that the upper Spiti Valley was glaciated in the past: [...] *the valley owes its shape, in part at least to the action of ice, the period during which a glacier flowed down the straight course of the Spiti river must have been very remote [...]*. He also describes physical evidence such as roches moutonnées near Losar and envisages a glacial descent down to Dangkhar. Diener (1896) dedicated an article on the ice age in the Himalaya, including a reference to Spiti. He also concludes that glaciers in the Spiti Valley descended down to about 3000 m.

Oldham (1888) recognized the existence of the a paleolake by the presence of lake sediments and was able to reconstruct the former lake extent: [...] *At one time its valley for many a mile was occupied by a lake whose only vestiges are now whitened cliffs of fine laminated clay which can be seen at intervals from near the bridge at Mani to near Lara, a distance of 9 or 10 miles [...]*. Griesbach (1891) continued geologic investigations in Spiti for the Geological Survey of India and provides one of the first detailed geological cross sections and sketches of the Dangkhar area (Fig. 1.4a & b).

Hayden (1904) established the basis for the lithostratigraphic division of the rocks of Spiti and also continued refining the geological maps of Spiti and adjacent areas. Since then, numerous geologic mapping campaigns involving Austrian geologists were conducted (e.g. von Krafft 1899; Diener 1912; Fuchs 1982; Draganits 2000; Wiesmayr and Grasemann 2002; Neumayer et al. 2004; Hornung et al. 2007; Kaspar and Kieffer 2015). Fuchs (1982) mapped large parts of the Pin Valley at 1:50.000 which was modified and extended by Wiesmayr (1997; 1999) and Neumayer et al. (2004). A more general geologic map is provided by Bhargava and Bassi (1998) and Bhargava (2008).

Besides the structural geological and paleontological investigations, also tectonic, climatic and geomorphic studies are emerging in the region (Phartiyal et al. 2009; Anoop et al. 2012; Kaspar and Kieffer 2015). Recently, the peculiar geological situation at the Ancient Dangkhar Monastery made it subject to investigations concerning geological and geotechnical remediation strategies (Kieffer and Steinbauer 201).

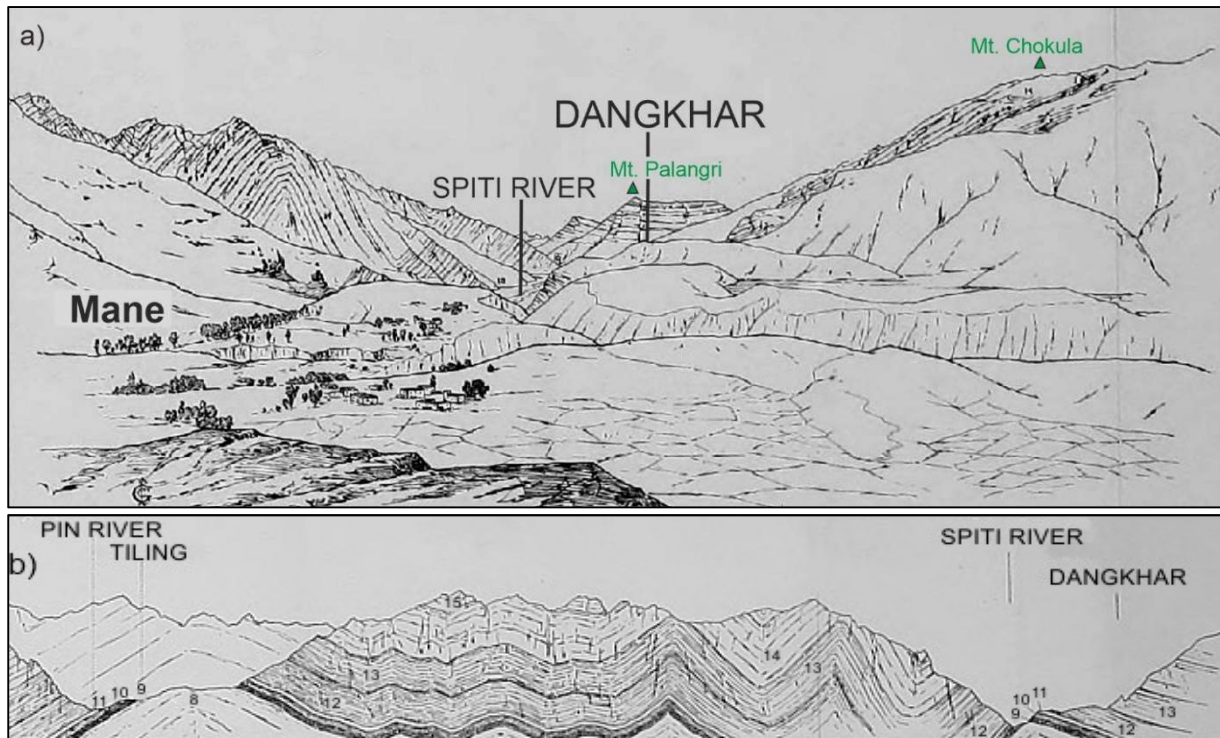


Fig. 1.4 Early geologic sketches of the Dangkhar area by Griesbach (1891). a) Geological cross section of the Spiti Valley near Dangkhar (8 – Ganmachidam Formation, 9 – Kuling Group, 10 & 11 – Mikin Formation, 12 – Kaga to Rongtong Formation, 13 – Alaror & Rangrik Formation, 14 & 15 – Kioto Group; formation names updated after Bhargava (2008). b) Sketch of the Dangkhar and Mane area looking northwest, upstream the Spiti Valley

2 BACKGROUND

2.1 Characteristics of non-catastrophic extremely large landslides

Most large landslides occur in the steepest 5% of the world's Cenozoic mountain ranges, are restricted to deep valleys (Korup et al. 2007) and linked to neotectonic activity (Varga 2006). Examples from the European Alps demonstrate how glacial retreat and subsequent debuitressing resulted in large, deep-seated landslides in post ice age times (Ambrosi and Crosta 2006). Such glacially preconditioned or paraglacial rock slope deformations affecting entire mountain slopes are also referred to as *rock mass deformation* (Slaymaker 2004) or *mountain slope deformation* and *rock slope deformation* (Hungri et al. 2014). These terms account for large scale slopes with a relief of 1 km or more and several diagnostic features, including: (i) presence of morphostructures such as lineaments and scarps, (ii) size of the landslide equivalent to the slope, (iii) slow, long-term movement (mm/yr), and (iv) presence of secondary landslides and other instabilities within the parent landslide (Fig. 2.1). The diagnostic morphostructures are referred to as *slope tectonics* (Zischinsky 1968; Jaboyedoff et al. 2011). Slope tectonic features are non-seismic, neotectonic, geomorphologic structures produced by landslide activity, resembling those of a tectonic origin (McCalpin 2013). Common slope tectonic structures (Fig. 2.2a, b) produced by extremely large landslides include scarps, double scarps and counter or antislope scarps, but also folding (Agliardi et al. 2001; Hewitt et al. 2008).

Extremely large landslides are bedrock landslides controlled by rock mass structure, lithology, topography, vegetation, hydrology, seismicity and climate (Hutchinson 1988, Agliardi et al. 2001) resulting in various mechanisms (Fig. 2.3). Formerly this landslide type was also referred to as *deep-seated gravitational slope deformation* (DSGSD, Agliardi et al. 2012), *Talzus Schub* (Stini 1941 – German for *closing-up of the valley*, Zischinsky 1968; or *valley obstruction*, Hermann and Bucksch 2014), *Sackungen* (German for *sagging*; Zischinsky 1966), *Bergzerreiung* (German for *mountain splitting*, Zischinsky 1968; Hermann and Bucksch 2014), or *block-type movements* (Pasek 1974). Most widely the above mentioned terms have been used to describe landslides where their internal deformation is large compared to the actual bulk movement along a well-defined basal slip surface (e.g. Radbruch-Hall 1978).

Dating of extremely large landslides has shown that the majority of landslide activity does not occur directly after the ice retreat, but rather some thousand years later during climatic conditions similar to those of recent times. This lag-time – or pre-failure endurance (Ballantyne 2002) – is attributed to the time it takes the slope to readjust to the stress and strength conditions after debuitressing. In some cases, extremely large landslides are capable

of deforming and bulldozing the glacial ice near the toe area so that slow rates of movement can already be achieved before deglaciation is completed (McColl and Davis 2013).

The trigger is generally subject to uncertainty, but typically includes glacial debuttressing, earthquakes or changes in ground water conditions (Agliardi et al. 2001; Krautblatter 2013).

However, non-catastrophic, slowly moving extremely large landslides cluster in the post-glacial valleys of alpine mountain regions and are generally considered as the result of long-term changes of slope morphology and stress conditions (Moser et al. 2017; McColl 2012).

The landslides experience their largest movements soon after initiation and are then subject to differential movements over various parts of the sliding mass that can occur over several thousand years (Agliardi et al. 2012).

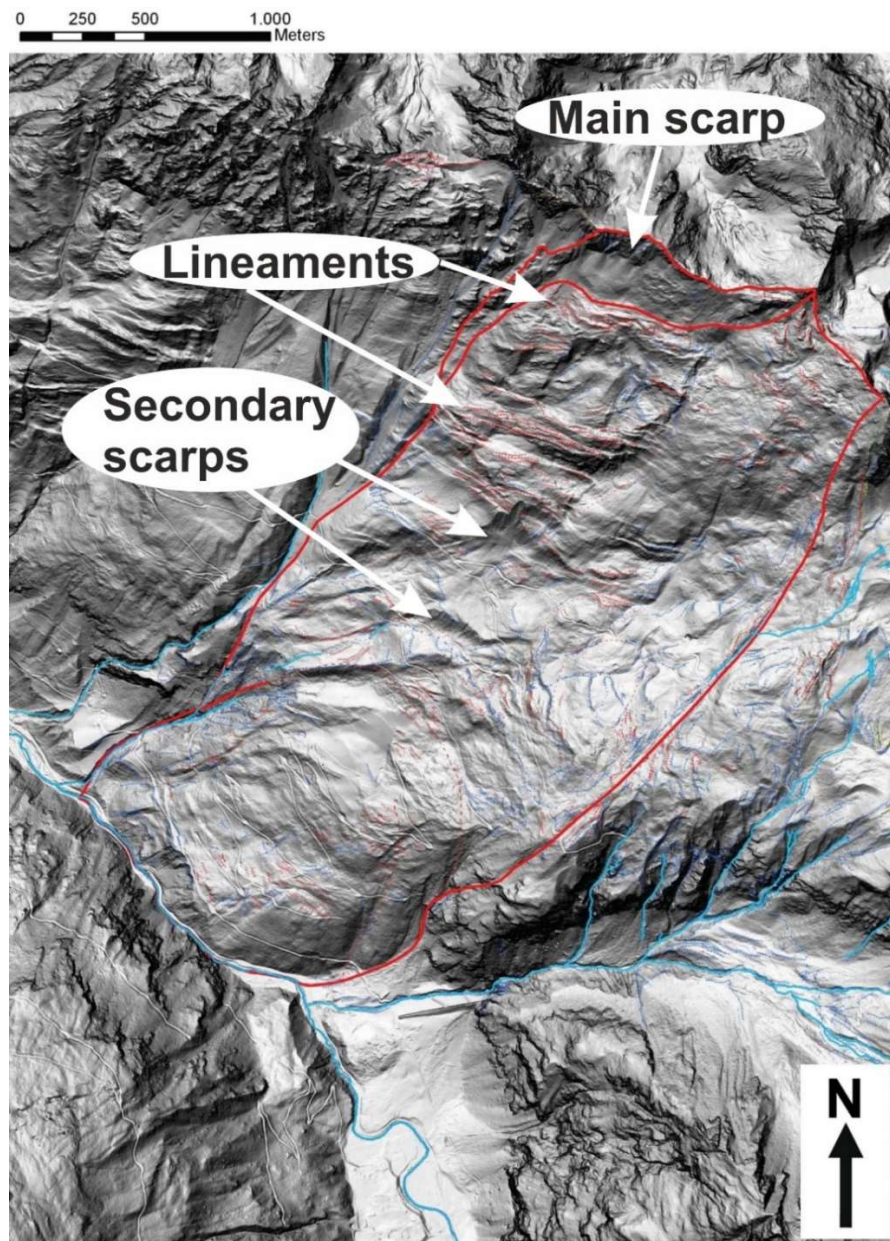


Fig. 2.1 Laserscan model of the Stupfarri Landslide (modified after Weißflog et al. 2010)

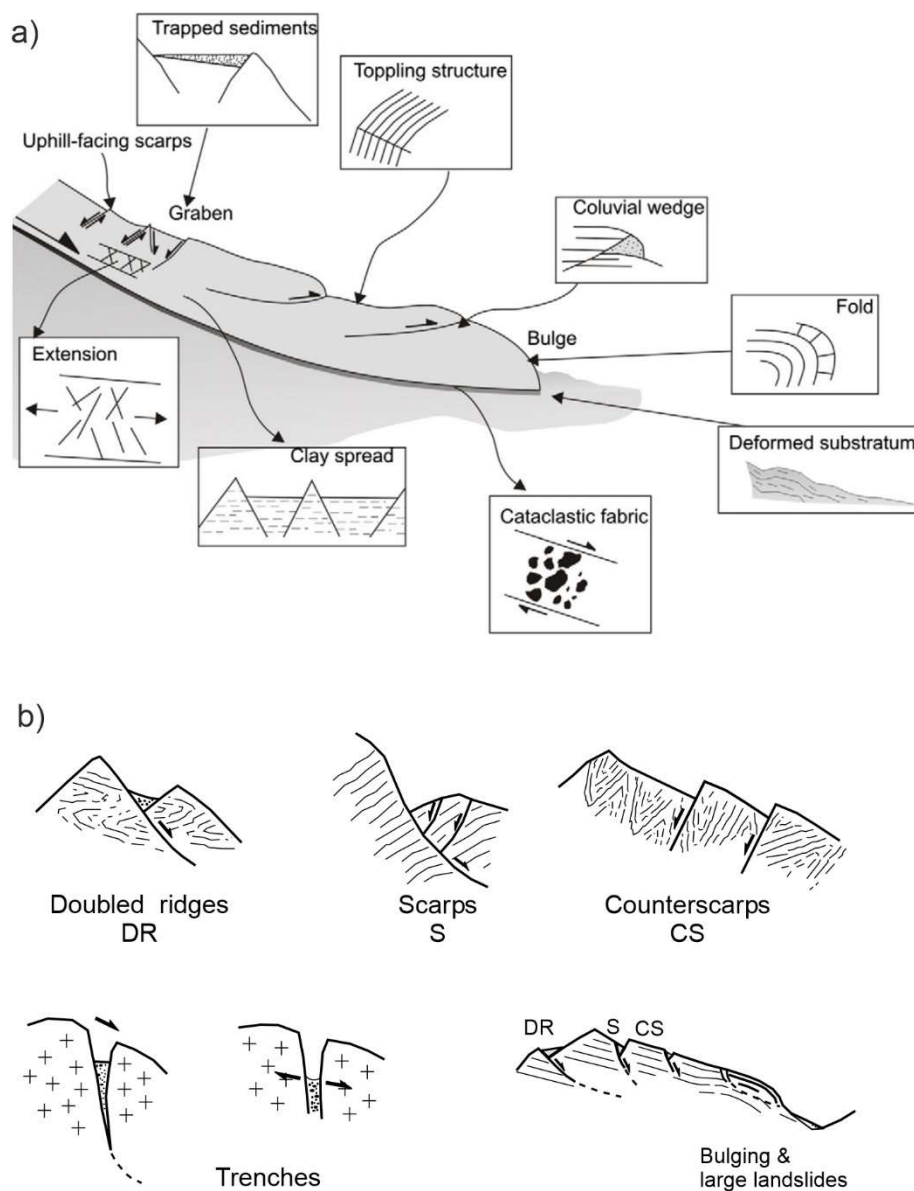


Fig. 2.2 Slope tectonic features of extremely large landslides. a) Landslide deformation structures. b) characteristic morphostructures of extremely large, non-catastrophic landslides (after Jaboyedoff et al. 2013; Agliardi et al. 2001)

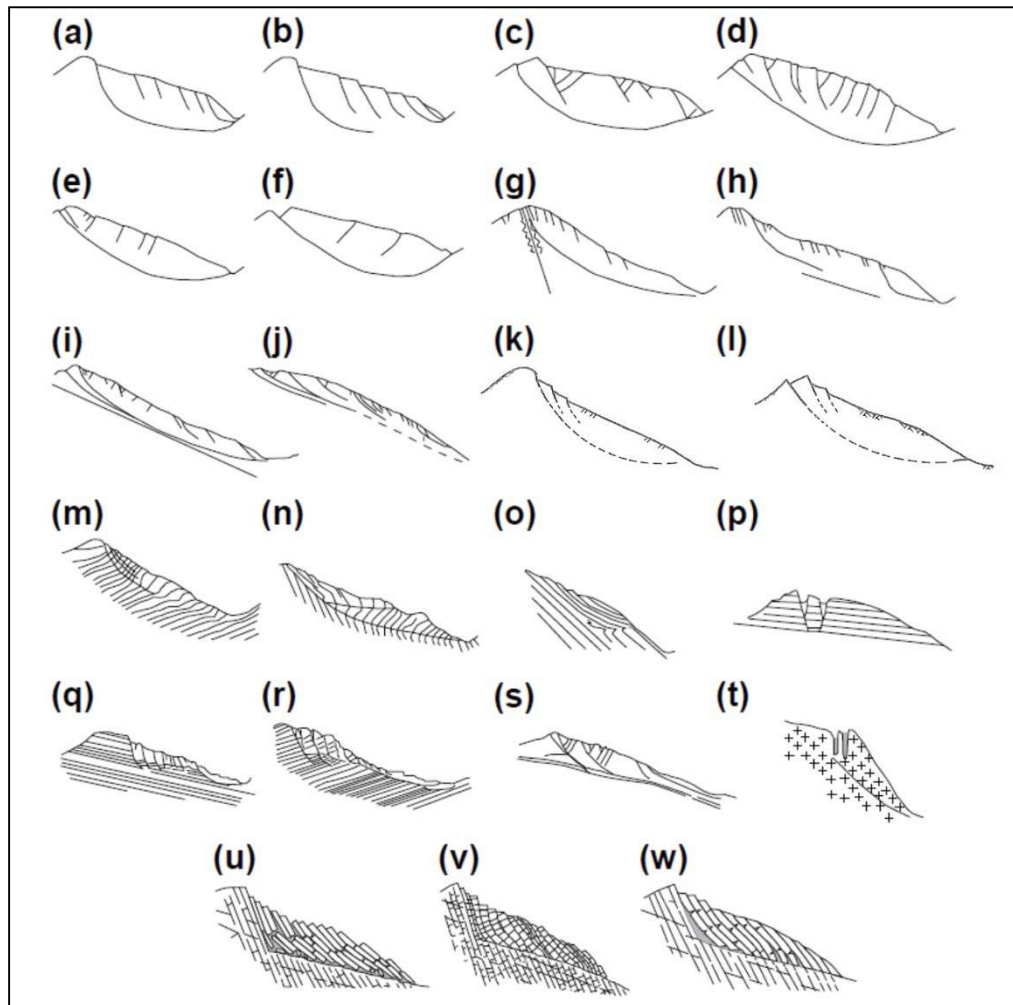


Fig. 2.3 Different mechanisms of large-scale slow rock slope deformations reported in literature. (a), (b), (c), (f) Bois et al. (2008); (d) Mahr (1977); (e), (g), (h), (i) Ambrosi and Crosta (2006); (j) Agliardi et al. (2001); (k), (l) Hutchinson (1988); (m), (n) Zischinsky (1966); (o), (p), (t) Chigira (1992); (q), (r) Nemcok (1972); (s) Agliardi et al. (2009b); (u), (v), (w) Kieffer (1998). Compiled by Agliardi et al. (2012), for detailed references see there

2.2 Landslide geochronology

The timing of landslide occurrence and activity is a key aspect in landslide studies. Factors affecting landslide activity include paleo-climatic and (paleo)-seismic conditions, but also the nature and type of the landslide, i.e. if a landslide is a short lived catastrophic or long term non-catastrophic event, Activity classes furthermore distinguish between active, reactivated, suspended, inactive (including dormant, stabilized, abandoned or relict) and fossil or ancient (Cruden and Varnes 1996; Mather et al. 2003). Initial estimates on the age of landslides can be made by geomorphologic field observations and mapping. While tropical climates tend to longer preserve evidence of landslides, arid environments show a less high potential for preservation over geologic times. Evidence of fossil and/or relict landslides can be identified back to about 100000 years (Tab. 2.1, Mather et al. 2003). Large bedrock landslides are among those with the highest preservation potential (Clague 2015).

Advances in analytical methods have greatly increased the possibilities to assess landslide ages (Lang et al. 1999; Ballantyne et al. 2014; Pánek 2014). These analytical methods (Fig. 2.4) constitute a suite of direct and indirect dating techniques providing event ages and minimum or maximum ages of landslide events, respectively (Lang et al. 1999). With indirect dating techniques (Fig. 2.4) rather than the landslide itself, landslide related features are being dated. This includes sediment accumulations formed after the landslide event containing organic material (radiocarbon dating), exposed boulders (CRE dating), or cemented landslide debris (Uranium/Thorium dating). Direct dating techniques analyze features directly affected by the landslides event such as trees (dendrochronology) and lichens (lichenometry). Stratigraphic techniques assess the relative positions and cross cutting relations of sedimentary bodies distinguishing between *above*, *below* and *mixed within* the landslide (Lang et al. 1999). A more detailed explanation of radiocarbon dating, which was applied in the present study, is provided in the appendix.

Considering the geomorphological context of the sample site is critical in order to obtain correct time series for landslides. Extremely large landslides can reactivate over time, introducing multiple time stamps, which not all might be datable or are not detectable, ultimately underestimating the actual landslide activity (Lang et al. 1999).

Activity state	Identification of causes of movement	Condition of main scarp	Condition of lateral margins	Internal morphology	Estimated age (years) ^a
Active – currently moving (includes inactive landslides that have been reactivated)	Causes of movement identifiable and active	Sharp; unvegetated	Sharp; unvegetated; streams at edge	Hummocky; fresh scarps; reverse slopes; undrained depressions; fresh tension cracks; active movement	< 100 (historic)
Suspended – moved within the last 12 months and likely to become active again	Causes of movement identifiable and likely to re-occur	Sharp; unvegetated	Sharp; unvegetated; streams at edge	Hummocky; fresh scarps; reverse slopes; undrained depressions; identifiable tension cracks	< 100 (historic)
Dormant – young (inactive)	Cause of movement still identifiable and could re-occur	Relatively sharp; partially vegetated	Relatively sharp; partially vegetated; lateral streams fed by small tributaries flowing off the main body of the slide	Hummocky; relatively sharp and fresh scarps; reverse slopes; undrained depressions; tension cracks closed and vegetated but marked by small depressions	100–5000 (late Holocene)
Dormant – mature (inactive); described as abandoned by Dikau <i>et al.</i> (1996)	Cause of movement still identifiable but not likely to re-occur	Smooth; vegetated	Smooth vegetated; lateral streams fed by tributaries flowing off the main body of the slide	Smooth rolling topography; disrupted and disjointed internal drainage network	5000–10,000 (early Holocene)
Dormant – old (inactive) or relict ^b	Causes of movement may be inferred but associated with different climatic or geomorphological conditions	Dissected; vegetated	Vague lateral margins; no lateral drainage	Smooth, undulating topography; normal stream pattern	10,000–100,000 (Late Pleistocene)
Fossil (inactive) or ancient ^b	Causes of movement unknown but associated with different climatic and geomorphological conditions	May not be identifiable; likely to be at least partially, if not completely, removed by erosion	May not be identifiable; likely to be at least partially, if not completely, removed by erosion	Fully integrated into the existing topography and very little indication of the former landslide morphology remains	> 100,000

Tab. 2.1 Landslide activity states and estimated age based on geomorphologic conditions (after Mather et al. 2003 and references therein)

The applicability of the dating methods depends also on the type of landslide and the source areas of datable material that might be allochthonous. Catastrophic landslides killing trees can be ideal to obtain event ages, whereas trees can survive and travel on slowly moving landslides resulting in incorrect ages (Clague 2015).

However, in order to reliably interpret absolute age dates, the type, nature and distribution of landslide features have to be considered in their geomorphic context (Lang et al. 1999).

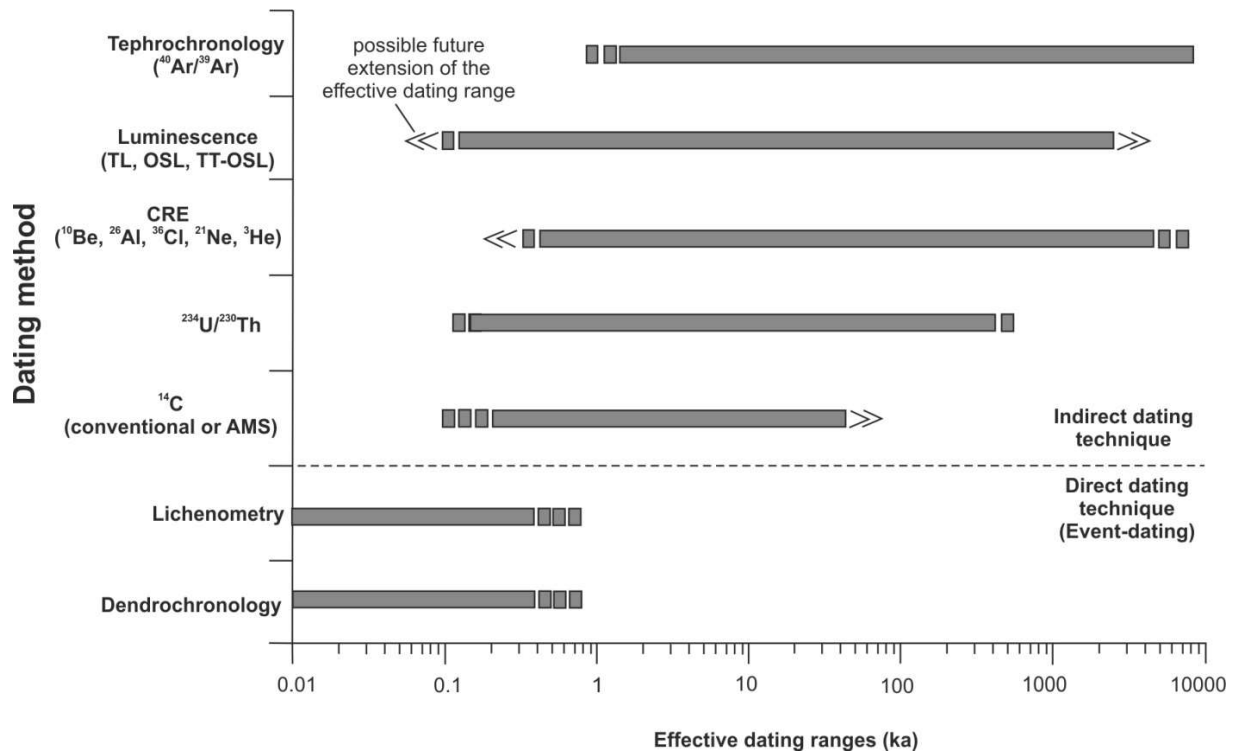


Fig. 2.4 Dating methods applied in landslide studies. TT OSL/OSL = (Thermally Transferred/Optically Stimulated Luminescence, TL = Thermoluminescence, CRE = Cosmic Ray Exposure, AMS = Accelerator Mass Spectrometry; modified after Pánek 2014)

3 REGIONAL CONDITIONS

3.1 The Himalayan orogen

The Himalayas (Sanskrit: *hima* = snow; *ālaya* = dwelling) are the result of a continent – continent collision between Asia and India (Fig. 3.1a, b & c) that commenced about 56 million years ago (Sciunnach and Garzanti 2012). The ongoing northward movement of the Indian plate led to the creation of the world's highest peaks. The Himalayan Mountain Belt is subdivided into four zones separated by large scale fault zones Gansser (1964). The main zones from south to north are: Subhimalaya, Lesser Himalaya, High Himalaya and Tethys (Tibetan) Himalaya. The zones are separated from each other by four large scale north-dipping fault zones (Fig. 3.2 and Fig. 3.3) as a result of the Asian backstop (e.g. Hornung et al. 2007). From south to north the fault zones are the Main Frontal Thrust (MFT), Main Boundary Thrust (MBT), Main Central Thrust (MCT) and the South Tibet Detachment System (STD or STDZ; DiPietro and Pogue; Yin 2006).

The study area is located within Tethys Himalaya rocks, a sedimentary sequence of Proterozoic to Mesozoic rocks deposited on the northern margin of India before the collision with Asia. The characteristics of the respective zones are briefly described in the following section from north to south.

3.1.1 Indus Tsangpo Suture Zone (ITSZ) and Transhimalaya

The 3000 km long Indus Tsangpo Suture Zone (ITSZ; e.g. DiPietro and Pogue 2004; Hodges 2000), Indus Yarlung Suture Zone (ISZ), or Indus Tsangpo Melange Zone (ISMZ; e.g. Wyss et al. 1999) marks the boundary between Indian and Asian continent (Fig. 3.2). It consists of an ophiolitic mélangé (Neo-Tethys Ocean remnants) with a mixture of turbidites, radiolarites, mantle rocks such as peridotites and serpentinites, basalts and other island arc rocks and associated flysch deposits (Steck 2003; Draganits 2000). The southern and northern limit are defined by the Great Counter Thrust system (GCT) and Karakoram Fault, respectively. The region beyond the ITSZ is referred to as Transhimalayas accounting for the rocks of the Tibetan plateau (Fig. 3.2 and Fig. 3.3), comprising the Lhasa terrane, Qiangtang terrane and associated Batholiths. The molasse of the Kohistan-Ladakh Arc Complex locally overlies the Lhasa terrane in the NW Himalaya (Fig. 3.2 and Fig. 3.3).

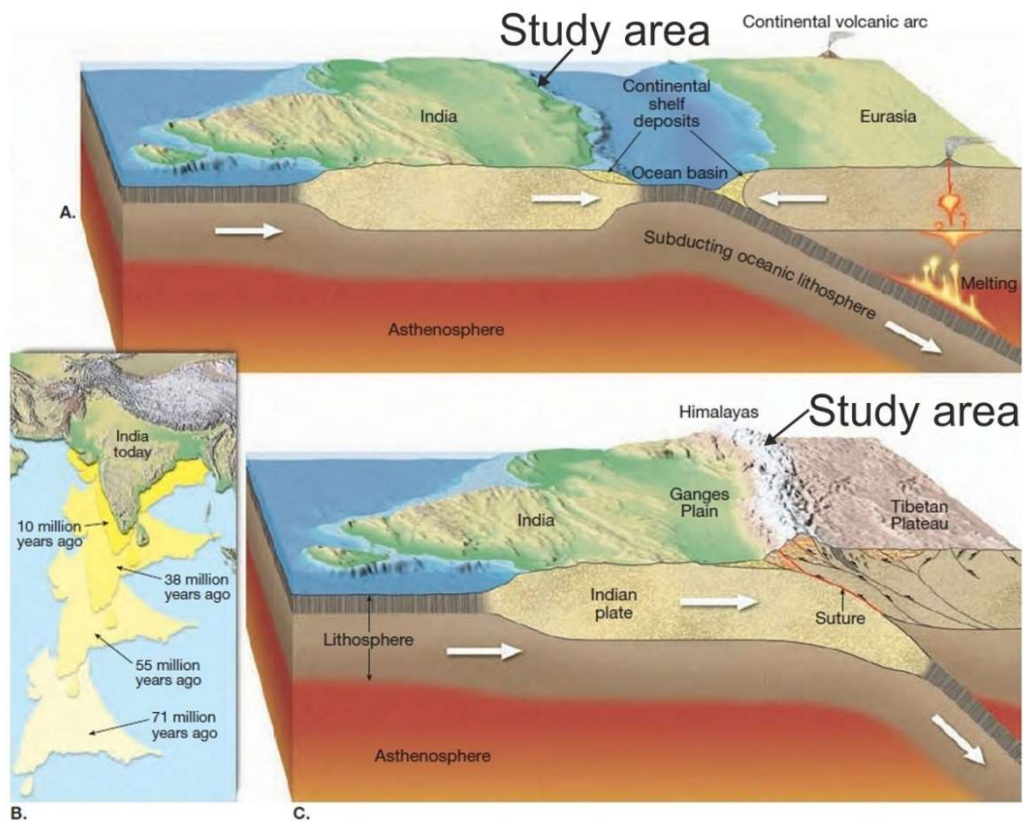


Fig. 3.1 Evolution of the Himalayan orogen. a & b) The Indian subcontinent approaches Asia closing the Tethys ocean basin. c) Present day situation of the Himalaya with extensive development of thrusting, nape stacking and subsequent emplacement of marine deposits at high elevations (modified after Lutgens et al. 2012)

3.1.2 Tethys (Tibetan) Himalaya and Higher Himalaya

The Tethys Himalaya (TH) represents the neotethyan shelf part of the High Himalaya (HH). The HH is separated by the TH into the High Himalaya Crystalline Sequence (HHC or Vaikrita crystalline; Thöni et al. 2012; Draganits 2000) and the North Himalayan Crystalline (NHC; Girard et al. 1999; Thöni et al. 2012).

The TH contains an almost continuous stratigraphic succession from the Neoproterozoic to Eocene, resting as detached synclinoria over the Vaikrita crystalline of the HH (Fig. 3.2 and Fig. 3.3; Bhargava 2008). The study area is located within the Spiti Valley, which is part of the northwest to southeast trending Zaskar – Spiti synclinorium (Fig. 3.2) built up of several alternating syn- and anticlines and faults (Bhargava 2008). The dominant lithologies are sandstones, carbonates, shales, and metasediments such as quartzites and marbles (Phartiyal et al. 2009). The boundary between the TH and HH is expressed as the STD, whereas to the north the TH is limited by the ITSZ. In the NW Himalaya, the STD is locally referred to as Zaskar Shear Zone.

However, defining a clear boundary between the TH and the HH is not always trivial as the HHC, predominantly consisting of amphibolite grade gneiss and migmatite rocks of the Vaikrita Group (Fuchs 1981) and subordinate Paleozoic and Tertiary plutonic rocks (Wyss et al. 1999), often gradually passes into the unmetamorphosed Haimanta-Tanawal rocks at the base of the TH (Girard et al. 1999). The Haimanta-Tanawal rocks are considered to be the crystalline base of the Tethys Himalaya (Yin 2006) and unmetamorphosed equivalent of the upper part of the HHC (Dèzes et al. 1999). Along strike variations additionally complicate the relationship between the MCT and the STD. The MCT (aka. Vaikrita Thrust in the NW Himalaya) is a 2 to 10 km thick shear zone (Yin 2006), separating the HH from the Lesser Himalaya (LH).

3.1.3 Lesser Himalaya

The Lesser Himalaya (LH) is bound to the north by the MCT and to the south by the MBT (Fig. 3.2 and Fig. 3.3). It consists of two units: (i) the Lesser Himalayan Sediments (LHS) containing the Proterozoic to Paleozoic sedimentary cover representing an older, more proximal part of Gondwana with respect to the Tethys Himalaya (Hodges 2000). It is predominantly composed of quartzites, phyllites, slates and metavolcanic rocks, granites and diabase (Steck 2003), and (ii) the locally occurring Lesser Himalayan Crystalline (LHC) made up of high grade metamorphosed sediments and Proterozoic intrusions (e.g. Wyss et al. 1999). The LHC is considered to be either part of the MCT hanging wall or out-of-sequence thrust sheets (Munsiari Thrust; MT) of the MCT footwall (Yin 2006, Wiesmayr and Grasemann 2002). Locally, LH units are exposed in tectonic windows within the Higher Himalaya (e.g. Larji-Kulu-Rampur Window; Yin 2006, Fig. 3.2 and Fig. 3.3).

3.1.4 Subhimalaya

The Subhimalaya (SH) or Siwalik foothills are composed of up to 8000 m thick Tertiary molasse to shallow marine sediments (Steck 2003) overridden by the Lesser Himalaya along the MBT (Draganits 2000; Wyss et al. 1999). It is the result of erosion of the Himalayan Mountain Belt and subsequent sediment accumulation in the foreland basin which formed due to flexural loading of the Indian plate (Steck 2003). The footwall contact to the Indo-Gangetic plain is defined by the MFT.

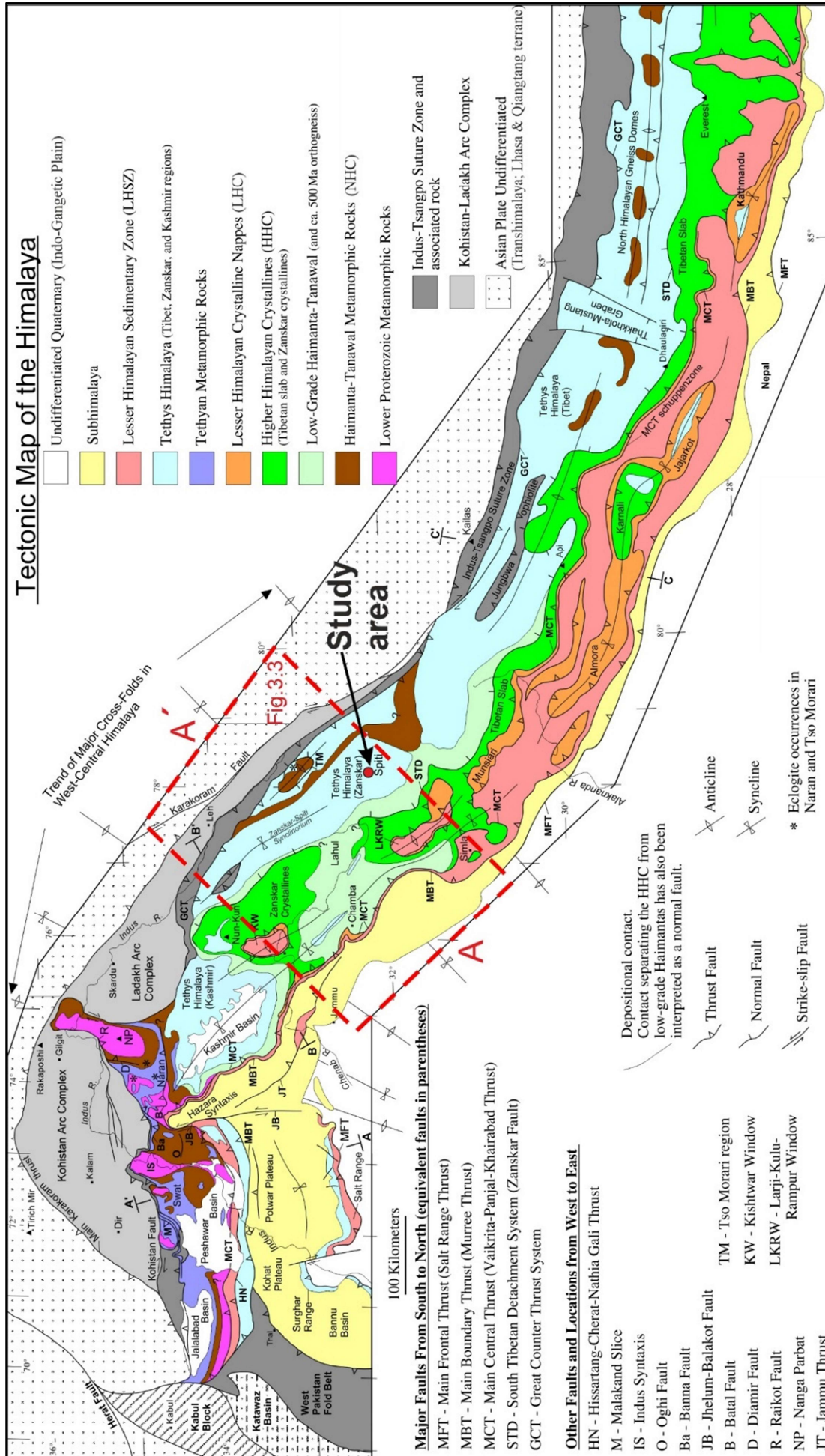


Fig. 3.2 Tectonic map of the central and northwestern Himalayan Mountain Belt. Block diagram cross section A – A' is shown in Fig.3.3 (modified after DiPietro and Pogue 2004)

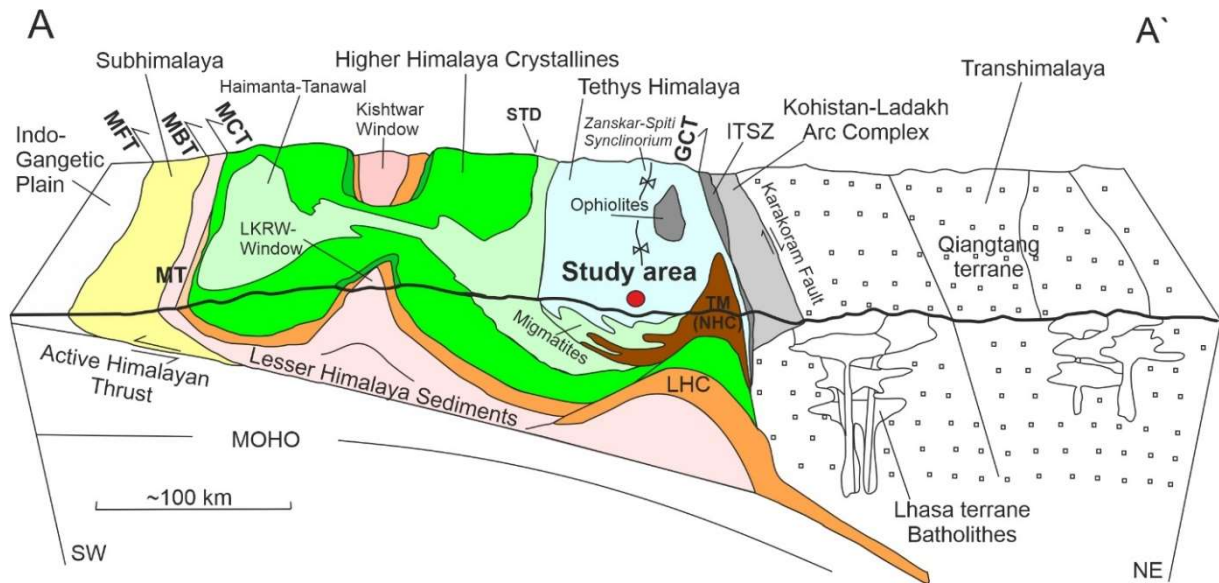


Fig. 3.3 Schematic block diagram cross section through the northwestern Himalaya region illustrating the main structural components of the Himalayan Mountain Belt. The study area in Spiti is situated within the Tethys Himalaya. For abbreviations see text and Fig 3.2 (modified and compiled after Steck 2003; DiPietro and Pogue 2004; Hornung et al. 2007; Thöni et al. 2012; Wiesmayr and Grasemann 2002)

3.2 The Spiti Valley

3.2.1 Geologic and geomorphologic conditions

The study area is located in the remote, rugged, arid, high mountain Spiti Valley, Himachal Pradesh, India (Fig. 3.4a) at elevations between 3400 – 5600 m. The Spiti Valley shows properties of a youthful landscape with high elevation up to nearly 6000 m and local relief which is represented as almost vertical cliffs up to approximately 800 m in height. The Spiti Valley extends approximately 150 km westward from the headwaters at Kunzum pass to Khab where it merges with the Sutlej River (Fig. 3.4b). The Spiti basin catchment with its major tributaries occupies about 5320 km² with an average gradient of about 17 m/km (Phartiyal et al. 2011). Originating at the Nogpo-Tokpo Glacier near Kunzum Pass (Srivastava et al. 2013), the Spiti river gains volume over a total length of about 185 km by various tributary streams along its way before joining with the Sutlej River. The majority of the tributary streams exhibit a trellis to dendritic pattern. Springs are quite common in the area and of fracture and seepage type, with the latter ones occurring on talus slopes (Balpande and Singh 2007). The discharge of these perennial and seasonal springs varies and depends on the recharge by snowfall and rainfall (Balpande and Singh 2007).

Geomorphically, the Spiti Valley can be divided into upper and lower reaches. The north to northwest trending upper Spiti Valley has been sculpted by Quaternary fluvial, paraglacial and mass wasting processes (Bhargava 1990). The study area located around Dangkhari village is characterized by a broad, braided channel that is bounded by fluvial and lacustrine terraces, and the terrain locally exhibits badland erosional features such as up to 60 m high hoodoos or khatpas (Spitian), U-shaped valley profiles, and talus mantled slopes dissected by ephemeral stream channels (Kieffer and Steinbauer 2012). Soil development in the study area is poor and can be classified as orthent (entisols) or lithosols according to the USDA (United States Department of Agriculture) and FAO (Food and Agriculture Organization) classifications, respectively. The vegetation of Spiti is scarce and can be chiefly classified as high mountain arid steppe (Kuhle 1990) characterized by about 30 cm high shrubs and grassy spots on the colluvium covered slopes and single trees on the valley floors. Locally, the colluvium covered slopes are used for agriculture.

The lower Spiti Valley is characterized by a straight to meandering river channel, bound by steep slopes and tributaries with waterfalls (Phartiyal et al. 2009). The Pin and Lingti Rivers are major tributaries of the Spiti River and border the study area to the west and northwest, respectively. The study area coincides with the abrupt morphological transition from the upper to the lower Spiti Valley (Fig. 3.4b). Rarely the Spiti Valley is subdivided into three sections, i.e. upper, middle, and lower (Marh and Rana 2014).

The study area is located within Permian to early Jurassic sedimentary to low grade metamorphic rocks dominated by limestone, dolomite, shale and sandstone of the Kuling Group and Lilang Supergroup (Hayden 1904; Bhargava 2008). In the Upper Spiti Valley, the Spiti River flows in northwest to southeast direction eroding its course along the axis of the Spiti Anticline (Fuchs 1982; Bhargava 2008; Srivastava et al. 2013). Between Kaza and Lingti this anticline is overturned towards the southwest (Fuchs 1982).

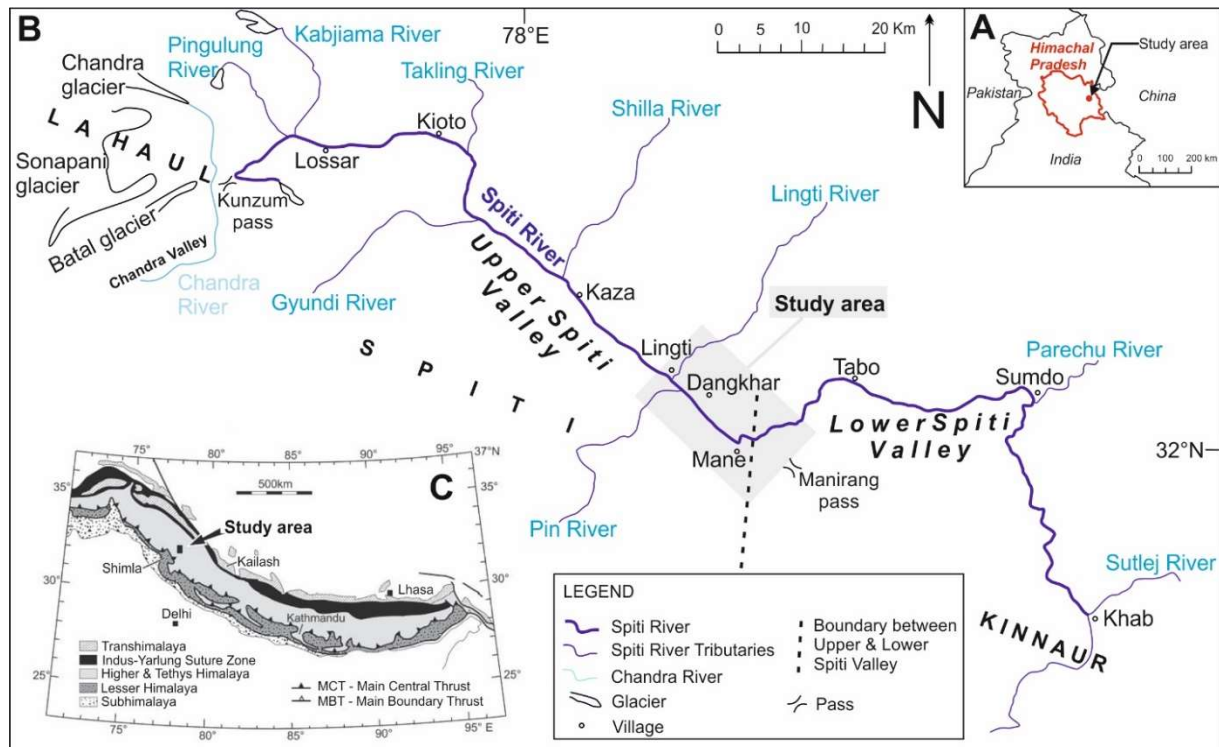


Fig. 3.4 Location map of the study area. a) Geographic location of the study area within Himachal Pradesh, India. b) The Spiti Valley with its major rivers and villages. c) Simplified tectonic map of the Himalaya (modified after Neumayer et al. 2004)

3.2.2 Regional seismotectonics and landsliding

The Lahaul-Spiti region is one of the most active tectonic regions in India (BMTPC 2003) with several active faults which are predominantly normal faults (Fig. 3.5; Tab. 3.1). Major recent earthquakes such as the M_b 6.2 1975 Kinnaur Earthquake occurred along the Kaurik-Chango Fault (Ni and Barazangi 1985), and also the Spiti Valley Fault (SVF) ruptured during that event (GSI 2011a). The SVF is a major southeast to northwest trending active normal fault in the study area, extending valley parallel for about 35 km (GSI 2011a; Bhargava and Bassi 1998). The SVF has been episodically active throughout the Holocene as documented within displaced strata of lake sediments at 7.8, 7.4, 6.5 and 6.1 thousand years ago (Anoop et al. 2012) and exposed fault segments in the Spiti River (Bhargava 1990). The present seismicity of the Spiti Valley Fault is on average one to two earthquakes per day with magnitudes of two or less, whereas the seismicity of the SVF in general increases towards northwest (GSI 2011a). The majority of the earthquakes in the study area occur at hypocentral depths of 10 – 25 km (GSI 2011a), with rare events recorded at depths up to 70 km (IRIS 2015).

Shanker and Shubham (2018) provide local peak ground acceleration (PGA) data for Himachal Pradesh. The estimated PGA values for the study area lie between 15 to 20 % of gravity. According to the Vulnerability Atlas of India (BMTPC 2003), the study area falls into zone VIII (Fig. 3.6) of the Medwedew-Sponheuer-Kárník (MSK) scale where PGA values between 25 to 30 % of gravity are typically expected. The Global Seismic Hazard Assessment Program estimates the study area has a 10% chance of exceeding a PGA in the range of 30 to 40% of gravity, within the next 50 years (Shedlock et al. 2000). As a comparison, ground motions at the site that could develop based on the Holocene active regional faults were estimated using surface rupture length-magnitude regressions (Wells and Coppersmith 1994) and ground motion attenuation relations for the Himalayan region (Singh et al. 1996; Jain et al. 2000). These results are generally commensurate with the values cited in literature (Tab. 3.1), with the exception of the SVF. Based on the regression analysis, the SVF has the potential to generate a PGA on the order of 100 % of gravity.

Fig. 3.5 also shows thirteen major late Pleistocene and Holocene landslides that occurred along slopes bordering the Spiti and Sutlej Valleys (Bookhagen et al. 2005). Tab. 3.2 lists details of these landslides. The 1.4 km³ Mane Landslide, also known as the Sichling Landslide (Bookhagen et al. 2005) or Sichling rock avalanche (Dortch et al. 2009) and the approximately 0.5 km³ Lingti Landslide (Bookhagen et al. 2005) occur partly within the study area. Deposits of the Mane Landslide created a landslide dam, blocking the Spiti River for about 2550±80 years from 8700 to 6100 BP (Bookhagen et al. 2005; Anoop et al. 2012). Lake sediments of this Mane paleo-lake developed 20 km upstream along the flanks of the Spiti Valley and parts of its side valleys, such as the Lingti and Pin Valley (Anoop et al. 2012).

Catastrophic landslides in the Spiti Valley such as the 1975 Parechu Landslide, the ca. 8700 BP Mane Landslide, Hansa paleo-landslide and a landslide which occurred in 2009 at a location approximately 25 km northwest of the site are evidence for seismically triggered landslides (Anoop et al. 2012) and are partly related to the activity of the SVF (GSI 2011b).

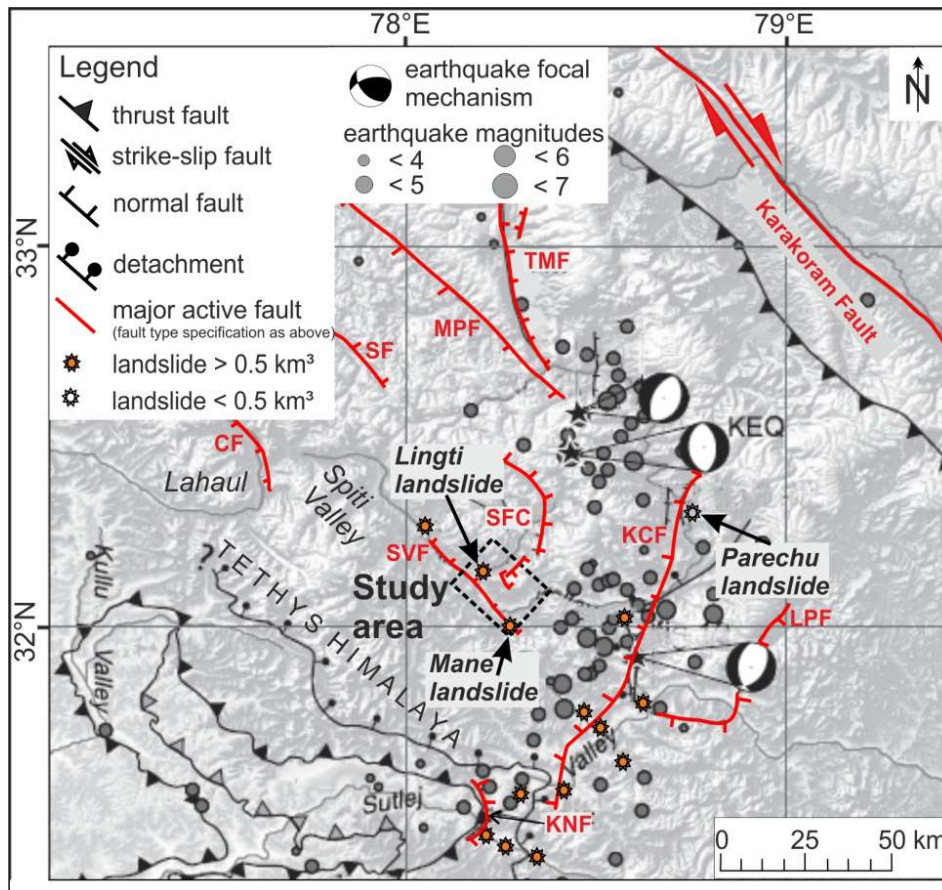


Fig. 3.5 Seismotectonic map of the study area and surrounding regions (compiled after Bhargava 1990; Bhargava and Bassi 1998; Bookhagen et al. 2005; Hintersberger et al. 2010; Anoop et al. 2012). CF – Chandra Fault, KCF – Kaurik-Chango Fault, KNF – Karcham Normal Fault, LPF – Leo Pargil Fault, MPF – More Plain Fault, SF – Sarchu Fault, SFC – Syarma Fault Complex, SVF – Spiti Valley Fault, TMF – Tso Morari Fault. Moment tensors shown for major large earthquakes (KEQ – Kinnaur Earthquake). Landslide details are listed in Tab. 3.2

Fault name	Fault type	Total fault length [km]	Ruptured fault segment length [km]	M_w max. Wells & Coppersmith (1994)	Distance to study area [km]	PGA [g] Jain et al. (2000)	PGA [g] Singh et al. (1996)
SVF	normal	35	12	6.3	1	0.92	1.23
KCF	normal	124	41	7.0	46	0.08	0.20
SFC-1	normal	34	11	6.3	16	0.11	0.22
SFC-2	normal	8	3	5.4	6	0.14	0.22
SFC-3	normal	6	2	5.3	4	0.17	0.26
TMF	normal	82	27	6.8	66	0.05	0.13
LPF	normal	75	25	6.7	60	0.05	0.14
KNF	normal	20	7	5.9	56	0.03	0.08
SF	normal	50	17	6.5	68	0.04	0.11
MPF	normal	75	25	6.7	60	0.05	0.14
CF	normal	38	13	6.3	72	0.03	0.09
Karakoram Fault	strike slip	730	243	7.8	141	0.05	0.18

Tab. 3.1 Seismic characterization of the study area. Fault abbreviations as in Fig. 3.5. Earthquakes are assumed to occur within ruptured fault segments of the respective faults, which are considered to be about one third of the total fault length (Wells and Coppersmith 1994; Shanker and Shubham 2018)

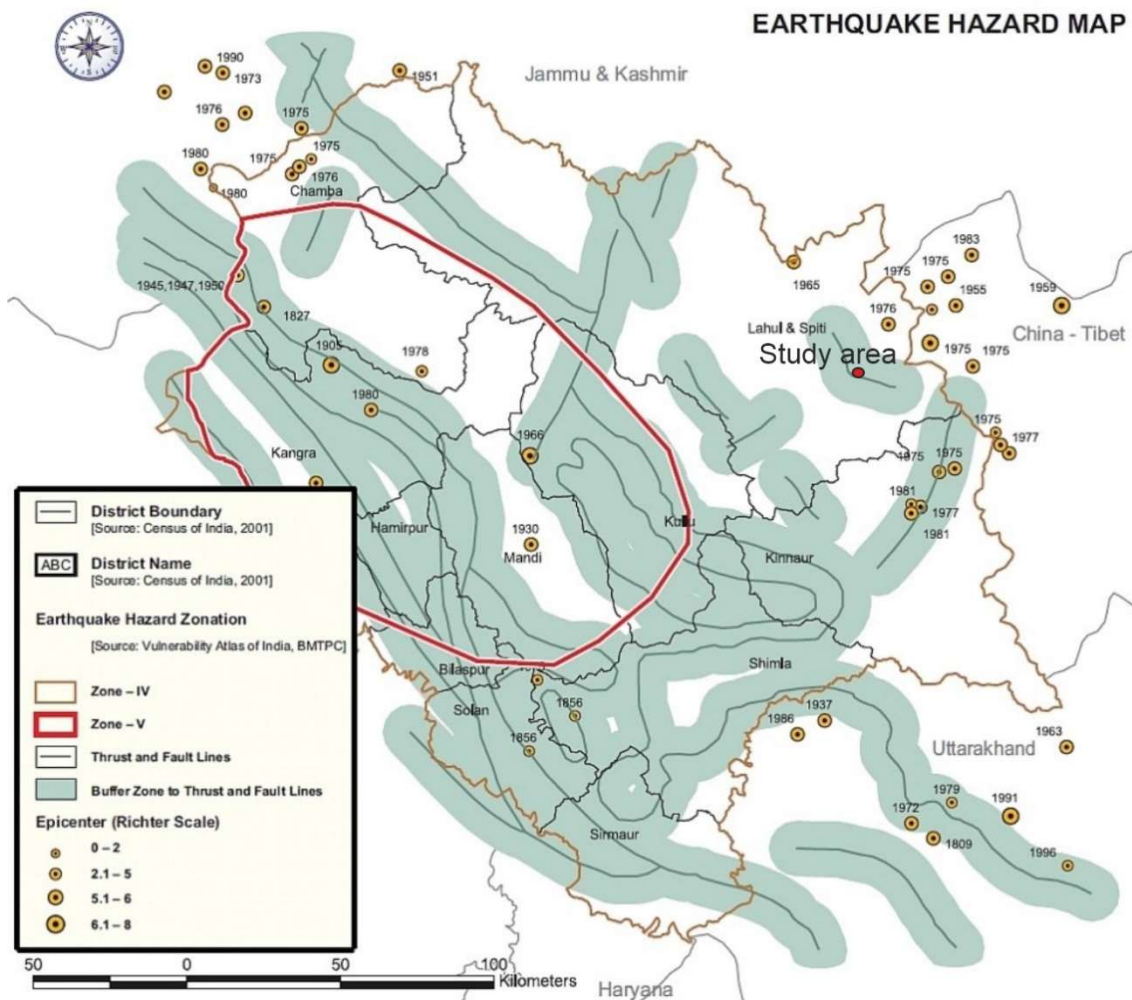


Fig. 3.6 Earthquake hazard map of Himachal Pradesh (Vulnerability Atlas of HP). The study area falls under Zone IV of the Vulnerability Atlas of India, which corresponds to zone VIII of the MSK scale, rating the region as a high damage risk zone (after SEEDS 2009)

Recent studies suggest a clustering of landslides in the northwestern Himalaya at the end of Pleistocene to Holocene glaciation phases accompanied by intensified monsoon phases (Srivastava et al. 2013). Coinciding intensified precipitation and glacial retreat with subsequent debutting of slopes has been suspected as driving factors for landslides in the Spiti Valley (Srivastava et al. 2013).

Presently, landslides are a common phenomenon in the Spiti Valley and are related to heavy monsoon rainfall events causing blocked roads (Times of India 2018). Large areas of the Spiti district are classified as zone of high risk with respect to landsliding (Fig. 3.7).

Per iod	#	Landslide (Blocked River)	Calibrated age (1 σ) [yr B.P.]		Landslide location	Land- slide volume [10 ⁹ m ³]	Area of dammed lake [10 ⁶ m ²]	Volume of lake sediments [10 ⁶ m ³]
			bottom	top				
Holocene	A	Kaza (Spiti)	N.D.	2860 \pm 70	78°05.5' E 32°10.5' N	0.5	2.9	0.4
	B	Lingti (Lingti)	N.D.	N.D.	78°12.4' E 32°08.1' N	0.3	3.4	0.5
	C	Sichling / Mane (Spiti)	8711 \pm 68	6158 \pm 12 6737 \pm 19	78°10.5' E 32°06.7' N	1.4	4.7	1.6
	D	Akpa (Sutlej)	N.D.	N.D.	78°23.5' E 31°34.8' N	0.5	4.5	0.7
	E	Rekong Peo (Sutlej)	N.D.	N.D.	78°14.8' E 31°30.9' N	1.0	5.4	0.9
	F	Kuppa (Baspa)	7594 \pm 27	5297 \pm 17 5223 \pm 59	78°14.3' E 31°26.0' N	0.6	5.6	1.2
	G	Rakchham (Baspa)	N.D.	N.D.	78°16.5' E 31°24.9' N	0.5	2.6	0.4
	H	Khorgala (Baspa)	N.D.	N.D.	78°18.9' E 31°24.3' N	0.4	1.5	0.1
Late Pleistocene	I	Chango (Spiti)	28570 \pm 920 28590 \pm 920 28920 \pm 1160	N.D.	78°35.6' E 32°04.1' N	1.0	31.5	5.5
	J	Khab (Spiti)	N.D.	N.D.	78°37.8' E 31°49.4' N	0.8	3.5	0.3
	K	Tirang (Tirang)	N.D.	N.D.	78°35.5' E 31°42.5' N	0.4	2.5	0.2
	L	Rupa II (Rupa)	N.D.	N.D.	78°28.1' E 31°45.8' N	0.5	3.5	0.2
	M	Shaso (Rupa)	27130 \pm 540	N.D.	78°30.5' E 31°43.3' N	0.6	2.2	0.3

Tab. 3.2 List of Quaternary river damming giant (> 0.5 km³) landslides in the Spiti-Satluj River region. The Holocene Lingti Landslide (B; #GP www.gigapan.com/gigapans/178309) and Sichling/Mane (C) Landslide are partly located within the study area. Name of blocked river is given in parentheses next to the name of the landslide. (N.D. = not dated; after Bookhagen et al. 2005)

Formation of landslide dams and subsequent heavy rainfall events favored the formation of landslide lakes in the region (Gupta and Sah 2008). In 2005, a catastrophic failure of such a dam has led to a Landslide Lake Outburst Flood (LLOF) causing severe damages and loss of lives. During the 2005 event a partial dam breach in the Parechu River Valley (Fig. 3.7) released 64 million m³ of water, causing 156 fatalities (Gupta and Sah 2008).

Also the Pin Valley (Fig. 3.7) west of the study area was partly blocked in three consecutive years by debris flows resulting from Glacial Lake Outburst Flood (GLOF) in a tributary valley (Jayabalan et al. 2015).

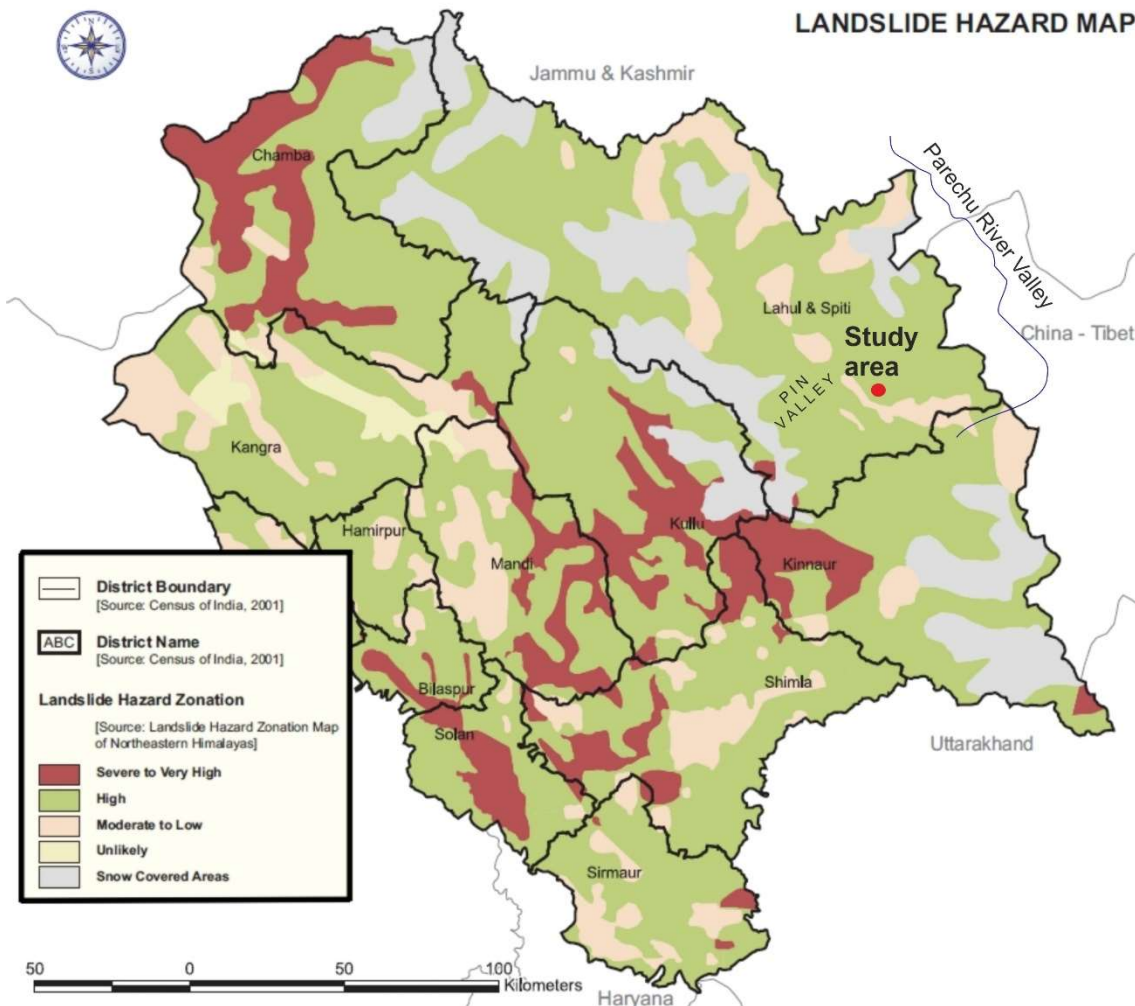


Fig. 3.7 Landslide hazard map of Himachal Pradesh. The study area around Dangkhar village is situated in the high hazard zone shown in green (after SEEDS 2009)

3.2.3 Climate

The Spiti area is referred to as the cold desert (Bhargava and Bassi 1998). According to the Köppen-Geiger climate classification (Kottek et al. 2006), the study area is situated in the ET climatic zone, indicating polar (E) tundra (T) conditions. It is characterized by snow dominated winters with strong continental influences and cool summers. The precipitation is controlled by two major weather systems: (i) the Indian southwest Summer Monsoon (ISM), and (ii) the winter westerly disturbances (Yao et al. 2012; Rawat et al. 2015) transporting moisture from the Mediterranean, Black and Caspian Seas (Owen et al. 2001).

Rainfall is as little as 50 mm/yr (Fig. 3.8) (Verma 1997; Scherler et al. 2010; Srivastava et al. 2013) due to shielding of the ISM by the High Himalaya (Bhargava and Bassi 1998). During abnormal monsoon years (AMY) moisture loaded clouds reach beyond the High Himalaya mountain barrier resulting in an average basin precipitation of up to 850 mm/yr in the Upper Spiti Valley (Bookhagen et al. 2005). The area around Dangkhari receives approximately 50 % – 100 % more rainfall during AMY (Bookhagen 2005). During winters, the precipitation occurs as snowfall, normally resulting in less than 200 cm of accumulation. Temperatures throughout the year vary from – 25 C° in winters to + 30 C° in summer time (Srivastava et al. 2013; Phartiya et al. 2009).

The contemporary glacier distribution shows that Lahaul is stronger glaciated than Spiti (Fig. 3.10), where the ISM is stopped by the topographic barrier of the High Himalaya (Pir Panjal Range, Fig. 3.10). Together, Lahaul and Spiti form the most intensely glaciated areas of Himachal Pradesh (Dobhal and Kumar 1996). The majority of the Himalayan glaciers belong to the summer accumulation type receiving their mass gain from ISM precipitation (Qiao and Yi 2017).

Since the end of the 19th century, the Lahaul and Spiti areas experienced phases of glacial retreat. In 2007, about 622 km² of the Spiti basin were glaciated. The glaciers of Spiti exhibit the highest recession rate among the Himalayan basins of India with a loss of 13.4 % of glacier area from 2001 to 2007 (ISRO 2011). The retreat of the Spiti glaciers is comparable to those of Zaskar, while glaciers of Lahaul showed higher absolute recession rates (ISRO 2011). Modern snow line contours (Scherler et al. 2010) for Lahaul are between 4800 – 5500 m (Owen and Benn 2005) and are roughly in the same range for the Spiti area (Fig. 3.8).

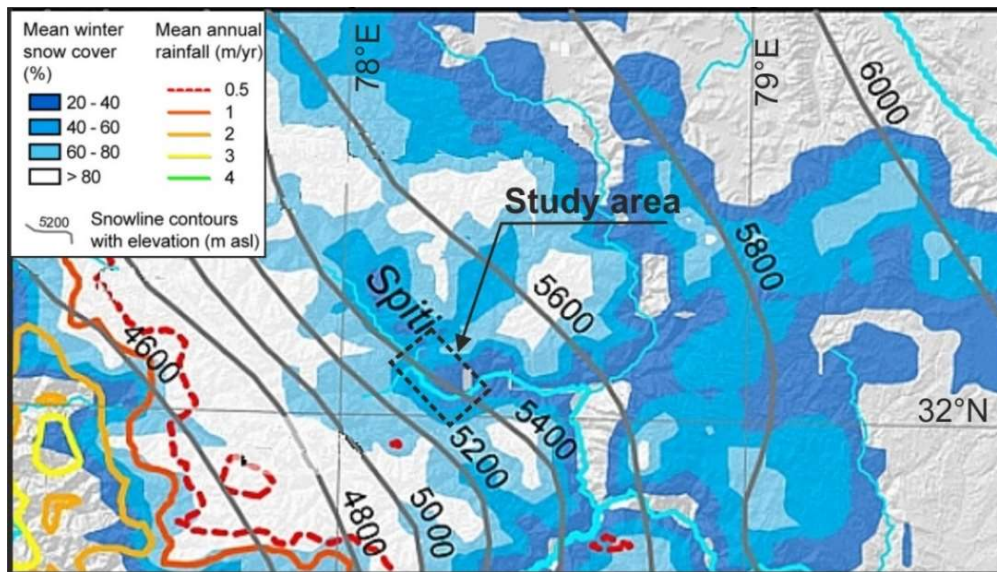


Fig. 3.8 Climatic characteristics of the study area (modified after Scherler et al. 2010)

3.2.4 Paleoclimate

On the Indian continent the monsoon initiated about 23 – 7 million years ago and was subject to fluctuations resulting in different glacial stages (Singhvi and Krishnan 2014). During Holocene and Pleistocene times, intensified monsoon activities led to precipitation further inland compared to the present day monsoon front (Fig. 3.9, Rawat et al. 2015; Owen 2007).

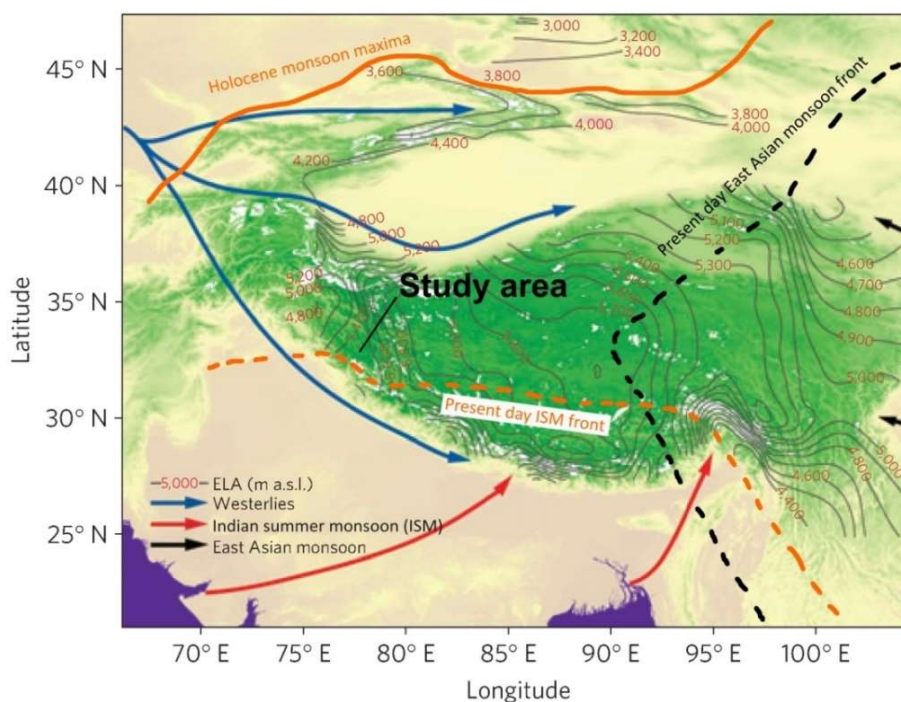


Fig. 3.9 Monsoon systems in the Himalaya acting during the Holocene and present times. ELA = Modern Equilibrium Line Altitudes (compiled after Yao et al. 2012; Rawat et al. 2015)

Numerous studies (e.g. Owen et al. 1996, 1997; Owen 2009; Dortch et al. 2013; Murari et al. 2014) have shown that the northwestern Himalaya has experienced significant, often asynchronous, climatic variations during the geologic past (Hedrick et al. 2011). Glacial stages associated with the climatic changes in the NW Himalaya are named after glaciers and localities in Lahaul (Fig. 3.10) and include, from oldest to youngest, the Chandra stage, Batal stage, Kulti stage, and Sonapani I and II stages (Owen et al. 1997; Hedrick et al. 2011; Dortch et al. 2013; Owen and Dortch 2014). Fig. 3.11 shows the glacial stages reconstructed for the past approximately 400 thousand years in regions around the study area (Fig. 3.11).

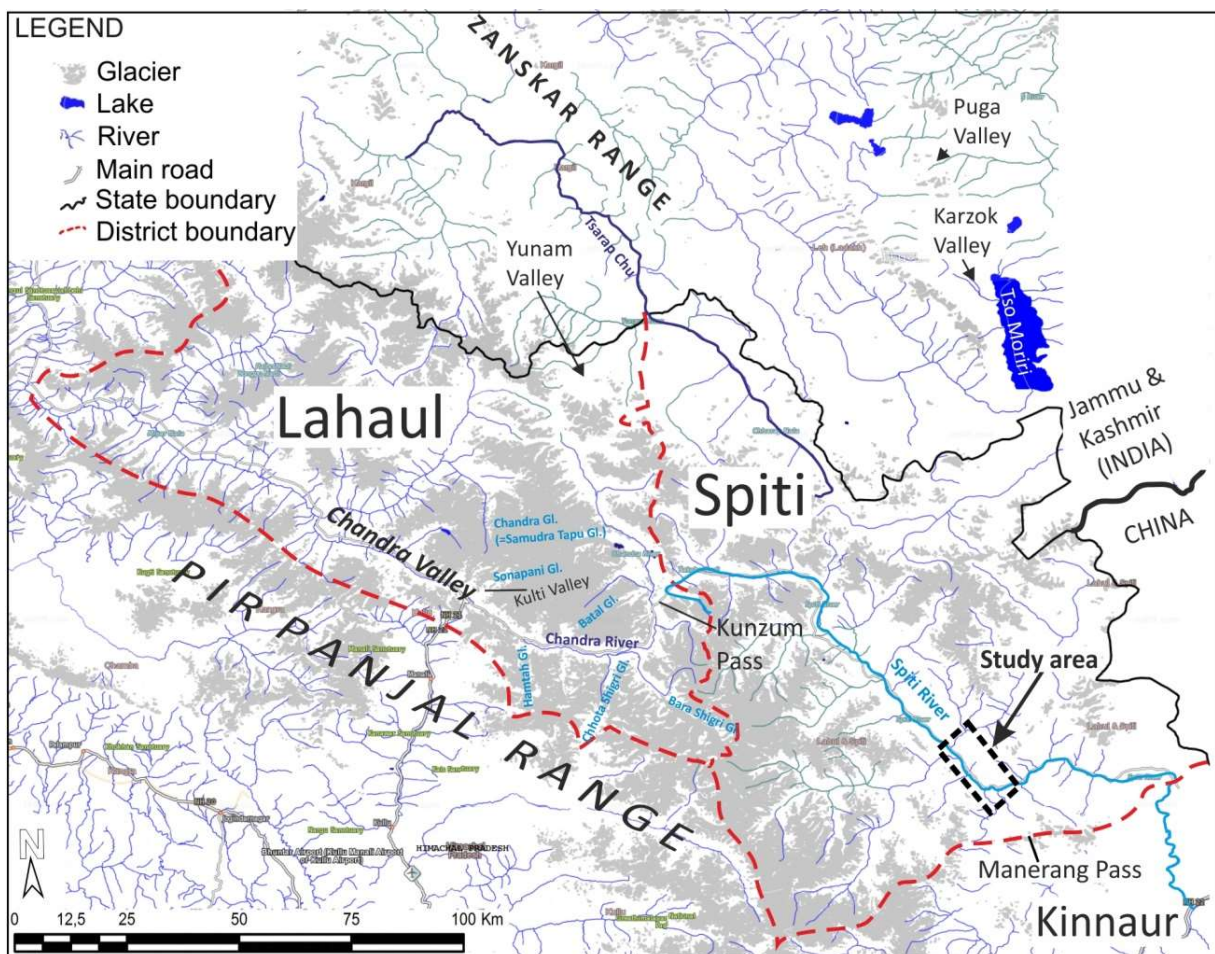


Fig. 3.10 Contemporary glaciation and river network of the Lahaul, Spiti and Zanskar regions. Important glaciers are labelled in light blue. Locations investigated in previous studies are labelled together with names of valleys and river basins referred to in the text for comparison. Lahaul and Spiti district boundaries are approximate (modified after NRSC 2013)

The extent of the respective glaciations decreases from old to young and the asynchronous timing of glacial advances in nearby areas is commonly caused by the sensitivity of Himalayan glacial systems to the local variabilities of weather systems and microclimatic variations due to topographic conditions (Owen et al. 1997; Owen 2014; Eugster et al. 2016).

In general, regional glacial stages older than 21 thousand years in the semi-arid northwestern Himalayan Tibetan regions are correlated with intensified monsoon activity during greenhouse phases with increased summer snowfall at high altitudes (Owen et al. 2001; Owen and Dortch 2014). Younger glacial stages can broadly be correlated with northern hemisphere climatic events such as Oldest, Older and Younger Dryas, Roman Humid Period and Little Ice Age (Dortch et al. 2013). The extent of the global Last Glacial Maximum (LGM) in the northwestern Himalaya occurred around 20 – 21.4 thousand years ago (Singhvi and Krishnan 2014), and the interpretation by Shi (1992) is the most widely accepted one today (Fig. 3.12).

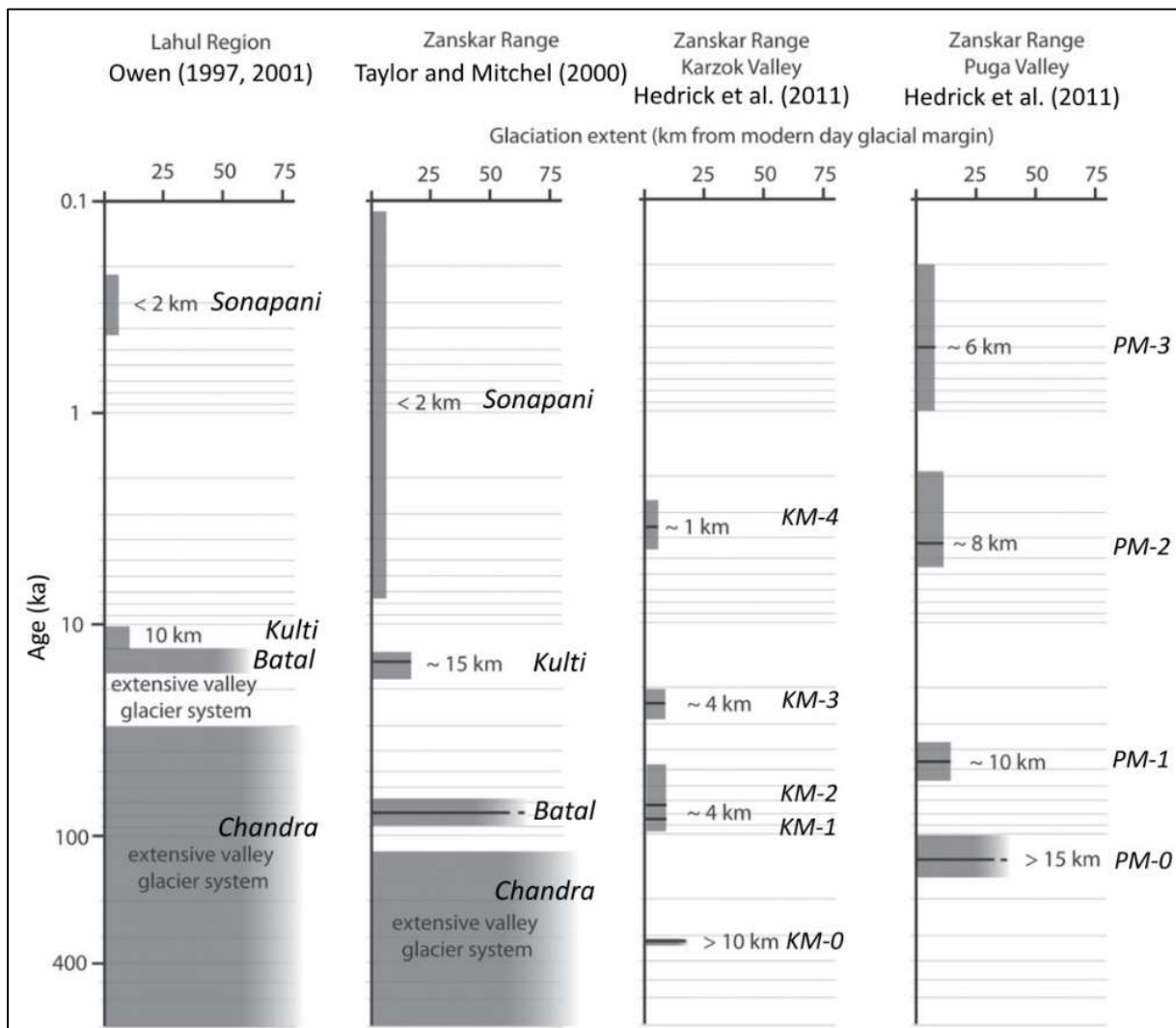


Fig. 3.11 Extent, duration and names of glacial stages in the Lahaul Region and Zanskar Range. Age in thousand years (ka). For locations of study sites see Fig. 3.10. (modified after Hedrick et al. 2011)

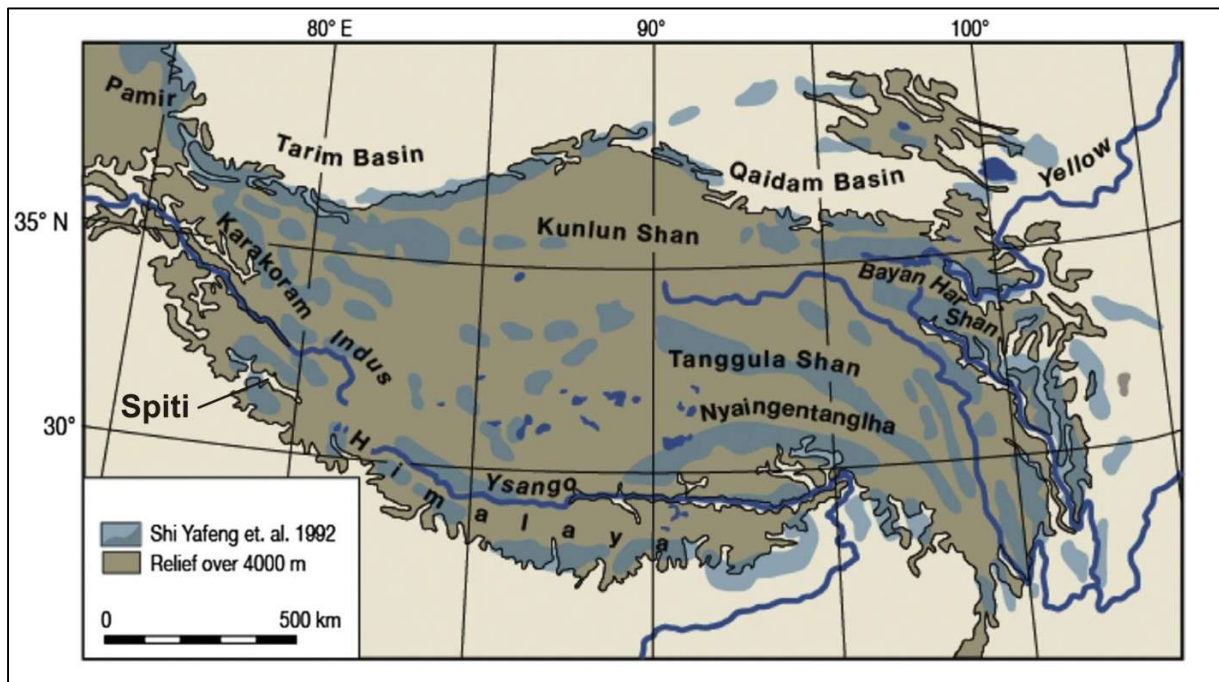


Fig. 3.12 Distribution of glacialized areas during the Last Glacial Maximum (LGM) for the Himalayan Tibetan region. Shi's map is considered the most likely reconstruction of the last major Himalayan glaciation (after Shi 1992 in Owen and Dortch 2014)

The following paragraphs provide an overview on the characteristics of the glacial stages of the northwestern Himalaya with emphasis on the Lahaul Region and the Zaskar Range. Finally, information and evidence of glacial events recorded in the Spiti Valley are presented.

The Chandra glacial stage

The Chandra glacial stage is the oldest, most extensive, and least well known glacial stage. Few descriptions exist about relict glacial landforms attributed to this stage in the Zaskar Range and Lahaul Region (Mitchell et al. 1999; Taylor and Mitchell 2000; Owen et al. 2001). Glacial advance of up to 100 km from contemporary glaciers for the Zaskar Range (Taylor and Mitchell 2000) and 200 km for Chandra Valley in the Lahaul Region are reported. The Chandra Valley was occupied by an over one km thick valley glacier that retreated since the past approximately 20 thousand years after the LGM (Eugster et al. 2016). Also Taylor and Mitchell (2000) interpret the nature of the Chandra glacial stage in the Zaskar Range to be a massive ice cap type within broad valleys (Fig. 3.13). Later glaciations were mostly restricted to deep valleys (Taylor and Mitchell 2000).

Taylor and Mitchell (2000) describe lithified tillite deposits from the Zaskar Range occurring at elevations about 280 m above the present day river level, which they refer to as "tors of fanglomerate". For the upper Zaskar Range these deposits provide evidence for a valley

glaciation (Fig. 3.13a, b) which deposited material at a higher level (Taylor and Mitchell 2000). Breccia deposits at Dangkhar are situated at similar altitudes above the current level of the Spiti River sticking out of the surrounding terrain (details are presented in chapter 4.2.6 and 4.2.8). In the Lahaul Region, trim lines at several hundred meters above the present day valley floor provide evidence of the Chandra glacial stage, but geologic deposits from that time are rare (Owen 1997).

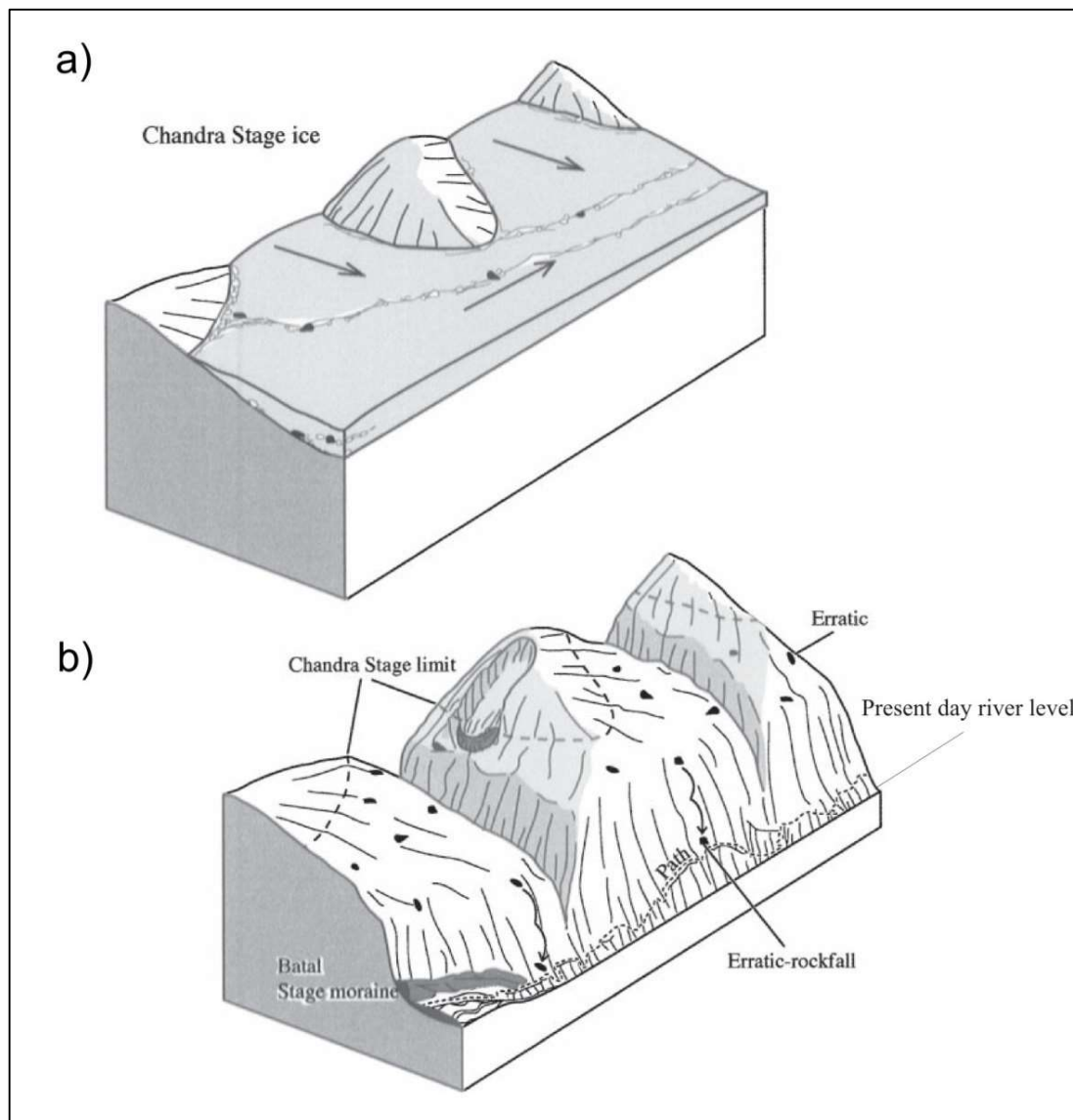


Fig. 3.13 Schematic valley evolution during and after the Chandra glacial stage. a) Valley glacier expansion during the Chandra glacial stage. b) Post-valley glacier morphology and river incision. Grey patches mark deposits of later glaciations (i.e. Batal stage moraine) in the already incised valley (modified after Taylor and Mitchell 2000)

The Batal glacial stage

The Batal glacial stage occurred around 15.5 – 12 thousand years ago (Owen 2001; Saha et al. 2016) possibly as part of the Younger Dryas (Owen 2009), a global cold phase prior to the early Holocene warming phase. For the Lahaul Region this glacial advance occurred during a phase of intensified monsoon (Srivastava et al. 2013). Eugster et al. (2016) envisage that the Batal glacial stage might have occurred earlier and closer to the LGM and the preceding Chandra glacial stage. The style of the Batal glaciation was similar to that of the Chandra glacial stage with valley glacier systems, but less extensive.

The Kulti glacial stage

The early Holocene Kulti glacial stage followed shortly after the Batal glacial stage from 11.4 – 10.6 thousand years ago (Owen 2001; Owen and Dortch 2014) and was restricted to tributary valleys partly reaching into the main valleys (Hedrick et al. 2001). Moraines are smaller compared to those of the Batal glacial stage suggesting a rather short lived event (Owen et al. 2001).

The Sonapani I glacial stage

A possibly early mid-Holocene glacial advance (Owen et al. 1997) with deposits of that glacial stage showing sparse vegetation. Owen et al. (1996) place the transition from valley- side glaciers to rock glaciers in the time of Sonapani I. This advance is considered to be in broad context with the global “8.2 ka cold event” interrupting the warm and wet hypithermal conditions. A moraine dated in the nearby Pin Valley, yielded an age of 7.0 ± 0.7 thousand years ago (Scherler et al. 2010) falling into this timeframe.

The Sonapani II glacial stage

The Sonapani II glacial stage is regarded to represent the Little Ice Age (LIA) in the Lahaul and Spiti region (Owen et al. 1997). In Lahaul, the LIA initiated around 1303 AD (Rawat et al. 2015) and peaked around 1880 to 1890 (Mayewski and Jeschke 1979; Rawat et al. 2015). Tree ring data from the Lahaul Region also reflect cooler conditions after 1500 AD with the coldest period from 1700 to 1900 AD (Yadav et al. 2011). Also pollen data obtained near Kunzum Pass suggest that global events such as the medieval warm period and the LIA are documented in the Lahaul Region (Chauhan et al. 2000).

During the LIA, the Bara Shigri Glacier (Fig. 3.14a) advanced several kilometers down into the Chandra Valley in 1836 and 1860 blocking the Chandra River for three months and for three years, respectively (Egerton 1864; Harcourt 1871). Since the end of the LIA, the Bara Shigri Glacier experienced rapid recessional phases with rates of up to 62.5 m/yr (Mayewski and Jeschke 1979).

For the Zaskar Range, Taylor and Mitchell (2000) reported deposits attributed to the LIA, located within a maximum distance of 2 km from contemporary glaciers (Hedrick et al. 2011), but are on average only a few hundred meters away from them (Owen 2009).

Very common remnants of the Sonapani II glacial stage are rock glaciers reflecting the ongoing retreat of glacial ice since the late Holocene (Owen and England 1998). Many still active rock glaciers exhibit steep, unvegetated frontal slopes and surficial lobes and ridges and formed due to reduced precipitation during the LIA (Owen 2009). Formation of these rock glaciers was attributed to the increased debris supply from talus slopes as a result of rock fall events, mantling the former glacial ice (Owen and England 1998).

Glaciation in the Spiti Valley

In Spiti glaciers advanced between 28 – 14 thousand years ago and drier conditions prevailed (Srivastava et al. 2013), coinciding with the timeframe of the Chandra glacial stage. Pollen records confirm this pattern during the late Pleistocene about 26 thousand years ago, when the region attained its desert character (Bhattacharyya et al. 2006). Glaciers descended down into the Spiti Valley from Kunzum pass attaining a thickness of 300 m (Saha et al. 2016) to 600 m (Eugster et al. 2016). Evidence for a glaciation around Kunzum pass is furthermore supported by striated rock surfaces indicative of a movement towards the Spiti River (Owen et al. 1997, 2001; Bhargava and Bassi 1998). The extent of glaciation during the Pleistocene until early Holocene varies throughout the literature. Srivastava et al. (2013) envisage a glacial advance to Kioto (Fig. 3.14a) while Marh and Rana (2014) and Bhargava and Bassi (1998) suggest an extensive glaciation covering the entire upper Spiti Valley based on the enormous accumulations of debris and the U-shaped valley geometry. Also Kuhle (2005) sees the entire upper Spiti Valley being glaciated around 60 – 18 thousand years ago.

Glacial deposits in the Pin and Parahio Valleys west of the study area are nowadays about 20 km away from present day glaciers pointing to a massive glaciation in the past 16 thousand years. However, a reliable reconstruction of the glacial history of the area was not yet feasible (Scherler et al. 2010).

A regional Holocene glacial advance occurred between 7.6 – 6.8 thousand years. The glacial advance is recorded in the Mane paleolake sediments showing a cooler climate during stronger winter westerlies while summer monsoon was weaker (Anoop et al. 2013). In contrast to the Lahaul Region, the Spiti glaciers are controlled by winter westerlies rather than summer monsoon precipitation (Anoop et al. 2013; Owen et al. 2001).

Another glacial advance is recorded by pollen analysis in the upper Spiti Valley from about 2300 to 1500 thousand years ago (Chauhan et al. 2000; Bhattacharyya et al. 2006). From the past 900 years onwards, colder climatic conditions prevailed until recent times towards the LIA (Chauhan et al. 2000).

Early expeditions from the 19th century to Spiti provide insight on the time around the LIA in the Manirang area, just southeast of the study area (Fig. 3.14a). The glacierized Manirang pass was frequently used to enter Spiti from Kinnaur and observations on the glacier were documented in the early scientific expeditions (Theobald 1862; Griesbach 1891). Theobald (1862) reports the position of glacier terminus, which is located approximately 4.8 km away from the Sopona camp site (Fig. 3.14b). Griesbach (1891) mentioned the glacial Mane Lake (Sopona Lake) and the position of the glacier, which discharges meltwater into the lake. According to his report, the debris which limits the lake is about 8 km away from the glacier and marks the former maximal extent of the Manirang glacier (Fig. 3.14b). Although he misinterpreted the debris damming the lake as a terminal moraine that was later assigned to the Mane Landslide, it nevertheless allows comparing their observations to the contemporary position of the glacier. The two reports by Theobald (1862) and Griesbach (1891) refer to the same location where presently fresher, unvegetated moraine deposits are visible on satellite images (Fig. 3.14b). The present day snout of the Manirang glacier lies about 1.5 kilometer up the valley from the described location (Fig. 3.14b), inferring an average recession rate of about 12.5 m/yr. The area around the Sopona camp site nowadays exhibits, slightly vegetated deposits on the right valley flank attributable to two moraine pulses (Fig. 3.14b) which are from pre-LIA times. Trimlines on higher levels along the valley flanks (Fig. 3.14b) point to a former glacial stage of the Manirang glacier where it reached down into the Spiti Valley. Photographs taken by Bourne (1870) in the summer of 1866 feature one slightly vegetated pre-LIA moraine ridge (Fig. 3.15a) located uphill from the Sopona camp site and also the situation of the Manirang glacier near the Manirang pass (Fig. 3.15b). Comparisons to recent photographs confirm the significant recession of the Manirang glacier (Fig. 3.15c).

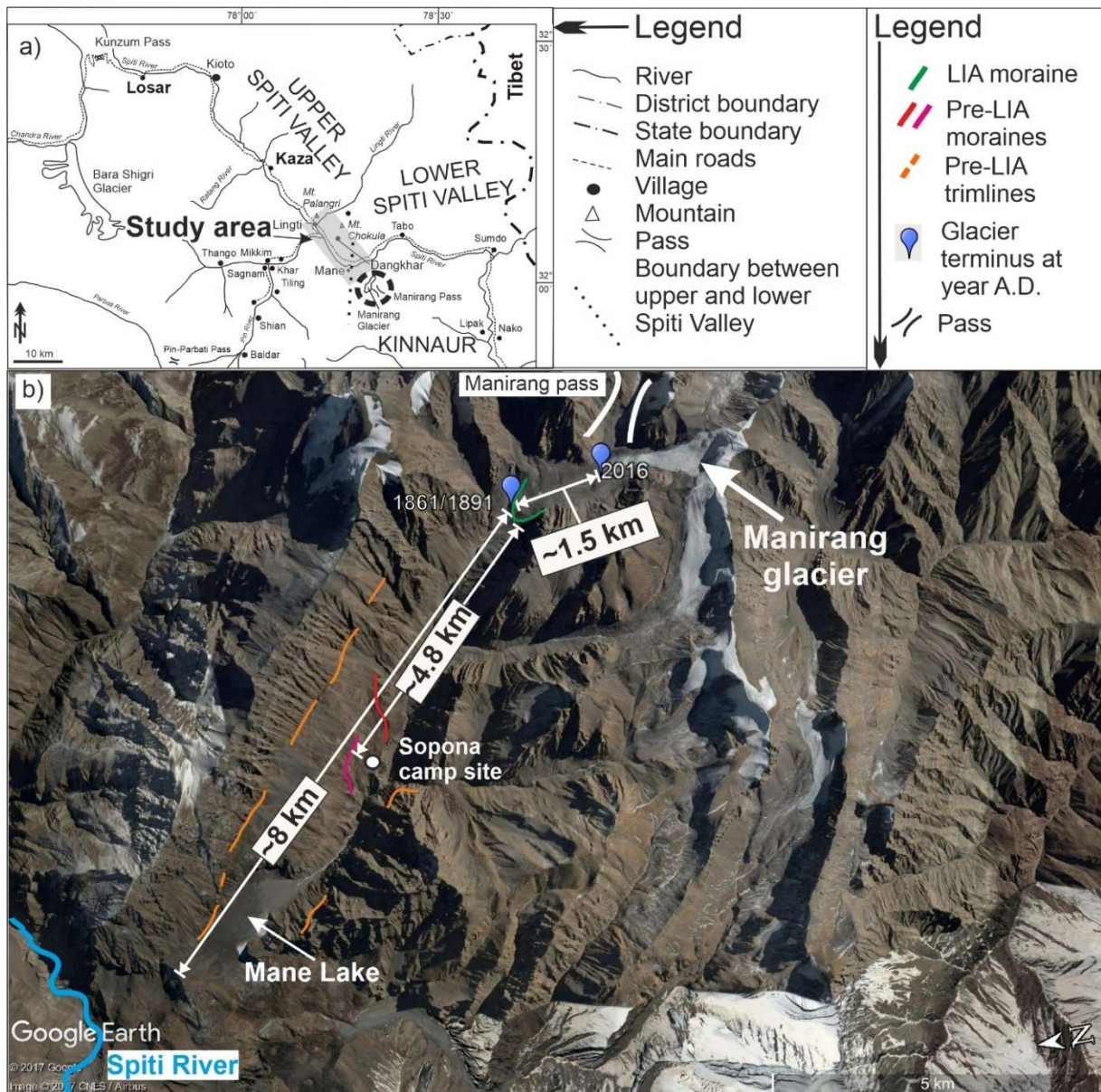
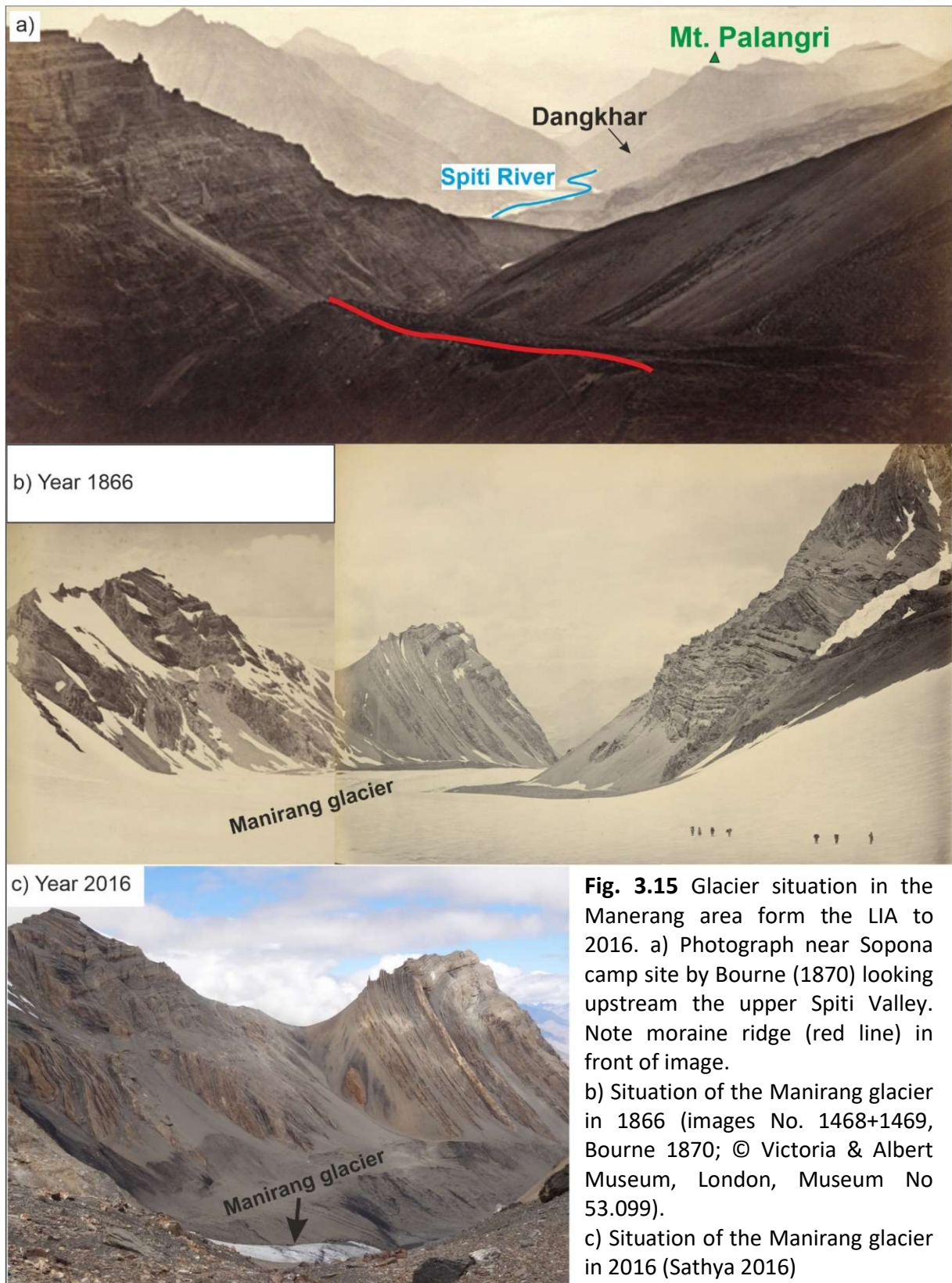


Fig. 3.14 The Manirang area. a) Location of the Manirang area (bold dashed circle), located southeast of the study area. b) Manirang glacier recession reconstructed from historic reports of Theobald (1862), Bourne (1870), Griesbach (1891) and satellite imagery acquired in 2016 (Google Earth Pro).



4 THE DANGKHAR LANDSLIDE

4.1 Investigative methods

Investigations performed to evaluate the Dangkhari Landslide are summarized below. Details about the methods are provided in the appendix.

- Compilation and review of existing geologic, seismic and climatic data and reports covering the study area dating back to the 1820s together with information provided by local inhabitants. Literature review concerning extremely large landslides providing an overview on the thematic background of the thesis, summarizing the current state of knowledge and research.
- ASTER (Advanced Spaceborne Thermal Emission and Reflection Radiometer) derived DEMs (Digital Elevation Models) with a 30 m spatial resolution for a 3D- visualization of landforms and features of the Dangkhari Landslide and creation of derivative maps such as hillshade maps, slope aspect maps and slope inclination maps to assess geomorphic and geometric properties of the study area. A hypsometric analysis of the DEM serves as index for the maturity of the landscape.
- Remote and field based geomorphologic mapping of study area. High resolution satellite photointerpretive mapping of geomorphic features such as lineaments, hummocky terrain, closed depressions, breaks-in slope, ephemeral stream channel patterns and distribution of surface waters, secondary landslides and glacial deposits. The resulting geologic and geomorphic reconnaissance field maps were utilized to calibrate satellite photointerpretive mapping, to assess site-specific geologic and geomorphic features, and to identify locations for rock and sediment sampling. The terminology used to describe landslide features broadly follows the suggestions by the IAEG commission on landslides (1990), the WP/WLI (1990), Cruden and Varnes (1996) and Mather et al. (2003).

- Detailed geologic field mapping on an ArcGIS generated 1:15,000 topographic base map with 20 meter elevation contour intervals. Identification and delineation of bedrock units around and within the landslide mass and their lateral continuation. Identification of the overall bedrock structure and geometry, mapping of the extent and limits of landslide debris and other surficial deposits such as glacio fluvial, lacustrine and talus deposits.
- Hand auger drilling for organic samples within lake sediments and depressions located on the landslide to assess a minimum age of emplacement of the Dangkhar Landslide and its relation to glacial deposits (Radiocarbon dating).
- Recording of ultra-high resolution Gigapixel images to create a permanent digital archive of selected sites of the study area using the GigaPan EPIC Pro system.
- Laboratory testing of solids and liquids:
Sampling of solid rock material for thin section analysis, X-ray powder diffraction analysis, cathodoluminescence imaging, stable carbon and oxygen isotope analysis to obtain insight on the origin of primary and secondary, altered and/or remobilized landslide material. Water samples were analyzed by means of stable hydrogen and oxygen isotope data.
- Establishing of a morphostratigraphy of glacial deposits and landslide features (i.e. relative and absolute age implications and cross cutting relationships based on morphostratigraphic positions and weathering characteristics).
- Implementation of the generated DEMs and geologic cross sections in an ArcGIS and ArcScene framework to conduct landslide volume estimates using TIN difference modelling and 3D visualizations of the Dangkhar Landslide, respectively.
- Block theory (Goodman and Shi 1985) was utilized to assess the kinematics and failure mode of the Dangkhar Landslide. A seismic evaluation of the removable block was performed in order to assess the triggering potential of earthquakes on the Dangkhar Landslide.

4.2 Results and findings

4.2.1 Dangkhar Landslide geomorphology

The study area has a minimum elevation of 3400 m along the Spiti River and reaches a maximum elevation of 5600 m at the peak of Mt. Chokula (Fig. 4.1). The northwest trending Spiti River and northeast trending Lingti River traverse the study area and the Spiti River marks the southwestern toe of the southwest facing Dangkhar hillslope. The Dangkhar hillslope is characterized by an overall gentle slope topography with a prominent peak and ridge in the uppermost part around Mt. Chokula (Fig. 4.1; Fig. 4.2). Mt. Chokula exhibits a rugged, rocky terrain with perennial snow cover in its highest parts. The Dangkhar hillslope is characterized by a system of topographic normal and obsequent breaks-in-slope (Fig. 4.3) that trend approximately parallel to elevation contours. The overall pattern of topographic breaks is expressed as smooth hummocky topography and forms the Dangkhar Landslide deposit (Fig. 4.4). The area around Mount Chokula forms the headscarp and is characterized by an up to 400 m high bedrock outcrop, exhibiting a nearly vertical cliff with a southwestward-concave arcuate embayment flanked by talus fans in its central part (Fig. 4.4). The talus occupies the transition from bedrock to the Dangkhar Landslide deposit. The bedrock in the ridge area exhibits numerous large-scale, vertical joints forming small caves. The slope toe area comprises both, bedrock and debris material and a clustering of springs.

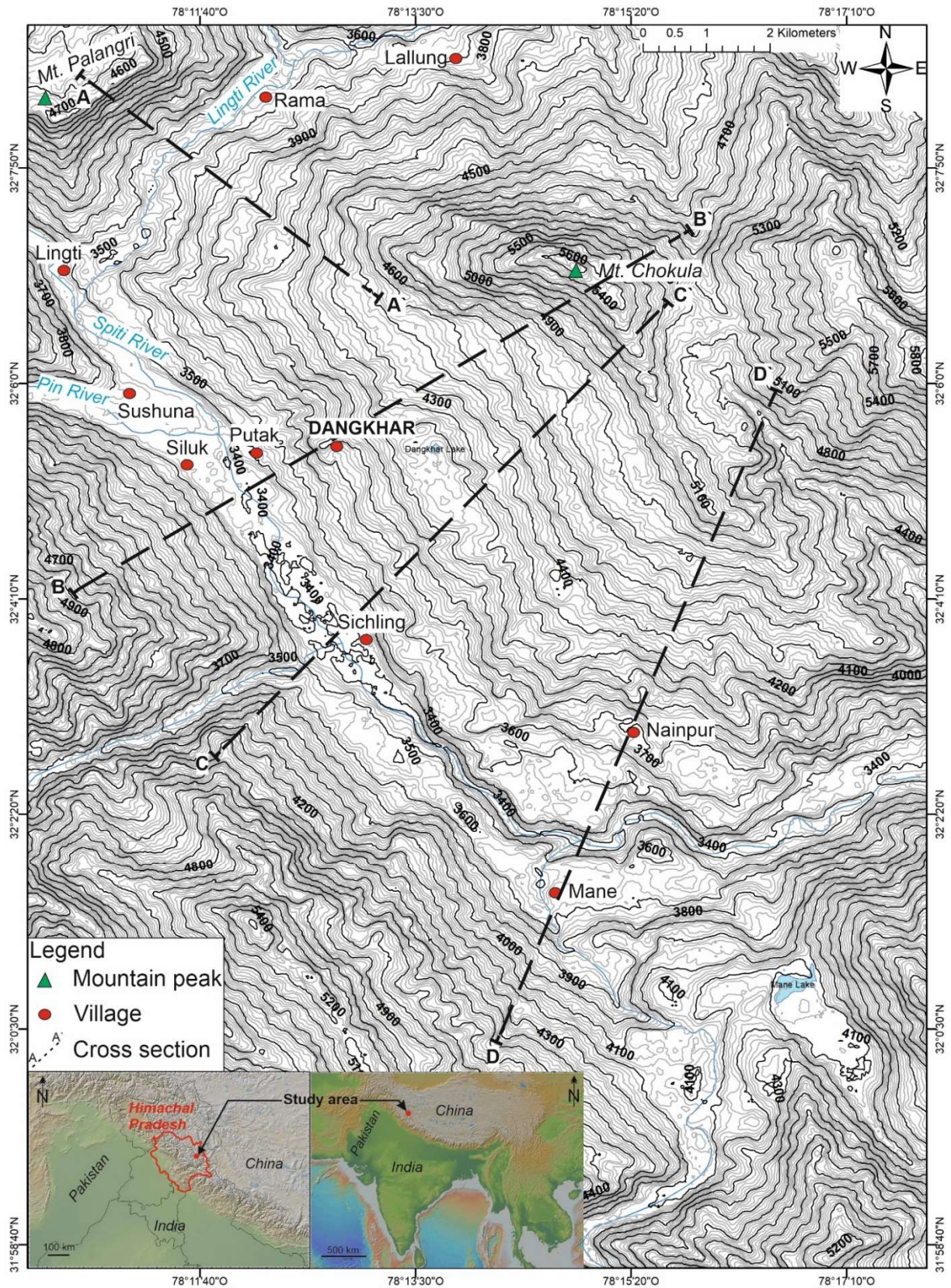


Fig. 4.1 Topographic map of the study area; inset images: GeoMapApp (Ryan et al. 2009)

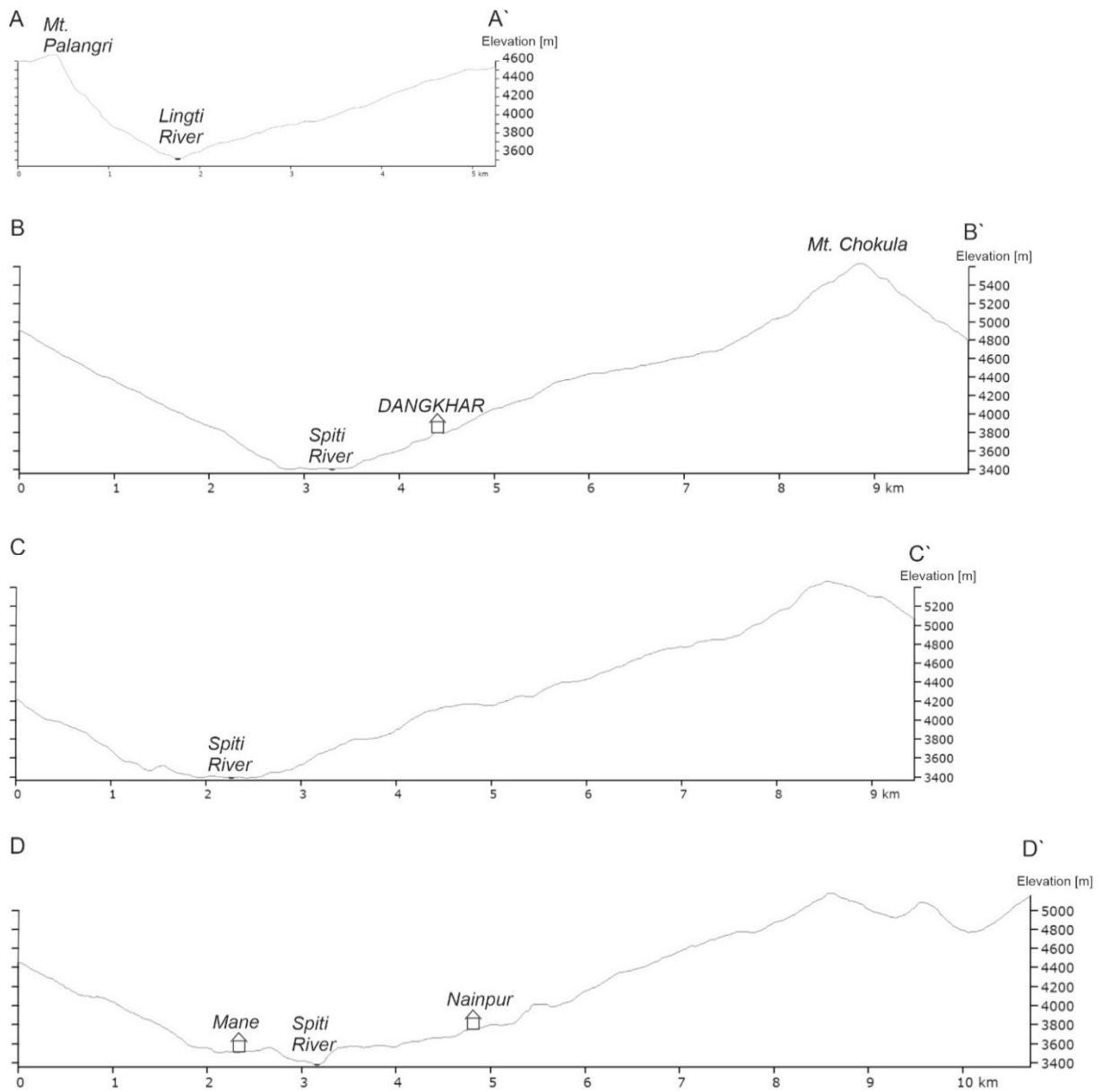


Fig. 4.2: Topographic profiles of the study area. Locations of profiles shown in Fig. 4.1

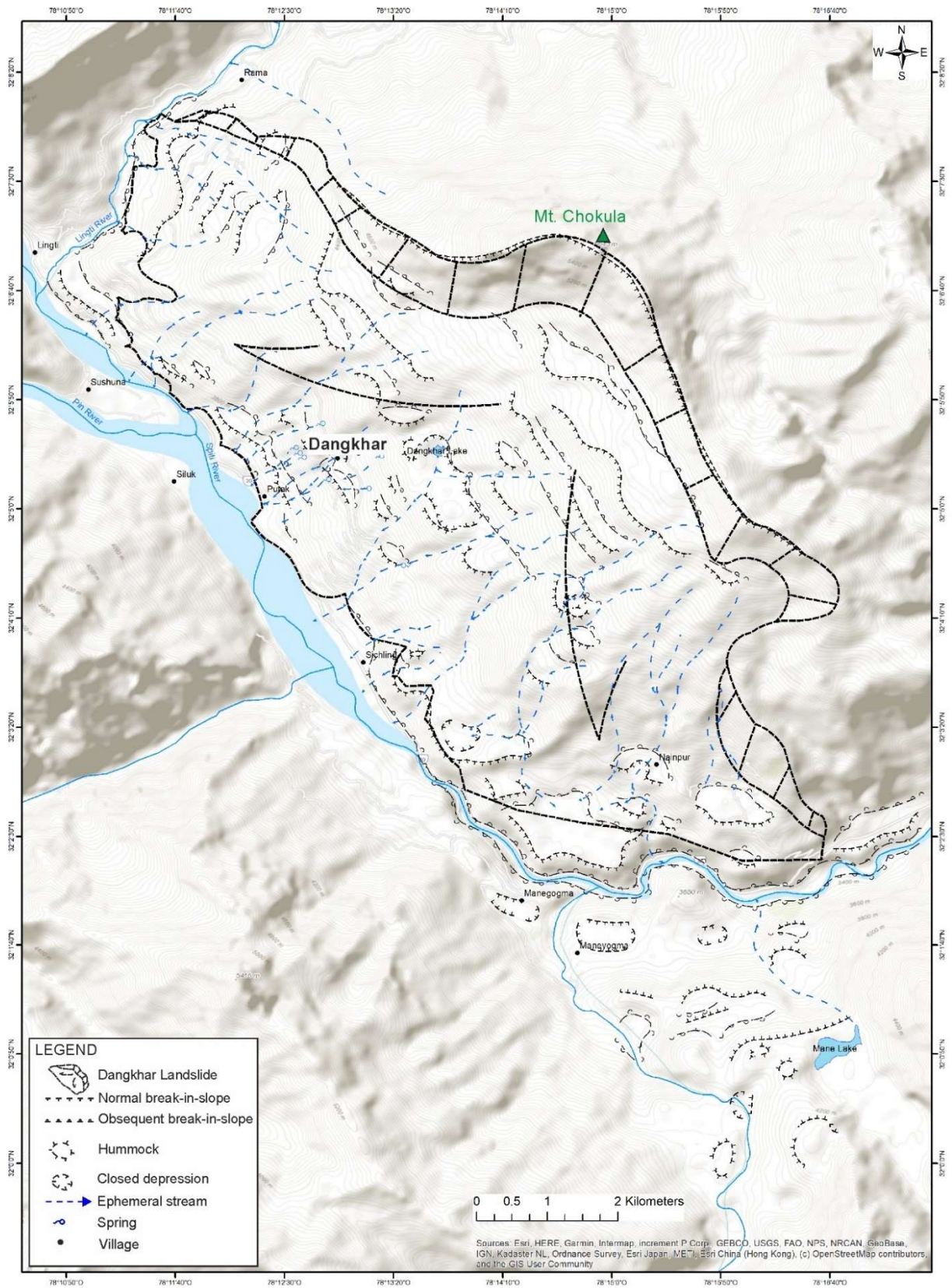


Fig. 4.3 Geomorphologic map of the Dangkhar Landslide

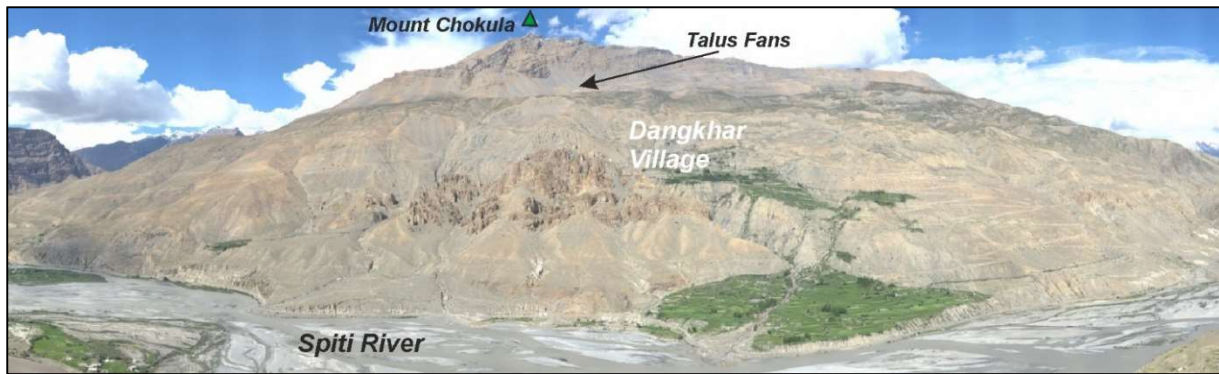


Fig. 4.4 Characteristic gentle, hummocky topography of the Dangkhar landslide southwest of Mt. Chokula. Note prominent bedrock outcrop around the peak of Mt. Chokula (#GP <http://www.gigapan.com/galleries/13306/gigapans/178308>)

In general, the topography of the Spiti Valley exhibits moderately inclined valley flanks of about 30 to 40° with steep to nearly vertical peaks and cliffs towards the higher elevations (Fig. 4.5). The DEM visualizations of the Dangkhar Landslide also reveal the distinct overall smooth topography, a flatter mid-slope bench and an upper flat area are in the central slope area and west of the peak of Mt. Chokula, respectively (Fig. 4.5a & b). The Dangkhar Lake formed on this mid-slope bench.

The slope inclination map (Fig. 4.5c) highlights the overall flatter inclination of the slope compared to the surrounding slopes of the Spiti Valley. The majority of the Dangkhar Landslide deposit is not steeper than about 20°. A pattern of alternating bands of steep and flat portions of the slope is decipherable. The Mane Landslide deposits are represented as a flat area incised by the Spiti River forming a canyon (Fig. 4.5c). The contact of the Mane Landslide to the Dangkhar Landslide is visible as a slightly curved arc with approximately 30° steep sidewalls. The sliding plane of the Mane Landslide developed as a dip slope along bedrock bedding planes from the opposing valley side.

The slope orientation map depicts that the Dangkhar Landslide is formed by three slopes. These are the Dangkhar slope, the Spiti SE slope, and the Lingti NW slope (Fig. 4.5d). These three slopes form the surfaces of a block, which will be discussed in the block theory evaluation (Chapter 4.2.10.1). The approximately 0.5 km³ Lingti Landslide is located on the Lingti NW slope. South facing slopes in the southern part of the Dangkhar hillslope reflect the bend of the Spiti River at the transition from the upper to the lower Spiti Valley.

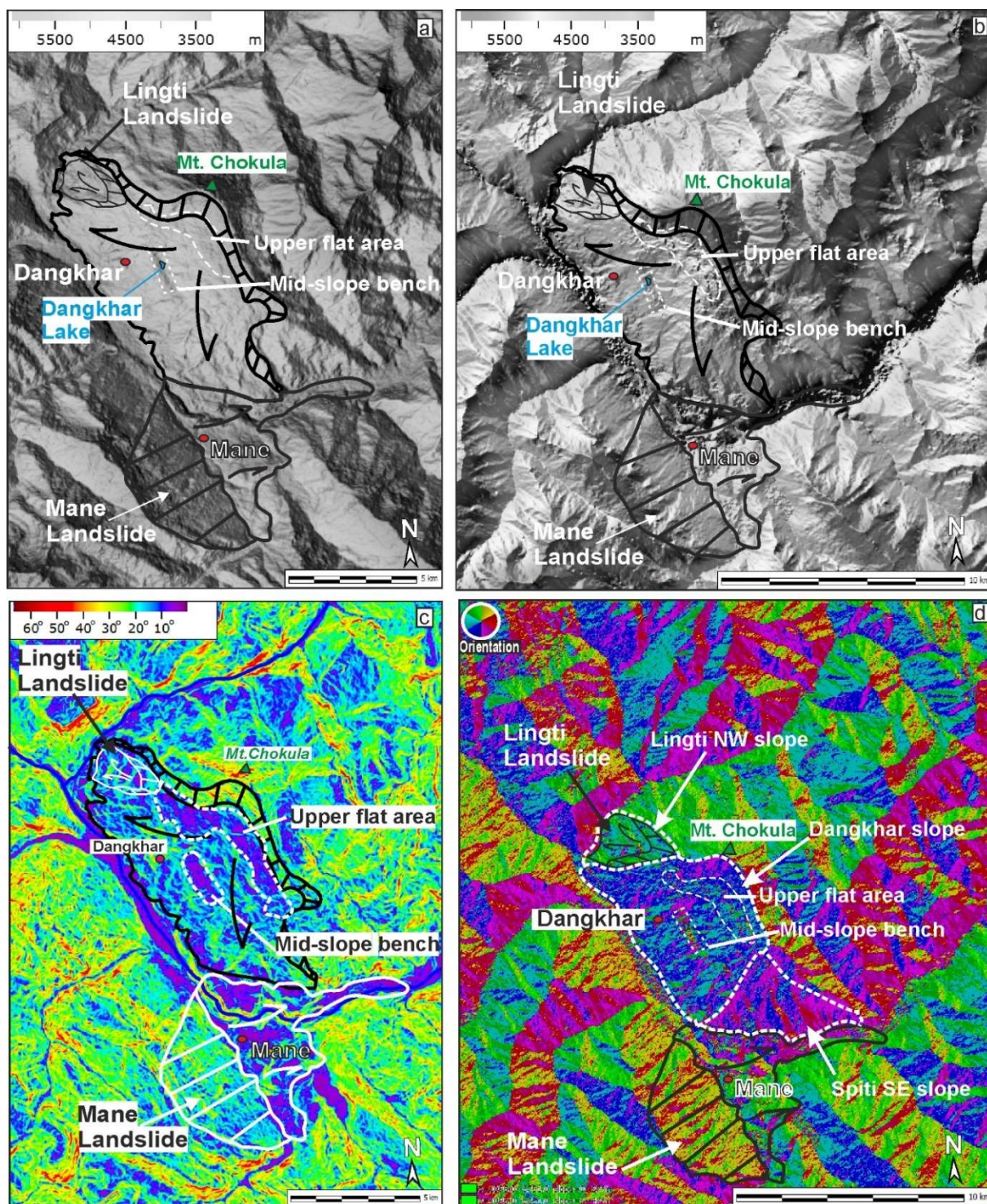


Fig. 4.5 DEM representations of the study area depicting various geomorphic features. a) Hillshade map (illumination from 270° azimuth). b) Hillshade map – 2x vertically exaggerated. c) Slope inclination map. d) Slope orientation map

The hypsometric analysis of the DEM dataset includes a frequency distribution of altitudes of the Dangkhar Landslide. The resulting hypsometric histogram shows a polymodal distribution of elevation (Fig. 4.6). It reveals characteristic landforms and structures identified on the DEM visualizations and on high resolution images. The H_i value of 0.36 indicates a mature stage of the Dangkhar hillslope.

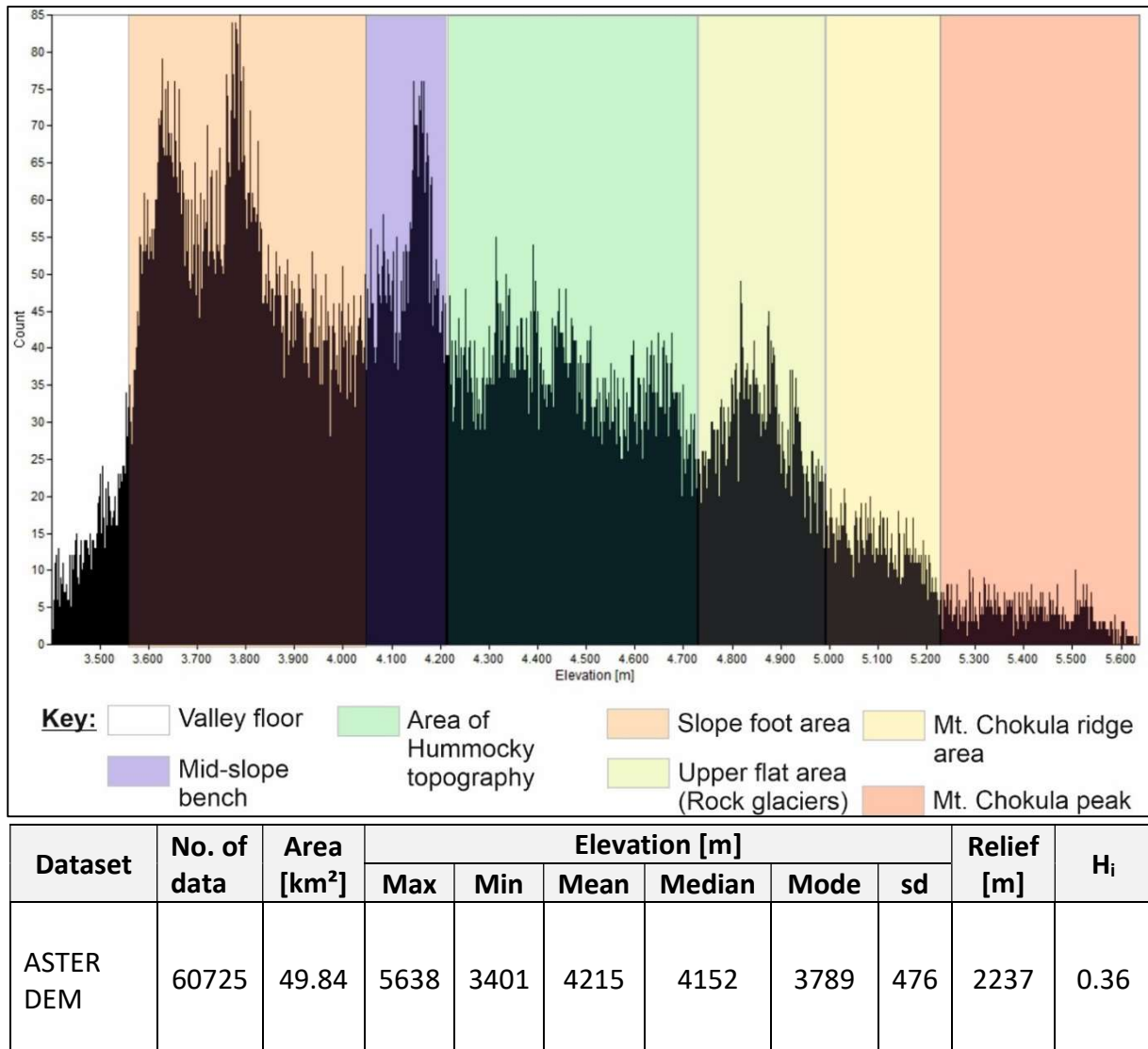


Fig. 4.6 Hypsometric histogram of the Dangkhar hillslope (1 m intervals) and statistical parameter of the DEM used for the histogram (sd = standard deviation, H_i = hypsometric integral; for hypsometric curve see appendix)

Systematic mapping revealed that the Dangkhari Landslide deposit exhibits geomorphic lineaments, ephemeral stream channels, rock glaciers and secondary landslides of varying scale (Fig. 4.7). 806 and 36 lineaments were identified on the Dangkhari Landslide and the Mane Landslide, respectively (Fig. 4.7), reaching lengths up to one kilometer and are aligned parallel to the Spiti Valley. The lineaments are formed by ridges and trenches within the debris of the Dangkhari Landslide. Very prominent crevasse type lineaments forming large scale ridge and trench changeovers are observable downhill from the mid-slope bench and in the upper flat area (Fig. 4.8a, b, c, d). The lineaments are expressions of internal ruptures (internal shear surfaces or secondary landslides) and are partly filled with fine grained silty, clayey material. The lineaments exhibit varying degree of vegetational cover and appear subtle to sharp on the satellite images and in the field indicating a formation at different points in time (Fig. 4.8a-e). Towards the southern margin of the Dangkhari Landslide, the lineaments form a set of parallel counterscarps displacing bedrock blocks resulting in toppling structures exposed in an ephemeral stream channel (Fig. 4.8e).

The secondary landslides exhibit the classic topographic signatures of rotational landslides with concave down and convex uphill oriented elevation contours (Sowers and Royster 1978) and their upper and lower limits generally coincide with normal and obsequent breaks-in-slope. The secondary landslides occur around the slope toe area and uphill from the Dangkhari Lake. The secondary landslides exhibit displacements of several tens to approximately hundred meters (Fig. 4.9). Locally, the secondary landslides incorporated rock blocks preserving the original bedrock structure, but the orientation of bedrock strata deviates from the overall bedrock geometry indicating a back rotation (Fig. 4.9).

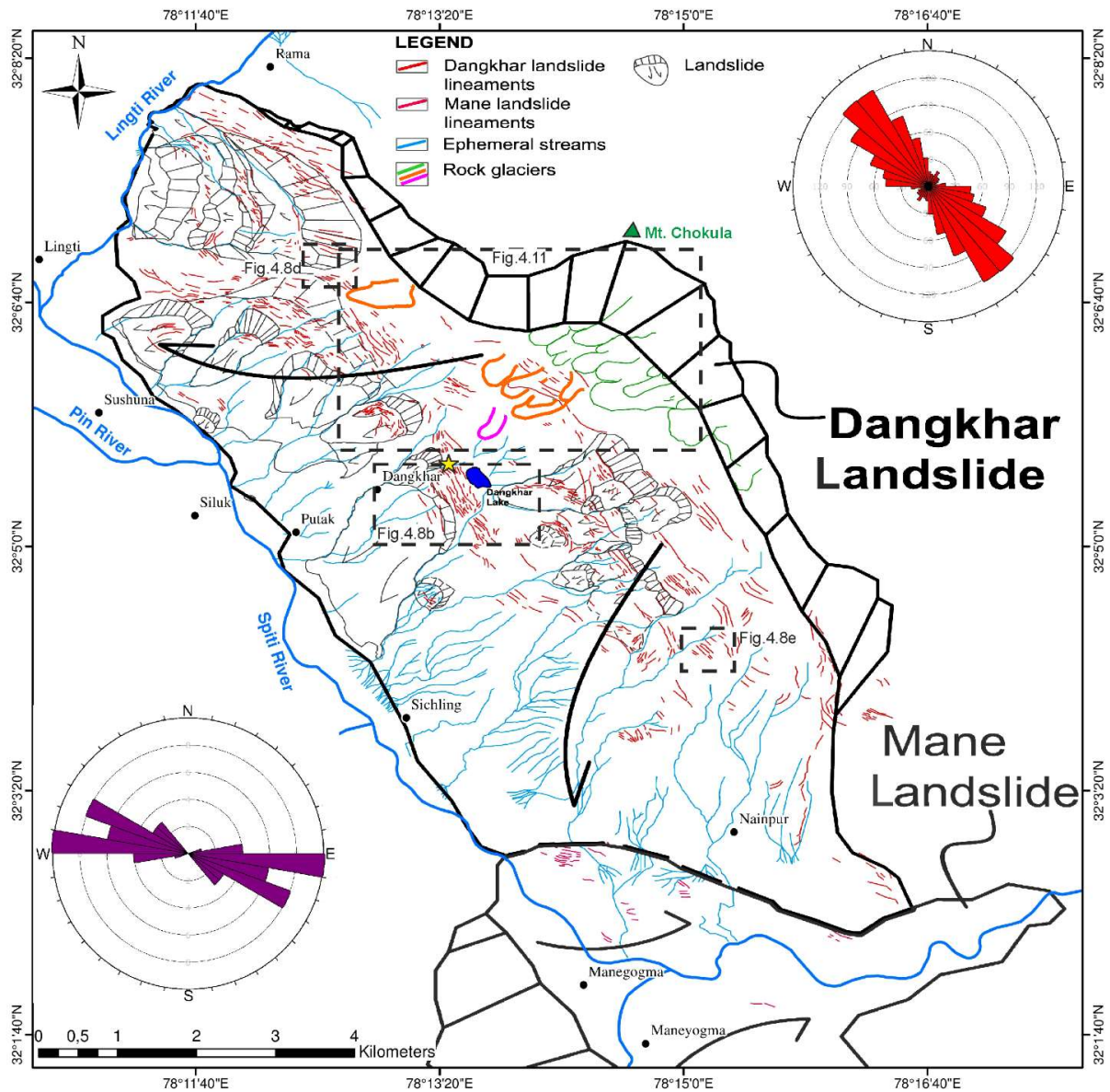


Fig. 4.7 Satellite photointerpretive lineament map of the study area. Alignment of lineaments within the Dangkhar Landslide and the Mane Landslides are shown in rose diagrams (top right and bottom left corner, respectively). Note valley parallel alignment of the lineaments. Yellow star marks viewpoint of Fig. 4.8c towards the southeast

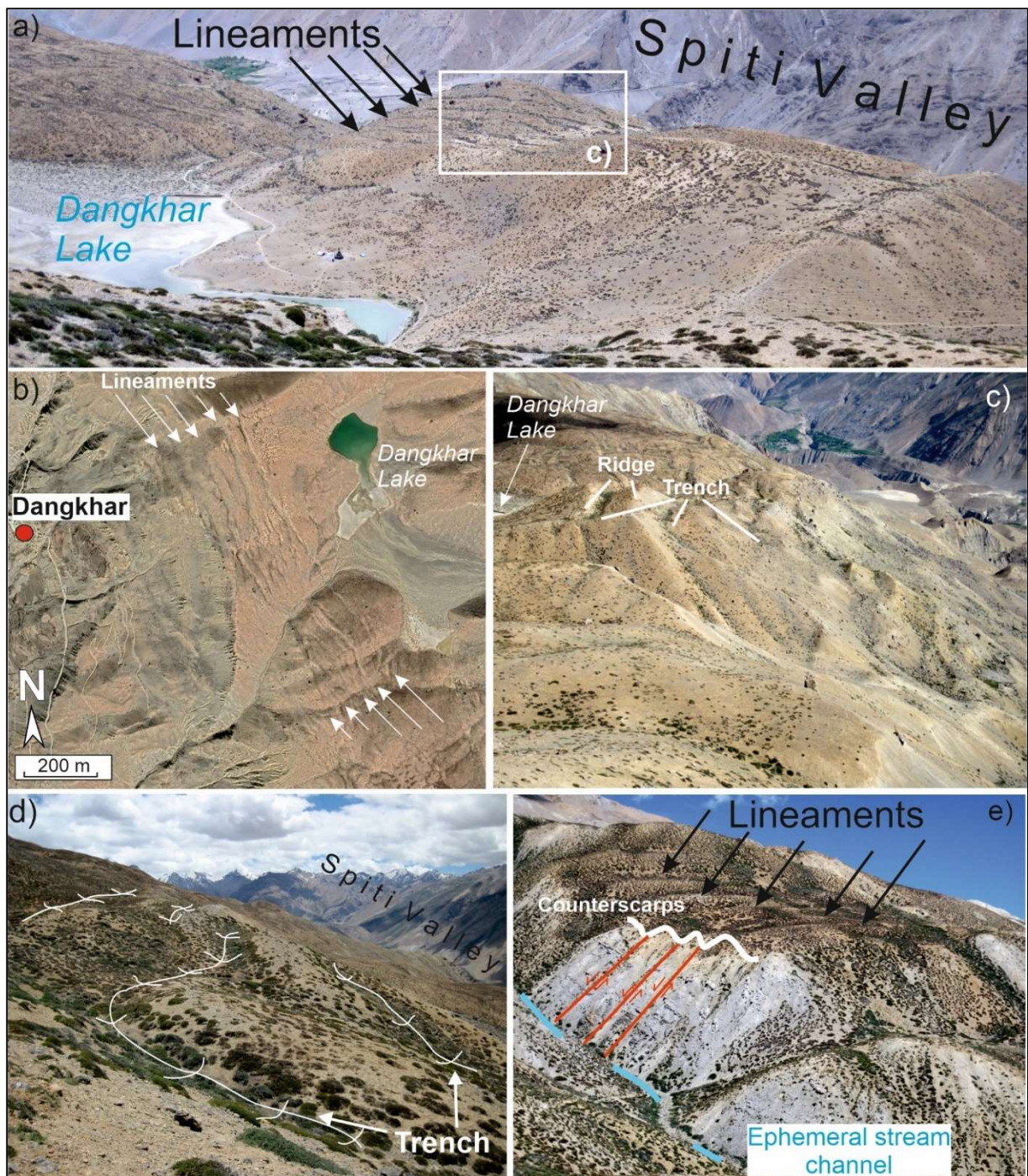


Fig. 4.8 Major geomorphologic features of the Dangkhar Landslide. a) Parallel array of lineaments on the mid-slope bench downhill from the Dangkhar Lake b) Satellite image of lineaments downhill from the Dangkhar Lake c) Field photograph of the lineaments shown in (a) expressed as ridges and trenches. d) Ridge and trench formed in the upper part of the Dangkhar Landslide deposit. e) Cross section of lineaments in an ephemera stream channel exposing counterscarps (red lines indicate slip surfaces active during toppling)

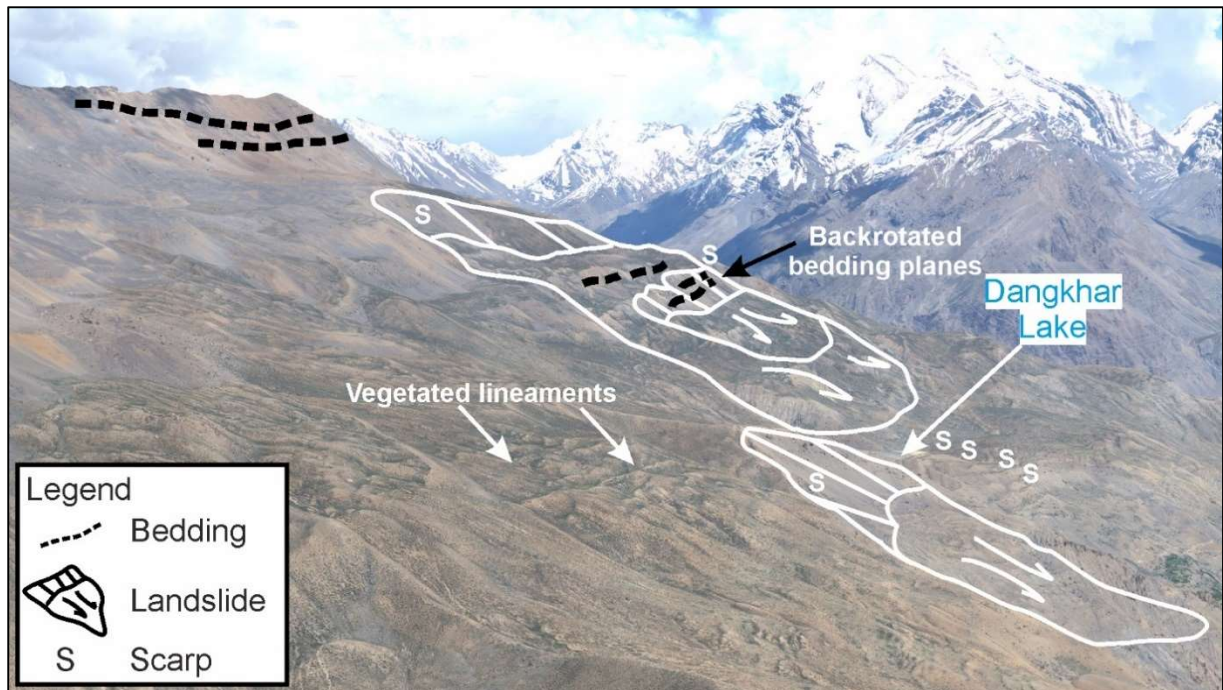


Fig. 4.9 Characteristic Dangkhar Landslide slope features; secondary landslides, lineaments and scarps

Deposits representing three generations of rock glaciers occur on the upper flat area, west of the peak of Mt. Chokula are partly located within the favorable permafrost zone (Fig. 4.10; Gruber 2012). They exhibit lobate shaped deposits with surficial furrows and ridges, which get progressively subdued on satellite images (Fig. 4.11a). The two generations of subdued glacial deposits are regarded to be relict rock glacier moraines while the third generation located within the permafrost zone represents the contemporary rock glaciers. The rock glaciers record advances down to elevation 4250, 4400 and 4600 m and represent an overall pattern of progressive retreat. The distance between the most subdued rock glaciers to the contemporary rock glaciers is about 1.2 km.

The contemporary rock glacier generation exhibits about 35° – 40° steeply dipping, unvegetated frontal slopes and a tongue shaped lobate form in map view. Their surface is characterized by fresh ridges and furrows and they stand out from the surrounding environment (Fig. 4.11b & c). The proximity to the bedrock outcrop at Mt. Chokula suggests that the rock glaciers are of protalus type, fed by debris supply.

The valley parallel lineaments of the Dangkhar Landslide show cross cutting relations with the rock glaciers (Fig. 4.11a & b). The first and second rock glacier generations, exhibit a higher degree of vegetation cover and their boundaries to the surrounding environment become more diffuse, and they are cut and displaced by the lineaments (Fig. 4.11b & c).

The third rock glacier generation near Mt. Chokula overrides the slope parallel lineaments, but is not displaced by them (Fig. 4.11b).

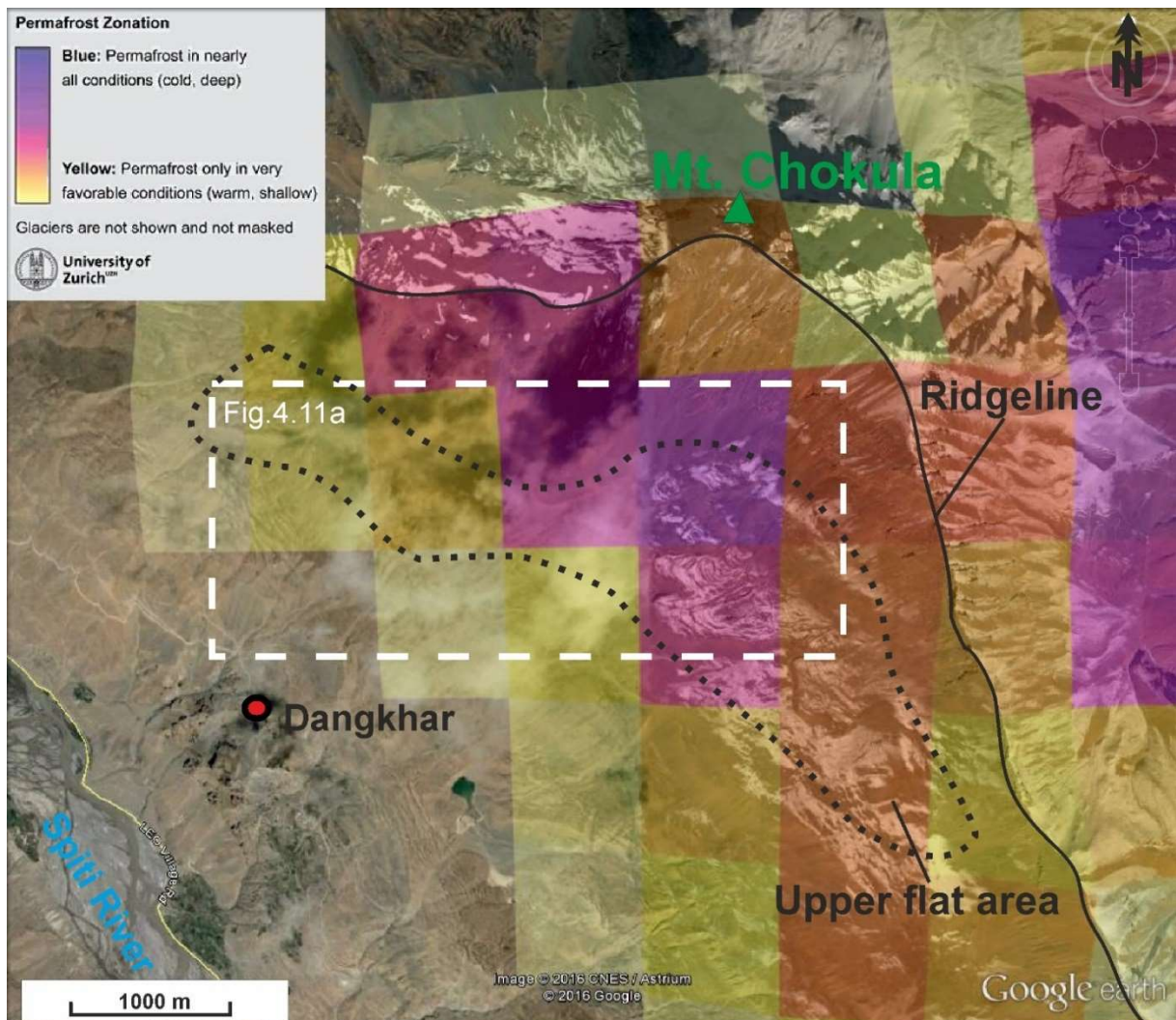


Fig. 4.10 Permafrost zonation (after Gruber 2012) on the Dangkhar Landslide. Ridgeline of Mt. Chokula shown for orientation

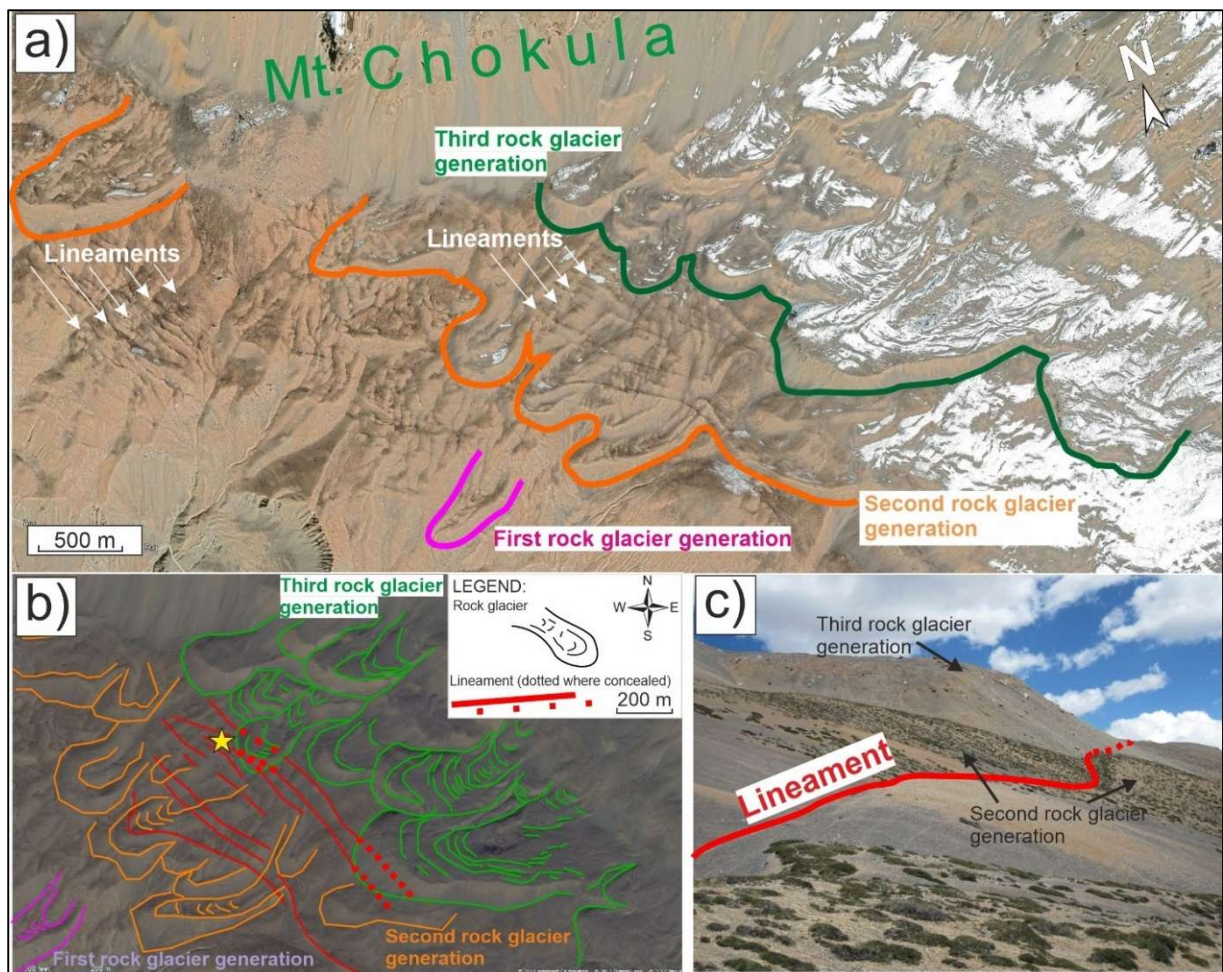


Fig. 4.11 Rock glaciers near Mt. Chokula. a) Satellite image of the rock glacier generations and lineaments. Note how rock glacier generations get more subdued from first to third generation. b) Mapped rock glacier generations and lineaments showing their cross cutting relation (yellow star marks location of field photograph shown in c. c) Field photograph of third rock glacier generation overriding a lineament (dotted where concealed)

4.2.2 Dangkhar Landslide hydrology

Ephemeral stream channels exhibiting straight, parallel to dendritic drainage patterns, dissect the Dangkhar Landslide deposit, partly exposing rock blocks. In general, surface waters are rare and restricted to small streams. Springs preferentially occur along the lower part of the slope projected downhill from the rock glaciers (Fig. 4.12) suggesting a meltwater source from this area.

Several lake beds exist in the study area, which are fed by tributary streams (Fig. 4.12). The majority of streams carrying water is restricted to the area around Dangkhar Village and the Dangkhar Lake and are partly routed towards the fields to water the crops.

During the summer field seasons, the Dangkhar Lake, situated at an elevation of 4140 m east of Dangkhar is the only lake in the study area with water in it. The Dangkhar Lake is about 250 m in length and approximately 100 m wide at the time of inspection. Annual water level fluctuations are on the order of 1 m to 3 m (communication with locals). The lake is fed by three ephemeral streams of which only one showed discharge during the summer field seasons. The Dangkhar Lake has one surface outlet towards the Spiti River, but is not operating due to the low water level in the lake. Distribution of Dangkhar Lake sediments on the mid-slope bench showing shrinkage cracks, indicate the former maximum extent of the Dangkhar Lake within the Dangkhar Lake basin (Fig. 4.12).

The second lake is situated adjacent northwest of the Dangkhar Lake at about the same elevation. This empty lake is a narrow ellipsoid shaped, dry, meadow covered plain. Its long axis is aligned parallel to the slope and one dry tributary stream projects from the rock glaciers uphill. Its downhill side towards Dangkhar is open by means of an outlet ditch. Presumably the outlet ditch formed after a breach of the downhill side releasing water in a sudden event. Evidence for such an event are elaborated and discussed in more detail in Chapter 4.2.8.

The lake beds of Dry Lake 1 and Dry Lake 2 are located near the Spiti Valley floor and on the Mane Landslide debris, respectively. The two lakes contain water after snowmelt during springtime (communication with locals).

Water presently plays an important role in the erosion of the Dangkhar Landslide. Debris flows, commonly occur after heavy rainfall events (communication with locals, own observations). The debris flows mobilize material on the Dangkhar hillslope and descend downslope via the ephemeral stream channels depositing material along the banks of the Spiti River (Fig. 4.13a). The debris flows typically result from blockage of the ephemeral stream channels. Subsequent bursts of the blockage lead to a catastrophic release of a mix of water and material resulting in a debris flow. When the debris flows reach the valley floor, and are not confined any more by the ephemeral stream channels, spread out into the Spiti

River bed thus forming a lobe (Fig. 4.13a). The debris flow material consists of a mixture ranging from clay to boulders with incorporated blocks up to several meters in diameter. Along the toe area, several tens of meters above the Spiti Valley floor, more subdued and vegetated deposits exhibiting an approximately triangular shape exist (Fig. 4.13b). These deposits partly overly the early mid-Holocene Mane paleolake sediments and are commonly dissected by ephemeral stream channels. The deposits form a fan and are evidence for historic debris flows and colluvial erosion processes on the Dangkhar Landslide, and formed due to consecutive debris flow events.

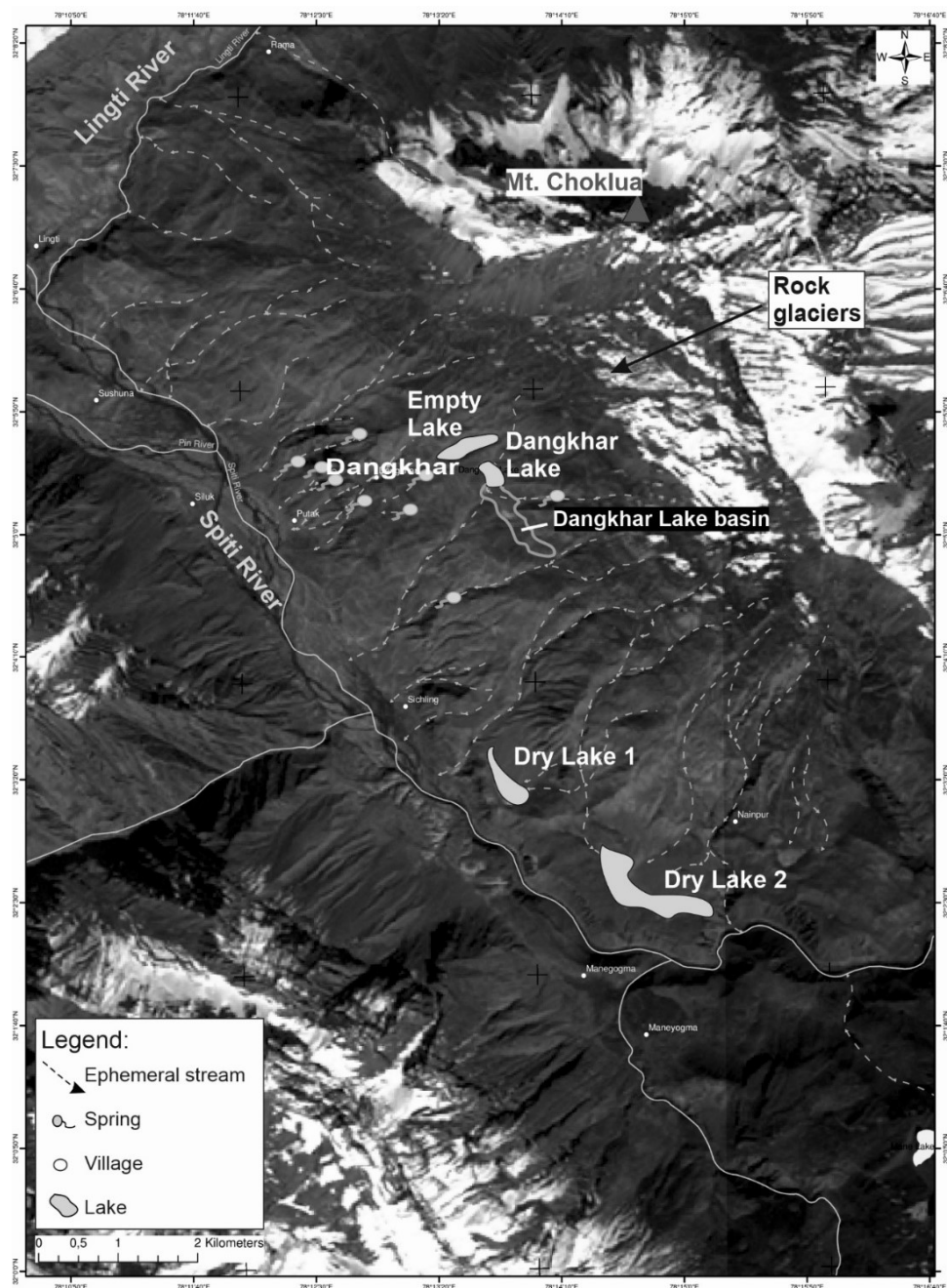


Fig. 4.12 Surface water distribution of the Dangkhar hillslope (image source: NRSC 2016)

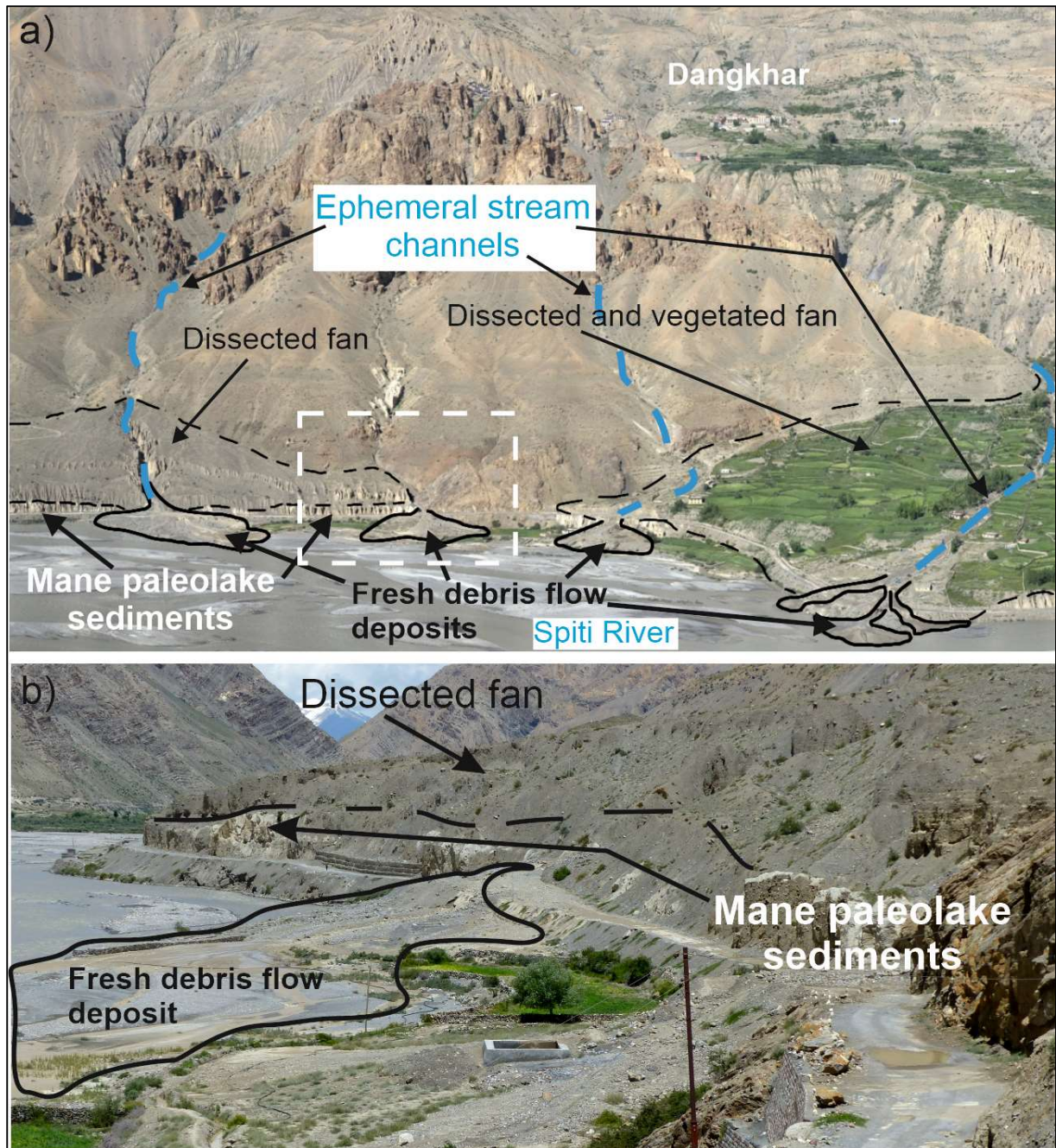


Fig. 4.13 Fluvial processes on the Dangkhar Landslide. a) Fresh debris flows triggered after a heavy thunderstorm event during the night from July 21st to 22nd, 2015. Dissected fans overlying Mane paleolake sediments (pale yellow deposits) Dashed rectangle shows location of features shown in b). GigaPan panorama was taken at Siluk the day after the thunderstorm event #GP www.qigapan.com/qigapans/178319 (Snapshots: Debris flows). b) Field photograph after the debris flow events. Dashed line marks contact between the Mane paleolake sediments and the deposits of the dissected fan

4.2.3 Geologic units and structure

The most recent stratigraphic classification by Bhargava (2008) was adopted for mapping of the bedrock units (Tab. 4.1). It is based on Hayden (1904), who first established a lithostratigraphic system accounting for the rocks of Spiti. Hayden's formation names are based on their respective fossil content and Bhargava (1987) and Bhargava and Bassi (1998) adopted Hayden's work and assigned his units to eight formations. Those units are referred to as the Lilang Supergroup and account for the Mesozoic carbonate rich sequence of Spiti.

The study area exhibits features of bedrock and quaternary geology, such as glacio-fluvial, fluvial, talus deposits and mass wasting phenomena. Bedrock geology of the site is built up of upper Permian to lower Jurassic rocks of the Tethys (Tibetan) Himalaya and occur quite consistently throughout the study area and due to almost no vegetation in the region these units can be traced fairly well along strike even from a certain distance.

Bedrock primarily consists of thick bedded carbonates of the Kioto Group, Chomule and Rongtong Formations, along with shale of the Alaror, Rangrik and Rama Formations and subordinate rocks of the Kuling Group (Fig. 4.14). Bedrock outcrops are concentrated at the head and toe of the Dangkhar hillslope, with Quaternary surface deposits occupying the intermediate area and the valley floor.

The thick bedded limestone and dolomite of the Kioto Group occupies most of the highest altitudes and forms steep cliffs, up to 600 m to 700 m high at Mt. Palangri. The Mt. Chokula peak and ridge area which forms the headscarp is chiefly composed of the Kioto Group rocks forming a curved, nearly vertical ridge up to 400 m high in its central part, with bedding dipping southwestwards at varying inclinations of 30 to 45°. Towards the southeast, the Mt. Chokula ridge gets less steep and is composed of shales of the Alaror Formation.

In the Lingti Valley mostly bedrock assigned to the Lilang Supergroup is exposed. Only at the confluence of the Spiti and Lingti River Permian rocks of the Kuling Group are encountered and juxtaposed against the Lilang rocks by a fault. They occur as a conspicuous plateau just south of Lingti. The Permian rocks also crop out along the toe of the slope beneath Dangkhar along the main road at Putak.

The overall bedrock geometry is highlighted in the geologic cross sections (Fig. 4.15) and includes an open, asymmetric synclinal flexure (concave dipslope) with an axial surface trending subparallel to the Spiti Valley and passing through Dangkhar Village (Fig. 4.14; Fig. 4.16a, b). The synclinal flexure is defined by bedding dipping at 30-40° to the southwest near Mt. Chokula, and 10-15° to the northeast at the toe of the slope. The syncline marks the trace of the Spiti Synclinorium (Hayden 1904) in the study area. Southwest of the syncline are the sub-parallel Spiti Valley Anticline and Spiti Valley Fault (SVF).

The inferred curved basal slip surface of the Dangkhar Landslide follows this shape and is chiefly located within the shale rich Rama Formation. To the west of the study area the bedrock is formed by alternating successions of tightly folded synclines and anticlines.




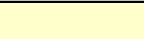

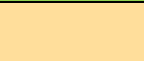


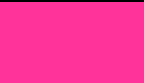






The vast debris accumulation depicted on the geologic map forms the Dangkhar Landslide deposit. The debris constituting the Dangkhar Landslide deposit is primarily composed of crushed, angular to subangular carbonate and shale rock fragments and subordinate of sandstone and siltstone fragments covering an area of about 40 km². Grainsizes for the debris vary from clay sized particles to boulders having a maximum dimension of several meters. Along the toe region of the Dangkhar Landslide, carbonate cements have lithified the debris to form outcrops of carbonate breccia (Fig. 4.17a). The breccia can be classified as a Block-In-Matrix rock type (Kieffer and Steinbauer 2012). The carbonate breccia locally shows internal stratification and signs of dissolution and precipitation of carbonates expressed as a white salt crust on the surface (see chapter 4.2.6 for details).

The contact from the bedrock units to the Dangkhar Landslide deposit is not sharply defined. The transition-zone outcrop is exposed north of Dangkhar Village in an erosional gully, and exhibits characteristics commonly associated with mylonitic fault zones. It is characterized by reworked bedrock material of the Rama Formation with subtle bedding, gradually passing into the Dangkhar Landslide debris above (Fig. 4.17b, c). For the most part, the transition zone at the toe area is concealed by debris.

Lake sediments associated with the Mane paleo-lake occur upstream along the toe region of the Dangkhar Landslide and are partly overlain by alluvial fan deposits. Minor occurrences of lake sediments on the Dangkhar Landslide deposit are related to meltwater lake beds. From the spatial distribution of lake sediments on the midslope bench, the maximum historical extend of the Dangkhar Lake was estimated, indicating that it occupied a stretch of about 1.4 km southeastwards from the present day Dangkhar Lake.

Isolated rock blocks within the Quaternary surface deposits, having maximum dimensions up to one kilometer, are of the same lithologies exposed near the peak of Mt. Chokula. These massive rock blocks are best exposed within ephemeral stream channels opposite from Mane (Fig. 4.16a; #GP www.gigapan.com/gigapans/178378; Snapshot: rock blocks). The isolated rock blocks generally dip approximately parallel to the slope surface at 20° to 30°, and exhibit wavy folding at a scale of tens to rarely 100 m in the upper part and show intense internal folding towards the lower part (Fig. 4.17d, e) and are partly dissected by ephemeral stream channels (Fig. 4.17d). The isolated rock blocks located within the sliding mass towards the southern margin represent rafted blocks (Fig. 4.14; Fig. 4.18) displaced by translational movement parallel to the bedrock strata orientation along the longer dipslope limb of the asymmetric syncline (Fig. 4.15). Their orientation is consistent with the overall bedrock

geometry and they are not affected by folding. The characteristic hummocks occurring throughout the landslide deposit comprise bedrock cores and are folded with wavelengths of usually not more than several tens of meters having their axis aligned parallel to the slope (Fig. 4.17e).

	Map Color	Geologic Unit	Main Lithology	Broad Age
Surficial Deposits		Alluvium	Sorted gravel, sand	Holocene
		Talus Fans	Limestone, dolomite clasts	Holocene
		Lake Sediments	Laminated silt, clay	Holocene
		Mane Landslide Deposit	Unassorted silt, sand, gravel, blocks	Holocene
		Rock Glacier Deposits	Limestone, dolomite clasts	Late Pleistocene – Holocene
		Breccia	Carbonate breccia, partly crudely stratified	Late Pleistocene – Holocene
		Dangkhar Landslide Deposit	Unassorted silt, sand, gravel, blocks	Late Pleistocene – Holocene
Bedrock		Kioto Group	Limestone, dolomite	Late Rhaetic – Lias
		Alaror & Rangrik Formation <i>(Monotis Shales & Juvavites Beds)</i>	Shale, sandstone, limestone	Early – Late Noric
		Rongtong Formation <i>(Tropites Beds)</i>	Dolomite, limestone	Middle – Late Carnic
		Rama Formation <i>(Grey Beds)</i>	Shale, sandstone, limestone	Early – Middle Carnic
		Chomule Formation <i>(Halobia and Daonella Limestone)</i>	Limestone	Ladinic – Early Carnic
		Kaga Formation <i>(Daonella Shales)</i>	Shale, siltstone, limestone	Ladinic
		Mikin Formation <i>("Muschelkalk")</i>	Limestone	Induan – Anisian
		Gungri Formation	Shale	Dzulfian – ? Early Dorashamian
		Gechang & Ganmachidam Formation	Conglomerate, sandstone, shale	Asselian – Late Carboniferous

Tab. 4.1 Lithostratigraphic sequence of the Tethys Himalaya within the study area. For the formations of the Lilang Supergroup the equivalent historic formation names of Hayden (1904) are given in italics in parentheses (modified after Bhargava 2008; Fuchs 1982 and references therein)

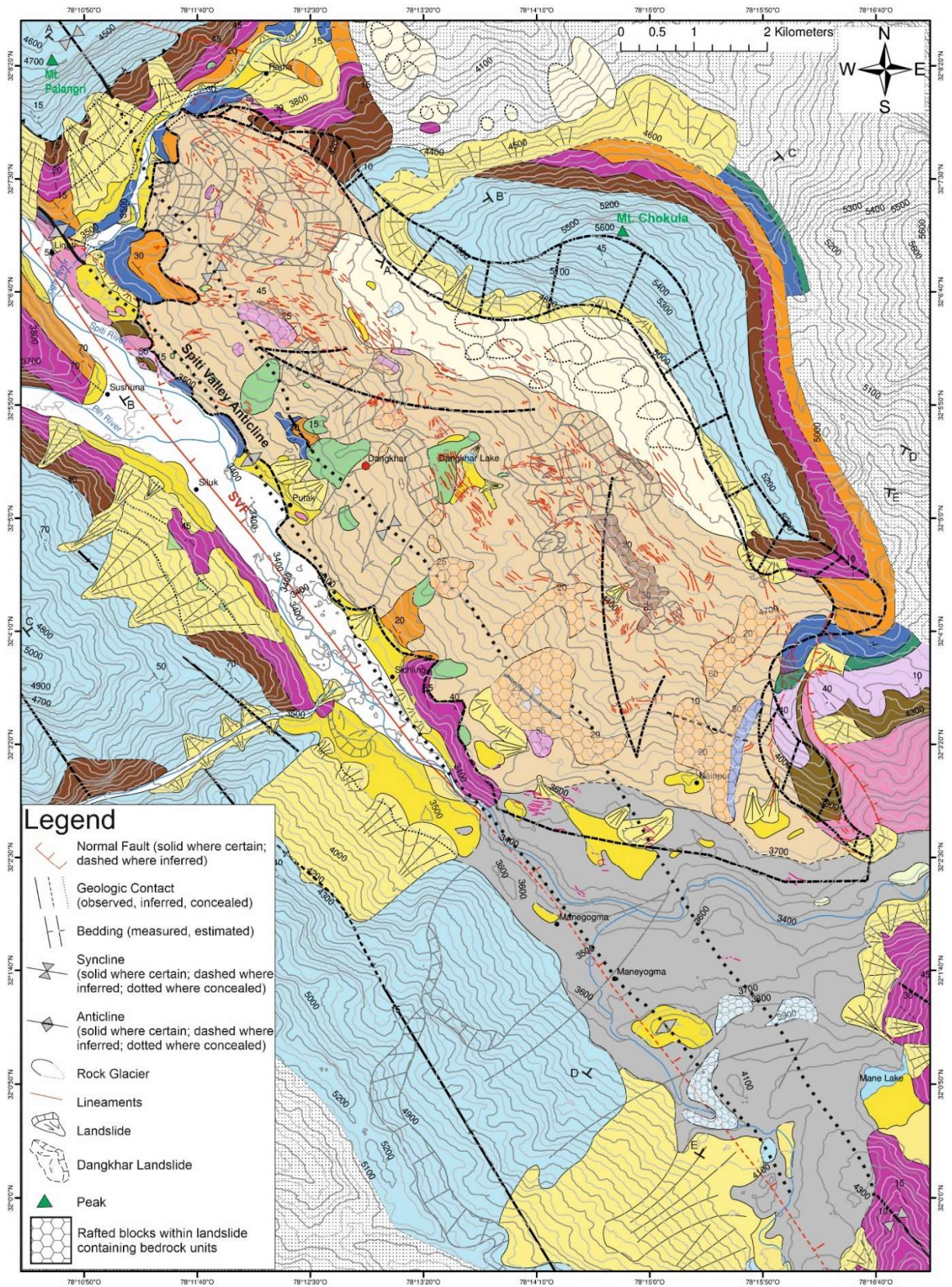


Fig. 4.14 Geologic map of the Dangkhar Landslide. Geologic units as in Tab.4.1

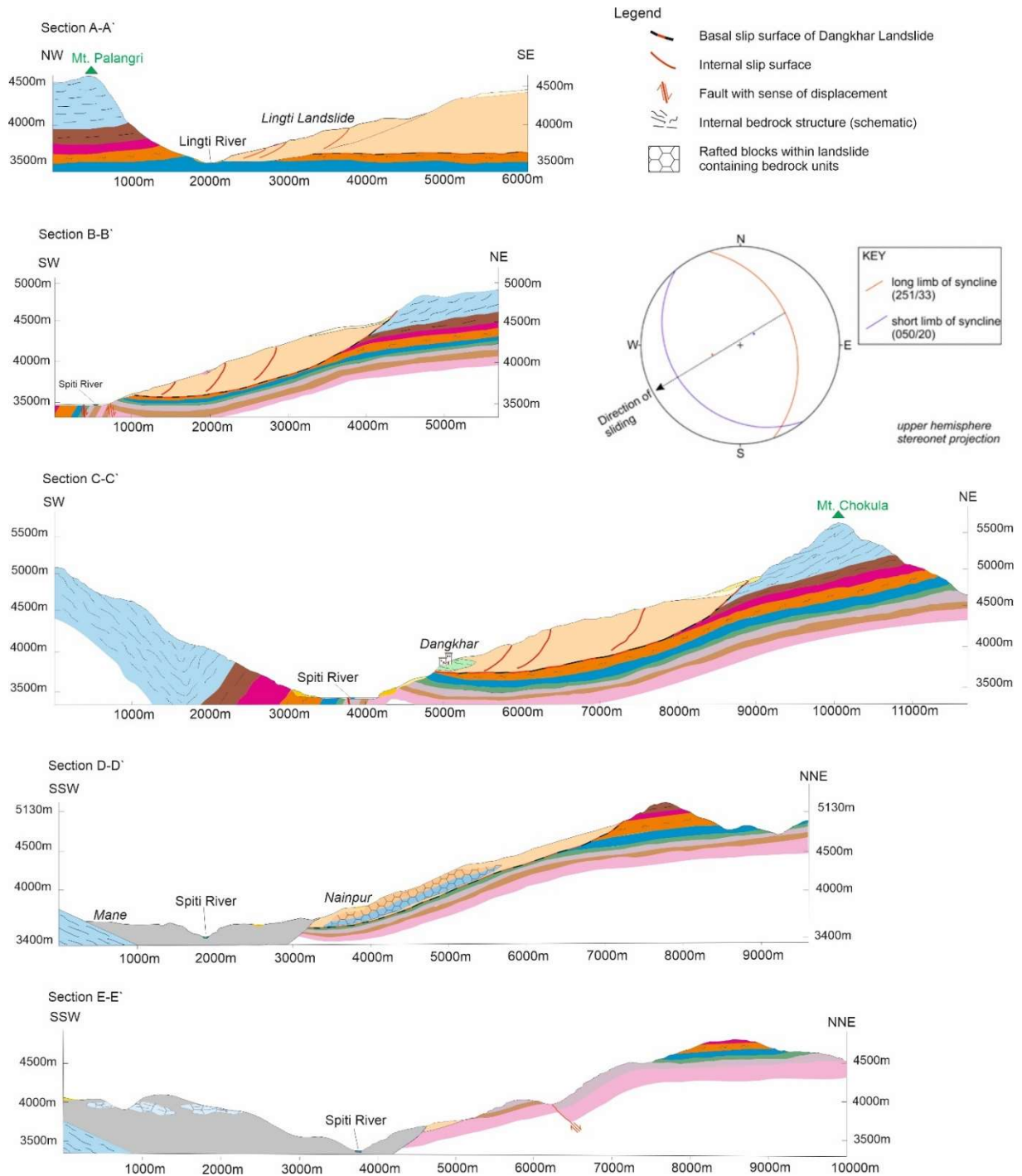


Fig. 4.15 Geologic cross sections through the study area and stereographic plot of syncline limbs. Upper hemisphere projection is used to be consistent with orientations of cross section and map view (geologic units as in Fig. 4.14)

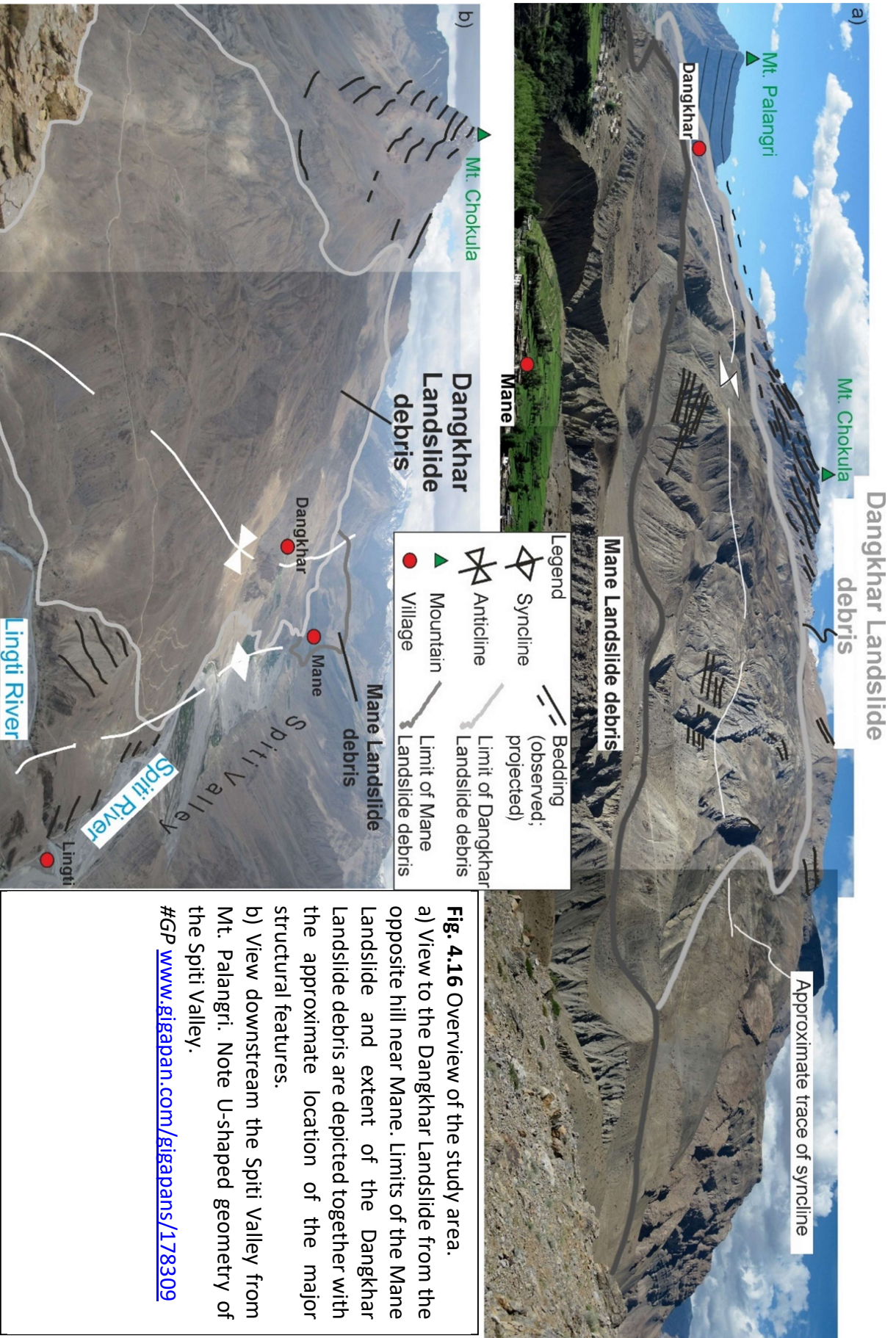


Fig. 4.16 Overview of the study area.

a) View to the Dangkhar Landslide from the opposite hill near Mane. Limits of the Mane Landslide and extent of the Dangkhar Landslide debris are depicted together with the approximate location of the major structural features.

b) View downstream the Spiti Valley from Mt. Palangri. Note U-shaped geometry of the Spiti Valley.

#GP www.gisapan.com/gisapans/178309

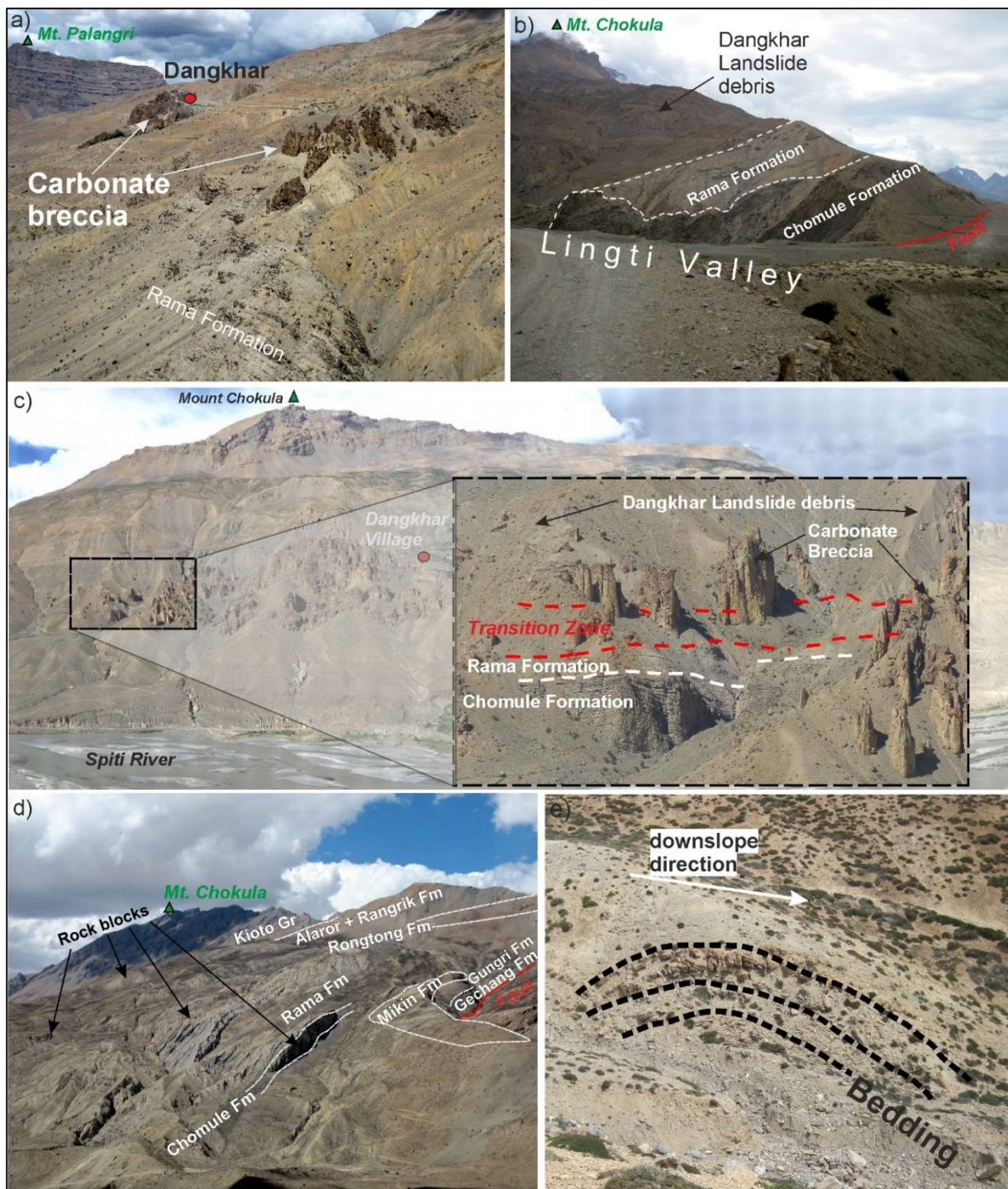


Fig. 4.17 Characteristic Dangkhār Landslide structures. a) Carbonate breccia patches near the slope toe area. b) Exposed bedrock units in the Lingti Valley. c) Transition zone from bedrock to debris and carbonate breccia (#GP <http://www.gigapan.com/gigapans/178308> Snapshot: Transition Zone). d) Southern part of the Dangkhār Landslide showing bedrock blocks within the debris. e) Folded strata within the Dangkhār Landslide

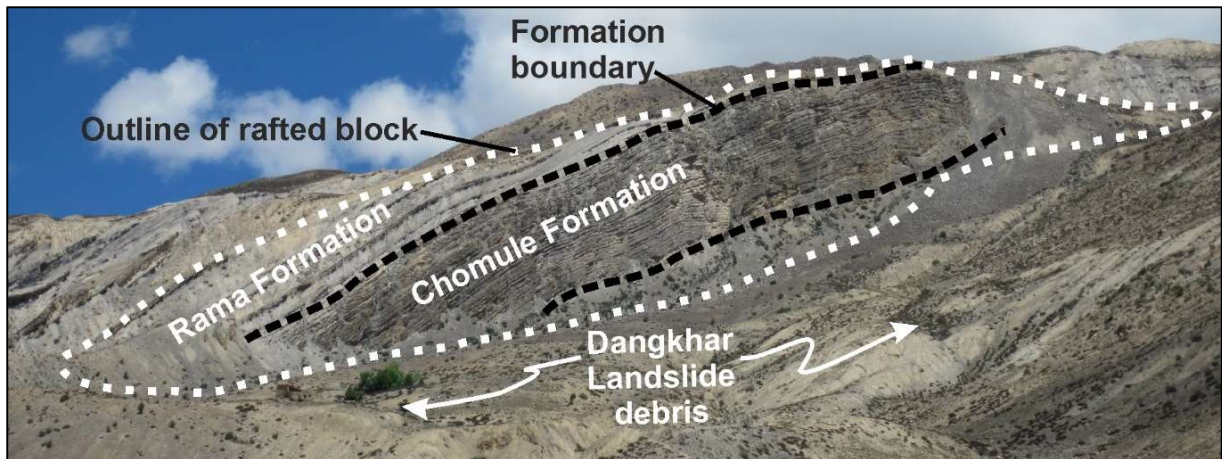
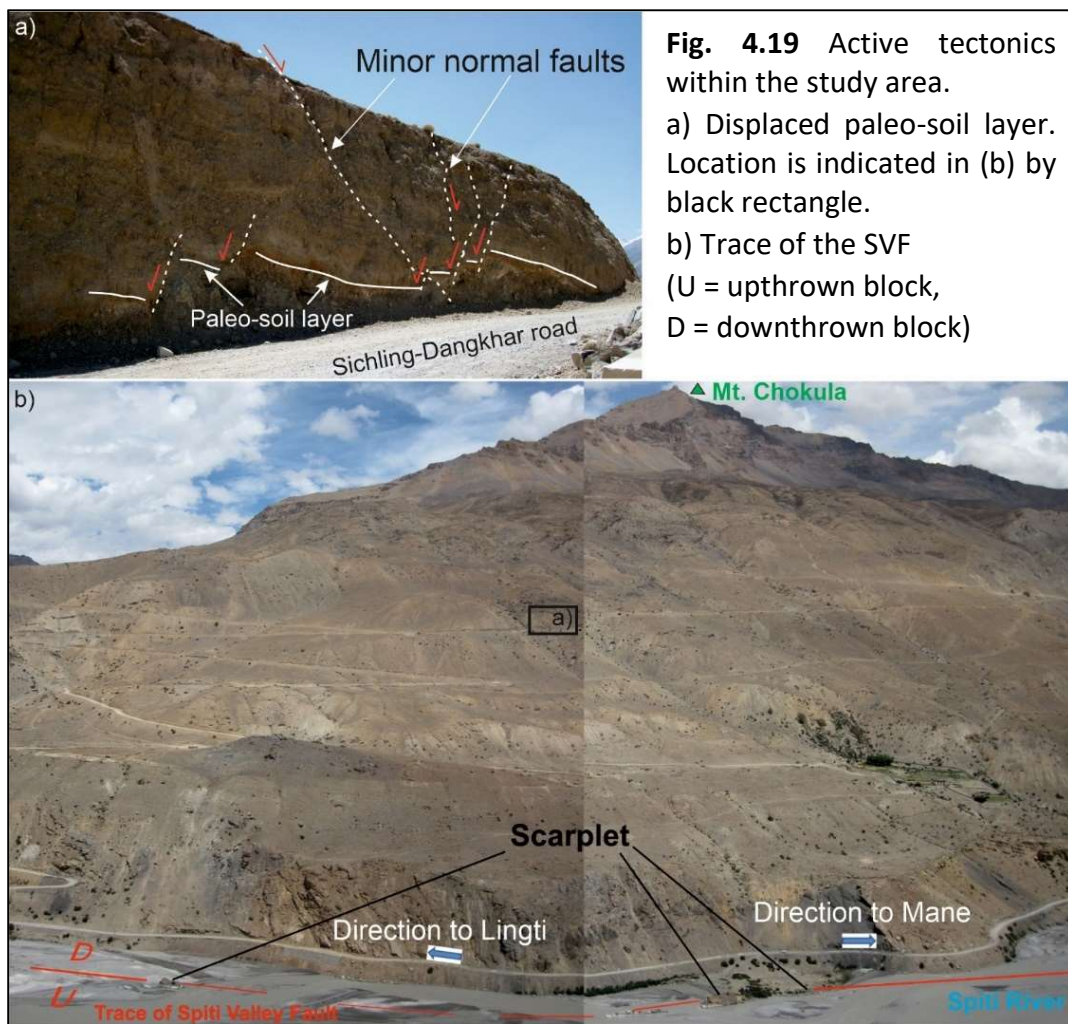


Fig. 4.18 Rafted block within the Dangkhar Landslide debris incorporating the Rama and Chomule Formations

Along the Sichling-Dangkhar road, landslide debris and paleo-soil layers are offset by minor normal faults (Fig. 4.19a), which run parallel to the main SVF. Bedrock scarplets of the SVF surrounded by alluvium are exposed within the bed of the Spiti River (Fig. 4.19b). These features are the result of active tectonics within the study area.



The southern part of the study area includes deposits of the Mane Landslide, a rockslide (Anoop et al. 2012; own observations) with the sliding plane developed along a 55° steep northeast facing anticline limb (Fig. 4.20). The sliding plane is located within the thickly bedded Kioto limestone. The Mane Landslide debris consists of crushed carbonate rocks, which travelled across the Spiti River to the opposite side of the Spiti Valley, leaving a surge on the southern margin, unconformably overlying the Dangkhar Landslide debris (Fig. 4.21).



Fig. 4.20 The Mane Landslide seen from the Dangkhar hillslope. White arrows indicate direction of sliding (#GP www.gigapan.com/gigapans/178300)

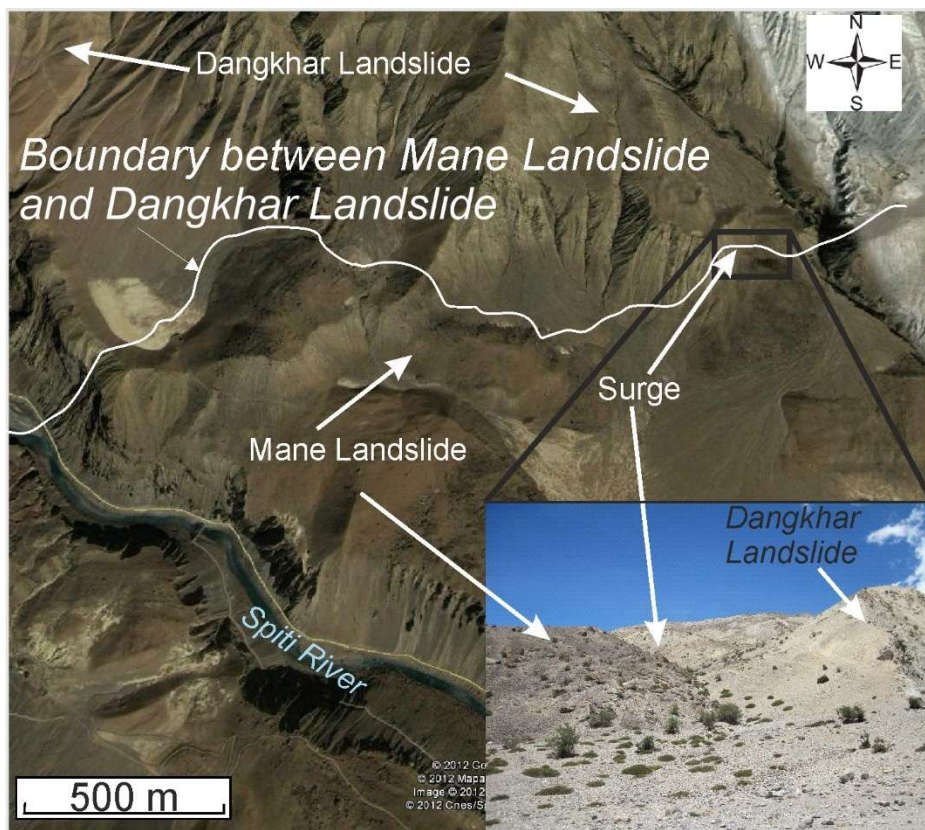


Fig. 4.21 Boundary between the Dangkhar and the Mane Landslide debris. Note difference in color of the two deposits in the image in bottom right corner

4.2.4 Extent and dimensions of the Dangkhar Landslide

The Dangkhar Landslide occupies the left slope of the Spiti Valley between Lingti and Nainpur (Fig. 4.22a). Along the southwestern and southern toe area, the Spiti River marks the limit of the landslide debris, whereas along the northern to northwestern toe area the Lingti River limits the landslide. The Mt. Chokula peak area represents the crown of the Dangkhar Landslide. Several secondary landslides occur within the Dangkhar Landslide, with the Lingti Landslide being the largest one with a volume of 0.3 km^3 (Fig. 4.22a; Bookhagen et al. 2005). The Dangkhar Landslide is situated at elevations from 3400 m to 5600 m (Fig. 4.22b) exhibiting a total vertical height (H_v) of 2200 m (toe to crown). The total length (L) from crown to tip is about 6938 m, with the inferred tip located at the left bank of the Spiti River. The length of the displaced mass (L_d) from the top to the tip stretches over 6000 m. The maximum depth of the displaced mass (D_d) and the original sliding mass (D_r) is estimated at 583 m and 490, respectively (Fig. 4.22b; Tab. 5.1). The inferred basal slip surface follows the shape, of the overall bedrock geometry defined by the asymmetric synclinal flexure where the longer limb of the syncline dips towards the valley.

The length of the basal slip surface (L_r) stretching from the crown to the toe is about 5625 m. Vertical (V_c) and horizontal (H_c) components of L_r are 1900 m and 5100 m, respectively. The ratio of D_r/L_r is used as an indicator for the relative deepness of a landslide and is in the range of 0.15 to 0.33 for rotational slides in clays or shales (Skempton and Hutchinson 1969). Some slopes however can develop ratios around 0.1 or lower. The Dangkhar Landslide exhibits a D_r/L_r ratio of 0.09, indicating a relatively shallow landslide geometry. In general, landslides tend to get relatively shallower as size increases (Kalderon-Asael et al. 2008).

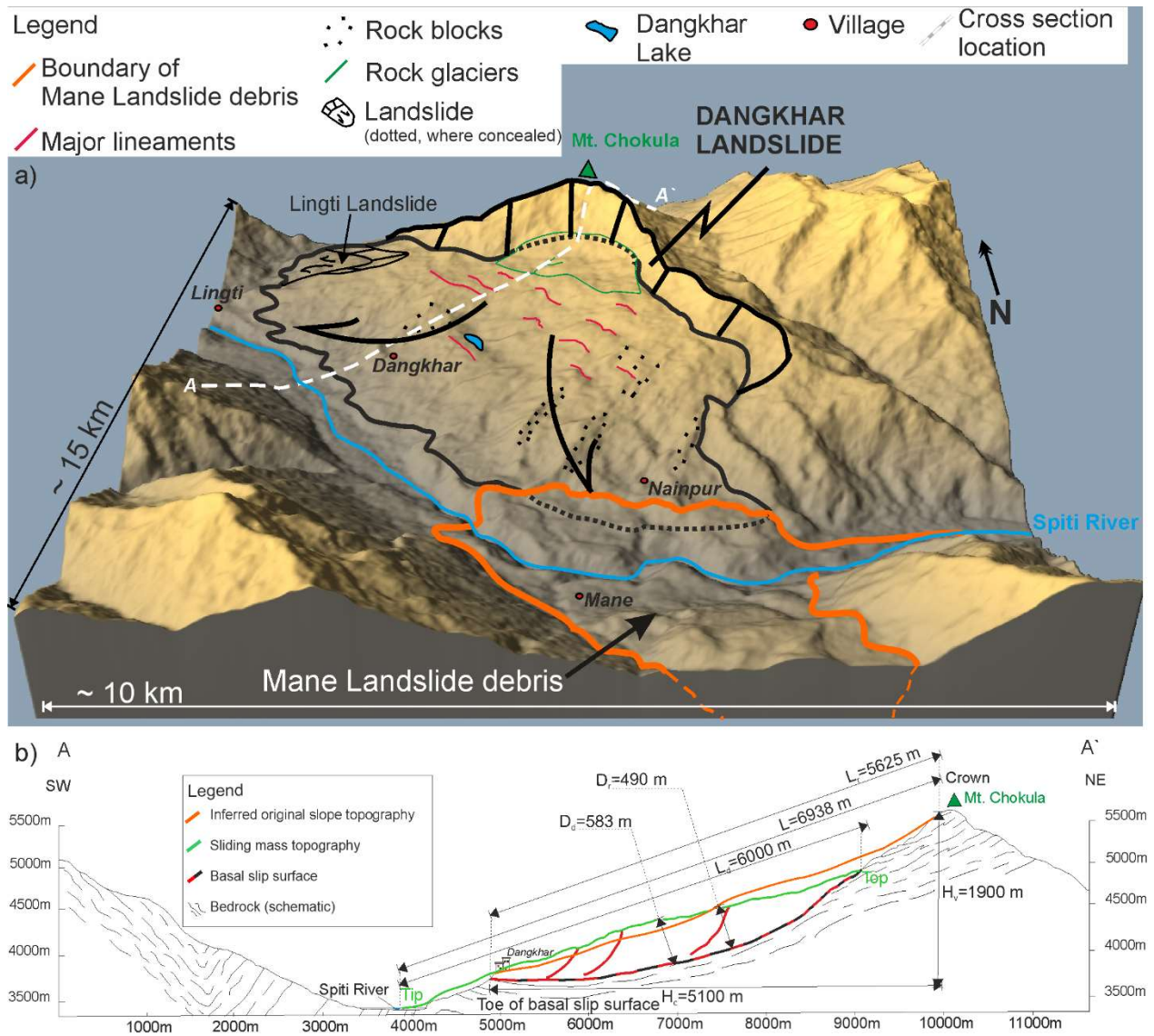


Fig. 4.22 The Dangkhar Landslide. a) 3D digital elevation model of the Dangkhar Landslide outlining the major geomorphic features. b) Schematic cross section with 2D landslide dimensions. Morphometric details are also listed in Tab. 4.2

The Dangkhar Landslide deposit and headscarp cover an area of about 40 km² and 14 km², respectively (Fig. 4.23). To the southeast, the Mane Landslide deposit is in contact with the Dangkhar Landslide deposit (Fig. 4.23). Tab. 4.2 summarizes the morphometric characteristics of the Dangkhar Landslide.



Fig. 4.23 Areal extent of the Dangkhar Landslide deposit (40.44 km²) and the Mane landslide deposit (16.90 km²). Image and data source: ArcGIS Explorer Online

Parameter	Value
Vertical component – V_c [m]	1900
Horizontal component – H_c [m]	5100
Length displaced mass – L_d [m]	6000
Length of surface of rupture – L_r [m]	5625
Total length – L [m]	6938
Width of displaced mass – W_d [m]	14230
Width of surface of rupture – W_r [m]	13692
Depth of displaced mass – D_d [m]	583
Depth of surface of rupture – D_r [m]	490
Total area – A_{total} [km ²]	54
Area of displaced mass – A_d [km ²]	40.5
Volume of ruptured mass – Vol_r [km ³]	19.80
Volume of displaced mass – Vol_d [km ³]	24.70
Swell Factor – SF [-]	0.25

Tab. 4.2 Morphometric characteristics of the Dangkhhar Landslide (after WP/WLI 1990; Varnes 1978). Subscripts “d” and “r” indicate properties attributed to the displaced material and the surface of rupture, respectively

4.2.5 Dangkhhar Landslide volume estimates

Methods to estimate the Dangkhhar Landslide volume included: (1) TIN difference modelling of the basal slip surface and the ASTER DEM dataset in ArcGIS 10.1; (2) the average end-area (AEA) method, (3) morphometric dimensions and landslide volume formulas provided by the Working Party on World Landslide Inventory (WP/WLI 1990), and (4) a Cut and Fill operation performed in MicroDEM.

The Cut and Fill operation and TIN difference modelling, involve the ASTER DEM dataset related operations, the AEA method uses cross sections through the landslide deposit estimating the position of the basal slip surface. The DEM volume estimates can only consider the present state of the topography and do not account for the changes of the deposit over time (e.g. original pre-failure topography, erosion). On the other hand, it allows modelling of irregular basal slip surface morphology and takes changes in thickness of the landslide deposit into account. The volume estimate suggested by the WP/WLI (1990) provides calculation schemes for the initial landslide volume (i.e. before movement) and the post failure volume. However, this approach is based on an idealized geometry of a landslide (e.g. half of an ellipsoid) and might not adequately account for landslides with irregular geometries.

Average End-Area Method

The average End-Area method is a standard technique, commonly employed in earth work constructions to estimate volumes of bodies. The volume is calculated from cross sectional areas obtained from cutting a solid body into slices perpendicular to a reference line (Fig. 4.24). The inferred basal slip surface is projected from one cross section to another, where each of the cross section accounts for 50 % of the space between the adjacent ones. Only the cross section located closest to the margin of the landslide is stretched out to the maximum extent and adjusted according to the inferred geometry of the landslide body. In this case the shape of the margin is assumed to be a wedge (Fig. 4.24). The total volume of a body is the sum of the slices (Equation 5.1).

Equation 5.1:

$$V = A_{A-A'} \left(X_1 + \frac{d_1}{2} \right) + A_{B-B'} \left(\frac{d_1}{2} + \frac{d_2}{2} \right) + A_{C-C'} \left(\frac{d_2}{2} + \frac{d_3}{2} \right) + A_{D-D'} \left(\frac{d_3}{2} + X_2 \right)$$

where:

V = Volume of landslide body [km^3]

$A_{A-A'}$ = Area of individual cross section [km^2]

d = Distance between neighboring cross sections [km]

x = Distance from cross section to margin of body [km]

The hand drawn cross sections were digitized in AutoCAD in order to extract the area of the cross section as accurate as possible. The distance between the respective cross sections was measured in Google Earth Pro. The estimated volume obtained by this method is about 15.28 km^3 .

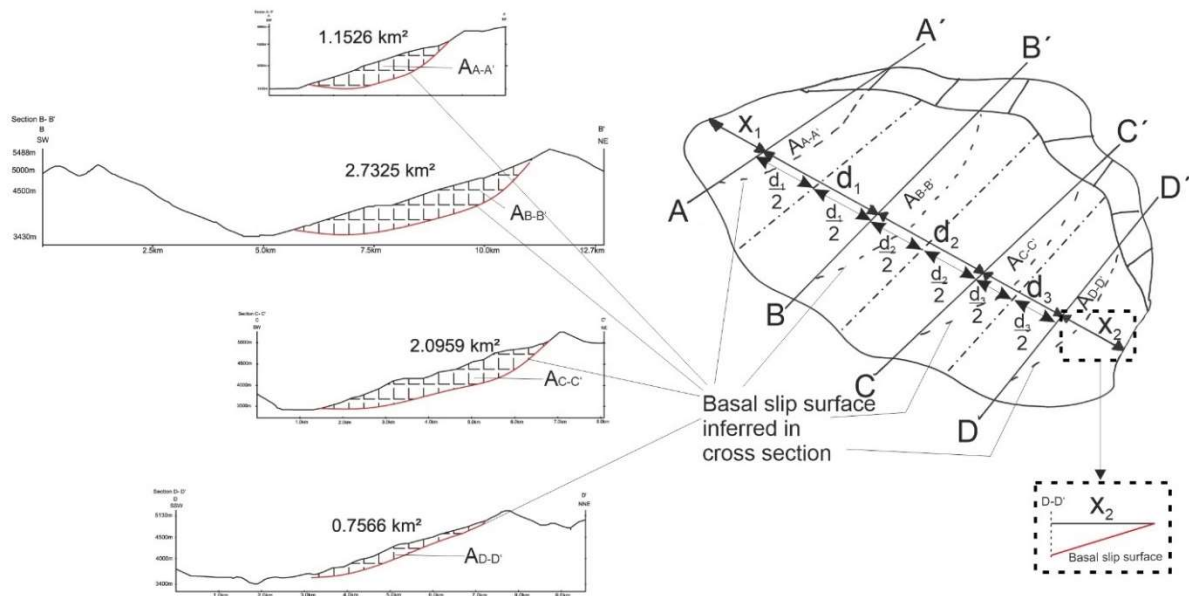


Fig. 4.24 Average End-Area method illustrated for the Dangkhar Landslide. Areas of cross sections ($A_{A-A'}$ to $A_{D-D'}$) are highlighted with hachures; red line indicates location of inferred basal slip surface. For abbreviations see equation 5.1

Based on the estimated value of 15.28 km^3 distributed over an area of about 40.44 km^2 , the average thickness of the landslide mass is approximately 380 meters. For the Mane landslide with a volume of 1.4 km^3 and an areal extent of about 16.9 km^2 , an average thickness of about 130 meters can be inferred. This corresponds roughly to the depth of the gorge the Spiti River has cut into the Mane Landslide debris.

Triangulated Irregular Network difference modelling

The Triangulated Irregular Network (TIN) difference modelling method calculates the void space between two defined surfaces. The two surfaces are first created as TINs in ArcGIS 10.1 using the TIN Management Toolset of the 3D Analyst Toolbox. In a second step the TINs are subtracted from each other by employing the TIN difference tool of the 3D Analyst. The calculated difference corresponds to the volume of the investigated sliding mass.

The present day surface constructed from the ASTER DEM and the inferred basal slip surface were used to estimate the volume of the Dangkhar Landslide. The position of the basal slip surface was interpolated between the neighboring cross section (Fig. 4.24). The input point

data containing the spatial information such as XY coordinates and altitude of the basal slip surface are retrieved from the cross sections and maps.

The TIN is created by fitting an interpolated plane through the point data. After the creation of the modelled basal slip surface, it is checked for plausibility, i.e. no unrealistic “peaks” or “holes” are present in the TIN surface. The 2nd order local polynomial interpolation has proven to work best for creating a smooth surface, realistically representing a basal slip surface of a landslide. The total volume compiled by TIN difference modelling is 15.70 km³ (Fig. 4.25). Fig. 4.26a and Fig. 4.26b show a 3D-visualization of the modelled TIN surfaces and a projection of the modelled basal slip surface on the field photograph, respectively.



Fig. 4.25 Dangkhar Landslide volume estimate using TIN difference modelling. Modelled volume lies above the basal slip surface (blue) and below the present day surface (green)

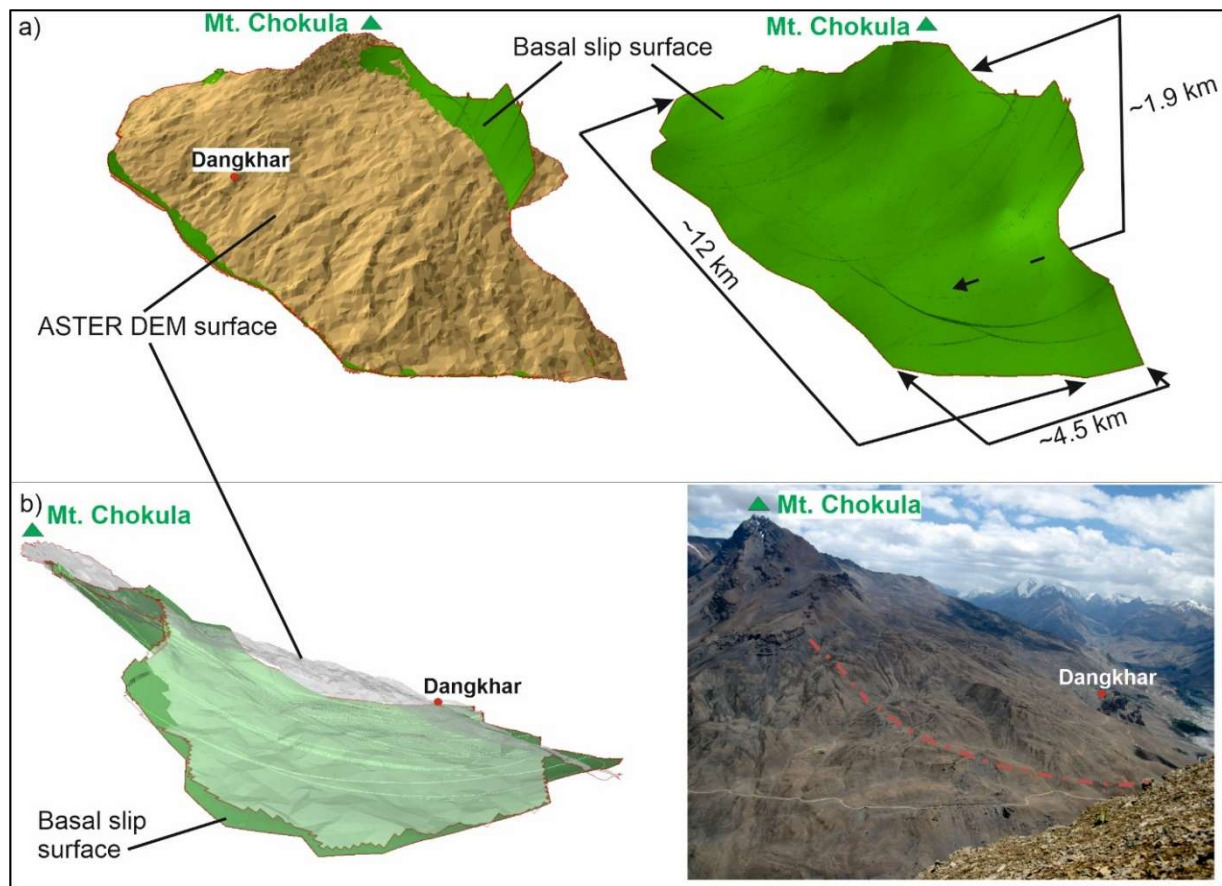


Fig. 4.26 3D-visualizations of the Dangkhar Landslide. a) View of the modelled Dangkhar Landslide. b) Modelled Dangkhar Landslide (left) and corresponding field photograph (right). Red dot-dashed line delineates approximate location of the basal slip surface

Cut and Fill Operation

To perform the Cut and Fill operation, a base level is defined above which the volume of the body is calculated. The areal extent of the landslide is outlined on the ASTER DEM surface and the volume corresponds to the body defined by the present day topography and the defined base level. The operation was performed in MicroDEM with a base level set at 3700 m where the location of the basal slip surface was anticipated. The total volume of the body bound between the ASTER DEM surface and the base level is approximately 20.14 km^3 (Fig. 4.27).

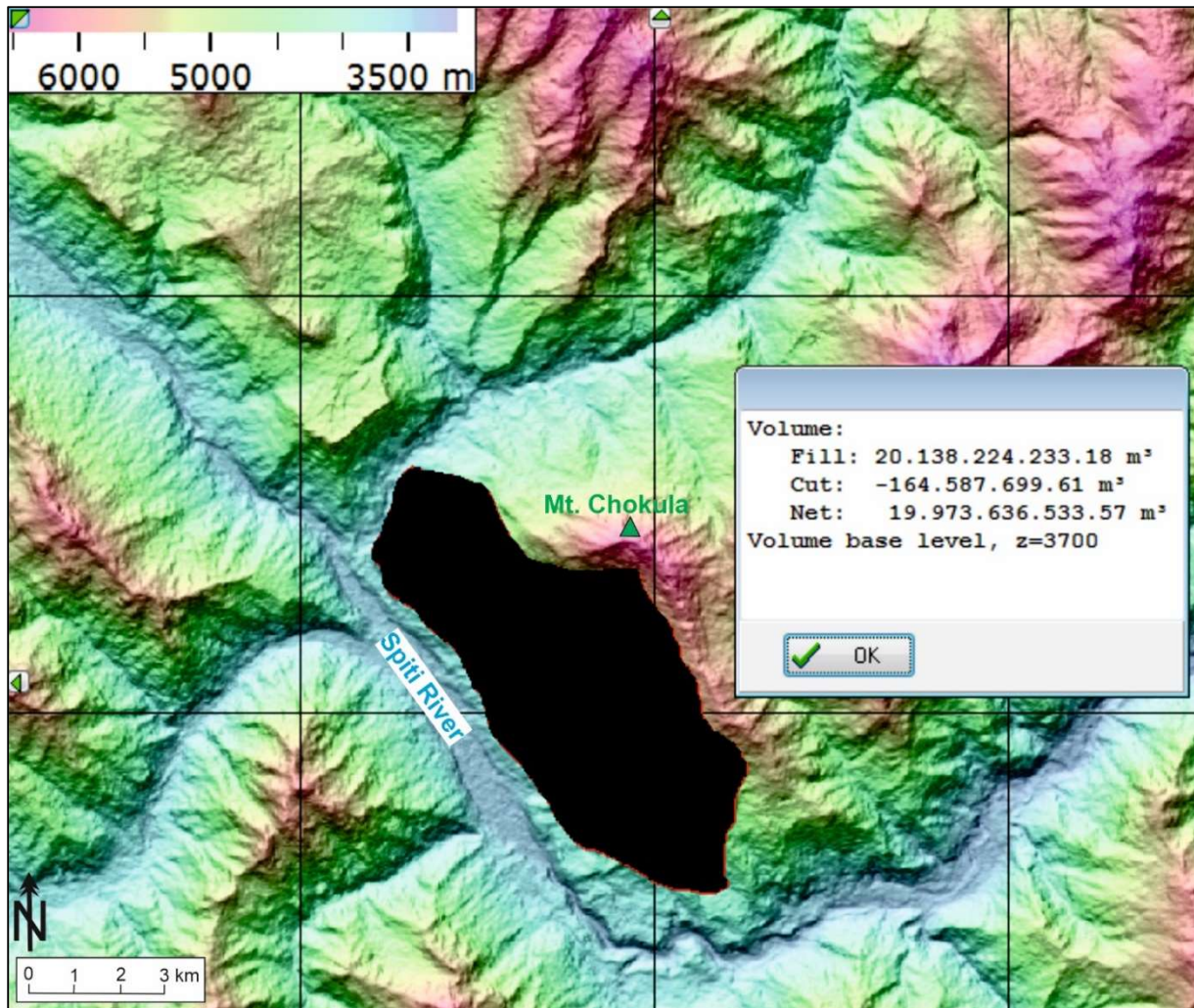


Fig. 4.27 Dangkhar Landslide volume estimate obtained by the Cut and Fill operation. Black plane represents the outlined areal extent of the Dangkhar Landslide.

Morphometric dimensions

The WP/WLI (1990) and Cruden and Varnes (1996) provide formulas to estimate pre- and post-failure landslide volumes (V_r , V_d) based on landslide morphometric dimensions presented in Tab. 4.2. The formulas consider a rotational slide with a sliding mass having a half ellipsoidal shape. The required parameters are L_d , D_d and W_d for post-failure volume (Equation 5.3) and L_r , D_r , and W_r for pre-failure volume.

Equation 5.3:

$$V_d = \frac{1}{2} \cdot \frac{3}{4} \pi \cdot L_d \cdot D_d \cdot \frac{1}{2} W_d$$

simplified to:

$$V_d = \frac{1}{6} \pi \cdot L_d \cdot D_d \cdot W_d$$

where:

V_d = Volume of displaced mass [m^3]

L_d = Length of displaced mass [m]

D_d = Depth of displaced mass [m]

W_d = Width of displaced mass [m]

Calculation of the pre-failure volume (V_r) is performed with the same formula by replacing the parameters with subscripts “d” with those of subscript “r” indicating the parameters related to the surface of rupture. Estimates of the pre-failure thickness by rebuilding the original topography is approximately 490 m. The pre-failure depth (D_r) of a sliding mass is subject to some uncertainties, are subjective to a certain degree and have an inferred precision between $\pm 25\%$ (Dortch et al. 2009). In fact, the morphometric landslide volume formula can be adjusted to the specific conditions and inferred shape of the sliding mass by fitting a geometric body (WP/WLI 1990). The difference between the V_r and V_d is expressed as swell factor (SF) accounting for the dilatancy the sliding mass experiences during movement (Equation 5.4).

Equation 5.4:

$$SF = \frac{V_d}{V_r} - 1$$

where:

SF = Swell factor [-]

V_d = Volume of displaced mass [m]

V_r = Volume of mass before the rupture [m^3]

The volume estimated using the morphometric dimensions yield a post displacement landslide volume (V_d) of 24.70 km³ and a pre-displacement volume (V_r) of 19.80 km³, with an associated swell factor of 0.25. The swell factor was used for assessing the corresponding V_r from the V_d of the TIN modelling and AEA method. Tab. 4.3 summarizes the volume estimates of the Dangkhar Landslide.

	Average End-Area method	TIN difference	Morphometric dimensions	Cut and Fill
Volume [km ³]	15.28/12.22	15.70/12.56	24.70/19.80	20.14
	(V_d/V_r)	(V_d/V_r)	(V_d/V_r)	(-)
	average V_r 14.86 average V_d 18.56			

Tab. 4.3 Summary of Dangkhar Landslide volume estimates

The accuracy of landslide volume estimates largely depends on the degree of burial, the type and complexity of landslide emplacement, erosion and the interpretation and interpolation of morphology and cross sections (Hewitt 2009). The Cut and Fill operation does not reproduce the shape of the basal slip surface and incorporates bedrock and landslide material above the base level. However, it provides a rough benchmark though for refining the volume estimates with the other approaches.

Estimates based on morphometric dimensions strongly rely on model conceptions of idealized landslide geometries and tend to oversimplify the geometry. Irregularities in the geometry of the basal slip surface and the sliding mass of are not considered since the values from only one representative cross section are used as input. The volume obtained from morphometric dimensions is larger than those obtained by TIN modelling or the Average End-Area method due to calculations of an idealized ellipsoid shaped sliding mass, not reproducing the irregular shape of the Dangkhar Landslide. Nevertheless, it considers the pre- and post-failure volume from which a swell factor for the sliding mass can be obtained. Swell factors depend on the material and type of landslide involved and may reach values up to 0.6 in catastrophic landslides (e.g. Dewitte et al. 2005; Church 1981).

The Average End-Area method together with TIN difference modelling is most capable of reproducing the present day volume. The difference in volume between these two methods is as small as 3 %.

The only subjective factor in this approach is the interpretation of the cross sections. Factors such as long-term erosion and dilatancy of the landslide material during movement may shift the volume estimates into one or another direction. Denudation rates for Spiti are in the range of 0.08 mm/yr during normal monsoon and 0.48 mm/yr during intensified monsoon precipitation, respectively (Bookhagen et al. 2005), resulting in a total annual removal of 3235 m³ to 19410 m³ of material. Based on the range of the average volume estimates ranging from 14.86 (V_r) to 18.56 km³ (V_d) and taking the 10 % error margin into account proposed for landslide volume estimates (Korup et al. 2007; Hancox and Perrin 2009), the Dangkhari Landslide volume is on the order of 15 – 20 km³.

4.2.6 Dangkhari carbonate breccia deposits

The carbonate breccia is a unique geological feature in the study area. Its striking nature has caught the attention of researchers since the first expeditions to the area (e.g. Gerard 1833). The carbonate breccia deposits rest on both sides of the Spiti Valley approximately 100 to 200 m above the Spiti Valley floor (Fig. 4.28a), forming indurated masses of rocks up to 250 – 300 m thick. The carbonate breccia occurs as several outcrops within the study area and can be traced along the flanks of the Spiti Valley at elevations between 3600 and 3900 m at the upper limits of the U-shaped curvature of the Spiti Valley (Fig. 4.28a). In the Lingti Valley one small outcrop is preserved along the right slope 150 m above the Lingti River. The outcrops mostly show a triangular to vermiform shape (Fig. 4.28a) similar to a fan or embankment, respectively. Their occurrence and extent are laterally limited and restricted to areas where ephemeral streams descend from the Dangkhari hillslope. The carbonate breccia deposits form precipitous cliffs standing out of the surrounding area and abruptly terminate in an almost vertical drop towards the Spiti Valley. The carbonate breccia exhibits a brownish weathered surface color and clasts are formed by black limestone as it occurs in the surrounding bedrock formations. Near Siluk, the bedrock exposed downhill from a carbonate breccia deposit near the valley floor exhibits polished surfaces (Fig. 4.28b).

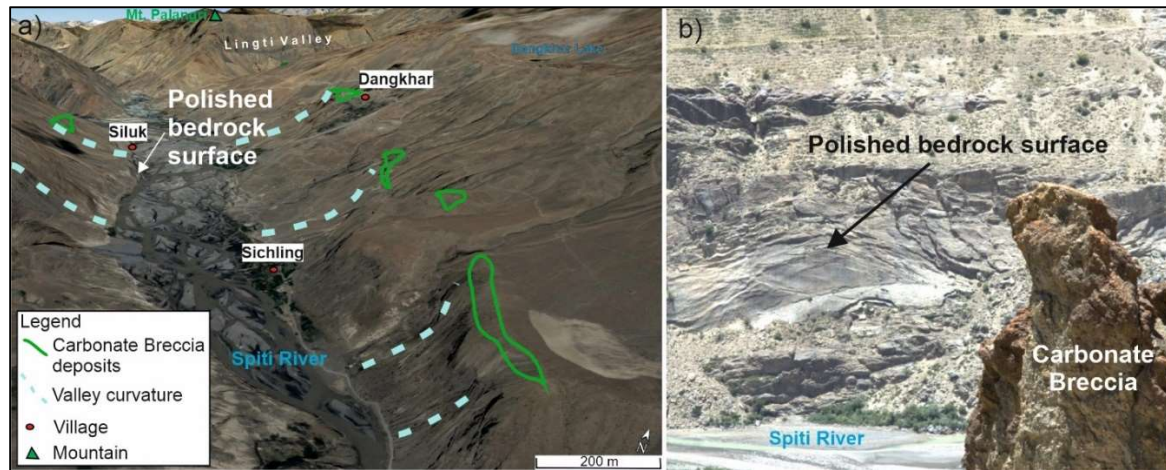


Fig. 4.28 a) View upstream the Spiti River highlighting the distribution of the carbonate breccia deposits along the U-shaped Spiti Valley flanks (Image: Google Earth Pro). a) Polished bedrock surface near Siluk on the right Spiti River bank. Blue arrow indicates flow direction of Spiti River and of former glacier ice #GP www.gigapan.com/gigapans/178298 (Snapshot: Polished bedrock surface).

The deposit around Dangkhar Village forms the largest outcrop of carbonate breccia. It is composed of three layers exhibiting different properties regarding grain size, roundness, and stratification (Fig. 4.29).

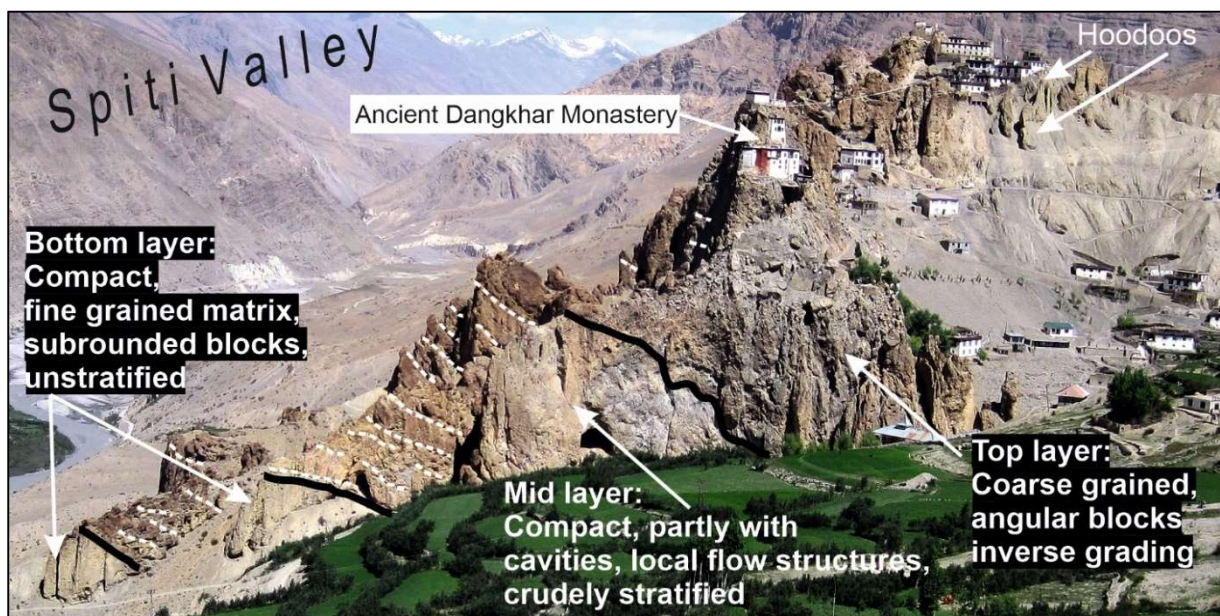


Fig. 4.29 Carbonate breccia around Dangkhar. Black solid line marks the contact between different layers. White dashed lines indicate stratification pattern.

The top layer exhibits a coarsening upwards trend (inverse grading) with angular blocks up to ten meters in size and forms the foundation rock of the Ancient Dangkhār Monastery (Fig. 4.30a & c). It is interpreted as a debris flow deposit.

The mid layer exhibits crude stratification dipping towards the slope between approximately 25° to 40° and locally exhibits wet sediment deformation structures expressed as contorted, smeared layers and flow structures (Fig. 4.30b). Locally, local salt precipitation, normal faulting, loading structures and cavities having diameters of up to 10 to 15 m exist (Fig. 4.30c). The wet sediment deformation structures suggest water rich conditions for the formation of this layer. Fig. 4.30e schematically shows the characteristic features of wet sediment deformation. The suspected process leading to the observed structures are either slowly flowing material such as deformation or meltout tills, or debris flows or a combination referred to as flow till. The cavities could support a glacial influence of the deposit as they could have formed by melting of ice incorporated within the sediment during deposition. Additionally, normal faulting within sediments can occur after melting of incorporated ice (Bennett and Glasser 2009). The preservation of the wet sediment structures points to a cementation soon after the emplacement.

The bottom layer is a compact diamictite, composed of a sandy to gravelly matrix with rounded boulders as well as subrounded blocks. The presence of rounded and subangular components embedded within a compact fine grained matrix suggests that the bottom layer has formed involving both, fluvial and gravitational processes acting on the sediment. The bottom layer of the carbonate breccia is interpreted as a lodgment till with a marked contact to an overlying, locally occurring fine grained layer with a thickness of two to three meters. The mid layer shows a sharp erosional contact to the fine grained layer. This fine grained layer is attributed to have resulted from colluvial outwash stream deposition.

Where erosive action was strong, it has sculpted the carbonate breccia into earth pyramids (hoodoos), up to approximately 60 m high, protected by a cap rock on top (#GP www.gigapan.com/gigapans/178304). The hoodoos typically narrow towards the base as a result of erosive action of surface water flows.

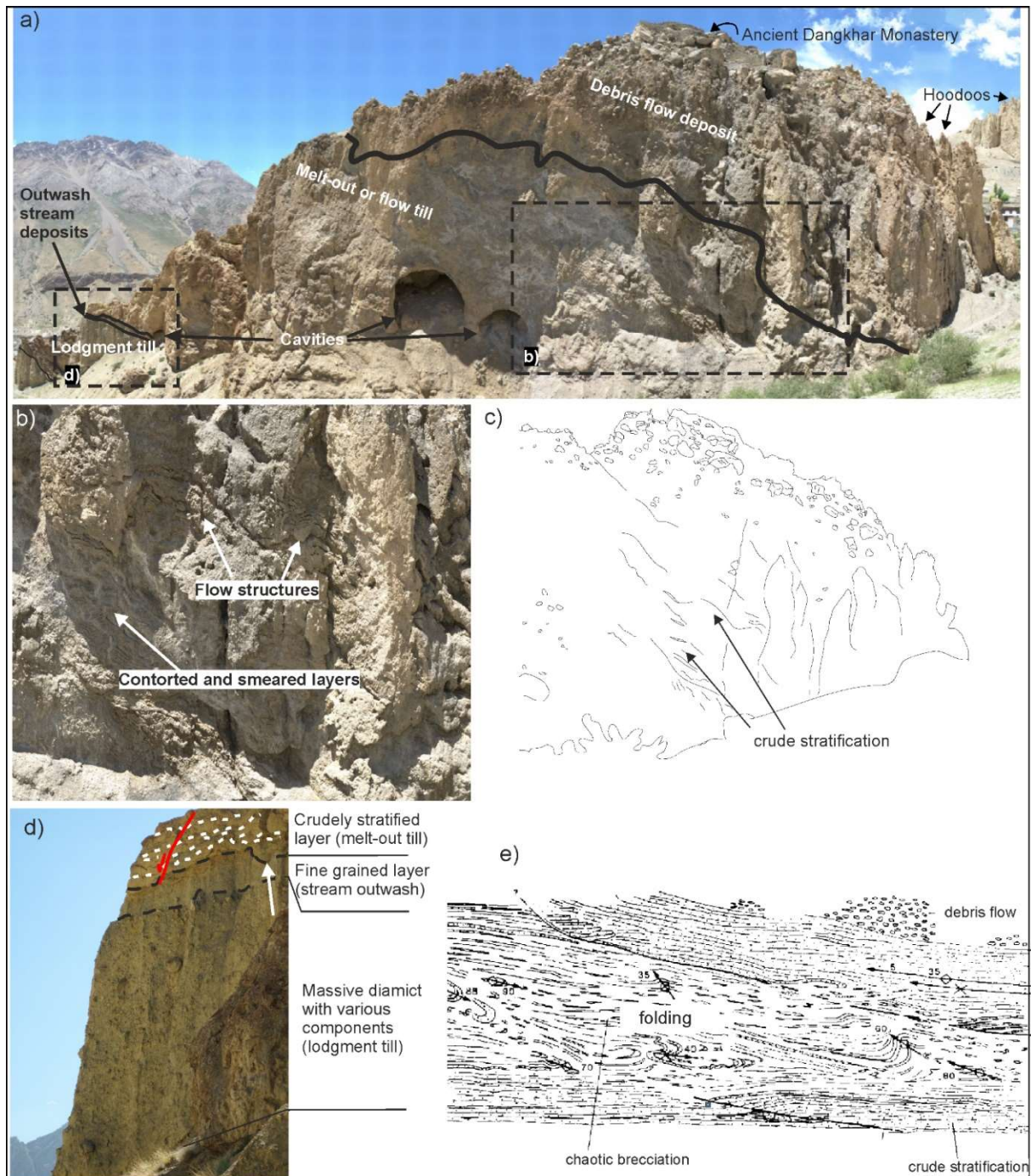


Fig. 4.30 Characteristics of the carbonate breccia. a) Dangkhar carbonate breccia section at the Ancient Dangkhar Monastery with the inferred origin of the breccia layers. b) Wet sediment deformation structures. c) Sketch of breccia highlighting inclined, crude stratification. d) Profile exposing different layers of the carbonate breccia (inferred origin is given in parentheses). Note normal faulting (red line) and loading structures (white arrow) in crudely stratified layer. e) Schematic sketch of characteristics of wet sediment deformation structures (after Pickering 1987). Details can be explored at #GP www.gigapan.com/gigapans/178298

The carbonate breccia uphill from Sichling exhibits inverse grading and is overlain by buff colored lake sediments and stratified gravel and sand (Fig. 4.31a), suggesting that sufficient water was present to form a lake after the breccia formation. At a later stage, the lake was filled with sand and gravel.

Similar to the carbonate breccia at Dangkhar, the deposits of the catastrophic Mane Landslide are partly indurated and cemented. Columns of cemented Mane Landslide debris (Fig. 4.31b) with blocks up to 10 m are exposed at the top and occur in the canyon created by the Spiti River. A subdivision into several layers as it is the case for the breccia at Dangkhar is not possible. Features such as fine grained layers and internal flow structures are absent within the Mane breccia indicating it was formed by a single event. The cementation of the Mane breccia is attributed to water provided by the Spiti River as it gradually incised the Mane Landslide deposit.

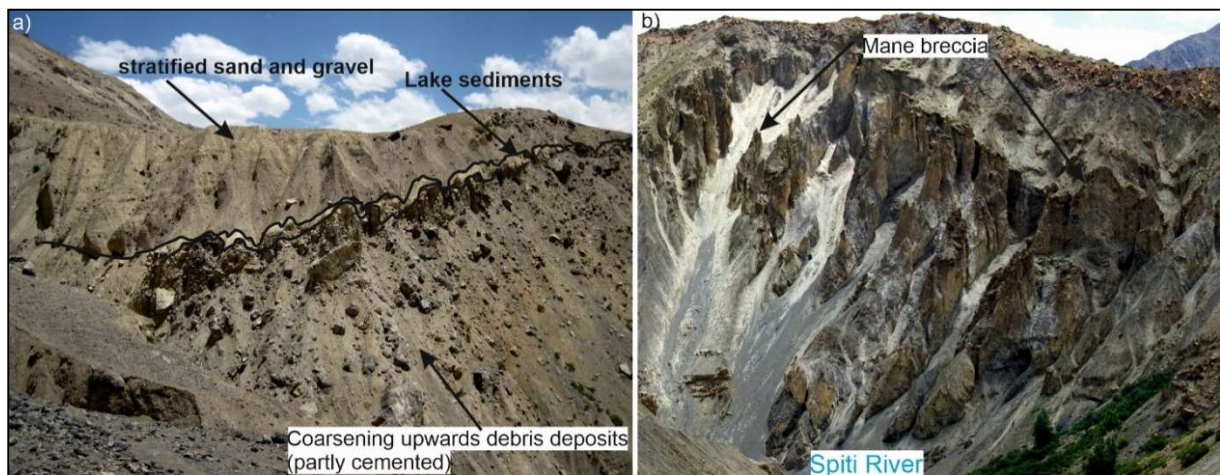


Fig. 4.31 Carbonate breccia of Sichling and Mane. a) Cemented carbonate breccia deposits uphill from Sichling overlain by a pale yellow layer lake sediments and stratified sand and gravel. b) Mane breccia along the right side of the Spiti River (#GP www.gigapan.com/gigapans/178685)

4.2.7 Laboratory testing

4.2.7.1 Solids – Mineralogy, microscopy and cathodoluminescence

A representative mix of the Dangkhar Landslide debris showed a composition of 54% calcite, 30% quartz, 4% muscovite, 4% plagioclase, 2% dolomite and 2% chlorite, 2% kaolinite and 2% smectite. The composition of the Dangkhar Lake sediments slightly varies from those of the debris and is composed of 51% calcite, 33 % quartz, 8 % muscovite, 3 % dolomite, and traces of chlorite and potassium feldspar. Additional analyses of bedrock samples of the units incorporated in the debris reveals that the debris is a combination of the surrounding bedrock units and their altered products (Tab. 4.4). The breccia cement is predominantly composed of calcite and dolomite with subordinate quartz. The dolomite and quartz are regarded to be finely grained, detrital clasts that could not be separated from the cement during sample preparation. Where almost pure cement filling was extractable, the amount of calcite is close to 100 %.

The carbonate breccia (Fig. 4.32a, b) is essentially monomict in their composition. Thin sections show a predominance of carbonate clasts and calcite spar cement filling of the intra clast void space with subordinate amounts of quartz. The boundaries between the clasts and the calcite spar cement filling is sharp (Fig. 4.32c, d). The ratio of clasts to cement is roughly in the range of 50:50 to 60:40. The size of the clasts vary from sub-millimeter to centimeter. The clasts are formed by angular to slightly rounded micritic grains and contain internal microfractures and veins predating the brecciation event (pre-breccia veins; Fig. 4.32e). Locally, the veins can be traced across grain boundaries and adjacent split clasts can be pieced together. The displacement along the fractures occur on a sub-millimeter scale (Fig. 4.32e, f). Füchtbauer and Richter (1983) introduced the term fitting for breccia grain relations. In general, the fitting is low and applicable to approximately <20 % of the grains. The growth shape calcite spar (Fig. 4.32d & f) forms a drusy, equant mosaic and dogtooth cement. The dogtooth cement exhibits sharply pointed crystals growing from the clast grain surfaces into the void space. Growth lamellae and zonation of subhedral calcite spar occur towards the central part of the void space and are depicted on the cathodoluminescence images (Fig. 4.32e, f).

Sample details			Bulk mineral composition								Clay fraction							
Sample ID	Location (Lat/Lon)	Sample detail	Mineral content [%]								Mineral content < 2 μ m [%]				Smectite _{effektiv}			
			Quartz	Muscovite	Chlorite	Plagioclase	Orthoclase	Calcite	Dolomite	Kaolinite	Smectite	Sum	Muscovite	Chlorite		Smectite	Kaolinite	
BH1_785	N 32.089 E 78.228	Dangkhar Lake sediments	33	8	Tr.		Tr.	51	3	5		100	61	21		18		
R24	N 32.118 E 78.220	Scree from Mt. Chokula	2					98				100						
R25	N 32.099 E 78.207	Rama Shale	45	6	6	11	3	29				100						
R26	N 32.074 E 78.223	Sichling Breccia (Cement)	0,5					99,5				100						
R27	N 32.048 E 78.270	Mikkin Lime-stone	13	Tr.	2			85				100						
R28	N 32.077 E 78.221	Dangkhar hillslope Debris	30	4	2	4		54	2	2	2	100	61	14	11	14	2	
R29	N 32,107 E 78,187	Gungri Shale	78	Tr.	Tr.	14	4	4				100						
R19	N 32.68909 E 78.21294	Dangkhar Breccia (Clast)	1						43	56		100						
		Dangkhar Breccia (Cement)	Tr.		Tr.				70	30								

Tab. 4.4 Mineralogical compositions of selected rocks (Tr. = traces)

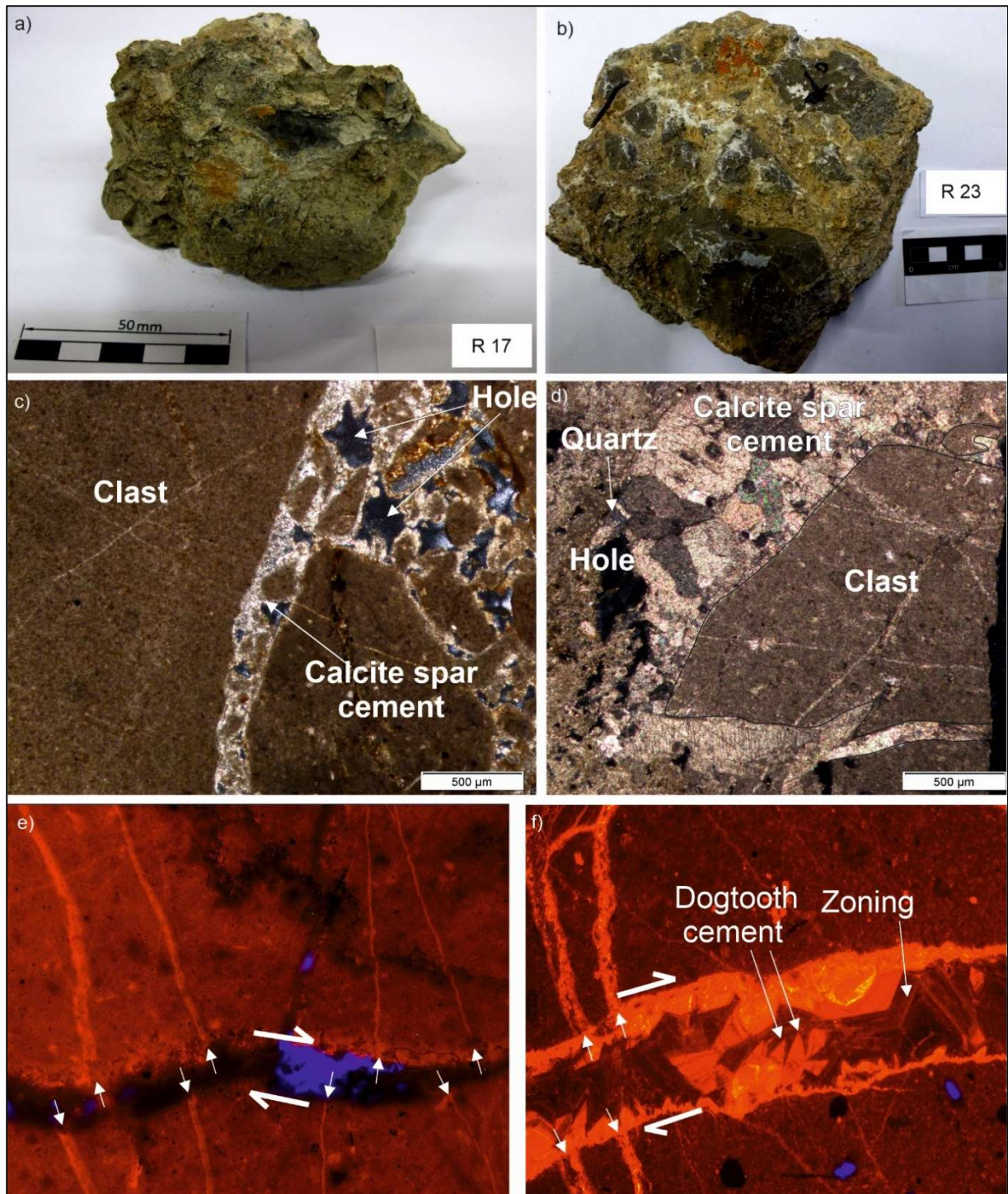


Fig. 4.32 Dangkhar carbonate breccia. a & b) Hand specimen of the carbonate breccia. c & d) Thin section photograph of the carbonate breccia showing clasts and calcite spar cement. e) Cathodoluminescence image of the carbonate breccia: split grains and displaced pre-breccia veins (small arrows) and sense of displacement (large arrows). f) Intra clast void space filled with drusy, equant, mosaic burial cement and dogtooth cement. Note zoning of crystals.

4.2.7.2 Stable isotope data of solids (Delta ¹⁸O, Delta ¹³C)

The isotope ratios were determined for the host rocks (i.e. breccia clasts) and interstitial cements (Tab. 4.5). They show a general trend towards more negative $\delta^{18}\text{O}$ values from the host rock to the cements (Fig. 4.33). Differences in the $\delta^{18}\text{O}$ values from host rocks to cements range from 3.99 ‰ to 7.49 ‰. Variations in $\delta^{13}\text{C}$ values from host rocks to cements are small and are within 0.16 ‰ to 0.32 ‰. The absolute $\delta^{13}\text{C}$ values ranging from 2.37 ‰ to 3.51 ‰ reflect the initial signal of marine carbonates. The more negative $\delta^{18}\text{O}$ values of the cements compared to the host rocks are typically caused by meteoric water influence. Only the two samples of R23 are outside the general cluster of the cements and are shifted to more positive ¹³C and ¹⁸O ratios.

Sample ID	VPDB ¹³ C [‰]	VPDB ¹⁸ O [‰]	VSMOW ¹⁸ O [‰]
1a	2.74	-10.25	20.34
1b	2.68	-11.53	19.02
2	2.96	-11.43	19.13
3	3.51	-7.8	24.40
4 (cement)	2.37	-20.23	10.05
R23-Rock (1)	3.31	-10.6	19.98
R23-Rock (2)	3.24	-10.97	19.60
R23-Cement (1)	5.92	-4.55	26.22
R23-Cement (2)	6.1	-3.51	27.29
R26-1-Rock (1)	2.99	-15.32	15.12
R26-1-Rock (2)	3.02	-15.15	15.29
R26-1-Cement (1)	2.82	-22.78	7.43
R26-1-Cement (2)	2.7	-22.64	7.57
R26-2-Rock	2.45	-17.45	12.92
R26-3-Rock	2.37	-16.93	13.46
R26-3-Cement-1	2.59	-21.48	8.77
R26-3-Cement-2	2.53	-20.92	9.34

Tab. 4.5 Stable isotope data of carbon and oxygen of the carbonate breccia cements. Oxygen isotope data are referred to VPDB standard and converted VSMOW standard

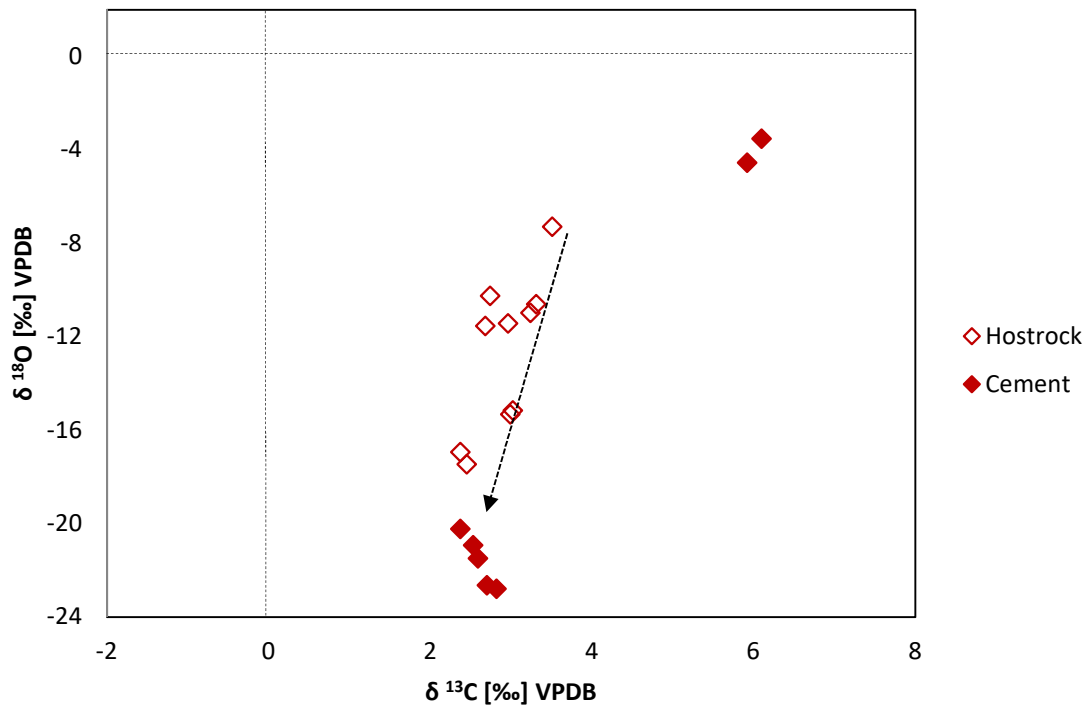


Fig. 4.33 Stable isotope data of carbon and oxygen of the carbonate breccia cements and host rocks (clasts). Dashed arrow indicates evolutionary trend of isotope composition from host rock to cements

4.2.7.3 Stable isotope data of liquids (Delta ^{18}O , Delta ^2H)

From the nine water samples (Tab. 4.6) eight were taken to construct a Local Meteoric Water Line for Dangkhar (Dangkhar MWL; Fig. 4.34 and Fig. 4.35). The analysis yielded a Dangkhar MWL defined by equation 4.4, only sample W5 was excluded based on residuals and by d-excess from the regression analysis. The Dangkhar MWL is plotted against the regional Western Himalaya Meteoric Water Line (WHMWL; equation 4.5) of Kumar et al. (2010) and Craig's GMWL, which serve as benchmarks against the local Dangkhar MWL.

Equation 4.4:

$$\delta^2\text{H} = 5.76 \delta^{18}\text{O} - 20.29 \text{‰}$$

Equation 4.5:

$$\delta^2\text{H} = 7.95 \delta^{18}\text{O} + 11.51 \text{‰}$$

The average deuterium excess (d-excess) of the nine samples calculated after Dansgaard (1964) is 9.43 ± 1.24 ‰. The constructed Dangkhar MWL exhibits a strongly negative d-excess of -20.29 ‰. Altitude effects of about 0.35 ‰/100 m for oxygen can be observed in the study area (Fig. 4.36). Fig. 4.37 provides a compound plot of rock and water isotope data normalized to VSMOW.

Sample ID	Delta ² H [‰] VSMOW	Delta ¹⁸ O [‰] VSMOW	Altitude [m]	d-excess [‰] VSMOW
W1	-95.47	-13.02	4041	8.69
W2	-96.44	-13.29	3912	9.88
W3	-96.84	-13.25	3772	9.16
W4	-99.38	-13.75	4064	10.62
W5	-97.85	-13.1	3757	6.95
W6	-97.57	-13.4	3883	9.63
W7	-10.6	-14.06	4308	10.88
W8	-95.25	-12.98	3855	8.59
W9	-99.28	-13.72	3856	10.48

Tab. 4.6 Stable oxygen and hydrogen isotope data of Dangkhar waters

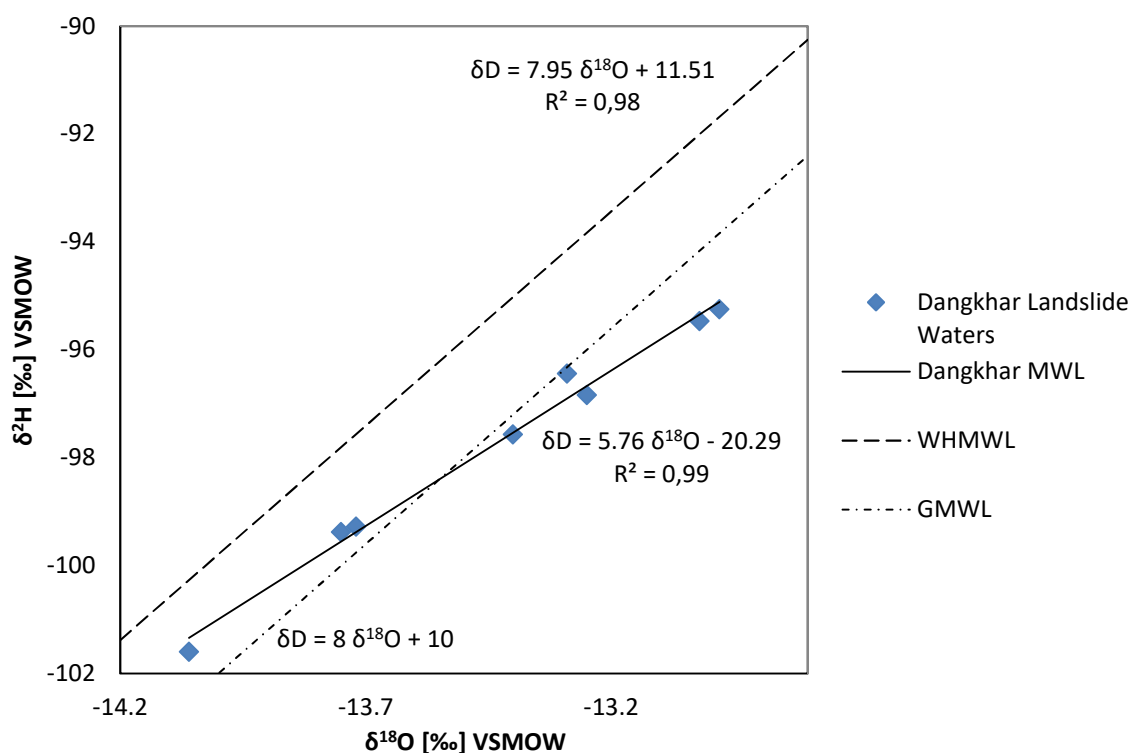


Fig. 4.34 Local Meteoric Water Line (Dangkhar MWL) constructed from stable isotopes of Dangkhar surface waters. WHMWL (Kumar et al. 2010); GMWL (Craig 1961)

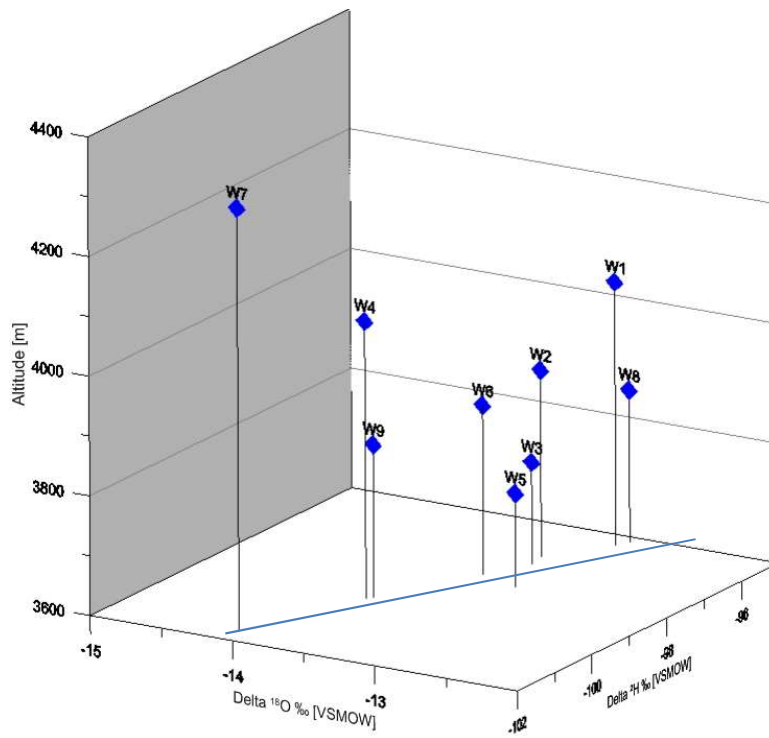


Fig. 4.35 3D plot of Local Dangkhar MWL. Blue line in XY plane represents the DMWL shown in Fig. 4.34. The altitudinal information of the water samples (W1 to W8) is projected in the z-direction.

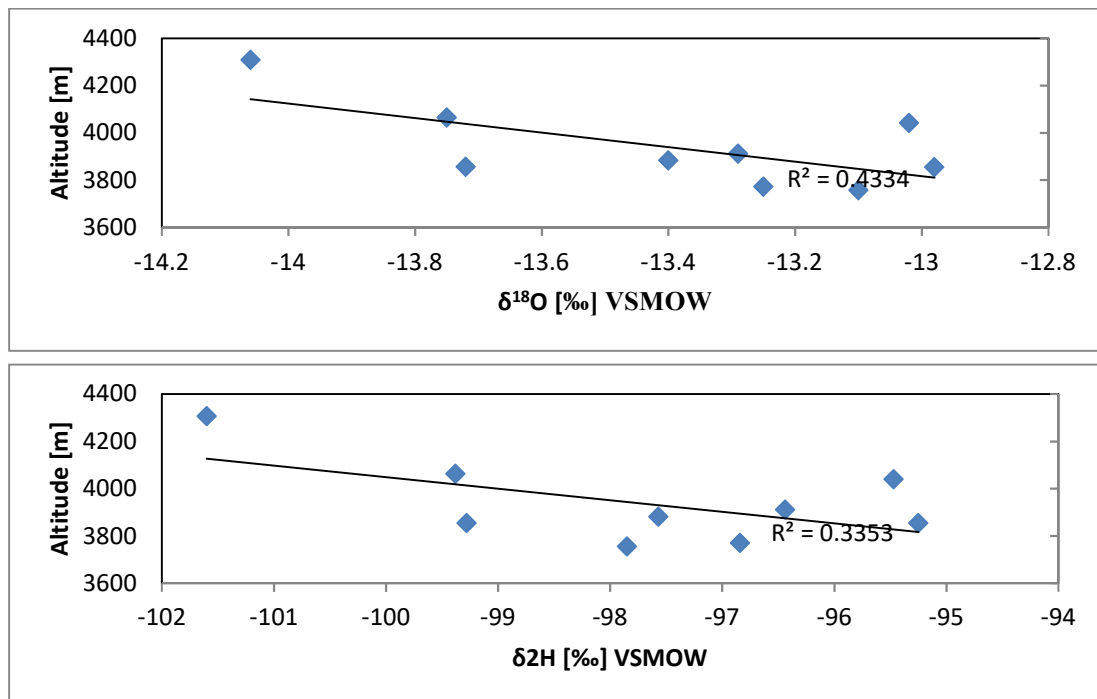


Fig. 4.36 Altitude versus stable isotope values of Dangkhar water samples

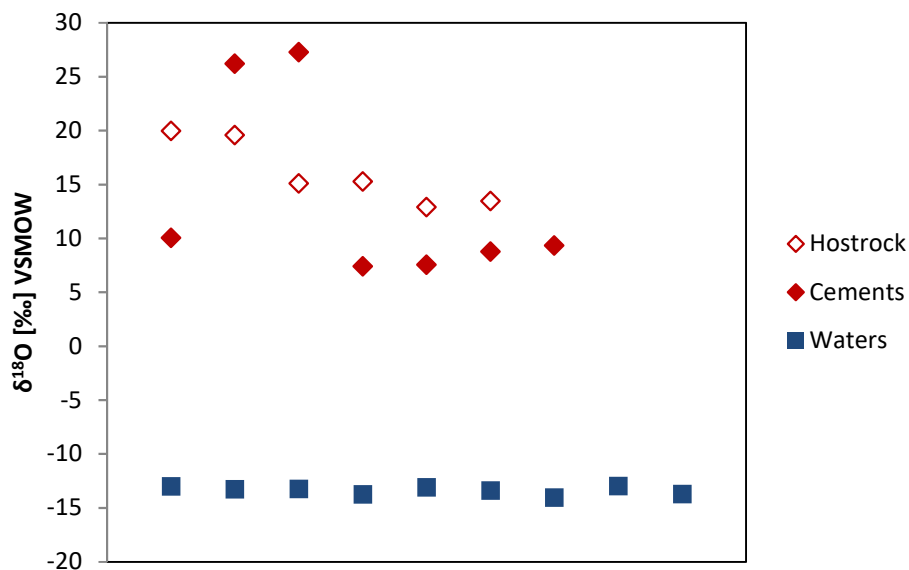


Fig. 4.37 VSMOW normalized stable oxygen isotope data of the carbonate breccia (host rock clasts and cements) and Dangkhar waters

4.2.7.4 Radiocarbon sampling and dating

Drilling was performed at three sites (Fig. 4.38) where sediment accumulated on the slope, potentially burying organic material (Tab. 4.7). The drilling was done until a blocky material, i.e. the underlying substrate was hit. A minimum age for the sediment formation can be constrained from material sampled close to the base of the deposit. The sediments at all sites were devoid of any decipherable stratification or varves that would allow a back calculation of the age by counting the number of couplets. The sediment material was dry or slightly moist, but no water was encountered in the boreholes (Fig. 4.39).

The first drilling site for boreholes 1, 2 and 3 is located within the Dangkhar Lake basin, but the sediment was thicker than the available drilling equipment in these boreholes. The second drilling site with borehole 4 lies within a lineament trench and the substrate was encountered at a depth of 4.30 m. The third site is located on top of a second generation rock glacier where sediment accumulated within a closed depression (Borehole 5, 6 and 7). The accumulated dark brown, peaty sediment allows indirect determination of the age of this glacial stage. The substrate was encountered at a depth of 1.30 m.



Fig. 4.38 Locations selected for organic sample drilling

BH	Longitude [°]	Latitude [°]	Depth [m]	Location detail	Comment	Sample ID
BH1	78.22820 E	32.08903 N	7.85	Dangkhar Lake sediments	base not reached	BH1_220, BH1_230, BH1_340, BH1_705, BH7_785
BH2	78.23037 E	32.08556 N	4.00		base not reached	BH2_270, BH2_410
BH3	78.23085 E	32.08527 N	-		Abandoned due to boulder	
BH4	78.21506 E	32.10638 N	4.30	Lineament trench	bottom reached	BH4_320, BH4_390 , BH4_425
BH5	78.21641 E	32.11209 N	1.25	Rock glacier depression	bottom reached	none
BH6	78.21645 E	32.11205 N	0.90		bottom reached	BH6_55 , BH6_70
BH7	78.21638 E	32.11203 N	1.30		bottom reached	BH7_80, BH7_90, BH7_115

Tab. 4.7 Borehole details. Sample labelling: *BoreholeNo_depth of sample in centimeters*. Sample names in bold indicate samples submitted for ^{14}C AMS dating

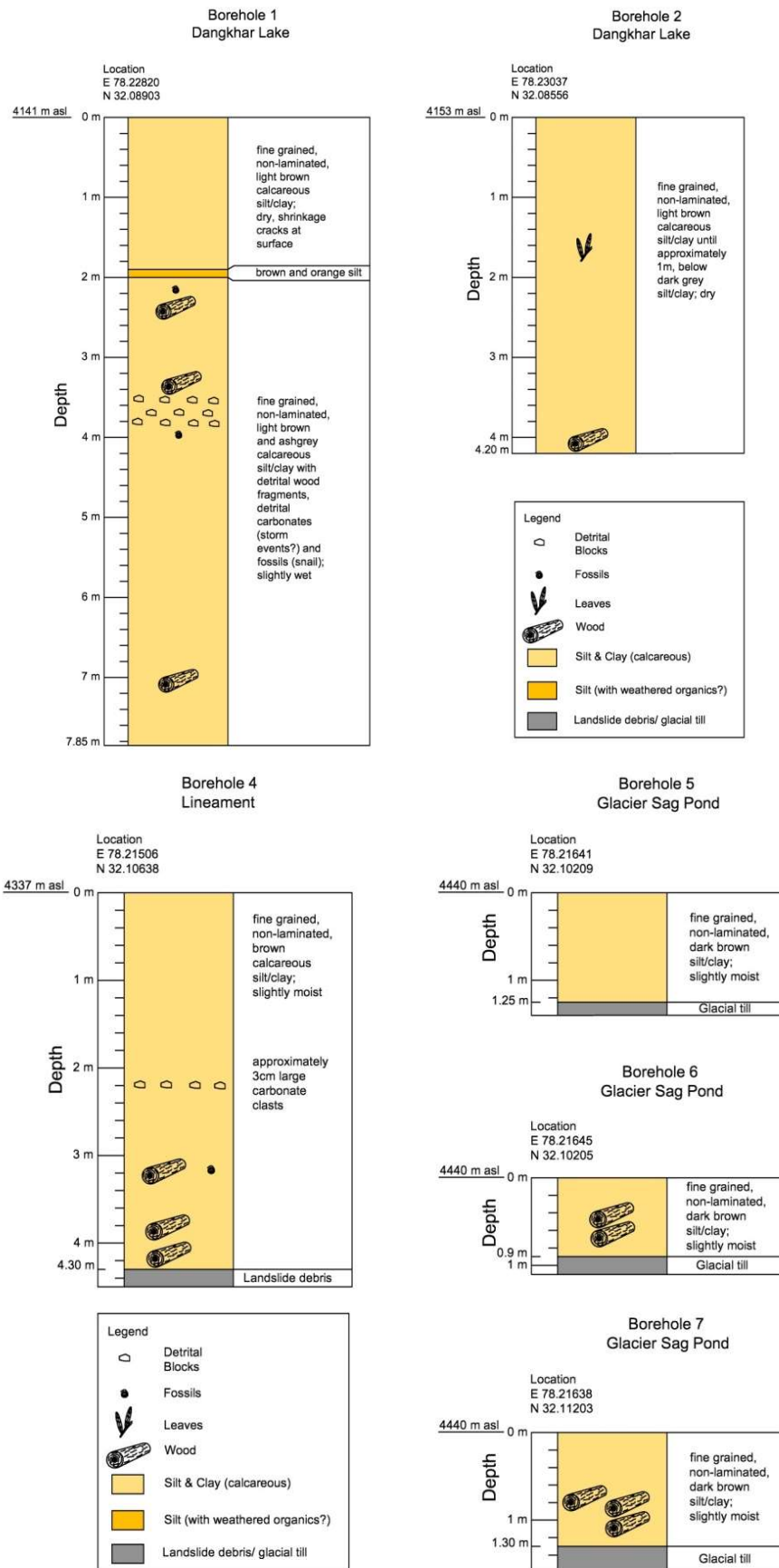


Fig. 4.39 Dangkhar borehole logs

Organic material in the sparsely vegetated Lahaul-Spiti region suitable for radiocarbon dating is rare (Owen et al. 1997). Care was taken during manual drilling, but the actual authenticity of the samples could not be evaluated until absolute ages were determined. Some samples yielded much younger ages than inferred from morphostratigraphic relations and weathering characteristics, possibly due to younger organic fragments falling into the borehole from the borehole walls or roots reaching deeper down into the sediment. The majority of the samples yielded ages pointing to the mid-20th century (pMC-values from 102.6 to 169.1). Young radiocarbon ages are delivered rather as pMC than BP values illustrating the limits of this method when analyzing young samples. The ages were considered in the morphostratigraphic context of the sample site to allow a reasonable interpretation of the obtained ages.

The result of sample BH6_55 is considered as the most unaltered age. BH6_55 yielded a pMC value of 102.6 ± 0.3 and was retrieved at a depth of 55 cm. The correlation of the raw data with the calibration curve places the age of the sample in the range of the LIA at the 18th to end of the 19th century or even younger (Fig. 4.40). Average sedimentation rates between 1.7 – 5.58 mm/yr can be derived for the obtained time window between 1700 AD and 1900 AD, respectively.

Assuming a constant sedimentation rate for the 130 cm thick sediment accumulation, the estimated minimum age of sediment accumulation within the depression is approximately 0.23 – 0.76 ka. See appendix for remaining calibration curves.

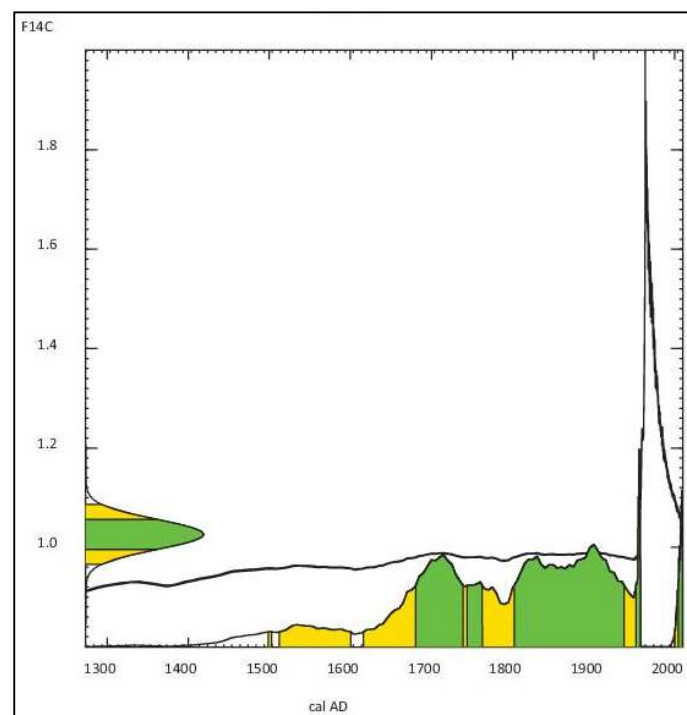


Fig. 4.40 ¹⁴C age plot for sample BH6_55. Black line = reference curve; green shaded area = one sigma range; yellow shaded area = two sigma range

4.2.8 Formation and evolution of the Dangkhar carbonate breccia

The laterally and altitudinally restricted extent of the carbonate breccia is attributed to a deposition during recession of a vast Spiti Valley paleo-glacier that blocked the debris from travelling further downslope bringing it to a sudden halt (Fig. 4.41a & b). The carbonate breccia outcrops are present on both valley flanks but are more abundant and thicker on the Dangkhar hillslope, where the Dangkhar Landslide provided larger amounts of debris.

After recession of the Spiti Valley paleo-glacier, the breccia deposits remained as isolated bluffs in the landscape and the Spiti Valley attained its overall U-shaped profile. The frontal limits of the carbonate breccia deposits still outline the former glacier limit (Fig. 4.41a). The outcrop of polished bedrock near Siluk is interpreted as an erosional feature of the Spiti Valley paleo-glacier (Fig. 4.41a) indicating that a certain stage the entire Upper Spiti Valley was glaciated. Such polished, smooth bedrock surfaces are typically formed by the Chandra glacial stage in the region (Owen et al. 1997).

Following debris flows were deposited at lower elevations spreading out into the valley floor after deglaciation (Fig. 4.41a & c). The clustering of carbonate breccia deposits around Dangkhar is favored by the presence of the large quantities of debris previously produced by the Dangkhar Landslide in combination with larger amounts of water which were available during phases of more extensive glaciation. The distribution of lake sediments within the Dangkhar Lake basin and other lake beds in the study area are evidence for water rich conditions in the past (Fig. 4.41a). Presently small springs originate from the carbonate breccia deposits and from the rock glaciers feeding the Dangkhar Lake serving as a source for water.

The different layers of the carbonate breccia represent environmental changes in the area during its formation. The formation of the breccia initiated during glacial conditions and continued until paraglacial conditions. The compact bottom layer of lodgment till of subrounded blocks within a fine grained matrix, is overlain by proglacial outwash material. A crudely stratified mid layer exhibiting wet sediment deformation and flow structures characteristic of a flow till (Benn and Evans 2010), and the top layer with inverse grading and large angular blocks representing a debris flow deposit follow.

Melting of the incorporated, buried ice within the mid layer of the carbonate breccia can lead to the observed normal faulting within glacial sediments right after or during their deposition (Bennett and Glasser 2009). However, normal faulting and dewatering phenomena can also occur in debris flows producing features similar to those of tills. Especially large landslides and slumps can exhibit internal structures that very much resemble that of glaciotectionic activity, producing massive to stratified diamictons difficult to distinguish from subglacial tills (Benn

and Evans 2010). The mid layer of the breccia also exhibits characteristics of a *Type II flow* (Benn and Evans 2010).

Type II flows typically have a water content of 15 – 20 % and use channels as pathways of their flow and form lobes during deposition. The sediment structures show curved shear planes and streaked out smears of fine grained material. The crude stratification and inverse grading of the breccia are characteristic of a water rich sediment source (Benn and Evans 2010). The term flow till is used by some authors referring to debris flows associated with glaciers or which are till derived (Dreimanis 1989).

The top layer of the carbonate breccia at Dangkhār is located along the projection of a relict rock glacier and an outlet ditch of the empty lake just north of the Dangkhār Lake basin (Fig. 4.41a). A burst of the of the downslope levée of the lake and subsequent Glacial Lake Outburst Flood (GLOF) is likely to have produced the top layer. Such an event is also capable of transporting large blocks in a surge of hyperconcentrated slurry of mud where the blocks are floating on top resulting in the observed inverse grading (Benn and Evans 2010). Such events are quite common in the Himalayas during phases of deglaciation (Iturrizaga 1999) when sufficient amounts of meltwater are provided. Presence of water is also required to form cementation of the breccia components. Especially in carbonate environments such cementation initiates geologically soon after the event (Ostermann et al. 2007). The breccia might therefore be a series of debris flows emplaced atop more rounded glacio-fluvial deposits. The breccia and present debris flows can be regarded as byproducts or secondary landslides of the Dangkhār Landslide. The plan view geometry of the breccia reveals a roughly triangular fan shape resulting from coalescing flow lobes. This also explains the sudden disappearance of the breccia along strike. Erosion finally shaped the top of the deposits into its present shape exhibiting the characteristic columnar structure.

In Zanskar, the “tors of fanglomerate” (Mitchell et al. 1999) represent deposits of ancient valley glaciations and occur as isolated, lithified diamictites at elevations > 200 m above the present valley floor. Analog to the Ancient Dangkhār Monastery (Fig. 4.42b, d, e), the Phuktal Monastery (Fig. 4.42a, c) in Zanskar was built on such lithified deposits, which are composed of the same geologic units as those at Dangkhār. Such isolated, lithified breccia deposits located at higher elevations above the valley floor represent characteristic remnants of the Chandra glacial stage in the NW Himalaya (Taylor and Mitchell 2000).

The laboratory analysis revealed further properties regarding the origin and development of the breccia on a microscopic scale. The monomict nature of breccia implies a local source (Tucker 2001). The material was derived from the slope and has not formed during the deposition of the surrounding bedrock formations (i.e. no marine slide or turbidity current).

The thin sections provide insight to the pre and post depositional alteration of the breccia deposit. Clast and matrix relations indicate an evolution involving transport, deposition, fracturing and burial cementation conditions based on the observed calcite spar and clast fabrics. Offset pre-breccia veins indicate fracturing and displacement on a local scale, while calcite crystal zonation is typical for several growth stages over time. Dogtooth cements use the clasts as a substratum to grow into the void space.

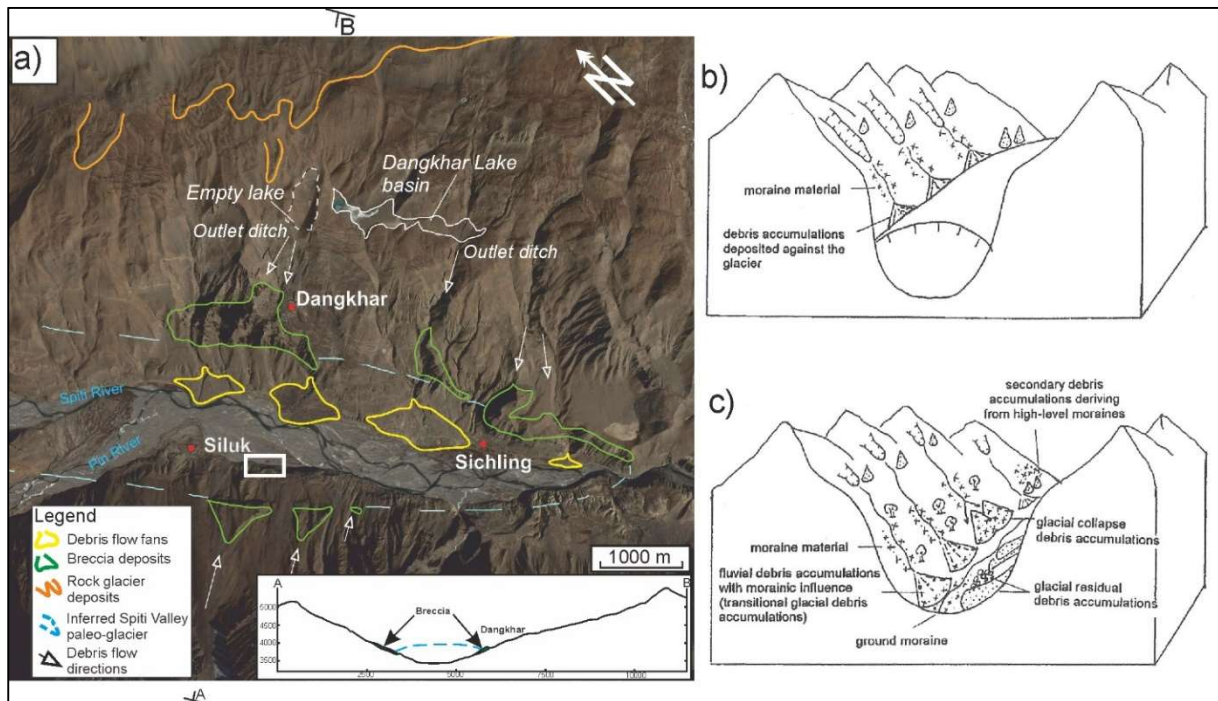


Fig. 4.41 Distribution and mechanism of carbonate breccia formation. a) Google Earth Pro satellite image and topographic profile through Dangkhar highlighting locations of carbonate breccia deposits and inferred Spiti Valley paleo-glacier. White box indicates location of polished bedrock surface (after Kaspar et al. 2019). b) Conceptual model of debris accumulation against a valley glacier at elevated levels of valley flanks during deglaciation. c) Debris accumulation after deglaciation near the valley floor (after Iturrizaga 1999)



Fig. 4.42 Characteristics of the deposits of the Phuktal and Ancient Dangkhar Monastery. a) The Phuktal Monastery surrounded by the lithified deposits above the Tsarap River (image: Flickr). b) Ancient Dangkhar Monastery situated on top of breccia deposits above the Spiti River. c) Detailed view of massive lithified deposits at Phuktal (image by Shakti; Wikipedia.org). d) Ancient Dangkhar Monastery located atop a massive breccia spur. e) Detailed view of an apron of inclined stratified layers of the carbonate breccia at Dangkhar

The amount of fitting of grains within the breccia together with the amount of ground mass can be used as diagnostic tool for the genesis of a breccia (Füchtbauer and Richter 1983), suggesting a mass flow origin for the breccia (Fig. 4.43) around the Ancient Dangkhar Monastery. Sharp clast/cement boundaries and split grains pieced together are a typical property of mass-flow breccias (Flügel 2010) or debris flow deposits (Owen 1994).

Mineralogical and structural properties of the cement point to a burial cement environment. The drusy, mosaic fabric and its dark appearance under cathodoluminescence are characteristic for near-surface meteoric cements (Tucker 2001; Flügel 2010). The source of the calcite can be either pore water, or pressure dissolution within the limestone (Tucker 2001). Meteoric water percolating downwards causes dissolution and recrystallization of the underlying material resulting in cementation of the pore space.

The crude stratification and inverse grading of the breccia are characteristic of a water rich sediment source (Benn and Evans 2010), and stable isotope data with shifts towards lighter oxygen isotope composition of the cements indicate presence of freshwater during formation. Stable isotope values for oxygen and carbon within the calcite cement range from $\delta^{18}\text{O}$ -22.78 to -20.23 ‰ VPDB and $\delta^{13}\text{C}$ 2.37 to 2.82 ‰ VPDB, respectively. The clasts exhibit values of $\delta^{18}\text{O}$ -10.25 to -17.45 ‰ VPDB and $\delta^{13}\text{C}$ 2.37 to 3.51 ‰ VPDB. The shift pattern from host rock to cement suggests influence of both, evaporation and a slight component of CO_2 -degassing (Sanders et al. 2010). Also the local Dangkhar MWL revealed an evaporation trend in the isotope composition of the water samples compared to the WHMWL and GMWL. Altitude versus Dangkhar MWL relationships of water samples suggest partial infiltration of isotopically lighter glacial meltwater at higher elevations, which percolates through the sliding mass emerging in the springs that cluster at lower elevations near the landslide toe area.

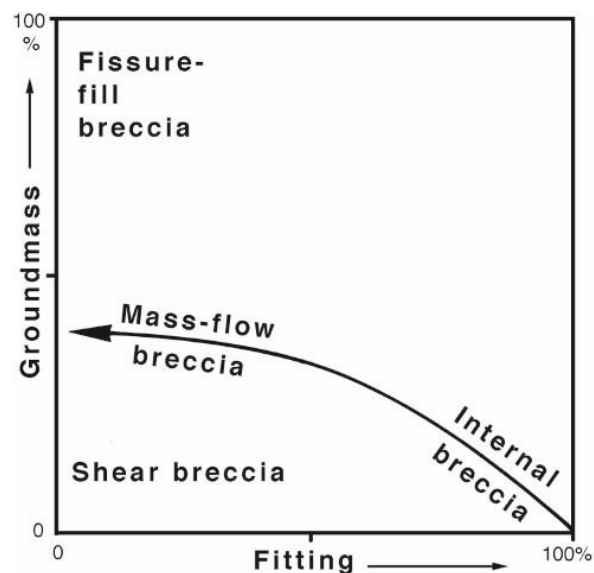


Fig. 4.43 Fitting of clasts versus groundmass (clast + cement ratio) as tool for identifying the origin of breccia types (after Füchtbauer and Richter 1983)

According to the early classification scheme of Norton (1917) the Dangkhar carbonate breccia exhibits the characteristics of a *Bajada breccia*. This breccia type develops under arid mountain conditions by intermittent streams carrying large quantities of material forming a mud or debris flow and are of local origin. They show imperfect stratification with crude bedding. The bajada breccia forms a wedge in plan view, but its extent is larger than that of a talus fan. After deposition the material is transformed into a compact rock. The hoodoos are also an indication for arid desert environmental conditions with little precipitation, and are derived from sedimentary formations that are subject to partial dissolution. The clasts of the breccia are cemented by a limestone matrix originating from calcareous waters.

4.2.9 Geochronology and evolution of the Dangkhari Landslide

From historic reports, published studies in nearby regions, field observations of landforms and their morphostratigraphic relations and weathering characteristics together with radiocarbon dating a timeframe for the Dangkhari Landslide activity is established. Since three generations of rock glacial deposits are preserved, and breccia deposits formed during recession of a Spiti Valley glacier, the Dangkhari Landslide must have been active over a timespan covering at least four consecutive glacial stages (Fig. 4.44).

The polished bedrock surfaces and the overall U-shaped Spiti Valley geometry are the result of a Spiti paleo valley glaciation. This major glacial advance in the Spiti Valley occurred around 28 to 14 ka (Srivastava et al. 2013) falling in the range of the regional Chandra glacial stage. Later glaciations in the Lahaul-Spiti region were restricted to side valleys and largely represented by rock glaciers (Owen 2009).

The first generation rock glaciers which are the least well preserved, are interpreted as the first deposits of slope glaciers after the recession of a Spiti Valley glacier. They might be the result of the cold event at 7.6-6.8 ka (Anoop et al. 2012) when glaciers advanced again in the Spiti Valley. The second generation rock glaciers were judged to be of mid-to-late Holocene age based on their fresh morphometric features (Kaspar and Kieffer 2015). An organic sample retrieved from a depth within a depression of a second generation rock glacier indicated a possible age of 0.23 to 0.76 ka. Since the age represents a minimum age, it raises the possibility that the formation is associated with an earlier late Holocene, cooler climatic period that prevailed in the Spiti Valley approximately 2.3 to 1.5 ka ago and is documented by pollen analysis (Chauhan et al. 2000; Bhattacharyya et al. 2006). Also Dortch et al. (2013) report a 1.6 ka cold event for the semi-arid western Himalaya, which is in good agreement with the pollen data. Moreover, such peaty material accumulations on landslides in general needs stable conditions and requires more than just a few hundred years to form (Lang et al. 1999).

The third generation rock glaciers which are located in the permafrost zone are characteristic remnants of the Little Ice Age (LIA) in the Lahaul and Spiti areas (Owen and England 1998) and exhibit a fresh character comparable to the LIA moraines in the adjacent Manirang area. LIA moraine deposits in the NW Himalaya usually exhibit fresh character and unvegetated cover (Taylor and Mitchell 2000; Owen 2009) and correspond to the Sonapani II glacial stage of Owen et al. (1996, 1997). Such LIA rock glaciers in the Himalayan-Tibetan areas are commonly encountered at altitudes above 4000 m in climatic settings with precipitation lower than 1000 mm/yr (Owen and England 1998; Owen 2009).

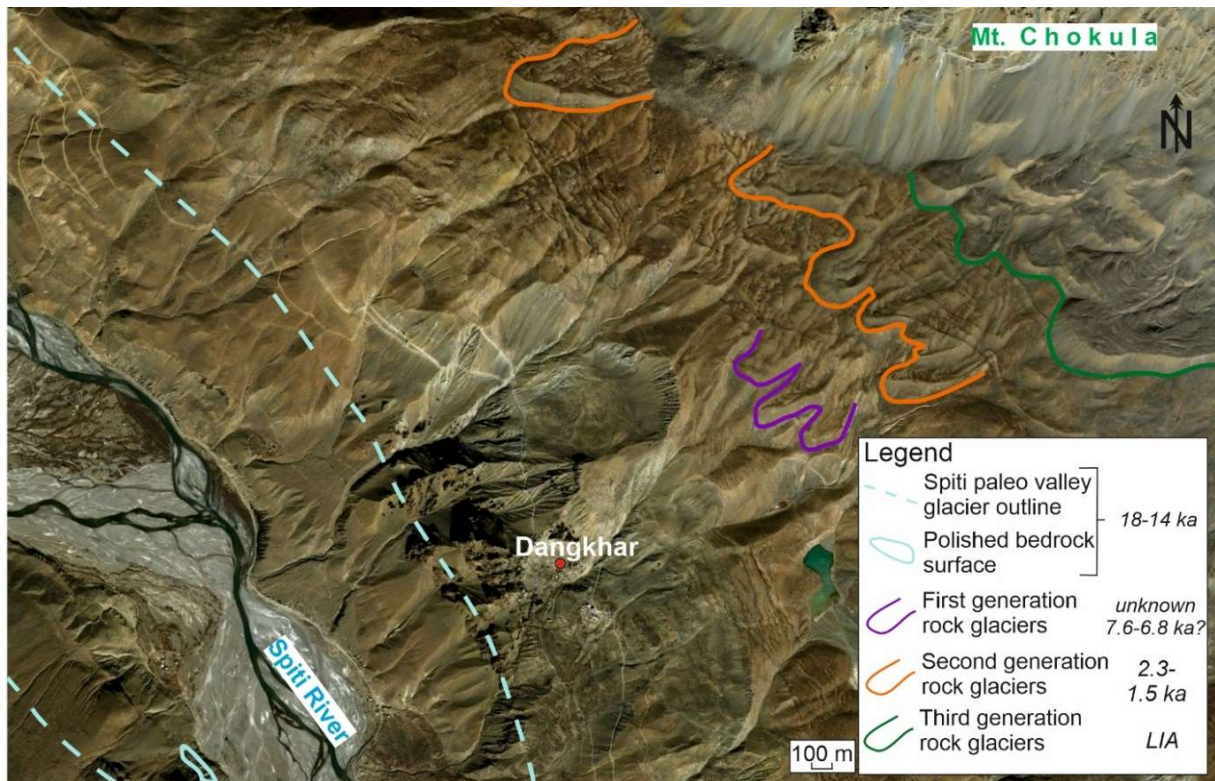


Fig. 4.44 Satellite image of the Dangkhar Landslide with the different features of glacial stages (image: Bing Maps) and tentative temporal framework.

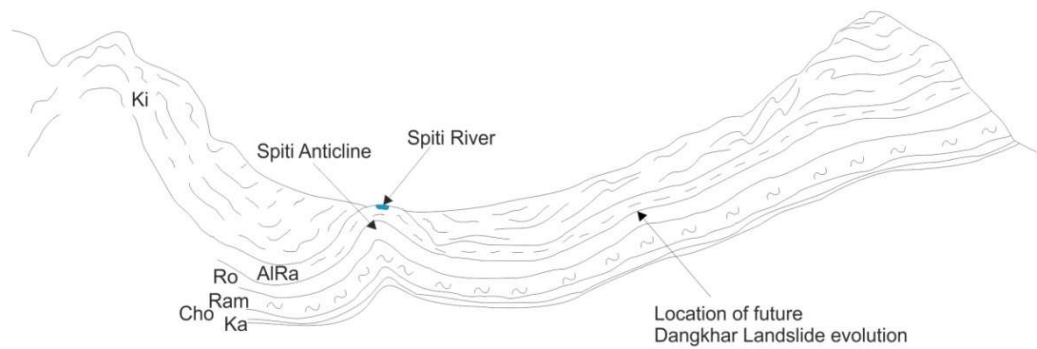
Fig. 4.45 sketches the hypothesized evolution of the Dangkhar Landslide through time. Stages 1 and 2 roughly sketch the pre-Quaternary tectonic evolution of the Spiti Valley when it was subject to the eo-himalayan folding, faulting and river incision along the Spiti anticline. Some of the faults formed during E-W extension were reactivated during neotectonic activity (Neumayer et al. 2004).

Initiation of Dangkhar Landslide activity is suspected towards the end of the last major Spiti Valley glaciation. Polished bedrock surfaces, U-Shaped valley geometry and breccia deposits represent remnants of this Pleistocene valley glaciation (Stage 3 – Fig. 4.45). Meltwater production led to the deposition lodgment till, fine grained and rounded glacial outwash material and flow till (Stage 3 – Fig. 4.45). The deposits form the bottom and mid layer of the carbonate breccia. Meltwater lakes formed on the slope which transported large amounts of debris during Glacial Lake Outburst Floods (GLOF) resulting in the top layer of the carbonate breccia layer (Stage 4 – Fig. 4.45).

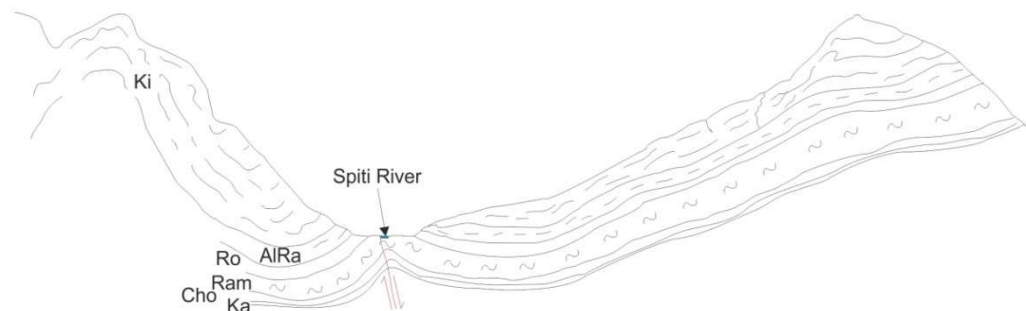
The till and debris material were later cemented into the crudely stratified carbonate breccia deposits (Stage 5 – Fig. 4.45) and remained at elevated positions after the valley glacier had disappeared.

The first stage rock glaciers were deposited during a minor glacial stage (Stage 5 – Fig. 4.45), and the oldest lineaments developed, displacing the first rock glacier deposits. The Mane Landslide in the southern part of the study area has been dated at 8.7 ka (Bookhagen et al. 2005), and unconformably overlies the Dangkhar Landslide, supporting early or pre- Holocene initiation. Due to the blockage of the Spiti River by the Mane Landslide and the formed Mane paleo-lake, sediments accumulated within the following approximately 2500 years along the toe area of the Dangkhar Landslide. The lake sediments are not directly influenced by the Dangkhar Landslide, but are overlain by alluvial fan and debris flow deposits, dissected by ephemeral stream channels and displaced by the Lingti Landslide. The second generation rock glaciers are again displaced by the lineaments and by secondary landslides (Stage 6 – Fig. 4.45). The third generation rock glaciers from the LIA have been deposited over the lineaments (Stage 7 – Fig. 4.45). The cross-cutting relations between the rock glaciers and the lineaments suggest that landslide deformations have continued to occur through the mid to late Holocene.

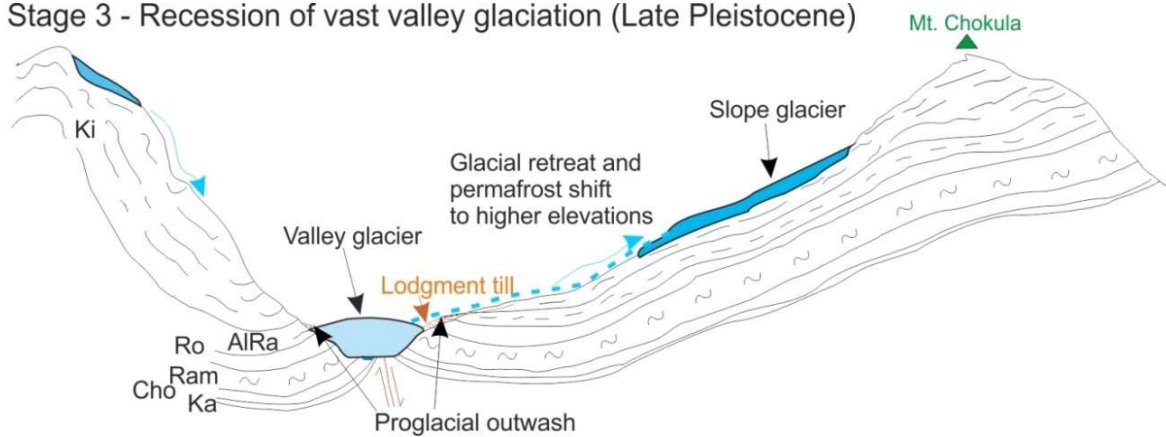
Stage 1 - some time after Eohimalayan folding and major uplift phase 20 Ma ago



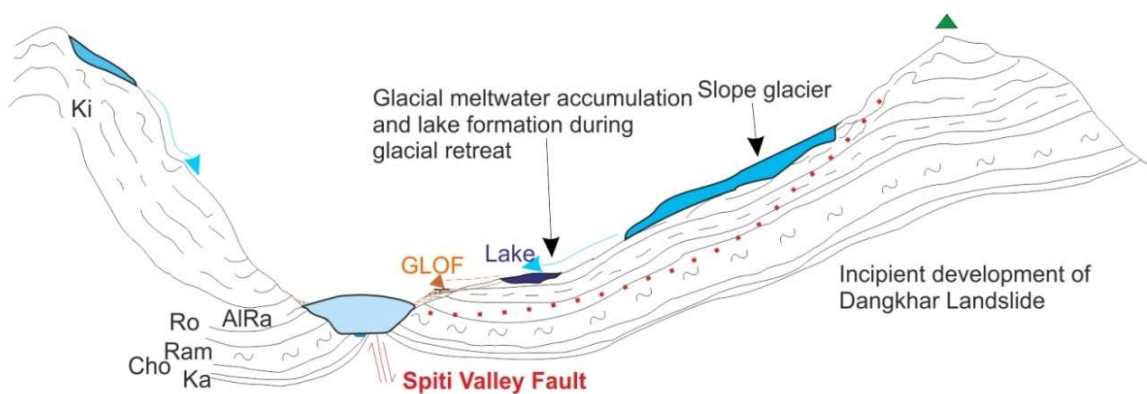
Stage 2 - River incision along Spiti Anticline and initial faulting activity (E-W extension)



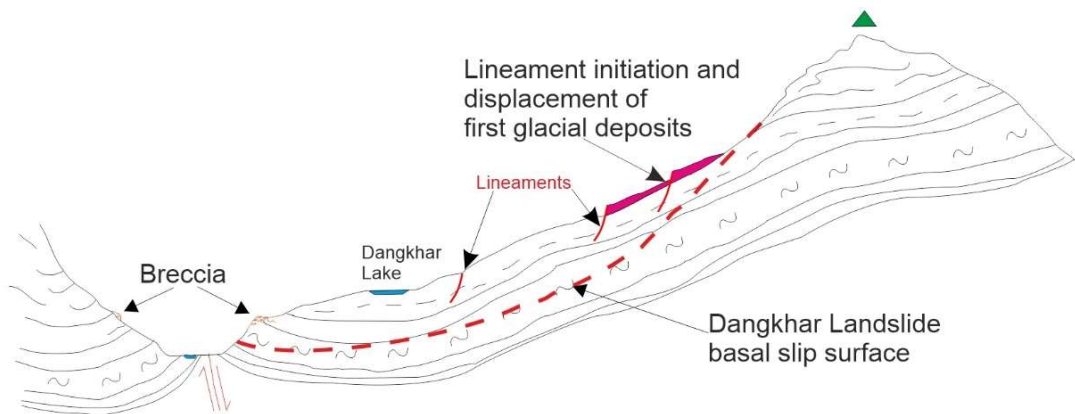
Stage 3 - Recession of vast valley glaciation (Late Pleistocene)



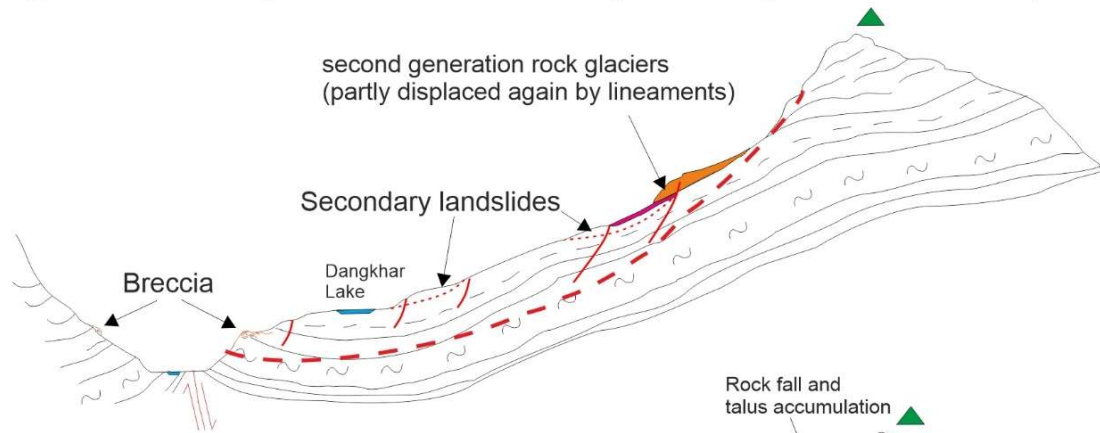
Stage 4 - Meltwater lake formation and breccia emplacement (Late Pleistocene)



Stage 5 - First rock glacier advance and lineament development (Early Holocene)



Stage 6 - Second rock glacier advance and secondary landslides (Mid- to Late Holocene)



Stage 7 - Subrecent rock glacier advance (Little Ice Age)

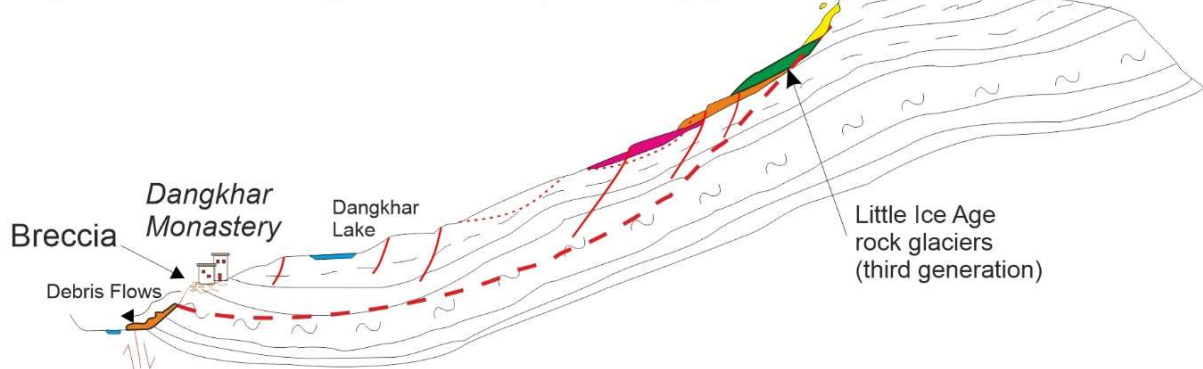


Fig. 4.45 Hypothesized evolution of the Dangkhar Landslide through time. Abbreviations: Ki = Kioto Gr., AlRa = Alaror and Rangrik Fm., Ro = Rongtong Fm., Ram = Rama Fm., Cho = Chomule Fm., Ka = Kaga Fm., Mi = Mikin Fm, GLOF = Glacial Lake Outburst Flood

In a regional and global context the timing of the Dangkhār Landslide falls in the cluster of Holocene landslides worldwide (McColl 2012). Also landslides within the northwestern Himalaya (Srivastava et al. 2013) exhibit a clustering after phases of deglaciation (Fig. 4.46) and intensified monsoon activity, while glacial phases occur during reduced monsoon activity and stronger winter Westerlies (Anoop et al. 2013).

The activity of the Dangkhār Landslides broadly coincides with the timing of other large landslides in the northwestern Himalaya (Fig. 4.46).

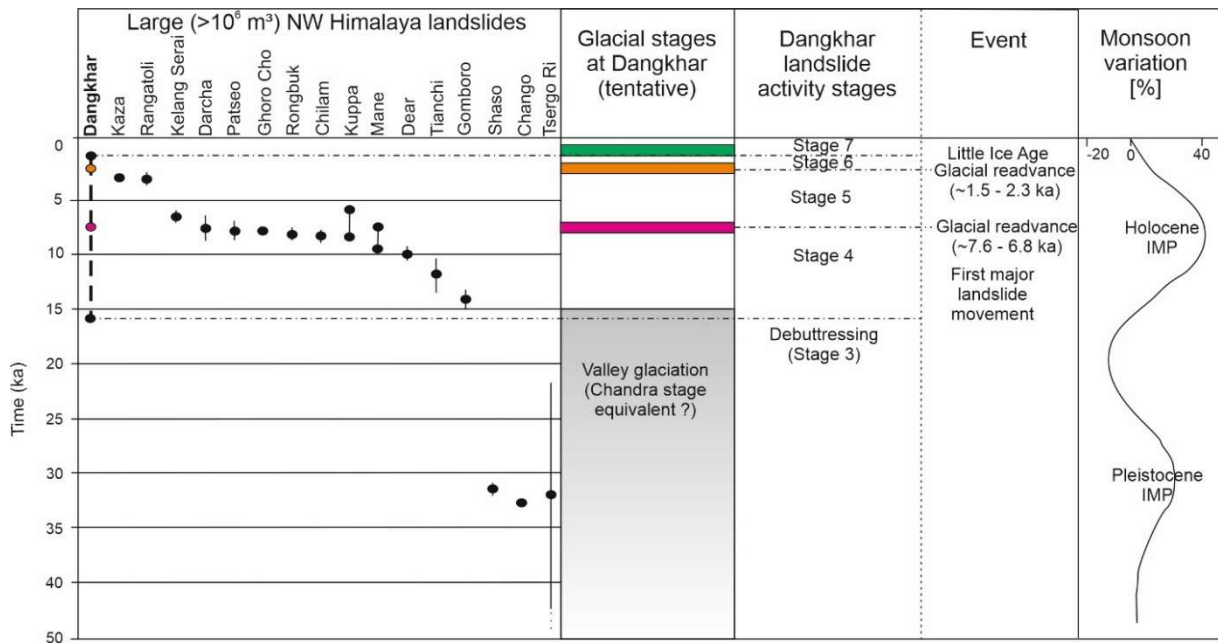


Fig. 4.46 Summary chart of the evolution of the Dangkhār Landslide in a broader regional context. Color bars correspond to glacial stages in Fig. 4.44 and Fig. 4.45. Total, episodic activity of the Dangkhār Landslide between the solid black dots. Dangkhār Landslide activity stages refer to stage numbers of Fig. 4.45 (modified and compiled after Srivastava et al. 2013; Anoop et al. 2012; Dortch et al. 2009; Bhattacharyya et al. 2006; Chauhan et al. 2000)

4.2.10 Geotechnical evaluation

4.2.10.1 Block Theory

In order to gain insight as to why such a massive landslide occurred at this particular geographic location, rigorous kinematic and stability analyses were performed using block theory (Goodman and Shi 1985). For kinematic and failure mode analyses, input parameters include the orientations of the: (1) free slope surfaces; (2) basal landslide slip surfaces; and (3) resultant force acting on the sliding mass. As shown in Fig. 4.47a, the hillslope has a complex geometry by virtue of the developed stream pattern. For this reason, the free slope surface is modeled as a composite surface composed of three best fit tangent planes. Similarly, the curved nature of the basal slip surface is modeled as a composite surface composed of two best fit tangent planes (Fig. 4.47b). Numerical values for all tangent planes are summarized in Tab. 4.8 Stereographic plots for assessing block removability (landslide kinematics) and failure mode are shown in Fig. 4.48a and Fig. 4.48b, respectively. According to Shi's Theorem, a block is removable only if its Joint Pyramid (JP) has no intersection with the Excavation Pyramid (EP) formed by the slope. Fig. 4.48a shows that JP 00 forms a kinematically removable block, and Fig. 4.48b indicates that under gravity loading the failure mode involves planar sliding along the base plane.

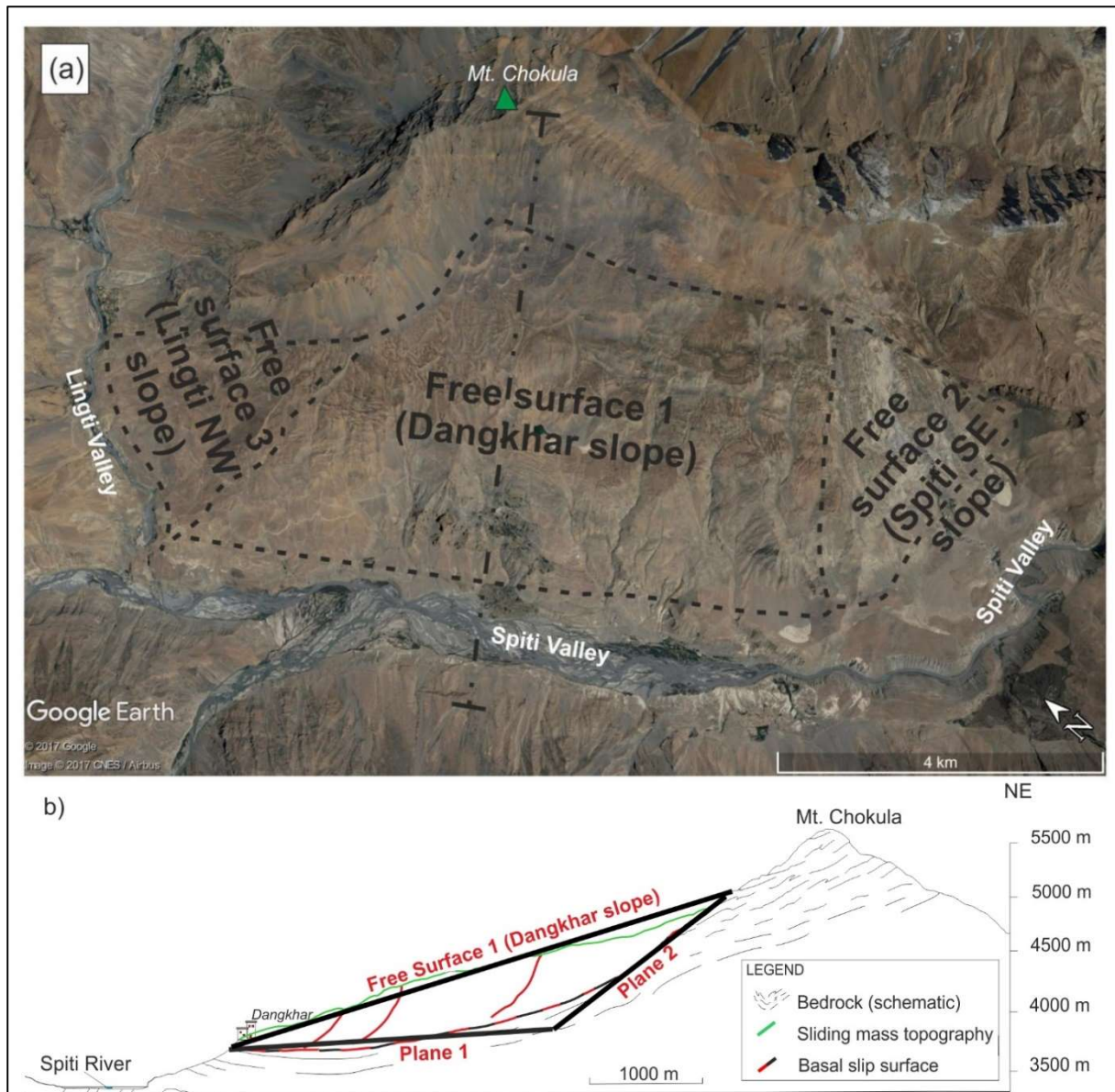


Fig. 4.47 Block Theory analysis setup. a) Map of the free surfaces and location of schematic cross section (dash-dotted line) shown in b (image: Google Earth Pro). b) Cross section with outlined wedge bound by bi-planar planes 1 and 2 and the free surface 1

Plane ID	Orientation (Dip direction/Dip)
Plane 1	251/03
Plane 2	251/40
Free surface 1 (Dangkhar Slope)	251/20
Free surface 2 (Spiti SE Slope)	154/14
Free surface 3 (Lingti NW Slope)	299/16

Tab. 4.8 Orientation data of the planes and free surfaces used in the Block Theory analysis

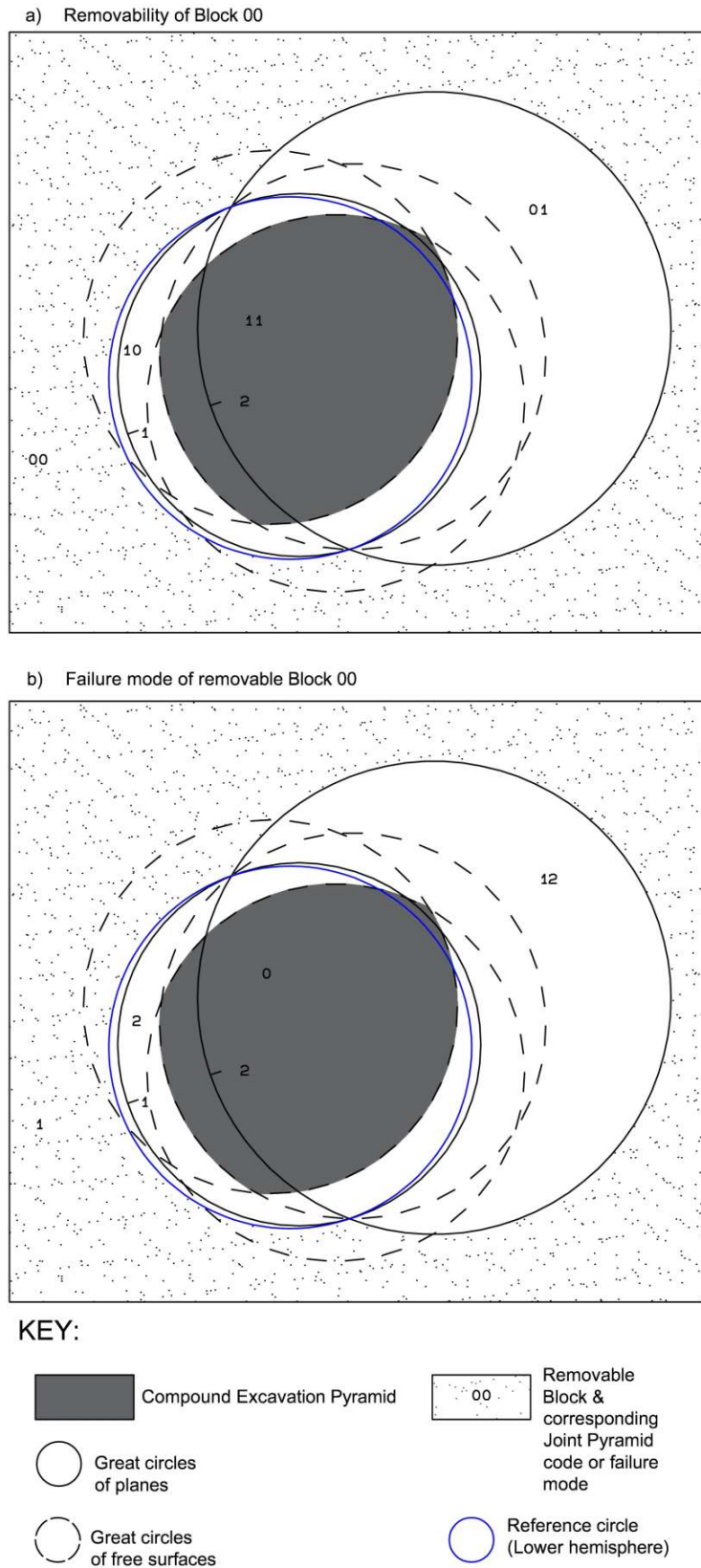


Fig. 4.48 Block Theory analysis for the Dangkhar Landslide. a) Removability plot of block 00; b) Failure mode of block 00 (Single digit indicates planar sliding on respective plane, i.e. Plane 1)

According to block theory, at least four surfaces (either slope surfaces or joint surfaces) must be involved in the creation of a kinematically removable block. At least one slope surface and one joint surface must be involved. Based on a tangent plane analysis that is intended to capture the overall slope character, Fig. 4.49 depicts the simplified geometry of the Dangkhar Landslide block. The developed stream pattern is the critical factor in forming the kinematically removable block, as the pattern provides for effective lateral releases at the upstream and downstream boundaries of the landslide.

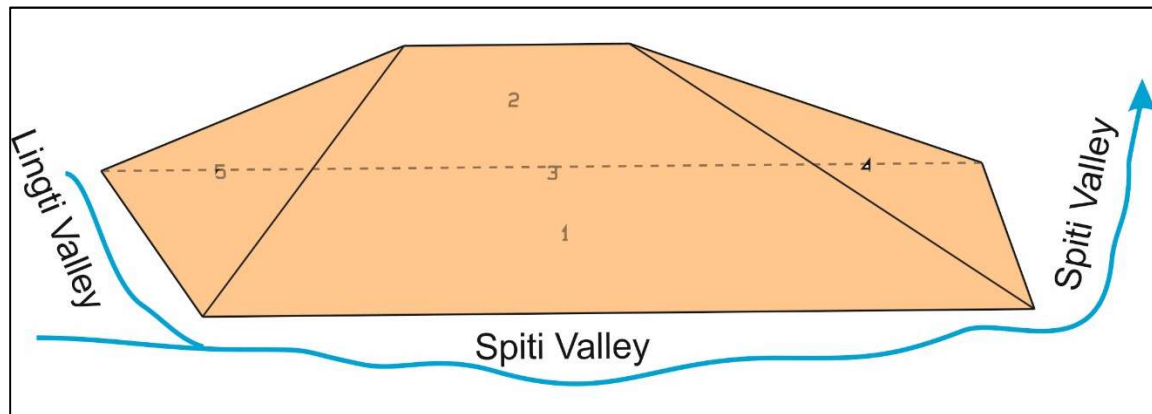


Fig. 4.49 Shape of identified removable block pyramid 00 111 (the first two digits relate to planes 1 and 2, digits three to five relate to the three free surfaces). Block schematically placed in the setting between the Spiti and Lingti Valley representing the sliding body of the Dangkhar Landslide

4.2.10.2 Triggering mechanism

The Dangkhar Landslide is located within a seismically active zone of the Himalaya raising the possibility of an earthquake trigger. The potential role of seismicity in triggering the Dangkhar Landslide was assessed in a pseudostatic framework (Chowdhury 2000). Assuming the hillslope is brought to the condition of limiting equilibrium during an earthquake, the pre-earthquake (static) factor of safety and yield acceleration can be estimated as a function of shear strength and shear plane inclination. In this simple case, the failure mode is assumed to involve planar sliding, and the static factor of safety is expressed as:

$$F_{\text{static}} = (a_y \cot\beta + 1) + a_y \tan\phi$$

Where a_y is the yield acceleration and β and ϕ are the shear plane inclination and friction angle, respectively.

With an average β value of 20° and for ϕ values ranging from 20° to 40° , Fig. 4.50 shows the relationship between the static (pre-earthquake) factor of safety and ground acceleration required to reduce the seismic factor of safety to unity. The maximum range of peak ground accelerations (PGAs) expected at the site from regional earthquake structures (excluding the SVF) are shown on Tab. 3.1, together with the maximum PGA associated with the SVF. The evaluation indicates earthquake shaking emanating from regional seismic sources could initiate instability if the static factor of safety were in the range of 1.25 to 1.93, or less. Earthquake shaking associated with the SVF (bordering the landslide toe) could initiate instability for static factors of safety up to approximately 5.40, indicating it is a highly capable potential seismic source.

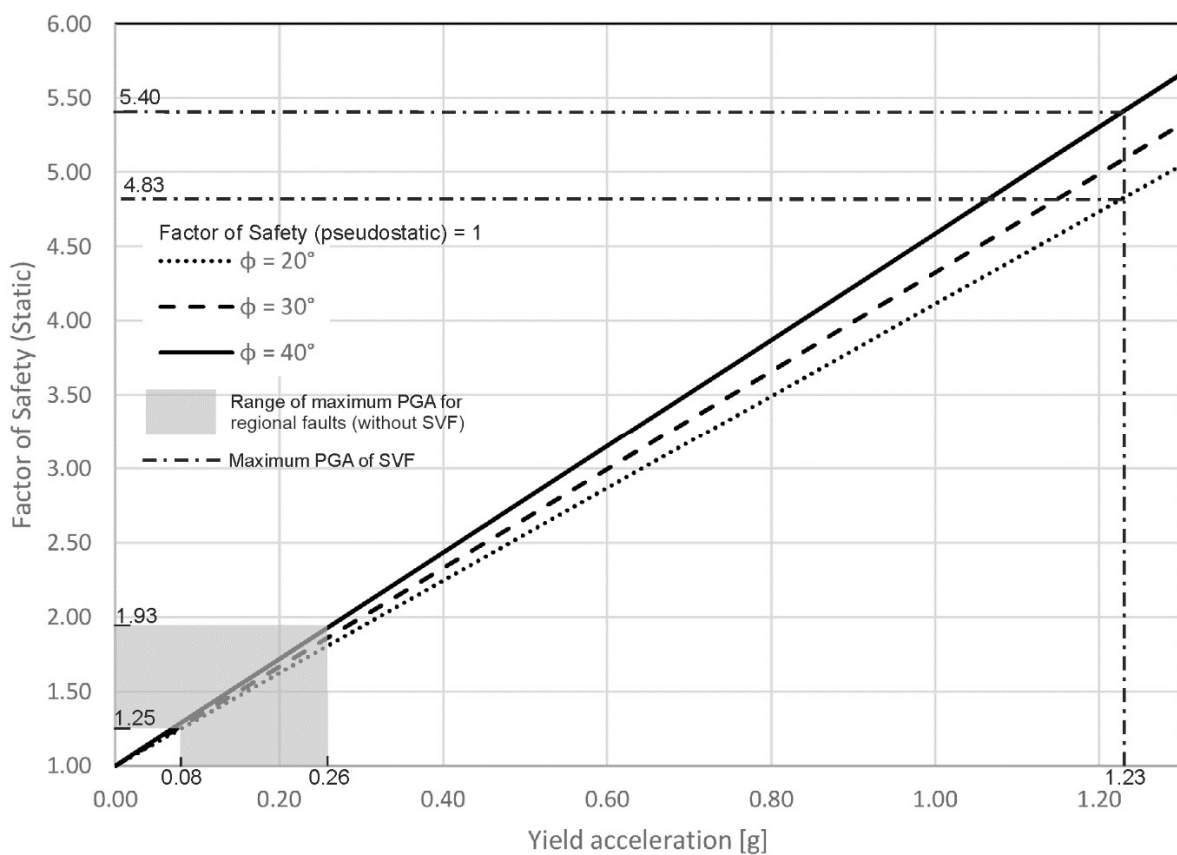


Fig. 4.50 Static factor of safety versus yield acceleration for the Dangkhar Landslide

Glacial debuttressing represents an additional potential triggering event. The primary mechanisms leading to failure under this scenario include: (1) removal of the physical stabilizing load applied to the hillslope; (2) elastic rebound of the hillslope, potentially leading to microcracking and weakening of the rock mass; and (3) increase in slope relief and steepness as a result of glacial downcutting and erosion.

Investigations on the buttressing capabilities of glaciers suggest that the incipient landslide motion can already occur while the glacier is still present in the valley (McColl and Davis 2013). The glacier reshapes the valley geometry and subsequently determines when the slope attains a critical state. Extremely large landslides are capable of deforming and bulldozing the glacial ice near the toe area so that slow rates of movement can already be achieved before deglaciation is completed (McColl and Davis 2013). Valley glaciers are responsible for debuttressing of slopes and permafrost degradation or changes in groundwater conditions plays an important role in triggering large bedrock landslides (Krautblatter et al. 2013). The carbonate breccia which formed during Spiti Valley glacier recession points to incipient Dangkhar Landslide activity already during glacial conditions. The contribution of the toe erosive action of the Spiti River as the trigger is considered unlikely, since the basal slip surface is located about 200 m above the river level. It serves as agent though for removing debris flow material from the toe area.

Slowly moving extremely large landslides situated within post-glacial valleys represent long-term changes of slope morphology and stress conditions (Moser et al. 2017; McColl 2012). Studies on landslides in earthquake regions show that strong seismic events usually trigger many smaller, catastrophic landslides rather than large, slowly moving landslides (Dortch et al. 2009; McColl 2012). In almost every case involving extremely large landslides, the trigger is a combination of several circumstances as the slope attains a critical state (Bonzanigo et al. 2006).

Eberhardt et al. (2016) introduced the term rock mass fatigue to express the influence of cyclic fluctuating conditions on the slope. The fatigue mechanisms include hydromechanical, thermomechanical, seismic and glacial mechanisms. Each of these mechanisms acts at different time scales and with different severity on the rock mass (Fig. 4.51). Initial glacial debuttressing has a major impact on the slope conditions, leading to failure initiation. The remaining factors such as seismicity, climatic and hydrogeological conditions (precipitation, temperature changes and ground water fluctuations) act at shorter intervals being responsible for reactivation and episodic activity of the landslide.

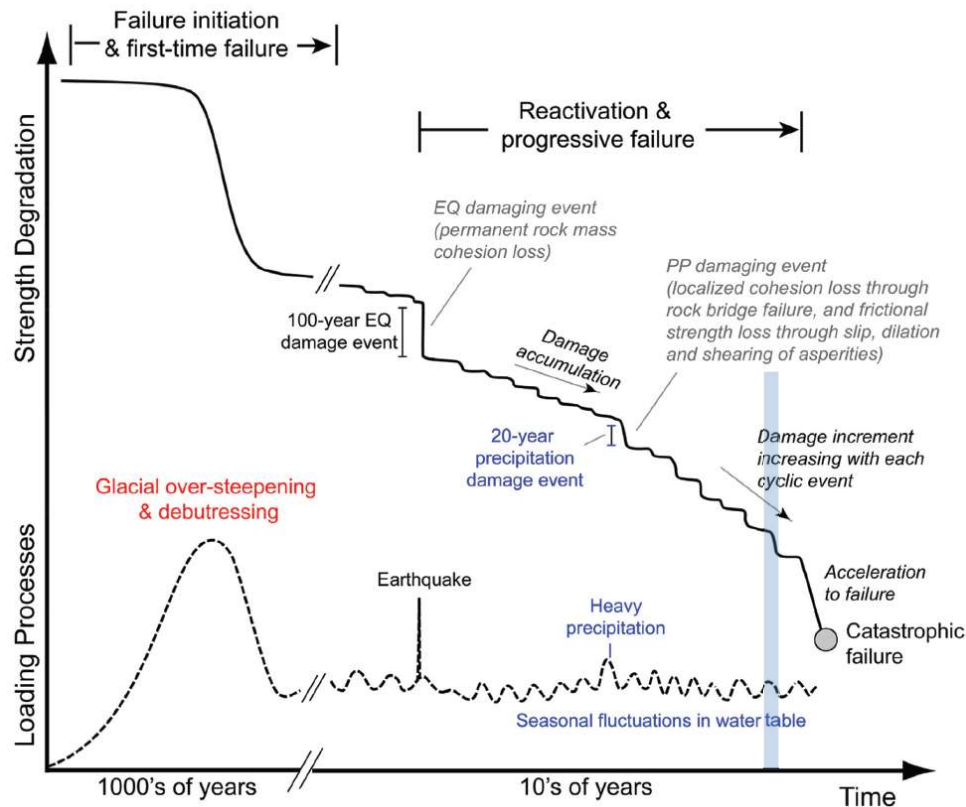


Fig. 4.51 Magnitude and type of rock strength degradation cycles (rock mass fatigue) at different geologic time scales. Blue bar indicates approximate state of the Dangkhar Landslide. Note strong strength degradation due to glacial activity (modified after Eberhardt et al. 2016)

4.2.11 Style of deformation and classification

Detailed field and remote investigations of geomorphological features provide crucial insight on the deformation mechanism of extremely large landslides (Weißflog et al. 2010). Rafted rock blocks displaced along the dip slope limb of the syncline, folded strata within the landslide deposit, hummocks, lineaments formed by ridges and trenches, and scarps within the sliding mass are the result of what is generally referred to as *slope tectonics* (Jaboyedoff et al. 2011, 2013). Due to their size and extent, the geomorphologic structures produced by slope tectonic processes resemble those of thin-skinned tectonics and are commonly present in extremely large, slowly moving landslides (Agliardi et al. 2001; Hewitt et al. 2008). The slope experienced differential movements, where the lineaments are the result of dilation and motion along discrete shear surfaces.

Episodic phases of acceleration, deceleration and interruption of motion occurring over the entire lifespan of the landslide are recorded in cross-cutting relations with the different rock glacier generations. The rock glaciers of the first and second generation are displaced on a scale of tens of meters, indicating that the entire sliding mass moved as a bulk in a quite coherent manner preserving many of its original features. The fact that the rock glaciers developed on a sliding mass additionally shows that the motion was slow and the rock glaciers were able to sustain the deformation imposed by the sliding mass. Extremely large, episodically active landslides can develop a “self-healing” mechanism or “braking effect” (Varga 2006) where they achieve a more stable state again if groundwater or climatic conditions change resulting in a *stick-slip* behavior (Moser 1996; Bonzanigo et al. 2007; Hungr et al. 2005). Phases of deformation and stabilization of landslides that occur over long periods are in general strongly controlled by ground water conditions within the slope (Petley and Allison 1997).

The absence of a well-defined or not completely developed basal slip surface at the Dangkhar Landslide and the debris terminating at the left bank of the Spiti River also suggest that the Dangkhar Landslide was moving in a slow and non-catastrophic way. The basal slip surface of the Dangkhar Landslide is chiefly located within shale rich rocks of the Rama Formation, which together with the asymmetric synclinal flexure geometry, provide favorable conditions for landslide formation. Such non-sharply defined contacts from bedrock to landslide material are referred to as transition zones (Eberhardt et al. 2007) or deformation belts (Soldati 2013) and their formation is largely controlled by the involved bedrock strata orientation and thickness (Chigira 1992). Their presence can be indicative for an incomplete, confined failure (Hutchinson 1988; Dikau et al. 2006; Eberhardt et al. 2007).

The Dangkhar Landslide presently is in the state of a landslide that experienced glacial debuitressing and glacial recession, but also seismic events during Holocene reactivation of the Spiti Valley Fault (Anoop et al. 2012), and phases of intensified precipitation during times of stronger summer monsoon activity (Bookhagen et al. 2005). However, it did not reach the stage of catastrophic failure.

Assessing the velocity of the landslide can be achieved by inferring it from the style of motion from the preserved geomorphologic features. Extremely large landslides in structural settings favoring sliding (i.e. dipslope conditions) generally move at rates of centimeters to 1 meter per year (Eberhardt et al. 2016; Moser 1996), but may reach displacements up to 7 meters per year (Moser 1996). The distribution of landslide debris restricted to the Dangkhar hillside is a characteristic feature of extremely large, slowly moving landslides which in general lack runoff debris (Ballantyne et al. 2014) with a low sediment release rate compared to other landslides (Slaymaker 2009).

Taking into account the level of preservation of the Dangkhar Landslide morphostructures and deposits and the entire timespan from post-glacial to sub-recent times, the overall average velocity ranges between slow and extremely slow.

The state of activity with respect to the initial mechanism is relict. The climatic and environmental conditions have changed considerably since the Dangkhar Landslide initiated. Initial glacial and postglacial conditions with larger permafrost distribution changed into a paraglacial, dry high mountain steppe climate. Only secondary landslides presently occur as debris flows.

The hydrogeological conditions of the Dangkhar Landslide are also characteristic for extremely large landslides covering areas of several square kilometers. They are commonly dissected by ephemeral streams, creating sub-basins on the slope (Agliardi et al. 2012). Gully erosion furthermore is a dominant landscape forming process on sediment-mantled slopes in paraglacial (Ballantyne 2002) and badland environments (Harvey 2004). Debris flow events transporting material downslope via the ephemeral stream channels, contribute to the long-term erosion of the Dangkhar Landslide. The mature stage ($H_i = 0.36$) of the Dangkhar hillslope is another factor favoring the formation of debris flows (Cheng et al. 2018).

Based on the diverse geomorphologic features and long episodic activity through time and its size, the Dangkhar Landslide is classified as a complex slide principally involving movement along a curved synclinal bedding surface. Since large scale landslides rather form landslide complexes exhibiting several mechanisms (e.g. Hewitt 2009), they cannot be put into existing classification schemes (Clague 2015). Current classification schemes most adequately identify the Dangkhar Landslide as: (i) slump earth flow to rock slump (rockslide with curved sliding plane; Varnes 1978; Dickau 2006), (ii) single sided rotational sagging (Hutchinson 1988), (iii) pre-collapse gravitational deformation, or (iv) mountain slope deformation (Hungr et al. 2014). This last type describes large-scale gravitational deformations of high mountain slopes with a relief of more than one kilometer, without a fully defined sliding plane and extremely slow rates of movement, resulting in the encountered morphological features such as scarps, trenches and benches. According to the definition of Aber and Ber (2011), a *sackung* (sagging) represents a glaciotectonic landform, as the result of the deformation of a mountain into the glacially excavated valley, and is applicable to the setting of the Dangkhar Landslide. The distribution of rock glaciers and permafrost is a diagnostic feature for determining favorable settings for large landslides (Fig. 4.52).

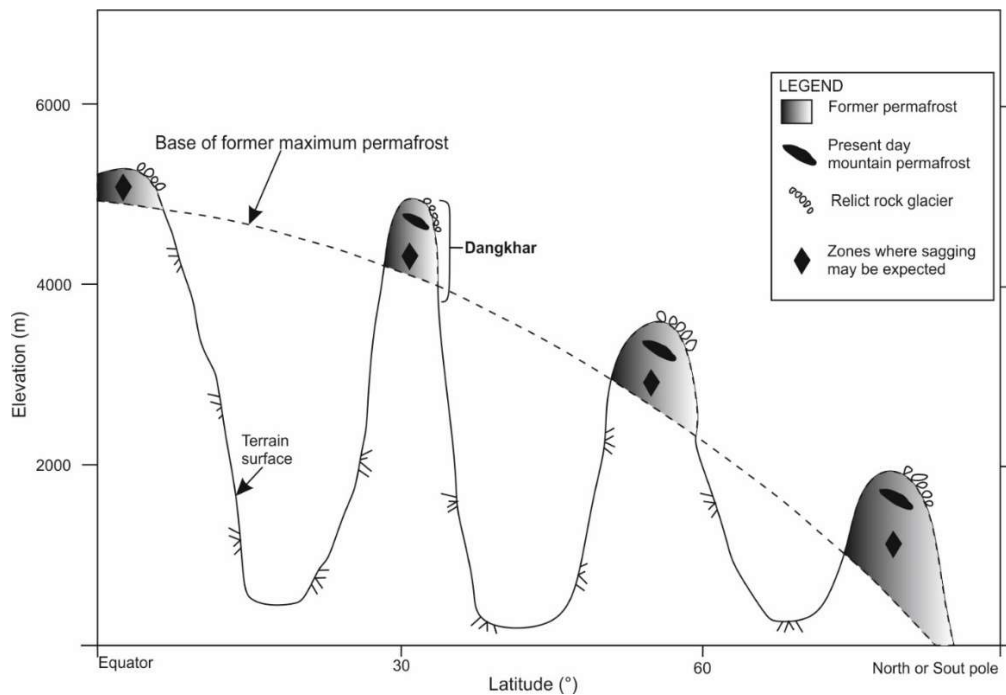


Fig. 4.52 Relationship between elevation, latitude and permafrost/ rock glacier distribution to determine slope settings favorable for large landslides such as sagging (modified after Hutchinson 2006). Bracket indicates approximate altitude and latitude range of the Dangkhar Landslide from toe to crown

The size of the Dangkhar Landslide in terms of both, area and volume, qualifies it to be a large landslide (area $>1 \text{ km}^2$ - Korup 2006, volume $>0.001 \text{ km}^3$ - Korup et al. 2006), mega landslide (area $>2 \text{ km}^2$ - Stout 1991), giant landslide (volume $>0.1 \text{ km}^3$ - Korup 2007; Hancox and Perrin 2009; volume $>1 \text{ km}^3$ - Weidinger and Korup 2009), or regional landslide (volume $>10 \text{ km}^3$ - De Blasio 2011). However, landslide volume terms such as large, very large and giant are not consistently used or universally valid defined and classified (e.g. De Blasio 2011). Other terms include super-large landslide ($>3 \times 10^8 \text{ m}^3$; Shang et al. 2003) extremely large landslide (Weidinger and Korup 2009) and monster landslide (De Blasio 2011).

Informally, the Dangkhar Landslide can be regarded as a *deep-seated* landslide although here definitions are very inconsistent as well, referring either to the depth of the basal slip surface ($>20 \text{ m}$ - Broms and Wong 1991; $>100 \text{ m}$ - Petley and Allison 1997; $>200 \text{ m}$ - Moser et al. 1996), the volume ($>100,000 \text{ m}^3$ - Dramis and Sorriso-Valvo 1994; Gischig et al. 2015), or the areal extent and short run out distances of the landslide (e.g. Roering et al. 2005), or height of the affected slope ($>100 \text{ m}$; Vallet et al. 2016).

5 SUMMARY AND CONCLUSION

This study has revealed the presence of the previously undetected, extremely large Dangkhari Landslide, employing a broad suite of remote, field and laboratory based methods, covering landslide characteristics (Fig. 5.1) from valley to microscopic scales. The presented key findings on geology, geomorphology, tectonics, climate, geomechanics and geochronology provided valuable information for establishing a holistic framework of the Dangkhari Landslide evolution (Fig. 5.2; Tab. 5.1). The list below summarizes the major findings with respect to its nature, size, geomorphologic and geologic setting, mechanism, timing, trigger and classification:

- The large-scale Spiti Valley parallel lineaments are the result of extensional stress conditions and represent normal faulting within the landslide mass.
- DEM analysis revealed the local morphological slope features such as alternating bands of steeper and flatter areas, breaks-in-slope, and hummocky topography, which are consistent with characteristics of extremely large landslides.
- The vast distribution of debris material on the hillslope containing folded and rafted blocks, partly preserving the original bedrock structure represents the landslide deposit. Folding of the incorporated bedrock strata, scarps and ridges on the slope are the result of slope tectonic processes.
- Existence of closed depressions, lakes and rock glacier deposits on the flatter portions of slope indicate periods of stable conditions where the landslide was not moving. The establishment and preservation of these features also point to a non-catastrophic movement of the landslide.
- Polished bedrock surfaces indicate a recession of a valley glacier resulting in debuttressing of the hillslope towards the end of the Pleistocene. Following glaciations were restricted to rock glacier generations on the hillslope recording an overall recession.
- Cross cutting relations between lineaments and rock glacier deposits indicate relative stages of episodic deformation activity through time.

- The 8.7 ka Mane Landslide, which unconformably overlies the Dangkhar Landslide, supports an early to pre-Holocene initiation.
- The bedrock geometry of the hillslope forms an asymmetric synclinal flexure favoring the formation of a structurally controlled failure.
- Transition zone from bedrock to landslide debris suggests an incomplete/discontinuous development of a basal slip surface and slow landslide movement.
- Secondary landslides in the toe region and mid-slope region of the Dangkhar Landslide are consistent with partial reactivation of the initial landslide.
- Distribution of springs around the toe area and downhill from the rock glaciers suggests water infiltration on the surface of the landslide mass.
- Extent of lakes and lake sediments and their spatial proximity to rock glacier deposits indicate presence of larger quantities of glacial meltwater in the past. The meltwater favored glacio-fluvial and debris flow processes reworking and re-depositioning parts of the Dangkhar Landslide material. The material accumulated near the toe area and was cemented forming the carbonate breccia. Debris flows still occur today mobilizing material from the Dangkhar Landslide.
- Stable oxygen and hydrogen isotope data of the breccia cements confirm a meteoric water influence on the landslide material after deposition.
- Removability analysis using Block Theory identifies the location as favorable for landslide development. The removable block is formed by the three free surfaces of the hillslope and the basal slip surface.
- The setting of the landslide within a tectonically active and glacially preconditioned region qualify a seismic source, glacial debuttressing or a combination of the two as a potential triggering mechanism.
- Volume estimates ranging from 15 – 20 km³ rank the Dangkhar Landslide amongst the largest five , continental, non-volcanic landslides on earth.

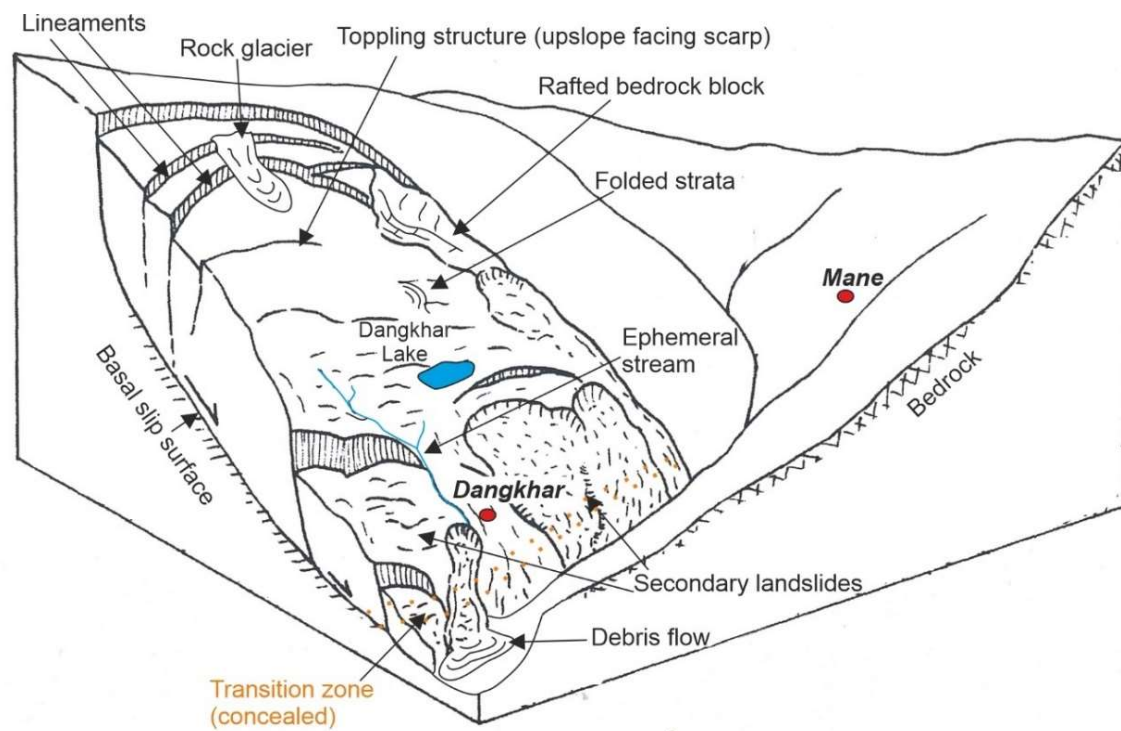


Fig. 5.1 Schematic Dangkhar Landslide block diagram with the identified characteristic features. General landslide layout modified after Dikau et al. (2006). Not to scale

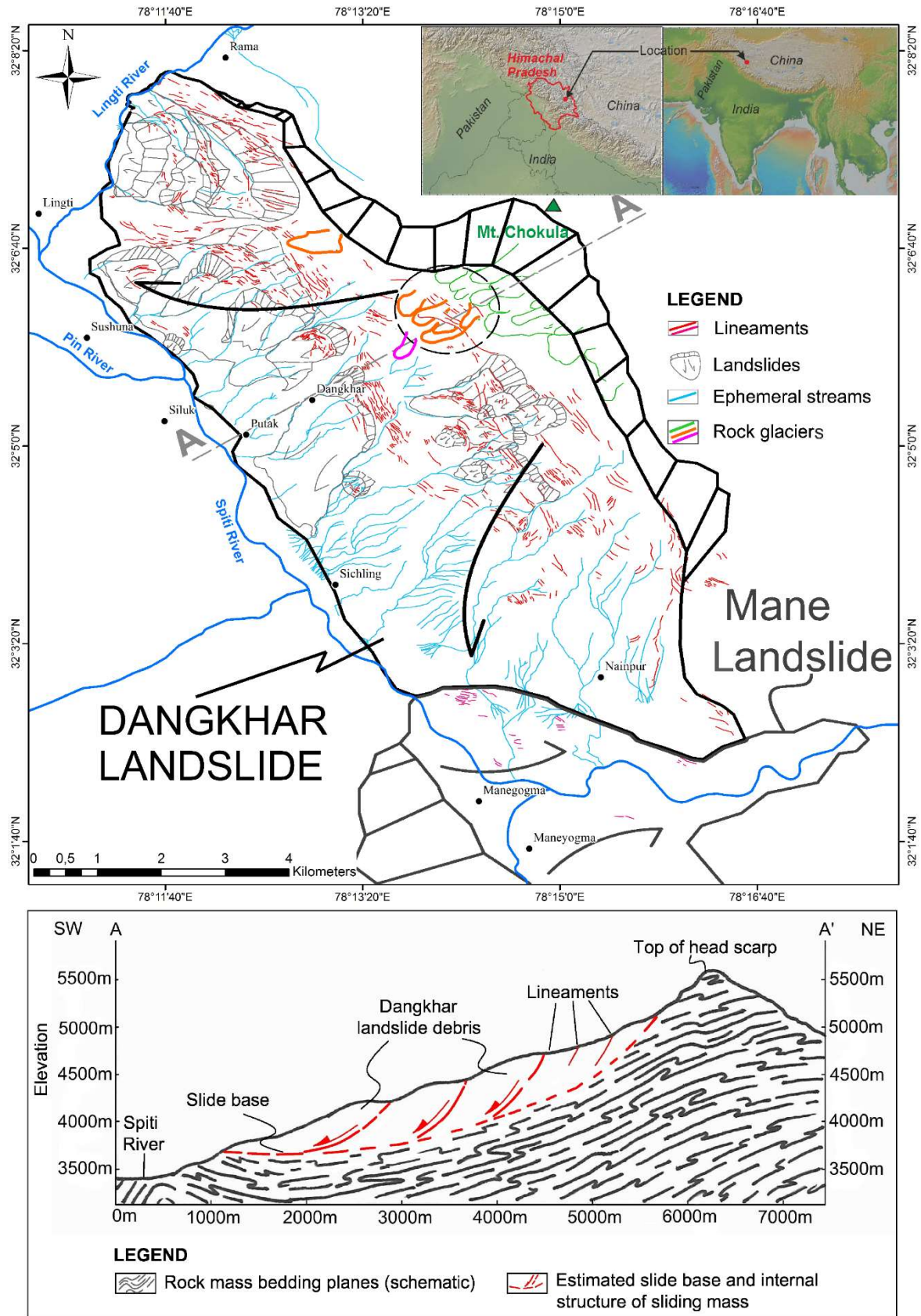


Fig. 5.2 The Dangkhhar Landslide (location map: GeoMapApp; Ryan et al. 2009)

Name	Dangkhar Landslide
Location	Spiti Valley (Himachal Pradesh), Indian Himalayas Centered around Dangkhar (32.09037° N, 78.21472° E)
Geological Environment	Tethys (Tibetan) Himalaya Sediments
Height (Toe to Crown)	2200 m
Elevation and exposure	(between 3400 – 5600 m a.s.l. towards southwest)
Areal Extent & Class by Area	Approximately 54 km ² (~40 km ² debris covered)
(after Korup 2006)	Large (affected area >1 km ²)
(after Stout 1991)	Mega-landslide (>2 to 175 km ²) – “Dragon-king” event
Volume & Class by Volume	15 – 20 km ³
(after Korup et al. 2007)	Giant (volume >0.1 km ³)
(after Weidinger and Korup 2009)	Extremely large (volume >2.5 km ³)
(after De Blasio 2011)	Regional (10 < volume <100 km ³) – “Monster landslide”
Type	
(after Varnes 1978)	Code: III Ag - (Sub-aerial) rotational rock slump, +V A - Bedrock flow (deep creep) = Slump-Rock Flow to Soil type slump
(after Hutchinson 1988)	C1, Rotational (R)-sagging (single sided) with deep-seated, continuous creep; mass creep.
(after Hungr et al. 2014)	Mountain slope deformation (Type 28); “Deep-seated landslide”
(after Varga 2006)	Pre-collapse gravitational deformation: dislocation type I – “deep-seated creep”
(after EPOCH, Dikau et al. 2006)	Rock flow (Sackung) to rotational slide (slump)
Current state of activity	
(after WP/WLI 1993)	Inactive: abandoned to relict
(after Clague 2015)	Prehistoric, Paleolandslide

Tab. 5.1 Dangkhar Landslide fact sheet

REFERENCES

- Aber JS, Ber A (2011) Glaciotectonic structures, landforms, and processes. In: Singh VP, Singh P, Haritashya UK. (eds) *Encyclopedia of Snow, Ice and Glaciers*, Springer, Dordrecht, pp 490–504
- Agliardi F, Crosta G, Zanchi A (2001) Structural constraints on deep-seated slope deformation kinematics. *Engineering Geology* 59:83–102
- Agliardi F, Crosta GB, Frattini P (2012) Slow rock-slope deformation. In: Clague JJ, Stead D (eds) *Landslides Types, Mechanisms and Modeling*, Cambridge University Press, Cambridge, pp 207–221
- Allègre CJ (2008) *Isotope Geology*. Cambridge University Press, Cambridge, 512p
- Ambrosi C, Crosta GB (2006) Large sackung along major tectonic features in the Central Italian Alps. *Eng Geol* 83:183–200
- Anoop A, Prasad S, Basavaiah N, Brauer A, Shahzad F, Deenadayalan K (2012) Tectonic versus climate influence on landscape evolution: A case study from the upper Spiti valley, NW Himalaya. *Geomorphology* 145–146:32–44
- ASTER GDEM (2011) Entity ID ASTGDEM_V2_0N32E078 and ASTGDEM_V2_0N31E078 (acquisition date October 17th, 2011); downloaded from US Geological Survey Earth Explorer: <https://earthexplorer.usgs.gov/>; ASTER GDEM is a product of NASA and METI
- Ballantyne CK (2002) Paraglacial geomorphology. *Quat Sci Rev* 21:1935–2017
- Ballantyne CK, Sandeman GF, Stone JO, Wilson P (2014) Rock-slope failure following Late Pleistocene deglaciation on tectonically stable mountainous terrain. *Quat Sci Rev* 86:144–157
- Balpande US, Singh B (2007) Ground water information booklet Lahaul and Spiti district Himachal Pradesh, Central Groundwater Board Northern Him Region, Dharamsala, GOI, MoWR, 24p
- Benn DI, Evans DJA (2010) *Glaciers and Glaciation*, 2nd edn. Taylor & Francis, London, 816p
- Bennett MM, Glasser NF (2009) *Glacial Geology: Ice Sheets and Landforms*, 2nd edn. John Wiley & Sons, New York, 400p

- Bhargava ON (1990) Holocene tectonics south of the Indus Suture, Lahaul-Ladakh Himalaya, India: a consequence of Indian Plate motion. *Tectonophysics* 174:315–320
- Bhargava ON (2008) An updated introduction to the Spiti geology. *J Pal Soc India*. 53(2):113–129
- Bhargava ON, Bassi UK (1998) Geology of Spiti Kinnaur Himachal Himalaya. *Geol Surv India Mem* 124:1–210
- Bhattacharyya A, Ranhotra PS, Shah SK (2006) Temporal and Spatial Variations of Late Pleistocene-Holocene Climate of the Western Himalaya based on Pollen Records and their Implications to Monsoon Dynamics. *J Geol Soc India* 68:507–515
- BMTPC (2003) Vulnerability atlas – 2nd edn. peer group, MoH & UPA; seismic zones of India. IS:1983-2002,BIS,GOI, Seismotectonic atlas of India and its environs, GSI, GOI
- Bonzanigo L, Oppizzi P, Tornaghi, Uggeri A (2006) Hydrodynamics and Rheology: Key Factors in Mechanisms of Large Landslides. *Proc ECI Conf in Geohazards, Lillehammer, Norway*, 46:1–15
- Bonzanigo L, Eberhardt E, Loew S (2007) Long-term investigation of a deep-seated creeping landslide in crystalline rock. Part I. Geological and hydromechanical factors controlling the Campo Vallemaggia landslide. *Canad Geotech J* 44:1157-1180
- Bookhagen B, Thiede RC, Strecker MR (2005) Late Quaternary intensified monsoon phases control landscape evolution in the northwest Himalaya. *Geology* 33:149–152
- Bourne S (1870) A photographic journey through the Higher Himalayas. *The British J of Photography*
- Broms BB, Wong KS (1991) Landslides. In: Fang HY (ed) *Foundation Engineering Handbook*, 2nd edn. Springer, New York, pp 410–446
- Catt JA (1988) *Quaternary Geology for Scientists and Engineers*, Wiley, Chichester, 340p
- Chauhan MS, Mazari RK, Rajagopalan G (2000) Vegetation and climate in upper Spiti region, Himachal Pradesh during late Holocene. *Current science* 79(3):373–377
- Cheng D, Cui Y, Su F, Jia Y, Choi CE (2018) The characteristics of the Mocoa compound disaster event, Colombia. *Landslides* 15(6):1223–1232
- Chigira M (1992) Long-term gravitational deformation of rocks by rock mass creep. *Eng Geol* 32:157–184

- Chowdhury RN (2000) Hazard of landsliding during earthquakes - critical overview of assessment methods. 12th World Conference on Earthquake Engineering, paper 1610:8p
- Church HK (1981) *Excavation Handbook*, McGraw-Hill, New York, 1024p
- Clague JJ (2015) Paleolandslides. In: Shroder JF, Davies T (eds) *Landslide Hazards, Risks, and Disasters - Hazards and Disasters Series*, 1st edn. Elsevier, Amsterdam, pp 321–344
- Craig H (1961) Isotopic variations in meteoric waters. *Science* 133:1702–1703
- Cruden DM, Varnes DJ (1996) Landslide types and processes. In: Turner AK, Schuster RL (eds) *Landslides Investigation and Mitigation*, Special Report 247. Transportation research board, US National Research Council, National Academy Press, Washington DC, pp-36–75
- Dansgaard W (1964) Stable isotopes in precipitation. *Tellus* 16(4):436–468
- De Blasio FV (2011) *Introduction to the Physics of Landslides*. Springer, Dordrecht, 408p
- Dewitte O, Demoulin A (2005) Morphometry and kinematics of landslides inferred from precise DTMs in West Belgium. *Nat Hazards Earth Syst Sci* 5:259–265
- Dèzes P, Vannay JC, Steck A, Bussy F, Cosca M (1999) Synorogenic extension: Quantitative constraints on the age and displacement of the Zaskar Shear Zone (NW Himalaya). *Geol Soc Amer Bull* 111:364–374
- Dickins AP (2005) *Radiogenic Isotope Geology*, 2nd edn. Cambridge University Press, Cambridge, 492p
- Diener CF (1896) Die Eiszeit im Himalaya. In: Jüttner JM (ed) *Mittheilungen kais. königl. Geogr Ges Wien* 39:1–35
- Diener CF (1912) The Trias of the Himalayas. *Geol Surv India Mem* 36:1–175
- Dietzel M, Tang, J, Leis A, Köhler SJ (2009) Oxygen isotopic fractionation during inorganic calcite precipitation — Effects of temperature, precipitation rate and pH. *Chem Geol* 268(1-2): 107–115
- DiPietro JA, Pogue, KR (2004) Tectonostratigraphic subdivisions of the Himalaya: A view from the west. *Tectonics* 23: TC5001
- Dobhal DP, Kumar S (1996) Inventory of Glacier Basins in Himachal Himalaya. *J Geol Soc India* 48:671–681

- Dortch JM, Owen LA, Haneberg WC, Caffee MW, Dietsch C, Kamp U (2009) Nature and timing of large landslides in the Himalaya and Transhimalaya of northern India. *Quat Sci Rev* 28:1037–1054
- Dortch JM, Owen LA, Caffee MW (2013) Timing and climatic drivers for glaciation across semi-arid western Himalayan–Tibetan orogen. *Quat Sci Rev* 78:188–208
- Draganits E (2000) The Muth Formation in the Pin Valley (Spiti, N. India): Depositional environment and ichnofauna of a lower Devonian barrier island system. PhD Thesis, University Vienna, 144p
- Draganits E, Grasemann B, Janda, C, Wiesmayr G (2004) Brief outline of the tectonic history of the NW Himalayas with emphasis on Spiti. *Albertiana* 30:11–20
- Dreimanis A (1989) Tills: their genetic terminology and classification. In: Goldthwait RP, Matsch CL (eds) *Genetic Classification of Glacigenic Deposits*, Balkema, Rotterdam, pp 17–84
- Duller GAT (2004) Dating methods. In: Gouldie AS (ed) *Encyclopedia of Geomorphology* Vol. 1, Routledge, London & New York, pp 221–224
- Eberhardt E, Bonzanigo L, Loew S (2007) Long-term investigation of a deep-seated creeping landslide in crystalline rock. Part II. Mitigation measures and numerical modelling of deep drainage at Campo Vallemaggia. *Canadian Geotech J* 44 (10):1181–1199
- Eberhardt E, Preisig G, Gischig V (2016) Progressive failure in deep-seated rockslides due to seasonal fluctuations in pore pressures and rock mass fatigue. *Landslides and Engineered Slopes. Experience, Theory and Practice*:121–136
- Egerton PH (1864) *Journal of a tour through Spiti to the Frontier of Chinese Thibet*. Cundall, Downes & Co, London, 68p
- Eugster P, Scherler D, Thiede RC, Codilean AT, Strecker MR (2016) Rapid Last Glacial Maximum deglaciation in the Indian Himalaya coeval with midlatitude glaciers: New insights from ¹⁰Be-dating of ice-polished bedrock surfaces in the Chandra Valley, NW Himalaya, *Geophys Res Lett* 43:1589–1597
- Flügel E (2010) *Microfacies of carbonate rocks – analysis, interpretation and application*, 2nd edn. Springer, Heidelberg, 984p
- Frenkel KA (2010) Panning for science. *Science* 5:748–749
- Fuchs G (1981) Outline of the geology of the Himalaya. *Mitt Österr Geol Ges* 74/75:101–127

- Fuchs G (1982) The geology of the Pin Valley in Spiti, H. P., India. *Jahrbuch der Geologischen Bundesanstalt Wien* 124:325–359
- Füchtbauer H Richter DK (1983) Relations between submarine fissures, internal breccias and mass flow during Triassic and earlier rifting periods. *Geol Rundsch* 72:53–66
- Gansser A (1964) *Geology of the Himalaya*. Interscience Publishers, Wiley & Sons. London, 289p
- Gerard A (1827) On the Valley of the Setlej River, in the Himalaya Mountains, from the Journal of Captain A. Gerard; with Remarks by Henry Thomas Colebrooke, Esq., Director R.A.S. *Trans Royal Asiatic Soc Great Britain and Ireland*, Vol 1(12):343–380
- Gerard JG (1833) Observations on the Spiti Valley and Circumjacent Country within the Himalaya. *Asiatic Researches Vol 28(2)*15, Bengal Military Orphan Press, Calcutta, pp 238–278.
- Girard M, Steck A, Thélin P (1999) The Dutung-Thaktote extensional fault zone and nappe structures documented by illite crystallinity and clay-mineral paragenesis in the Tethys Himalaya between Spiti river and Tso Morari, NW India. *Schweiz mineral petrogr Mitt* 79:419–430
- Gischig V, Eberhardt E, Moore JR, Hungr O (2015) On the seismic response of deep-seated rock slope instabilities— Insights from numerical modeling. *Eng Geol* 193:1–18
- Goodman RE, Shi G-H (1985) *Block Theory and its Application to Rock Engineering*, New Jersey: Prentice-Hall Inc, 338p
- Griesbach CL (1891) *Geology of the Central Himalayas*. *Geol Surv India Mem* 23:1–232
- Gruber S (2012) Derivation and analysis of a high-resolution estimate of global permafrost zonation. *The Cryosphere* 6:221–233
- GSI – Geological Survey of India (2011a) Active fault mapping of Spiti Valley Fault by micro-earthquake survey. *Case studies from GSI, Northern Region*, 40:4p
- GSI – Geological Survey of India (2011b) Rangrik landslide, Lahul-Spiti District, Himachal Pradesh. *Case studies from GSI, Northern Region*, 34:2p
- Gupta V, Sah MP (2008) Impact of the Trans-Himalayan Landslide Lake Outburst Flood (LLOF) in the Satluj catchment, Himachal Pradesh, India. *Nat Hazards* 45:379–390

- Hancox GT, Perrin ND (2009) Green Lake Landslide and other giant and very large postglacial landslides in Fiordland, New Zealand. *Quat Sci Rev* 28:1020–1036
- Harcourt AFP (1871) *The Himalayan districts of Kooloo, Lahoul, and Spiti*. WH Allen & Co, London, 381p
- Harvey A (2004) Badlands. In: Goudie A (ed) *Encyclopedia of Geomorphology Vol.2*, Routledge, London and New York, pp 45–47
- Hayden HH (1904) The geology of Spiti with parts of Bashahr and Rupshu. *Geol Surv India Mem* 36:1–121
- Hermann H, Bucksch H (2014) *Dictionary Geotechnical Engineering/Wörterbuch GeoTechnik (English - German/Englisch – Deutsch)*. Springer, Dordrecht, 1549p
- Hewitt K (2009) Glacially conditioned rock-slope failures and disturbance regime landscapes, Upper Indus Basin, northern Pakistan. In: Knight J, Harrison S (eds) *Periglacial and Paraglacial Processes and Environments*. *Geol Soc London Spec Pub* 320:23545–47255
- Hewitt K, Clague JJ, Orwin JF (2008) Legacies of catastrophic rock slope failures in mountain landscapes. *Earth Sci Rev* 87:1–38
- Hobbs WH (1904) Lineaments of the Atlantic border region: *GSA Bull* 15:483506
- Hobbs WH (1912) *Earth features and their meaning*: New York, Macmillan Co., 506p
- Hodges KV (2000) Tectonics of the Himalaya and southern Tibet from two perspectives. *Geol Soc Amer Bull* 112/3:32445–47350
- Horita J, Ueda A, Mizukami K, Takatori I (1989) Automatic dD and d¹⁸O analyses of multi-water samples using H₂- and CO₂-water equilibration methods with a common equilibration set-up. *Applied Radiation and Isotopes* 40:80145–47805
- Hornung T, Krystyn L, Brandner R (2007) Tethys-wide mid-Carnian (Upper Triassic) carbonate productivity decline: evidence for the Alpine Reingraben Event from Spiti (Indian Himalaya)? *J Asian Earth Sci* 30:28545–47302
- Hungr O, Corominas J, Eberhardt E (2005) Estimating landslide motion mechanism, travel distance and velocity. *Landslide risk management*, 99–128
- Hungr O, Leroueil S, Picarelli L (2014) The Varnes classification of landslide types, an update. *Landslides* 11:167–194

- Hutchinson JN (1988) General Report: Morphological and geotechnical parameters of landslides in relation to geology and hydrogeology. In: Bonnard C (Ed) Landslides – Glissements de terrain. Proceedings 5th International Symposium on Landslides, Lausanne, 1:3–35
- Hutchinson JN (2006) Massive rock slope failure: perspectives and retrospectives on state-of-the-art. In: Evans SG, Mugnozza GS, Strom A, Hermanns RL (eds) Landslides from Massive Rock Slope Failure, NATO Science Series IV-49 - Earth and Environmental Sciences, Springer, Dordrecht, pp 619–662
- IAEG (International Association Engineering Geology) Commission on Landslides (1990) Suggested nomenclature for landslides. Bull Int Ass Eng Geol 41:13–16
- IRIS – Incorporated Research Institutions for Seismology (2015) IRIS Earthquake Browser. www.iris.edu/ieb/
- ISRO– Indian Space Research Organisation (2011) Snow and Glaciers of the Himalayas. Space Applications Centre, Ahmedabad (India), 258p
- Iturrizaga L (1999) Typical debris accumulation forms and formations in High Asia – A glacial-history-based concept of the origin of Postglacial debris accumulation landscapes in subtropical high mountains with selected examples from the Hindu Kush, the Karakoram and the Himalayas. GeoJournal 47:277–339
- Jaboyedoff M, Crosta GB, Stead D (2011) Slope tectonics: a short introduction. In: Jaboyedoff M. (Ed.) Slope Tectonics. Geol Soc London Sp Pub 351:1–10
- Jaboyedoff M, Penna I, Pedrazzini A, Baroň I, Crosta GB (2013) An introductory review on gravitational-deformation induced structures, fabrics and modeling. Tectonophysics 605:1–12
- Jain SK, Roshan AD, Arlekar JN, Basu PC (2000) Empirical attenuation relationships for the Himalayan earthquakes based on Indian strong motion data. Proc 6th Int Conf Seism Zon, Palm Springs, California, 6p
- Jayabalan K, Chaubey RS, Rangari KD, Ilamkar PT (2015) An Overview of Glacio-Fluvial Lake Burst in the Upper Reaches of Kirgrang Nala (Yula Glacier), Pin Valley, District Spiti, Himachal Pradesh, India. In: Sayeed I, Khanna R (eds) Special Pub, J of Eng Geo (Ind Soc Eng Geol):478–492

- Kalderon-Asael B, Katz O, Aharonov E, Marco S (2008) Modeling the relation between area and volume of landslides. Report GSI/06/2008, Ministry National Infrastructures, Geol Surv Israel, 16p
- Kaspar M, Kieffer DS (2015) Preliminary Engineering Geological Characterization Of The ca. 20 km³ Dangkhari Landslide In The Spiti Valley, Himachal Pradesh, India. In: Lollino G, Giordan D, Crosta GB, Corominas J, Azzam R, Wasowski J, Sciarra N (eds) *Engineering Geology for Society and Territory* 2:891–894
- Kaspar M, Kieffer DS, Leis A (2019) The Dangkhari breccia: insights on the formation from remote, field and laboratory based investigations. In: *Mitt Österr Min Ges* 165:52
- Kieffer DS (1998) Rock slumping: A compound failure mode of jointed hard rock slopes. PhD thesis, University of California, Berkeley, CA, 183p
- Kieffer DS, Steinbauer C (2012) Geotechnical Remediation Strategies for the Ancient Monastery of Dangkhari Spiti Valley, Himachal Pradesh, India. Research and Restoration project, TU Graz, Annual report, 23p
- Kieffer DS, Kaspar M (2013) The Dangkhari landslide: a world class mega-event. *Geophys Res Abstr* 15 (EGU2013-9793, EGU General Assembly 2013)
- Korup O (2006) Effects of large deep-seated landslides on hillslope morphology, western Southern Alps, New Zealand. *J geophys research* 111:1–18
- Korup O, Strom AL, Weidinger JT (2006) Fluvial response to large rock-slope failures: examples from the Himalayas, the Tien Shan, and the Southern Alps in New Zealand. *Geomorphology* 78:3–21
- Korup O, Clague JJ, Hermanns RL, Hewitt K, Strom AL, Weidinger JT (2007) Giant landslides, topography, and erosion. *Earth Planet Sci Lett* 261:578–589
- Kottek M, Grieser J, Beck C, Rudolf B, Rubel F (2006) World Map of the Köppen-Geiger climate classification updated. *Meteorol Z* 15:259–263
- Krautblatter M, Funk D, Günzel FK (2013) Why permafrost rocks become unstable: a rock-ice-mechanical model in time and space. *Earth Surf Process Landforms* 38 (8):876–887
- Kuhle M (1990) The cold deserts of High Asia (Tibet and contiguous mountains). *GeoJournal* 20(3):319–323

- Kuhle M (2005) The maximum Ice Age (Würmian, Last Ice Age, LGM) glaciation of the Himalaya – a glaciogeomorphological investigation of glacier trim-lines, ice thicknesses and lowest former ice margin positions in the Mt. Everest–Makalu–Cho Oyu massifs (Khumbu and Khumbakarna Himal) including informations on late-glacial, neoglacial, and historical glacier stages, their snow-line depressions and ages. *GeoJournal* 62:193–650
- Lang A, Moya J, Corominas J, Schrott L, Dikau R (1999) Classic and new dating methods for assessing the temporal occurrence of mass movements. *Geomorphology* 30:33–52
- Libby WF, Anderson EC, Arnold JR (1949) Age determination by radiocarbon content: world-wide assay of natural radiocarbon. *Science* 109:227–228
- Lutgens FK, Tarbuck EJ, Tasa DG (2012) *Essentials of Geology*, 11th edn. Pearson Prentice Hall, New Jersey, 554p
- Marh BS, Rana VS (2014) *Cold Desert Geomorphology in the Trans-Himalayan Region: A Preliminary Analysis of Landforms of the Spiti River Valley*. Anamika Publishers & Distributors Ltd, New Delhi, 138p
- Mather AE, Griffiths JS, Stokes M (2003) Anatomy of a ‘fossil’ landslide from the Pleistocene of SE Spain. *Geomorphology* 20:135–149
- Mayewski PA, Jeschke PA (1979) Himalayan and Trans-Himalayan glacier fluctuations since AD 1812. *Arctic and Alpine Research* 11(3):267–287
- McCalpin JP (2013) Neotectonics. In: Bobrowsky PT (ed) *Encycl Nat Hazards*. Springer, Dordrecht, pp 730–732
- McColl ST (2012) Paraglacial rock-slope stability. *Geomorphology* 153–154:1–16
- McColl ST, Davis TRH (2013) Large ice-contact slope movements: glacial buttressing, deformation and erosion. *Earth Surf Process and Landforms* 38:1102–1115
- McMahon (1879) Notes of a tour through Hangrang and Spiti. *Rec Geol Surv India* 12:57–69
- Mitchell WA, Taylor PJ, Osmaston H (1999) Quaternary geology in Zaskar, NW Indian Himalaya: evidence for restricted glaciation and preglacial topography. *J Asian E Sci* 17:307–318
- Moorcroft W, Trebeck G (1841) *Travels in the Himalayan provinces of Hindustan, and the Panjab; in Ladakh and Kashmir; in Peshawar, Kabul, Kunduz, and Bokhara; from 1819 to 1825*. Asia Soc Calcutta, Vol 2:1–508

- Morrison J, Brockwell T, Merren T, Fourel F, Phillips AM (2001) On-line high-precision stable hydrogen isotopic analyses on nanoliter water samples. *Anal Chem* 73: 35703575
- Moser M (1996) The time-dependent behaviour of sagging of mountain slopes. In: Senneset (ed) *Proceedings 7th International Symposium on Landslides*, Balkema, Rotterdam, 2:809814
- Moser M, Amann F, Meier J, Weidner S (2017) *Tiefgreifende Hangdeformationen der Alpen: Erscheinungsformen – Kinematik – Maßnahmen*. Springer Spektrum, Wiesbaden, 290p
- Nemčok A, Pašek J, Rybář J (1972) Classification of Landslides and Other Mass Movements. *Rock Mechanics* 4:71–78
- Neumayer J, Wiesmayr G, Janda C, Grasemann B, Draganits E (2004) Eohimalayan fold and thrust belt in the NW-Himalaya (Lingti-Pin Valleys): Shortening and depth to detachment calculation. *Austrian J Earth Sci* 95-96:28–36
- Ni J, Barazangi M (1985) Active tectonics of the western Tethyan Himalaya above the underthrusting Indian plate: the upper Sutlej River Basin as a pull-apart structure. In: K. Kobayashi and I.S. Sacks (Eds) *Structures and Processes in Subduction Zones*. *Tectonophysics* 112:277-295
- Norton WH (1917) A Classification of Breccias. *J of Geol* 25(2):160–194
- NRSC (2013) *Inventory of glacial lakes and water bodies in Himalayas*, National Remote Sensing Centre, ISRO, Government of India, Hyderabad, India. Accessed through *Bhuvan* – Indian Geo-Platform of ISRO (Indian Space Research Organisation) <http://bhuvan.nrsc.gov.in/gis/thematic/index.php>
- NRSC (2016) *IRS LISS III satellite images (Tiles I44S04 and I44S08)*. National Remote Sensing Centre, ISRO, Government of India, Hyderabad, India. Accessed through *Bhuvan* – Indian Geo-Platform of ISRO (Indian Space Research Organisation) <http://bhuvan.nrsc.gov.in/data/download/index.php>
- Oldham RD (1888) Some notes on the geology of the NW Himalayas. *Rec Geol Surv India* 23:149–159
- O’Leary DW, Friedman JD, Pohn HA (1976) Lineament, linear, lineation: Some proposed new standards for old terms. *GSA Bulletin* 87(10): 463–1469

- Ostermann M, Sanders D, Prager C, Kramers J (2007) Aragonite and calcite cementation in “boulder-controlled” meteoric environments on the Fern Pass rockslide (Austria): implications for radiometric age dating of catastrophic mass movements. *Facies* 53:189–208
- Owen LA (1994) Glacial and non-glacial diamictos in the Karakorum Mountains and western Himalayas. In: Warren WP, Croot DG (eds) *Formation and deformation of glacial deposits*, Balkema, Rotterdam, pp 9–28
- Owen LA (2007) Late Quaternary in Highland Asia. In: Elias SA (ed) *Encyclopedia of Quaternary Science*, 1st edn. Elsevier, Amsterdam, pp 1109–1116
- Owen LA (2009) Latest Pleistocene and Holocene glacier fluctuations in the Himalaya and Tibet. *Quat Sci Rev* 28:2150–2164
- Owen LA (2014) Himalayan landscapes of India. In: Kale VS (ed) *Landscapes and Landforms of India*, 1st edn. Springer, Dordrecht, pp 41–52
- Owen LA, England J (1998) Observations on rock glaciers in the Himalayas and Karakoram Mountains of northern Pakistan and India. *Geomorphology* 26:199–213
- Owen LA, Benn DI (2005) Equilibrium-line altitudes of the Last Glacial Maximum for the Himalaya and Tibet: an assessment and evaluation of results. *Quat Int* 138/139:55–78
- Owen LA, Dortch JM (2014) Nature and timing of Quaternary glaciation in the Himalayan–Tibetan orogen. *Quat Sci Rev* 88:14–54
- Owen LA, Derbyshire E, Richardson S, Benn DI, Evans DJA, Mitchell WA (1996) The Quaternary glacial history of the Lahul Himalaya, northern India. *J Quat Sci* 11:25–42
- Owen LA, Mitchell WA, Bailey RM, Coxon P, Rhodes E (1997) Style and timing of Glaciation in the Lahul Himalaya, northern India: a framework for reconstructing late Quaternary paleoclimatic change in the western Himalayas. *J Quat Sci* 12:83–109
- Owen LA, Gualtieri L, Finkel RC, Caffee MW, Benn DI, Sharma MC (2001) Cosmogenic radionuclide dating of glacial landforms in the Lahul Himalaya, northern India: defining the timing of Late Quaternary glaciation. *J Quat Sci* 16:555–563
- Pánek T (2014) Recent progress in landslide dating A global overview. *Progr Phys Geogr* 39(2):168–198
- Pasek J (1974) Gravitational block-type slope movements. *Proceedings 2nd Int Cong Int Assoc Eng Geol*, São Paulo, Brazil

- Petley DN, Allison RJ (1997) The mechanics of deep-seated landslides. *Earth surface processes and landforms* 22:747–758
- Phartiyal B, Sharma A, Srivastava P, Ray Y (2009) Chronology of relict lake deposits in the Spiti River, NW Trans Himalaya: Implications of Late Pleistocene–Holocene climate tectonic perturbations. *Geomorphology* 108:264–272
- Pickering (1987) Wet-sediment deformation in the Upper Ordovician Point Leamington Formation: an active thrust-imbricate system during sedimentation, Notre Dame Bay, north-central Newfoundland. In: Jones ME, Preston RMF (eds) *Deformation of Sediments and Sedimentary Rocks*. Geol Soc Spec Pub 29, Blackwell Scientific Publications, Oxford, pp 204–239
- Pike RJ, Wilson SE (1971) Elevation–relief ratio, hypsometric integral and geomorphic area–altitude analysis. *Geol Soc Amer Bull* 82:1079–1084
- Qiao B, Yi C (2017) Reconstruction of Little Ice Age glacier area and equilibrium line attitudes in the central and western Himalaya. *Quat Int* 444:65–75
- Radbruch-Hall DH (1978) Gravitational creep of rock masses on slopes. In: Voight B (ed) *Rockslides and Avalanches, 1 Natural Phenomena*. Developments in Geotechnical Engineering 14(A), Elsevier, Rotterdam, pp 607–658
- Rawat S, Gupta AK, Sangode SJ, Srivastava P, Nainwal HC (2015) Late Pleistocene–Holocene vegetation and Indian summer monsoon record from the Lahaul, Northwest Himalaya, India. *Quat Sci Rev* 114:167–181
- Reimer PJ, Bard E, Bayliss A, Beck JW, Blackwell PG, Bronk Ramsey C, Buck CE, Cheng H, Edwards RL, Friedrich M, Grootes PM, Guilderson TP, Hafliðason H, Hajdas I, Hatté C, Heaton TJ, Hogg AG, Hughen KA, Kaiser KF, Kromer B, Manning SW, Niu M, Reimer RW, Richards DA, Scott EM, Southon JR, Turney CSM, van der Plicht J (2013) IntCal13 and MARINE13 radiocarbon age calibration curves 0–50000 years cal BP. *Radiocarbon* 55(4):1869–1887
- Roering JJ, Kirchner JW, Dietrich WE (2005) Characterizing structural and lithologic controls on deep-seated landsliding: Implications for topographic relief and landscape evolution in the Oregon Coast Range, USA. *Geol Soc Am Bull* 117:654–668
- Ryan WBF, Carbotte SM, Coplan JO, O'Hara S, Melkonian A, Arko R, Weissel RA, Ferrini V, Goodwillie A, Nitsche F, Bonczkowski J, Zemsky R (2009) Global Multi-Resolution Topography synthesis, *Geochem Geophys Geosyst* 10:Q03014

- Sabins FF (2007) Remote Sensing- Principles and Interpretation, 3rd edn. Waveland Press Inc., Longrove, 494p
- Saha S, Sharma MC, Murari MK, Owen LA, Caffee MW (2016) Geomorphology, sedimentology and minimum exposure ages of streamlined subglacial landforms in the NW Himalaya, India. *Boreas* 45:284–303
- Sanders D, Ostermann M, Brandner R, Prager C (2010) Meteoric lithification of catastrophic rockslide deposits: Diagenesis and significance. *Sedimentary Geology* 223:150–161
- Sathya (2016) Larsawe Pass / Manirang Pass - July to Aug 2016. <http://sathyastravels.blogspot.co.at/?view=classic>
- Scherler D, Bookhagen B, Strecker MR (2010) Timing and extent of late Quaternary glaciations in the western Himalaya constrained by ¹⁰Be moraine dating in Garhwal, India. *Quat Sci Rev* 29:815–831
- Sciunnach D, Garzanti E (2012) Subsidence history of the Tethys Himalaya. *Earth-Sci Rev* 111: 179–198
- SEEDS (2009) Vulnerability Atlas of Himachal Pradesh. 15/A Institutional Area, R.K.Puram, Sector IV, New Delhi-110022. www.seedsindia.org
- Shang Y, Yang Z, Li L, Liu D, Liao Q, Wang Y (2003) A super-large landslide in Tibet in 2000: background, occurrence, disaster, and origin. *Geomorphology* 54:225–243
- Shi Y (1992) Glaciers and glacial geomorphology in China. In: Stäblein G, French HM, Marcus MG (eds.) *Geomorphology and Geoecology: Glacial and Polar Geomorphology. Proceedings of the Second International Conference on Geomorphology: Geomorphology and Geoecology, Frankfurt/Main 1989 / Vol VIII. Zeitsch f Geom, Suppl Issue* 86:51–63
- Singh RP, Aman A, Prasad YJJ (1996) Attenuation relations for strong seismic ground motion in the Himalayan region. *PAGEOPH* 147(1): 161–180
- Singhvi AK, Krishnan R (2014) Past and the Present Climate of India. In: Kale VS (ed) *Landscapes and Landforms of India*, 1st edn. Springer, Dordrecht, pp 15–23
- Skempton AW, Hutchinson JN (1969) Stability of Natural Slopes and Embankment Foundations. *Proceedings 7th International Conference on Soil Mechanics and Foundation Engineering, Mexico City, State-of-the Art Volume*, pp 291–340

- Slaymaker O (2004) Paraglacial. In: Goudie AS (ed) *Encyclopedia of Geomorphology Vol.2*. Routledge, London and New York, pp 759–762
- Slaymaker O (2009) Proglacial, periglacial or Paraglacial? In: Knight J, Harrison S (eds) *Periglacial and Paraglacial Processes and Environments*. Geol Soc London Spec Pub 320:71–84
- Soldati M (2013) Deep-Seated Gravitational Slope Deformation. In: Bobrowsky PT (ed) *Encycl Nat Hazards*. Springer, Dordrecht, pp 151–155
- Sowers GE, Royster DL (1978) Field Investigation. In Schuster RL, Krizek RJ (eds) *Landslides: Analysis and Control*, special report 176. Transportation Research Board, National Academy of Sciences, Washington DC, pp 81–111
- Srivastava P, Ray Y, Phartiyal B, Sharma A (2013) Late Pleistocene-Holocene morphosedimentary architecture, Spiti River, arid higher Himalaya. *Int J Earth Sci (Geol Rundsch)* 102:1967–1984
- Stead D, Eberhardt E (2013) Understanding the mechanics of large landslides. *Ital J Eng Geol and Environ - Book Series* 6:85–108
- Steck A (2003) Geology of the NW Indian Himalaya. *Eclogae geol Helv* 96:147–196
- Stenström KE, Skog G, Georgiadou E, Genberg J, Johansson A (2011) A guide to radiocarbon units and calculations. Lund University internal Report LUNFD6(NFFR-3111)/1-17/(2011)
- Stini J (1941) Unsere Täler wachsen zu. *Geologie und Bauwesen* 13:71–79
- Stock GM, Bawden GW, Green JK, Hanson E, Downing G, Collins BD, Bond S, Leslar M (2011) High-resolution three-dimensional imaging and analysis of rock falls in Yosemite Valley, California. *Geosphere* 7(2):573–581
- Stoliczka F (1866) Geological section across the Himalayan Mountains, from Wangtu bridge on the River Sutlej to Sungdo on the Indus: with an account of the formations of Spiti, accompanied by a revision of all known fossils from that district. *Geol Surv India Mem* 5:1–154
- Stout ML (1991) Mega-landslides: Fact or Fiction? *Geol Soc Am Abstracts with Programs* 23(5): A 125, No 23485, San Diego
- Strahler AH (1952) Hypsometric (area-altitude) analysis of erosional topography. *Geol Soc Am Bull* 63(11):1117–1142

- Taylor PJ, Mitchell WA (2000) Late Quaternary glacial history of the Zaskar Range, North-west Indian Himalaya. *Quat Int* 65/66:81–99
- Theobald W (1862) Notes on a trip from Shimla to the Spiti Valley and Chomoriri (Tshomoriri) Lake during the months of July, August and September 1861. *J Asiat Soc Beng*, Vol 31:480–527
- Thomson T (1852) *Western Himalaya and Tibet: A Narrative of a Journey through the Mountains of Northern India, during the Years 1847-8*. Reeve and Co, London, 550p
- Thöni M, Miller C, Hager C, Grasemann B, Horschinegg M (2012) New geochronological constraints on the thermal and exhumation history of the Lesser and Higher Himalayan Crystalline Units in the Kullu–Kinnaur area of Himachal Pradesh (India). *J Asian Earth Sci* 52:98–116
- Times of India (2018) People worry for crops as landslides hit Lahaul-Spiti. *Times of India*, Aug 13 (online edition)
- Tucker ME (2001) *Sedimentary Petrology: An Introduction to the Origin of Sedimentary Rocks*, 3rd edn. Blackwell Science, Oxford, 272p
- Vallet A, Varron D, Bertrand C, Mudry J (2015) Hydrogeological threshold using support vector machines and effective rainfall applied to a deep seated unstable slope (Séchilienne, French Alps). In: Lollino G, Giordan D, Crosta GB, Corominas J, Azzam R, Wasowski J, Sciarra N (eds) *Engineering Geology for Society and Territory 2*:2143–2146
- Von Krafft A (1899) Stratigraphical notes on the Mesozoic rocks of Spiti. In: Griesbach CL (ed) *General report on the work carried on by the Geological Survey of India for the period from the 1st April 1898 to the 31st March 1899*. Calcutta, pp 199–229
- Varga AA (2006) Gravitational creep of rock slopes as pre-collapse deformation and some problems in its modelling. In: Evans SG, Mugnozsa GS, Strom A, Hermanns RL (eds) *Landslides from Massive Rock Slope Failure*, NATO Science Series IV- Earth and Environmental Sciences 49, Springer, Dordrecht, pp 103–110
- Varnes DJ (1978) Slope movement types and processes. In Schuster RL, Krizek RJ (eds) *Landslides: Analysis and Control*, special report 176. Transportation Research Board, National Academy of Sciences, Washington DC, pp 11–33
- Verma V (1997) *Spiti: A Buddhist land in Western Himalaya*. BR Publishing Corporation, 176p

- Weidinger JT, Korup O (2009) Frictionite as evidence for a large Late Quaternary rockslide near Kanchenjunga, Sikkim Himalayas, India — Implications for extreme events in mountain relief destruction. *Geomorphology* 103:57–65
- Weiflog M, Thuro K, Zangerl C (2010) Analysis of a large deep-seated creeping mass movement using GIS and DEM. In: Williams AL, Pinches GM, Chin CY, McMorran, Massey CJ (Eds.) *Geologically Active: Proceedings 11th IAEG Congress*. Auckland, New Zealand, 2571–2578
- Wiesmayr G, Grasemann B (2002) The Eohimalayan fold-thrust belt: implications for the geodynamic evolution of the NW-Himalaya (India). *Tectonics* 21(6):1058
- Willerich S, Thuro K, Mair V (2009) Integration of large deep-seated, creeping mass movements in a regional hazard map - an approach to determinate it's probability of occurrence. *Austr J Earth Sci* 102/2:61–68
- Wilson A (1875) *The Abode of Snow: Observations on a journey from Chinese Tibet to the Indian Caucasus through the upper valleys of the Himlaya*. Blackwood & Sons, Edinburgh & London, 475p
- WP/WLI (1990) – International Geotechnical Societies' UNESCO Working Party on World Landslide Inventory: A suggested method for reporting a landslide. *Bull Int Assoc Eng Geol* 41:5–12
- WP/WLI (1993) – International Geotechnical Societies' UNESCO Working Party on World Landslide Inventory: A suggested method for describing the activity of a landslide. *Bull Int Assoc Eng Geol* 47:53–57
- Wyss M, Hermann J, Steck A (1999) Structural and metamorphic evolution of the northern Himachal Himalaya, NW India (Spiti – eastern Lahul-Parvati valley traverse). *Eclogae geol Helv* 92:3–44
- Yadav RR, Braeunig A, Singh J (2011) Tree ring inferred summer temperature variations over the last millennium in western Himalaya, India. *Clim Dyn* 36:1545–1554
- Yin A (2006) Cenozoic tectonic evolution of the Himalayan orogen as constrained by along-strike variation of structural geometry, exhumation history, and foreland sedimentation. *Earth Sci Rev* 76: 1–131
- Yao T, Thompson L, Yang W, Yu W, Gao Y, Guo X, Yang X, Duan K, Zhao H, Xu B, Pu J, Lu A, Xiang Y, Kattel DB, Joswiak D (2012) Different glacier status with atmospheric circulations in Tibetan Plateau and surroundings. *Nature Climate Change* 2:663–667

Zischinsky U (1966) On the deformation of high slopes. Proceedings 1st Conf Int Soc Rock Mechanics 2:179–185

Zischinsky U (1968) Über Bergzerreiung und Talzuschub. Geol Rundsch 58(2):974–983

Software

3DEM – Version 20.7, Programming by Visualization Software LLC, Richard Horne

AutoCAD 2016 – Version M.49.0.0, Autodesk, Inc

Bing Maps 3D – Version 4.0, Microsoft Corporation

CorelDRAW 2019 – Version 21.1.0.643, Corel Corporation

ESRI (2013) ArcGIS Desktop: Release 10.2.1. Redlands, CA: Environmental Systems Research Institute

Google Earth Pro – Version 7.3.2.5776 (64-bit), Google LLC

Grapher 8 – Version 8.4.696, Golden Software, Inc.

Keyblock programs B02, B03 – Goodman and Shi (1989) modified by Liu (2004)

MicroDEM (2016) PETMAR Trilobite Breeding Ranch, Version 2016.4.28.199 by Peter Guth; Oceanography Department, US Naval Academy

Rocscience (2018) Dips 7.0 Graphical and statistical analysis of orientation data. Version 7.013. Rocscience Inc. Toronto

APPENDIX

Table of Contents

Appendix A – Methods.....	1
A.1 Lineament and landform mapping	1
A.2 Digital elevation model analysis	1
A.3 Gigapixel panoramic photography	2
A.4 Field mapping and sampling	2
A.5 Mineralogical and stable isotope analyses of solids.....	3
A.6 Stable isotopes analyses of water	4
A.7 Radiocarbon dating (¹⁴ C-Dating) – Method and theoretical background	6
Appendix B – Gigapixel photography.....	10
B.1 GigaPan panoramas access.....	10
B.2 GigaPan Image Log.....	11
Appendix C – Orientation data of lineaments	16
C.1 Azimuth data of the lineaments of the Dangkhar Landslide	16
C.2 Azimuth data of the lineaments of the Mane Landslide	17
Appendix D – Radiocarbon calibration curves.....	19
Appendix E – Hypsometry of the Dangkhar hillslope	25
E.1 Hypsometric curve	25
Appendix F – Geologic map	27
F.1 Geologic map units.....	27
F.2 Geologic map of the Dangkhar Landslide	27
F.3 Geologic cross sections	28
F.4 – 3D geologic map views of the study area.....	33
Appendix G – Geomorphologic map.....	36
G.1 Geomorphologic map of the Dangkhar Landslide.....	36

APPENDIX A – Methods

Appendix A – Methods

A.1 Lineament and landform mapping

In order to cover the entire area on a high level of details and due to the large nature of some lineaments and landform features, mapping was performed on high resolution satellite images. A morphometric, factual map of the site is obtained from this procedure. Lineaments are an expression of the subsurface structure in the ground (Hobbs 1904, 1912). They are mappable elements exhibiting a curvilinear or straight pattern expressing zones of weakness indicative of a subsurface phenomenon (O’Leary et al. 1976). Lineaments can be geomorphic or tonal. Tonal lineaments are caused by contrast differences (e.g. due to vegetation, different soil and rock compositions) whereas geomorphic lineaments are produced by relief forming processes such as incising streams (O’Leary et al 1976; Sabins 2007). In the context of mass movements, lineaments are an indicator for the presence of a large-scale, gravitationally driven landslide. They might resemble tectonic features, but are usually less persistent, are sharper defined and occur as sets of several adjacent scarps (e.g. Agliardi et al. 2012).

For the present study, high resolution images from the DigitalGlobe and GeoEye satellites accessible through Google Earth Pro and Bing maps were used to map out lineaments and landforms occurring within the study area by visual interpretation. The used satellite images provide a ground resolution of up to 1.65 m. Lineaments were drawn as *AutoCAD* layer on the imported satellite images. The *AutoCAD* layer was then imported as a vector drawing into a geographical information system (*ArcGIS 10.1; ESRI 2013*) in order to extract and export the azimuth data. The exported azimuth data were plotted as rose diagrams using *Dips 7.0* (Rocscience 2018). Other identified and mapped landforms include glacial moraine deposits, rock glaciers, and ephemeral stream network channels. Finally, the individual maps produced during the during field season and during remote sensing evaluation were merged in a single comprehensive map.

A.2 Digital elevation model analysis

The ASTER GDEM (*Advanced Spaceborne Thermal Emission and Reflection Radiometer Global Digital Elevation Model*; ASTER GDEM is a product of NASA and METI) dataset accessible through the US Geological Survey Earth Explorer was used to create a digital elevation model (DEM) and to produce a topographic base map of the study area. The base map was produced with 20 meter contour intervals in *ArcGIS 10*. DEM scenes are being delivered in a *Geographic Tagged Image File Format* (GeoTIFF) with geographic coordinates referenced to the 1984 World Geodetic System (WGS 84). The ASTER GDEM GeoTIFFs with entity IDs ASTGDEM2_0N32E078 and ASTGDEM2_0N31E078 (both acquisition date October 17th, 2011) covering the study area and neighboring regions were used. The DEM was used to produce derivative maps such as shaded relief (hillshade) maps, slope orientation maps, and slope inclination maps to visualize important geomorphic features such as scarps, large

scale lineaments, and to depict prominent slope angle changes. However, due to the resolution of the DEM only those landforms being an order of magnitude larger than the cell size (i.e. 300 m or larger) can be identified reliably (Adams et al. 2009). The generated maps and terrain models were combined with the satellite images using 3D visualization software to efficiently identify large-scale landforms. Programs used to process and visualize the DEM data include MicroDEM (by Peter Guth; Oceanography Department, US Naval Academy), 3DEM and ArcGIS 10.1.

A hypsometric analysis is performed reflecting the area-altitude relationship of the study area and to depict its geomorphic units and characteristics. The hypsometric integral (H_i) was determined (Pike and Wilson 1971) and serves as indicator for the maturity stages of the landscape (Strahler 1952). Traditionally three stages exist for the H_i , i. e. young (H_i greater than 0.6), mature (H_i between 0.35 and 0.60), and old (H_i less than 0.35).

A.3 Gigapixel panoramic photography

Gigapixel panoramic photography enables the creation of images achieving a resolution far higher than conventional photography (Stock et al. 2011). It uses hundreds or even thousands of single images that are merged and stitched together based on their content resulting in one single ultra-high resolution digital image (Frenkel 2010). The resolution of such images usually falls in the gigapixel range, i. e. images with a resolution of more than one billion pixels or 1000 megapixels.

The acquisition of these pictures is performed with a camera mounted on a robotic head scanning a predefined scene. The GigaPan EPIC Pro system together with a Panasonic Lumix DMC-FZ200 bridge camera was used in this study. The camera is equipped with a fixed Leica lens having a full frame equivalent focusing range of 25 to 600 mm. Each picture taken by camera was saved both, as .RAW and .jpg format at the camera's maximum resolution of 12 megapixels.

The camera settings for the .jpg images are: Contrast 0, Saturation 0, Sharpness +1, and Noise Reduction (NR) -1. For the final stitching of the panoramas the Kolor Autopano software and Adobe Photoshop were used. The final panoramas were uploaded to the GigaPan website for permanent access. The Gigapixel panoramas enable the researcher to virtually and interactively re-visit the study area after being to the site. This permanent digital archive of ultra-high resolution images allows a later evaluation of certain features and enables illustrating the area of interest to others, who have not been to the site.

A.4 Field mapping and sampling

Field work involved two trips to the study area in the summers of 2012 and 2015 with a total mapping activity of 3 months. Geologic and geomorphic mapping was performed on the generated topographic base map at a scale of 1:15.000. Local names of villages, peaks and places were added and/or updated based on comments by locals, since publicly available map services (Google maps, Bing maps) provide misplaced or incorrect locality names in certain places.

Communications with the local inhabitants also helped in gaining information about recent events such as landslides. The geomorphic mapping was performed broadly following the traverse method and boundary method of Catt (1988). It involves recording location and extent of landforms by walking parallel traverses and connecting characteristic breaks in slope, but also delineating boundaries of landforms across the slope, respectively. Lineaments, breaks in slope, closed depressions, locations of springs and ephemeral streams were documented as well as glacial, and glacio-fluvial landforms. The resultant geologic and geomorphic reconnaissance maps and interpretive geologic cross sections aimed to confirm and calibrate the photointerpretive mapping, to assess the specific geologic and geomorphic details and to identify key locations for retrieving samples for laboratory testing. Orientations of strata and landforms were recorded using a geologic compass or estimated where inaccessible. Rock samples were excavated using a chisel and a geologic hammer. The locations of samples and other observation points (e.g. GigaPan camera positions) were recorded using a handheld Garmin GPSmap 62s. Retrieving of wood samples for radiocarbon dating purposes was done by drilling into sediments using a manually operated soil auger (Veekay Industries, New Delhi) having an auger head of 150 mm and 100 mm and nine meters of extension rods. The samples were visually inspected for organic material (e.g. wood fragments or leaves) after every drilling interval, which was approximately 30 cm, and stored in sealed plastic bags. The depth of the retrieved samples was determined using a tape measure.

A.5 Mineralogical and stable isotope analyses of solids

Bulk and clay mineralogical analysis of rock and soil samples was done by X-ray powder diffraction (XRD) at the Institute of Applied Geosciences, Graz University of Technology. The samples comprise hard rock samples of bedrock and breccia, and soft soil material such as lake sediments and debris. Bulk mineral compositions were determined using a PANalytical X'Pert PRO diffractometer (Co K α radiation 40 kV and 40 mA; scan range: 4 - 85 °2 θ ; step size: 0.02 °2 θ ; time/step: 20 s). Semi-quantitative mineral analysis was done by comparing the measurements to reference mixtures of known composition.

Clay mineral compositions were determined using a Philips PW 1830 diffractometer (Cu K α radiation 40 kV and 30 mA; scan range 2.5 – 15° 2 θ ; step size: 0.01 °2 θ , time/step 2 s). Each sample is washed in deionized water under permanent shaking and exposed to ultrasonic treatment. After wet sieving of the fraction <63 μ m, the clay fraction (<2 μ m) is obtained by Atterberg separation from the suspension. The suspension containing the clay fraction is then divided into three parts to produce texturized samples. Two parts of a sample are treated with ion-exchange reactions (i.e. potassium and magnesium). The third one is left untreated. The texturized samples are prepared by vacuum-suction of the suspension onto ceramic plates. Expansion on the sample with potassium ion-exchange is induced by storing it in dimethylsulfoxid for 1 hour at 80°C and overnight at 40°C. Expansion on the sample with magnesium ion-exchange is induced by storing it in glycerin for three days.

Grainsize distributions of the clay and silt fraction were determined using a Micrometrics Sedigraph III Particle Size Analyzer. The sieved and dried material <63 μm is treated with a 0.04 mol tetrasodium pyrophosphate (TSPP) solution acting as a dispersive agent. The suspension is shaken for 12 hours and treated in an ultrasonic bath for three minutes prior to the measurement in the Sedigraph.

For thin sections samples were cut into a block of approximately 2 cm x 2 cm x 4 cm, glued on a glass plate, cut and polished to a thickness of about 40 μm for inspection under a transmitted light microscope (Leica DM LMP) and cathodoluminescence (CL) microscope. After inspection under the optical microscope, the polished thin sections are sputtered with carbon for the CL analysis. With the aid of CL images, a cement stratigraphy can be established, distinguishing between several phases of grain growth (Tucker 2001; Flügel 2010).

Stable carbon ($^{13}\text{C}/^{12}\text{C}$) isotope and oxygen ($^{18}\text{O}/^{16}\text{O}$) isotope ratios of the carbonate rocks were analyzed using a fully automated peripheral continuous-flow gas preparation device (Gasbench II) connected to a Finnigan DELTA plus XP Mass Spectrometer (Dietzel et al. 2009). The ratios of the stable carbon and oxygen isotopes are given as $\delta^{13}\text{C}$ and $\delta^{18}\text{O}$ values in ‰ relative to the Vienna Pee Dee Belemnite standard (VPDB) (Eq.A.1 and Eq.A.2).

Eq. A.1:

$$\delta^{13}\text{C} [\text{‰}] = \left[\frac{\left(\frac{^{13}\text{C}}{^{12}\text{C}} \right)_{\text{Sample}}}{\left(\frac{^{13}\text{C}}{^{12}\text{C}} \right)_{\text{VPDB}}} - 1 \right] * 1000$$

Eq. A.2:

$$\delta^{18}\text{O} [\text{‰}] = \left[\frac{\left(\frac{^{18}\text{O}}{^{16}\text{O}} \right)_{\text{Sample}}}{\left(\frac{^{18}\text{O}}{^{16}\text{O}} \right)_{\text{VPDB}}} - 1 \right] * 1000$$

A.6 Stable isotopes analyses of water

Water was sampled from nine different springs and seeps occurring within the study area. Essentially no rainfall events occurred during the field campaign, so the sampled waters are assumed to represent the average summertime groundwater composition. The samples were stored in sealed plastic vials. The stable hydrogen ($^2\text{H}/^1\text{H}$) and oxygen ($^{18}\text{O}/^{16}\text{O}$) isotope ratios of the water samples were analyzed at the Joanneum Research Center (Institute of Water Resources Management, Hydrogeology and Geophysics) in Graz. The measurements were performed on a Finnigan DELTA plus XP mass spectrometer. Continuous flow mode by chromium reduction technique (Morrison et al. 2001) was used for measuring the hydrogen isotopes. The oxygen isotopes were measured using the $\text{CO}_2\text{-H}_2\text{O}$ equilibrium method (Horita et al. 1989). The ratios of the isotope measurements are reported as $\delta^{18}\text{O}$

and $\delta^2\text{H}$ in permil [‰] relative to the Vienna Standard Mean Ocean Water (VSMOW) (Eq.A.3 and A.4). The achieved precision of the isotopic measurements is better than ± 0.1 ‰ for $\delta^{18}\text{O}$ and ± 1 ‰ for $\delta^2\text{H}$.

Eq. A.3:

$$\delta^{18}\text{O} [\text{‰}] = \left[\frac{\left(\frac{^{18}\text{O}}{^{16}\text{O}}\right)_{\text{Sample}}}{\left(\frac{^{18}\text{O}}{^{16}\text{O}}\right)_{\text{VSMOW}}} - 1 \right] * 1000$$

Eq. A.4:

$$\delta^2\text{H} [\text{‰}] = \left[\frac{\left(\frac{^2\text{H}}{^1\text{H}}\right)_{\text{Sample}}}{\left(\frac{^2\text{H}}{^1\text{H}}\right)_{\text{VSMOW}}} - 1 \right] * 1000$$

From the $\delta^{18}\text{O}$ and $\delta^2\text{H}$ isotope values the local meteoric water line (LMWL) is constructed by linear-regression analysis. The ratio between those two was first described by Craig (1961) as the Global Meteoric Water Line (GMWL; Fig. A.1) and is expressed by equation A.5. The deuterium excess (d-excess) determination after Dansgaard (1964) (Eq.A.6) was applied to the samples and serves as an index for the deviation from the GMWL.

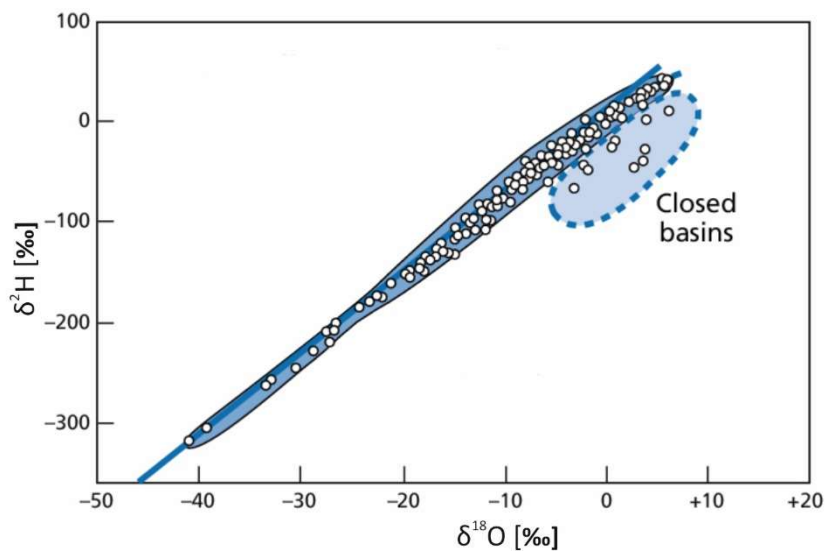


Fig. A.1 Global Meteoric Water Line (modified after Craig 1961 in Allègre 2008)

Eq. A.5:

$$\delta^2\text{H} = 8 \delta^{18}\text{O} + 10 \text{‰ VSMOW}$$

Eq. A.6:

$$d = \delta^2\text{H} - 8 \delta^{18}\text{O}$$

where: d = deuterium excess [‰]

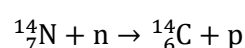
Trends and evolution of waters can be deduced from their isotope composition. Air masses originating from the source area (i.e. ocean water) gradually become lighter as a result of kinetic and equilibrium processes. During evaporation from the ocean, during rainout as they travel land inwards (continental effect), and with increasing altitude (altitude effect) the remaining water vapor becomes more depleted (i.e. enriched in lighter isotopes). Hydrogen becomes more fractionated by a factor of eight than oxygen due to its lighter atomic weight. Plotting isotope ratios of an area against the GMWL can serve as an index for the origin and evolution of the waters in the study area.

A.7 Radiocarbon dating (¹⁴C-Dating) – Method and theoretical background

Five samples were analyzed by the Beta Analytic Inc. laboratory using an AMS (Atomic Mass Spectrometer). It allows the analysis of very small samples with final carbon of 300 to 100 micrograms. The precision of the measurement compared to conventional techniques such as gas proportional counting or liquid scintillation counting is not decreased by the small amount of material analyzed. Analyses are performed on solid graphite samples after preparation via catalytic CO₂ reduction. The samples were retrieved from boreholes that were drilled using a manually operated soil auger with a 150 mm and 100 mm head and extendable rods allowing drilling up to a depth of six meters. Every soil sample retrieved from the auger head was carefully inspected for organic materials (leaves, wood fragments, roots, etc.) suitable for ¹⁴C-dating. The retrieved organic samples were stored in a plastic box. Due to the high elevation, dry climate and little soil development, the study area exhibits only scarce vegetation and organic material is restricted to small fragments of less than one centimeter in size. The provided pMC (percent Modern Carbon) values for young radiocarbon ages were correlated using the IntCal13 calibration curves for Northern Hemisphere Zone 2 (Reimer et al. 2013). Plotting the obtained F¹⁴C values against calendar years (cal AD), results in a graph indicating the age range in which the sample falls together with a probability of one and two sigma to be of a certain age.

Carbon exists as three different isotopes in nature. The most abundant one ¹²C accounts for 99.89 % of the earth's carbon, followed by ¹³C with 1.11 %. These two are stable, non-radioactive isotopes. The third one, ¹⁴C makes up only 0.0000000010 % or 1.18 x 10⁻¹² atoms per ¹²C atom (Allègre 2008). It is produced in the upper atmosphere by the bombardment of neutrons from cosmic rays on nitrogen ¹⁴N (Fig. A.2a). By capturing a neutron (n) and emitting a proton (p), the ¹⁴N turns into ¹⁴C (Eq. A.7) as the atomic number of nitrogen decreases (Dickins 2005; Allègre 2008; Lutgens et al. 2012).

Eq. A.7 (Dickins 2005):



Carbon is oxidized to CO₂ and absorbed by plants through photosynthesis and incorporated by animals and humans via food intake (Dickins 2005). During the lifetime of an organism the decay of ¹⁴C is compensated by fresh uptake. After the death of an organism the ratio of ¹²C to ¹⁴C changes and the concentration of ¹⁴C decreases by radioactive β-decay (Fig. A.2b) with a half-life time of 5,730±40 years (Duller 2004). The decay of carbon can be expressed by the general radioactive decay law (Eq. A.8 and A.9).

Eq. A.8:

$$A = A_0 e^{-\lambda t}$$

Where: t = Time

λ = decay constant

A = ratio of isotopes measured in sample

A₀ = Equilibrium radiation at beginning

Applying the formula of Eq.A.8 to ¹⁴C results in:

Eq. A.9:

$$(^{14}\text{C}/^{12}\text{C}) = 13.5e^{-\lambda t}$$

transformed to time gives:

$$t = \frac{1}{\lambda} \ln \left[\frac{13.5}{(^{14}\text{C}/^{12}\text{C}) \text{ sample}} \right]$$

Where: t = Time

λ = decay constant (1.209x10⁻⁴ yr⁻¹)

¹⁴C/¹²C = ratio of isotopes measured in dpm

13.5 = Steady state production of ¹⁴C in atmosphere (dpm)

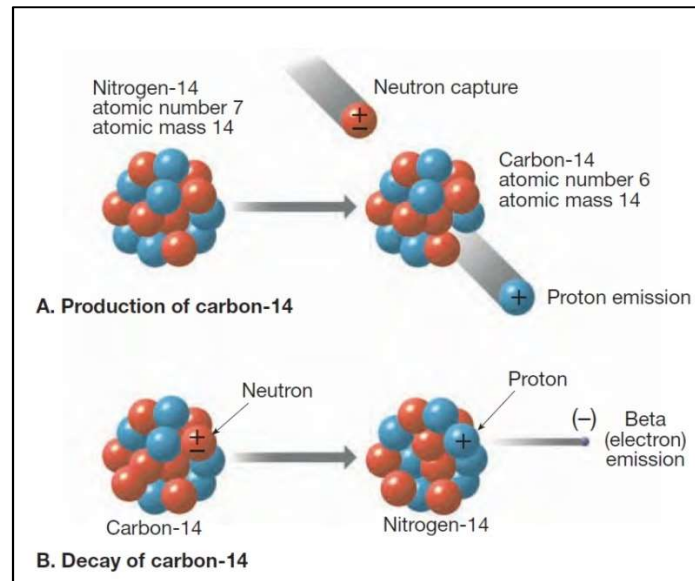


Fig. A.2 Production (A) and decay (B) of ^{14}C (after Lutgens et al. 2012)

This principle is used in radiocarbon dating where the ratio of the two carbon isotopes is measured and the age is determined by comparing it to standards. There is a steady state production of ^{14}C in the atmosphere and it is expressed in disintegrations per minute (dpm) per gram of carbon. In modern wood the production rate is 13.5 dpm/g (Libby et al. 1949). For young samples from the time of industrial revolution and post-bomb period, results are usually provided as percent Modern Carbon (pMC; Eq. A.10) or fraction modern carbon ($F^{14}\text{C}$; Eq. A.11). Simplified these two are expressed as:

Eq. A.10:

$$pMC = \frac{A_{SN}}{A_{ON}} \cdot 100\%$$

Where: A_{SN} = normalized specific activity of the sample

A_{ON} = normalized sample activity

Eq. A.11:

$$F^{14}\text{C} = \frac{pMC}{100\%}$$

Detailed information on the calculations regarding radiocarbon dating is provided by Stenström et al (2011).

APPENDIX B – Gigapixel photography

Appendix B – Gigapixel photography

B.1 GigaPan panoramas access

In total, 18 gigapixel panoramas were recorded from different vantage points (Fig.B1; Fig.B2) featuring the study area . The resulting panoramas exhibit resolutions up to 5.87 gigapixels and are composed of up to 814 single pictures featuring scenic overview and detailed close up outcrop shots. Snapshots within the panoramas point to areas of special interest.

The final panoramas were uploaded to the GigaPan website for public access and can be found in the gallery “Dangkhar, Spiti Valley (H.P.), India” by TUGEnGeo (#GP www.gigapan.com/galleries/13306). The blue hotlinks embedded in this text directly lead to the described features, where available. In the digital version of the text, the panoramas are easily accessible by clicking on the highlighted link embedded in the document. The GigaPan (GP) link is, for example, provided as #GP www.gigapan.com/gigapans/178302 (Snapshot: Old Dangkhar Monastery) with the name of the emphasized snapshot feature in parentheses, where available. Hardcopy readers please type the link into your internet browser to access the panoramas. The GigaPan image links are inserted in the chapters throughout this text where appropriate.



Fig. B.1 GigaPan EPIC Pro unit and Panasonic DMC-FZ200 camera set up on the roof of the Dangkhar Monastery Guest House. The panorama acquired in this scene can be viewed at: #GP www.gigapan.com/gigapans/178302

B.2 GigaPan Image Log

Number	Location	Approximate Center Bearing	Notes	Date Acquired	Number of Columns/Rows	Total number of Images
GP1	N 32.07612 E 78.23238	45°	Mt. Chokula – Dangkhar Landslide headscarp area	28/06/15	33/8	264
http://www.gigapan.com/gigapans/06e42ff53645c203961aefa6c4853266						
GP2	N 32.07612 E 78.23238	165°	Mane Landslide	28/06/15	8/10	80
http://www.gigapan.com/galleries/13306/gigapans/178295						
GP3	N 32.08914 E 78.21435	30°	Hoodoos along Dangkhar main road, India	30/06/15	14/8	112
http://www.gigapan.com/gigapans/d5888bed5335871c4b1dd1ba436a6843						
GP4	N 32.08812 E 78.21378	32°	Breccia beneath Old Dangkhar Monastery (300mm)	24/07/15	27/16	432
http://www.gigapan.com/galleries/13306/gigapans/178298						
GP5	N 32.06086 E 78.24580	152°	Mane Landslide	02/07/15	33/15	495
http://www.gigapan.com/galleries/13306/gigapans/178300						
GP6	N 32.08897 E 78.21604	263°	Dangkhar village	03/07/15	29/22	638 (637; 1 st pic didn't trigger)
http://www.gigapan.com/galleries/13306/gigapans/178302						
GP7	N 32.07612 E 78.23238	340°	Hoodoos along Dangkhar main road	03/07/15	16/12	192
http://www.gigapan.com/galleries/13306/gigapans/178304						

Number	Location	Approximate Center Bearing	Notes	Date Acquired	Number of Columns/Rows	Total number of Images
GP8	N 32.06152 E 78.24710	90°	Headscarp area and southern limit of Dangkhar Landslide	02/07/15	33/15 + 19/15	495 + 285
http://www.gigapan.com/galleries/13306/gigapans/178305 (Part 1)						
http://www.gigapan.com/galleries/13306/gigapans/178306 (Part 2)						
GP9	N 32.08987 E 78.21230	360°	Breccia north of Old Dangkhar Monastery	07/07/15	12/10	120
http://www.gigapan.com/gigapans/0f37d42490a64301f2d8640eb1b73caf						
GP10	N 32.08987 E 78.21230	30°	Dangkhar Hoodoos at sunset	07/07/15	13/15	195
http://www.gigapan.com/gigapans/69f31ea7b03bebb4ed9f63a9322aa4a1						
GP11	N 32.12675 E 78.17455	150°	Dangkhar Landslide seen from Palangri	14/07/15	37/22	814
http://www.gigapan.com/gigapans/1b15b231610524cb6d0a219668009479						
GP12	N 32.12675 E 78.17455	150°	Dangkhar Landslide seen from Palangri (250mm)	14/07/15	16/10	160
http://www.gigapan.com/galleries/13306/gigapans/178307						
GP13	N 32.07817 E 78.19447	65°	Dangkhar Landslide as seen from uphill of Siluk (250mm)	22/07/15	28/10	280
http://www.gigapan.com/galleries/13306/gigapans/178308						
GP14	N 32.07817 E 78.19447	45°	Dangkhar Landslide (central part) as seen uphill of Siluk	22/07/15	35/21	735
http://www.gigapan.com/galleries/13306/gigapans/178319						
GP15	N 32.08784 E 78.21217	345°	Breccia downhill of Old Dangkhar Monastery	23/07/15	17/23 + 11/18	391 + 198
http://www.gigapan.com/gigapans/9eed61280b05440d0cd3cc4dd33ccbf9 (Part 1)						
http://www.gigapan.com/gigapans/6d026b1c31d6e31cd38a39f4fa098241 (Part 2)						

Number	Location	Approximate Center Bearing	Notes	Date Acquired	Number of Columns/Rows	Total number of Images
GP16	N 32.03157 E 78.25563	322°	Canyon at Mane Landslide	28/07/15	36/20	720
http://www.gigapan.com/galleries/13306/gigapans/178377						
GP17	N 32.03489 E 78.25847	27°	Southern limit of Dangkhar Landslide seen from Mane (250mm)	28/07/15	17/11	187
http://www.gigapan.com/galleries/13306/gigapans/178378						
GP18	N 32.03489 E 78.25847	various	Mane Landslide Canyon	18/07/15	various	various
http://www.gigapan.com/galleries/13306/gigapans/178683 (Part 1) http://www.gigapan.com/gigapans/a2d191a5a0d43f2b45771acc375e5f10 (Part 2) http://www.gigapan.com/galleries/13306/gigapans/178685 (Part 3) http://www.gigapan.com/gigapans/fe7abba7f41fd49e6b5bb7d1b6ceff3c (Part 4)						

Tab. B.1: GigaPan (GP) Image Log. If not indicated otherwise, all pictures were taken using a full – frame equivalent zoom of 600mm. Gallery link: <http://www.gigapan.com/galleries/13306>

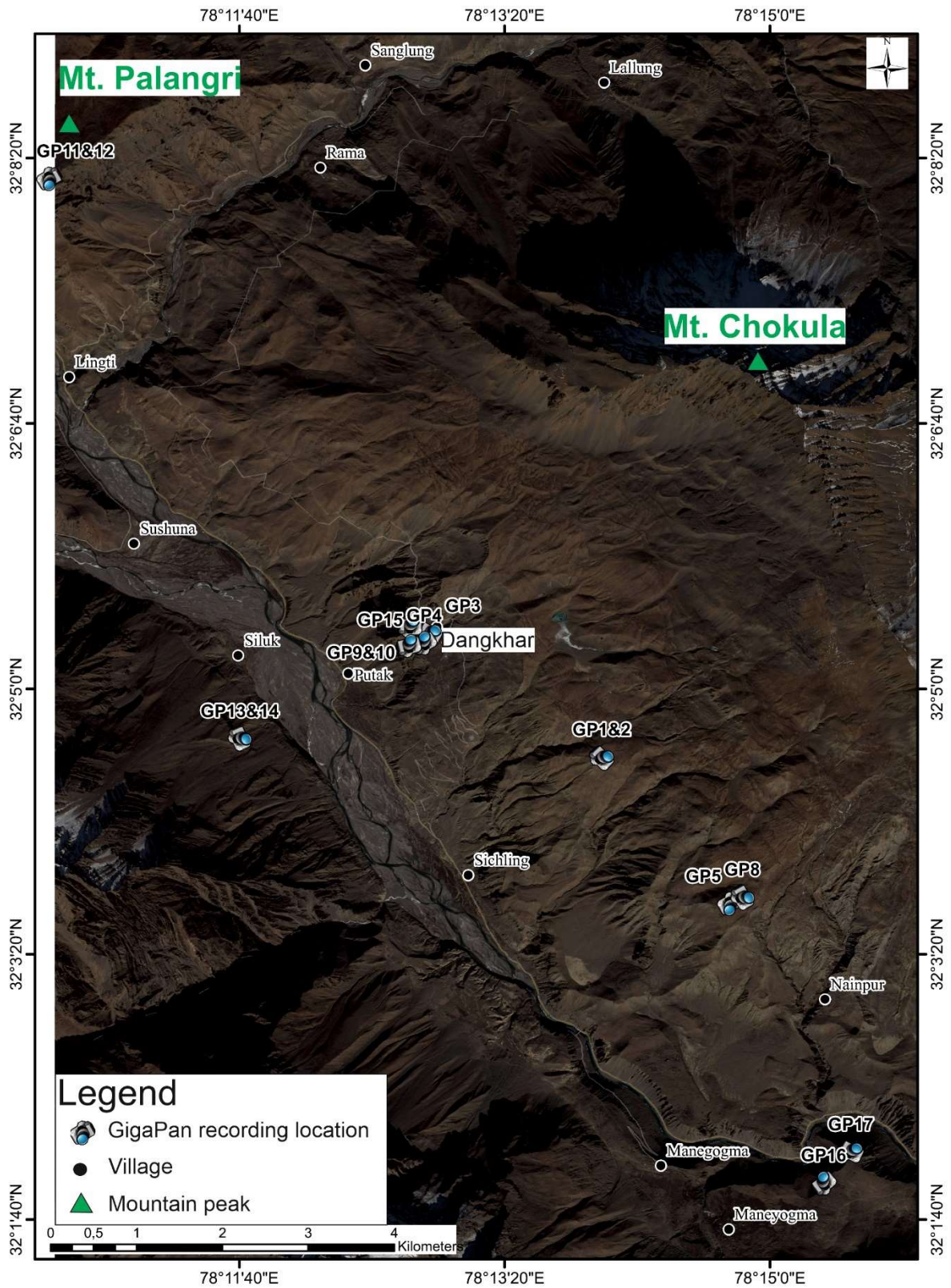


Fig. B.2 Recording locations of the GigaPan (GP) panoramas

APPENDIX C – Orientation data of lineaments

Appendix C – Orientation data of lineaments

C.1 Azimuth data of the lineaments of the Dangkhari Landslide

208, 210, 222, 222, 215, 196, 205, 1, 49, 211, 186, 187, 175, 169, 176, 180, 198, 189, 187, 199, 210, 214, 217, 220, 216, 213, 210, 209, 20, 195, 224, 221, 218, 229, 216, 210, 41, 218, 189, 187, 203, 181, 9, 184, 203, 189, 226, 217, 227, 216, 200, 202, 203, 195, 243, 226, 238, 232, 228, 227, 222, 227, 56, 96, 50, 58, 77, 53, 192, 188, 237, 255, 253, 223, 226, 228, 231, 225, 232, 185, 206, 180, 153, 170, 190, 200, 226, 240, 249, 220, 256, 228, 230, 50, 227, 227, 250, 224, 60, 228, 225, 236, 201, 203, 203, 182, 185, 225, 241, 216, 311, 310, 212, 190, 281, 224, 274, 259, 290, 214, 254, 266, 261, 267, 255, 239, 232, 311, 74, 240, 293, 303, 237, 203, 227, 223, 222, 4, 8, 358, 5, 31, 195, 11, 19, 185, 28, 157, 166, 175, 175, 182, 168, 178, 19, 23, 34, 209, 235, 195, 222, 189, 188, 250, 204, 218, 206, 193, 208, 196, 212, 207, 203, 223, 211, 202, 216, 219, 212, 205, 224, 32, 31, 222, 222, 218, 217, 222, 230, 233, 215, 215, 33, 247, 213, 248, 240, 249, 219, 213, 215, 230, 243, 231, 242, 239, 232, 245, 226, 226, 224, 218, 224, 238, 69, 208, 226, 227, 237, 239, 226, 258, 265, 241, 228, 229, 230, 222, 230, 230, 231, 236, 197, 195, 197, 336, 156, 349, 212, 191, 190, 166, 153, 174, 155, 270, 236, 230, 248, 219, 218, 39, 34, 225, 191, 218, 221, 200, 187, 207, 215, 226, 237, 223, 196, 219, 219, 227, 240, 199, 188, 205, 220, 50, 219, 206, 218, 213, 208, 230, 221, 187, 214, 217, 224, 188, 161, 201, 235, 19, 178, 186, 54, 182, 178, 238, 9, 194, 188, 199, 199, 192, 197, 324, 237, 243, 308, 139, 321, 327, 263, 224, 231, 327, 247, 250, 252, 245, 243, 226, 222, 221, 232, 222, 239, 255, 253, 255, 259, 255, 269, 273, 269, 273, 274, 304, 231, 229, 232, 232, 269, 248, 262, 239, 251, 254, 242, 250, 249, 61, 70, 247, 57, 58, 72, 239, 250, 243, 246, 61, 251, 258, 250, 256, 306, 282, 301, 269, 257, 230, 224, 233, 227, 245, 226, 242, 246, 220, 245, 269, 239, 227, 289, 226, 221, 191, 220, 257, 259, 232, 233, 193, 212, 209, 211, 200, 190, 206, 208, 208, 29, 23, 211, 201, 207, 191, 222, 210, 202, 235, 237, 243, 257, 266, 87, 246, 243, 239, 214, 235, 61, 240, 246, 243, 239, 239, 248, 279, 279, 94, 266, 222, 53, 186, 60, 264, 238, 243, 242, 238, 233, 232, 225, 223, 216, 231, 222, 224, 228, 230, 229, 220, 218, 221, 68, 91, 244, 261, 249, 301, 306, 298, 314, 245, 264, 269, 233, 225, 235, 228, 217, 243, 226, 220, 45, 237, 239, 243, 230, 233, 238, 232, 46, 223, 238, 237, 222, 245, 234, 241, 198, 210, 222, 224, 234, 207, 249, 62, 64, 41, 290, 228, 280, 184, 252, 252, 257, 238, 225, 233, 238, 233, 240, 234, 232, 239, 251, 52, 64, 235, 242, 55, 186, 19, 224, 219, 223, 214, 207, 221, 229, 232, 253, 231, 243, 218, 234, 227, 230, 230, 229, 223, 250, 249, 88, 72, 203, 205, 27, 147, 140, 248, 247, 248, 263, 103, 227, 228, 238, 238, 294, 303, 301, 53, 64, 217, 216, 240, 241, 220, 224, 220, 247, 252, 255, 254, 254, 276, 282, 261, 218, 218, 245, 237, 232, 233, 244, 231, 219, 213, 246, 260, 246, 64, 240, 247, 254, 188, 276, 274, 218, 217, 195, 39, 261, 243, 284, 77, 283, 245, 278, 282, 271, 241, 256, 233, 246, 257, 258, 284, 267, 250, 220, 209, 217, 201, 223, 235, 281, 136, 130, 197, 294, 288, 266, 286, 302, 148, 151, 262, 215, 223, 231, 228, 204, 214, 210, 204, 209, 209, 202, 203, 206, 196, 214, 201, 236, 234, 277, 199, 201, 0, 191, 156, 326, 158, 180, 178, 187, 298, 309, 292, 306, 310, 44, 252, 250, 267, 14, 239, 216, 222, 232, 225, 233, 196, 213, 226, 230, 227, 233, 239, 231, 210, 219, 218, 225, 179, 181, 192, 198, 178, 224, 208, 213, 194, 214, 199, 192, 213, 222, 228, 211, 212, 214, 130, 154, 208, 216, 184, 188, 202, 198, 25, 200, 321, 169, 221, 231, 237, 218, 357, 188, 174, 169, 170, 216, 241, 149, 324, 317, 138, 158, 318, 156, 233, 229, 237, 257, 254, 261, 57, 66, 54, 235, 228, 235, 243, 170, 217, 190, 190, 188, 324, 300, 307, 299, 305, 178, 189, 281, 118, 298, 145, 310, 298, 120, 132, 309, 146, 127, 291, 203, 219, 217, 211, 209, 213, 208, 223, 248, 238, 202, 254, 306, 269, 267, 180, 191, 176, 268, 228, 204, 184, 215, 30

C.2 Azimuth data of the lineaments of the Mane Landslide

98, 101, 105, 94, 103, 103, 100, 98, 98, 82, 90, 97, 88, 110, 111, 99, 254, 97, 92, 102, 116, 122, 133, 130, 117, 265, 90, 86, 124, 131, 290, 91, 114, 112, 117, 120

APPENDIX D – Radiocarbon calibration curves

Appendix D – Radiocarbon calibration curves

Calibration of 1.070000±0.030000 with NHZ2, intcal13.f14c,

```
# Northern Hemisphere Zone 2 compilation
#
#
# Quan Hua, Mike Barbetti, Andrzej Z Rakowski
# "ATMOSPHERIC RADIOCARBON FOR THE PERIOD 1950-2010",
# Radiocarbon, 55(4), 2013
#
#
##Atmospheric data from Reimer et al (2013);
# Reimer et al. 2013
# Reimer PJ, Bard E, Bayliss A, Beck JW, Blackwell PG, Bronk Ramsey C, Buck CE
# Cheng H, Edwards RL, Friedrich M, Grootes PM, Guilderson TP, Haffidason H,
# Hajdas I, Hattala C, Heaton TJ, Hogg AG, Hughen KA, Kaiser KF, Kromer B,
# Manning SW, Niu M, Reimer RW, Richards DA, Scott EM, Southon JR, Turney CSM,
# van der Plicht J.
# IntCal13 and MARINE13 radiocarbon age calibration curves 0-50000 years calBP
# Radiocarbon 55(4). DOI: 10.2458/azu_js_rc.55.16947
```

OneSigma

[cal AD 1955.94 :cal AD 1958.26]0.126

[cal AD 1995.23 :cal AD 2009.52]0.874

TwoSigma

[cal AD 1679.97 :cal AD 1763.53]0.079

[cal AD 1800.93 :cal AD 1938.62]0.160

[cal AD 1952.19 :cal AD 1958.85]0.103

[cal AD 1989.91 :cal AD 2009.52]0.658

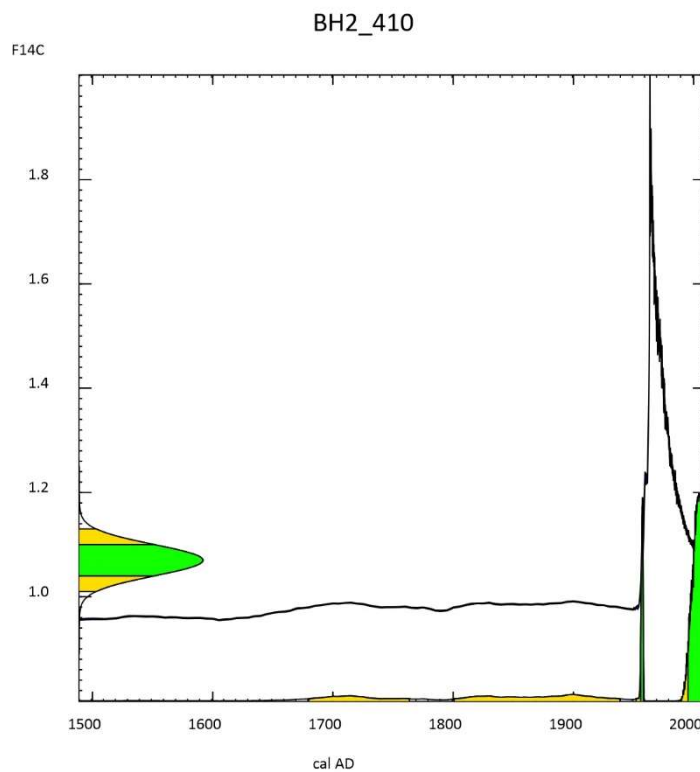


Fig. D.1 Sample BH2_410

Calibration of 1.160700±0.040000 with NHZ2, intcal13.f14c,

```
# Northern Hemisphere Zone 2 compilation
#
#
# Quan Hua, Mike Barbetti, Andrzej Z Rakowski
# "ATMOSPHERIC RADIOCARBON FOR THE PERIOD 1950-2010",
# Radiocarbon, 55(4), 2013
#
#
#
##Atmospheric data from Reimer et al (2013);
# Reimer et al. 2013
# Reimer PJ, Bard E, Bayliss A, Beck JW, Blackwell PG, Bronk Ramsey C, Buck CE
# Cheng H, Edwards RL, Friedrich M, Grootes PM, Guilderson TP, Hafliðason H,
# Hajdas I, Hattala C, Heaton TJ, Hogg AG, Hughen KA, Kaiser KF, Kromer B,
# Manning SW, Niu M, Reimer RW, Richards DA, Scott EM, Southon JR, Turney CSM,
# van der Plicht J.
# IntCal13 and MARINE13 radiocarbon age calibration curves 0-50000 years calBP
# Radiocarbon 55(4). DOI: 10.2458/azu_js_rc.55.16947
```

OneSigma

```
[cal AD 1958.07 :cal AD 1959.20]0.088
[cal AD 1985.02 :cal AD 1985.37]0.019
[cal AD 1985.72 :cal AD 1996.04]0.894
```

TwoSigma

```
[cal AD 1957.59 :cal AD 1961.67]0.124
[cal AD 1982.24 :cal AD 1982.57]0.001
[cal AD 1982.79 :cal AD 2002.90]0.874
```

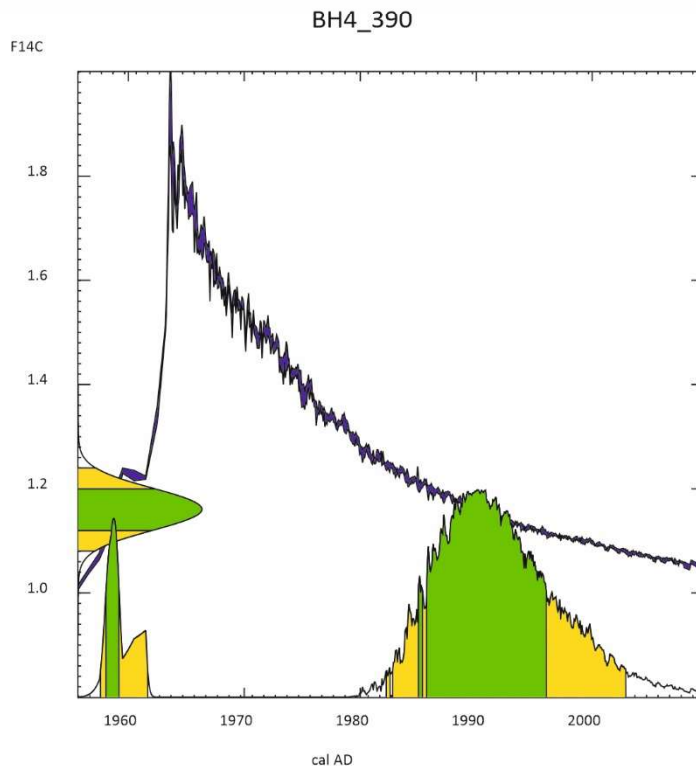


Fig. D.2 Sample BH4_390

Calibration of 1.168900±0.020000 with NHZ2, intcal13.f14c,

```
# Northern Hemisphere Zone 2 compilation
#
#
# Quan Hua, Mike Barbetti, Andrzej Z Rakowski
# "ATMOSPHERIC RADIOCARBON FOR THE PERIOD 1950-2010",
# Radiocarbon, 55(4), 2013
#
#
##Atmospheric data from Reimer et al (2013):
# Reimer et al. 2013
# Reimer PJ, Bard E, Bayliss A, Beck JW, Blackwell PG, Bronk Ramsey C, Buck CE
# Cheng H, Edwards RL, Friedrich M, Grootes PM, Guilderson TP, Hafflidason H,
# Hajdas I, Hattala C, Heaton TJ, Hogg AG, Hughen KA, Kaiser KF, Kromer B,
# Manning SW, Niu M, Reimer RW, Richards DA, Scott EM, Southon JR, Turney CSM,
# van der Plicht J.
# IntCal13 and MARINE13 radiocarbon age calibration curves 0-50000 years calBP
# Radiocarbon 55(4). DOI: 10.2458/azu_js_rc.55.16947
```

OneSigma

```
[cal AD 1958.56 :cal AD 1959.03]0.071
[cal AD 1985.85 :cal AD 1985.88]0.004
[cal AD 1986.25 :cal AD 1986.33]0.010
[cal AD 1986.86 :cal AD 1991.12]0.858
[cal AD 1991.38 :cal AD 1991.95]0.056
```

TwoSigma

```
[cal AD 1958.07 :cal AD 1959.29]0.091
[cal AD 1984.10 :cal AD 1984.25]0.003
[cal AD 1984.86 :cal AD 1994.88]0.906
```

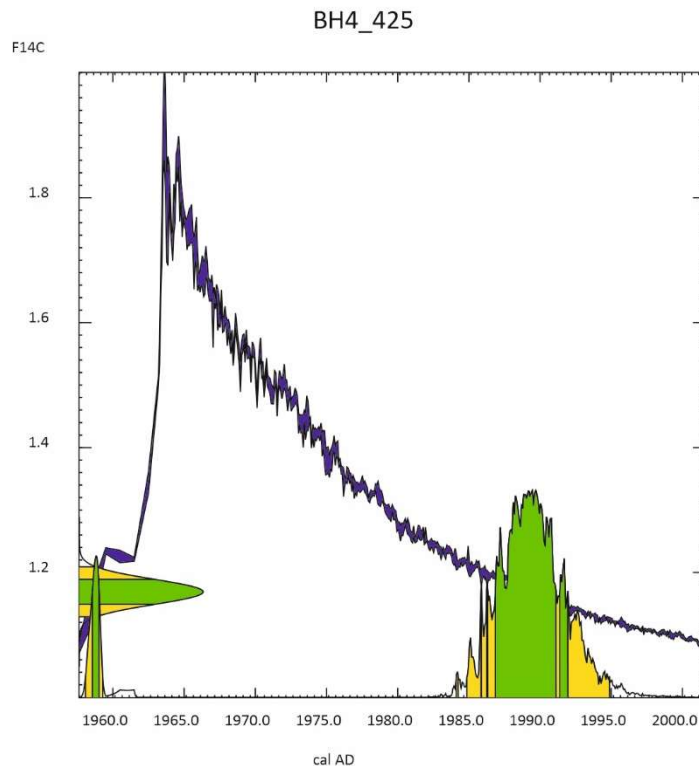


Fig. D.3 Sample BH4_425

Calibration of 1.028000±0.030000 with NHZ2, shcal13.f14c,

```
# Northern Hemisphere Zone 2 compilation
#
#
# Quan Hua, Mike Barbetti, Andrzej Z Rakowski
# "ATMOSPHERIC RADIOCARBON FOR THE PERIOD 1950-2010",
# Radiocarbon, 55(4), 2013
#
#
## Atmospheric data from Hogg et al (2013);
# Hogg et al. 2013
# Alan G Hogg, Quan Hua, Paul G Blackwell, Caitlin E Buck, Thomas P Guilderson,
# Timothy J Heaton, Mu Niu, Jonathan G Palmer, Paula J Reimer, Ron W Reimer,
# Christian S M Turney, Susan R H Zimmerman. Radiocarbon, 55: Nr 4, 2013
# DOI: 10.2458/azu_js_rc.55.16783
#
#
#
```

OneSigma

```
[*cal BP -59.63 :cal BP -52.91]0.050
[cal BP -7.63 :cal BP -1.55]0.045
[cal BP -1.33 :cal BP 147.92]0.700
[cal BP 219.56 :cal BP 268.16]0.206
```

TwoSigma

```
[*cal BP -59.63 :cal BP -49.01]0.041
[cal BP -8.04 :cal BP 329.93]0.911
[cal BP 368.14 :cal BP 441.59]0.048
```

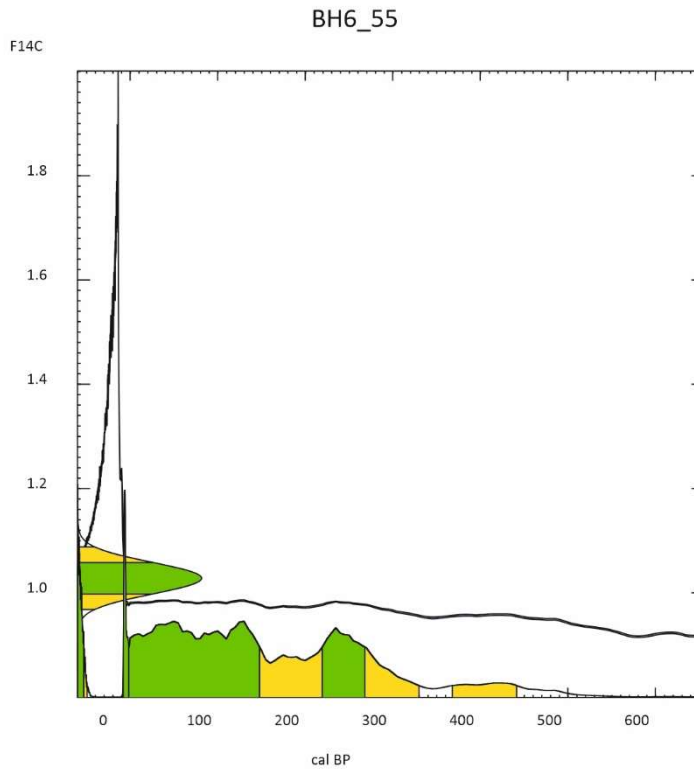


Fig. D.4 Sample BH6_55

Calibration of 1.117400±0.030000 with NHZ2, intcal13.f14c,

```
# Northern Hemisphere Zone 2 compilation
#
#
# Quan Hua, Mike Barbetti, Andrzej Z Rakowski
# "ATMOSPHERIC RADIOCARBON FOR THE PERIOD 1950-2010",
# Radiocarbon, 55(4), 2013
#
#
##Atmospheric data from Reimer et al (2013);
# Reimer et al. 2013
# Reimer PJ, Bard E, Bayliss A, Beck JW, Blackwell PG, Bronk Ramsey C, Buck CE
# Cheng H, Edwards RL, Friedrich M, Grootes PM, Guilderson TP, Haffidason H,
# Hajdas I, Hattala C, Heaton TJ, Hogg AG, Hughen KA, Kaiser KF, Kromer B,
# Manning SW, Niu M, Reimer RW, Richards DA, Scott EM, Southon JR, Turney CSM,
# van der Plicht J.
# IntCal13 and MARINE13 radiocarbon age calibration curves 0-50000 years calBP
# Radiocarbon 55(4). DOI: 10.2458/azu_js_rc.55.16947
```

OneSigma

```
[cal AD 1957.75 :cal AD 1958.43]0.058
[cal AD 1991.10 :cal AD 1991.39]0.021
[cal AD 1991.75 :cal AD 2001.05]0.909
[cal AD 2001.50 :cal AD 2001.71]0.011
```

TwoSigma

```
[cal AD 1957.12 :cal AD 1958.91]0.074
[cal AD 1988.25 :cal AD 1988.38]0.002
[cal AD 1988.80 :cal AD 2007.19]0.923
[cal AD 2007.49 :cal AD 2007.61]0.002
```

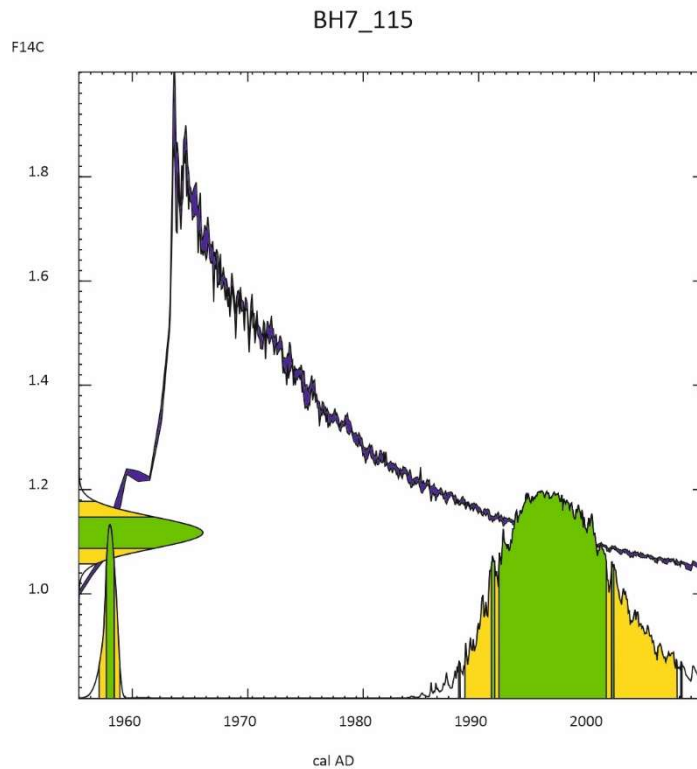


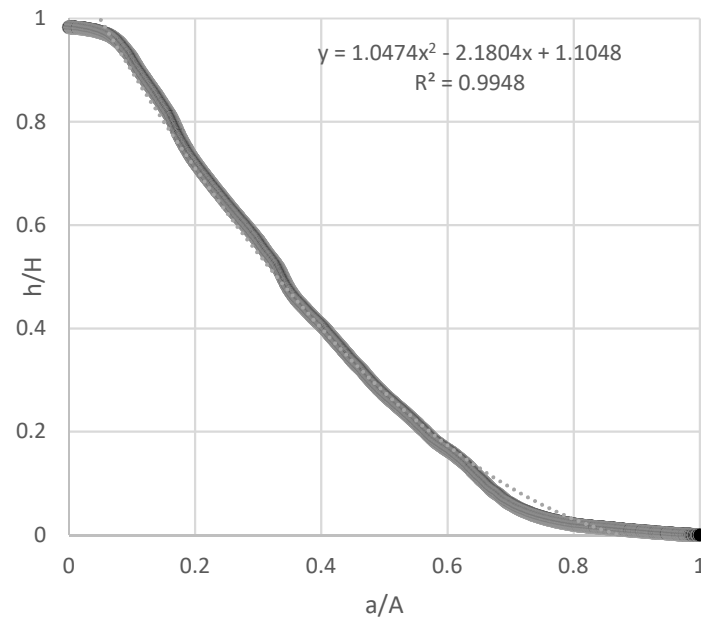
Fig. D.5 Sample BH7_115

APPENDIX E – Hypsometry of the Dangkhar hillslope

Appendix E – Hypsometry of the Dangkhar hillslope

E.1 Hypsometric curve

a)



b)

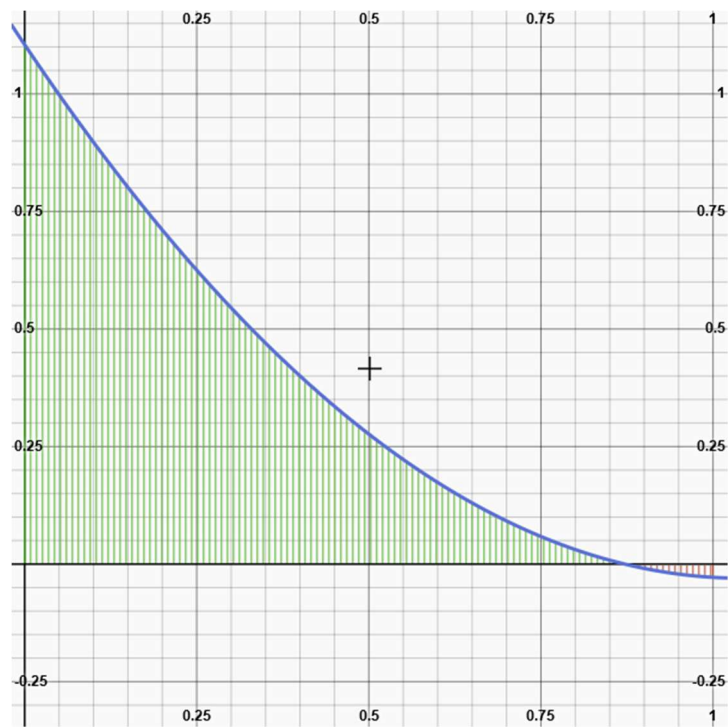


Fig.E.1 Hypsometric integral of the Dangkhar watershed used in Fig.4.16. a) Hypsometric integral curve of the Dangkhar watershed, b) Integral of the fitted curve

APPENDIX F – Geologic map

Appendix F – Geologic map

F.1 Geologic map units

Legend

	Map Color	Geologic Unit	Main Lithology	Broad Age	
Surficial Deposits		Alluvium	Sorted gravel, sand	Holocene	
		Talus Fans	Limestone, dolomite clasts	Holocene	
		Lake Sediments	Laminated silt, clay	Holocene	
		Mane Landslide Debris	Unassorted silt, sand, gravel, blocks	Holocene	
		Rock Glacier Deposits	Limestone, dolomite clasts	Late Pleistocene – Holocene	
		Breccia	Carbonate breccia, partly crudely stratified	Late Pleistocene – Holocene	
		Dangkhar Landslide Debris	Unassorted silt, sand, gravel, blocks	Late Pleistocene – Holocene	
Bedrock		Spiti Formation	Shale	Oxfordian – Early Valanginian	
		Kioto Group	Lilang Supergroup	Limestone, dolomite	Late Rhaetic – Lias
		Alaror & Rangrik Formation <i>(Monotis Shales & Juvavites Beds)</i>		Shale, sandstone, limestone	Early – Late Noric
		Rongtong Formation <i>(Tropites Beds)</i>		Dolomite, limestone	Middle – Late Carnic
		Rama Formation <i>(Grey Beds)</i>		Shale, sandstone, limestone	Early – Middle Carnic
		Chomule Formation <i>(Halobia and Daonella Limestone)</i>		Limestone	Ladinic – Early Carnic
		Kaga Formation <i>(Daonella Shales)</i>		Shale, siltstone, limestone	Ladinic
		Mikin Formation <i>(“Muschelkalk”)</i>		Limestone	Induan – Anisian
		Gungri Formation		Shale	Dzulfian – ? Early Dorashamian
		Gechang & Ganmachidam Formation		Conglomerate, sandstone, shale	Asselian – Late Carboniferous

Map symbols

	Normal Fault (solid where certain; dashed where inferred)		Rafted rock blocks within landslide
	Geologic Contact (observed, inferred, concealed)		Peak
	Bedding (measured, estimated)		
	Syncline solid where certain; dashed where inferred; dotted where concealed)		
	Anticline solid where certain; dashed where inferred; dotted where concealed)		
	Rock Glacier		
	Lineaments		
	Landslide		
	Cross section		
	Basal slip surface of Dangkhar Landslide (in cross section)		
	Sense of shear of fault (in cross section)		
	Internal bedrock structure (schematic)		

Tab.F1: Site stratigraphy

Quaternary deposits

Alluvium: mostly rounded well sorted gravels transported by the main rivers at the valley floor.

Talus Fans: sand, gravel and boulder material and unsorted clasts occupying the steep parts of the valley flanks and cliffs from which they originate from.

Lake Sediments: Fine carbonaceous sands, silts and clay (rarely laminated) exhibiting a pale yellow color.

Rock Glacial Deposits: not well rounded, unsorted, partly consolidated clasts of various grainsizes (diamicton) of black and brownish carbonates.

Mane Landslide Debris: unsorted and crushed clasts of silt, sand, and intact, predominantly carbonate blocks. Locally indurated and cemented.

Carbonate Breccia: cemented angular clasts in fine grained matrix (Block-In-Matrix rock). Contact between individual grains partly via tips.

Dangkhar Landslide Debris: unsorted silt, sand, gravel and blocks. Partly cemented forming clumps that disperse again under water influence, producing a milky carbonate slurry.

Triassic – Jurassic rocks

Spiti Formation: dark grey to black splintery shale with locally sandstone beds overlying the Kioto Formation carbonates. Abundant occurrence of belemnite fossils (Bhargava 2008).

Kioto Group: limestone and dolomite, grey at the base to greyish blue and arenaceous at the top (Bhargava 2008).

Triassic rocks

Alaror and Rangrik Formation: Dark grey to brownish shale and siltstone (brown to greenish where weathered) with subordinate limestone and dolomite in repeating cycles. Ripple marks are rarely developed (Bhargava and Bassi 1998).

Rongtong Formation: Nodular, bedded grey limestone and cliff forming dolomite with subordinate shale, sandstone, siltstone. Partly intertwined folding (Bhargava and Bassi 1998; Bhargava 2008).

Rama Formation: Characteristic grey colored shales with subordinate siltstones and carbonates (Grey beds on older maps). Repeating cycles of carbonates (Limestone/dolomite with earthy dolomite beds), and shales/siltstones from bottom to top (Bhargava and Bassi 1998; Bhargava 2008). Where formation is weathered, ash grey talus is present.

Chomule Formation: dark gray to black wavy bedded limestone (Bhargava 2008).

Kaga Formation: grey to brownish weathered calcareous, thinly bedded, splintery shale. Locally limestone and siltstone. In the study area it is best exposed on the right side in the Lingti valley at the base of Mt. Palangri.

Mikin Formation: bedded grey to ochre colored limestone of various thicknesses. Slightly reddish brown when weathered. Rarely shales with limited extent along strike. Abundant presence of fossils such as ammonites, conodonts, foraminifera (Bhargava and Bassi 1998).

Permian rocks

Gungri Formation: characteristic black color of shales, clay shale with partly silty, micaceous and cherty layers (Bhargava and Bassi 1998; Bhargava 2008). The unit is best exposed at a normal fault in the southeastern part of the study area.

Permian – Carboniferous rocks

Gechang and Ganmachidam Formation: White, cross bedded calcareous sandstone and conglomerates with subordinate shale (Bhargava and Bassi 1998; Bhargava 2008). Surfaces are usually altered to a slightly reddish-brown color. Both units are indistinguishable from each other at a distance (Bhargava 2008) and were mapped as one map unit. It is best exposed where it underlies the Gungri Formation on the left side of the Spiti River near the valley floor.

Carboniferous rocks

Po Formation: Alterations of quartzite and dark shales (Bhargava and Bassi 1998; Bhargava 2008). Occurs only at two minor outcrops in the study area along the left river flank of the Spiti River within the debris of the Mane landslide.

F.2 Geologic map of the Dangkhari Landslide

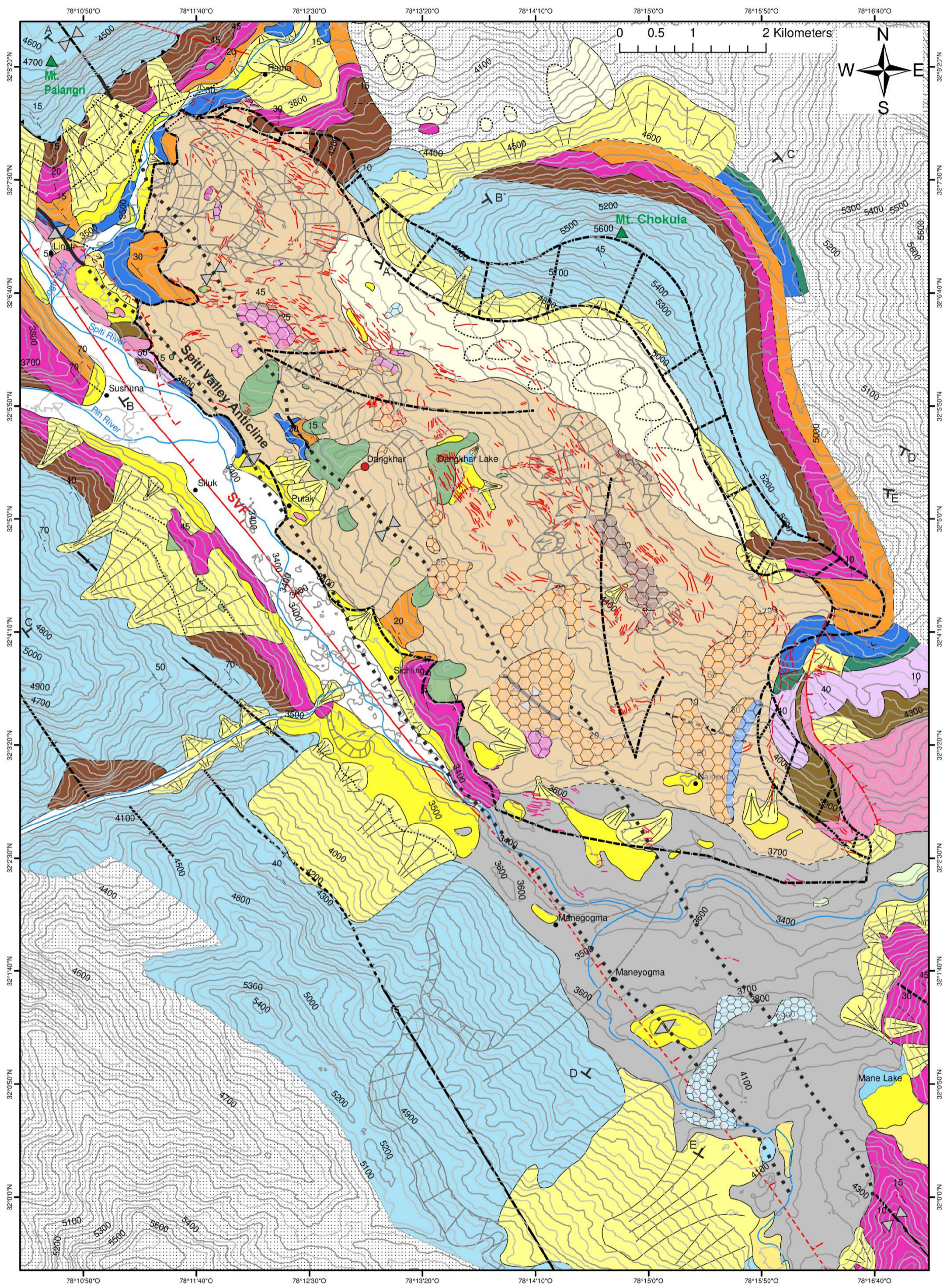


Fig.F.1 Geologic map of the Dangkhari Landslide

F.3 Geologic cross sections

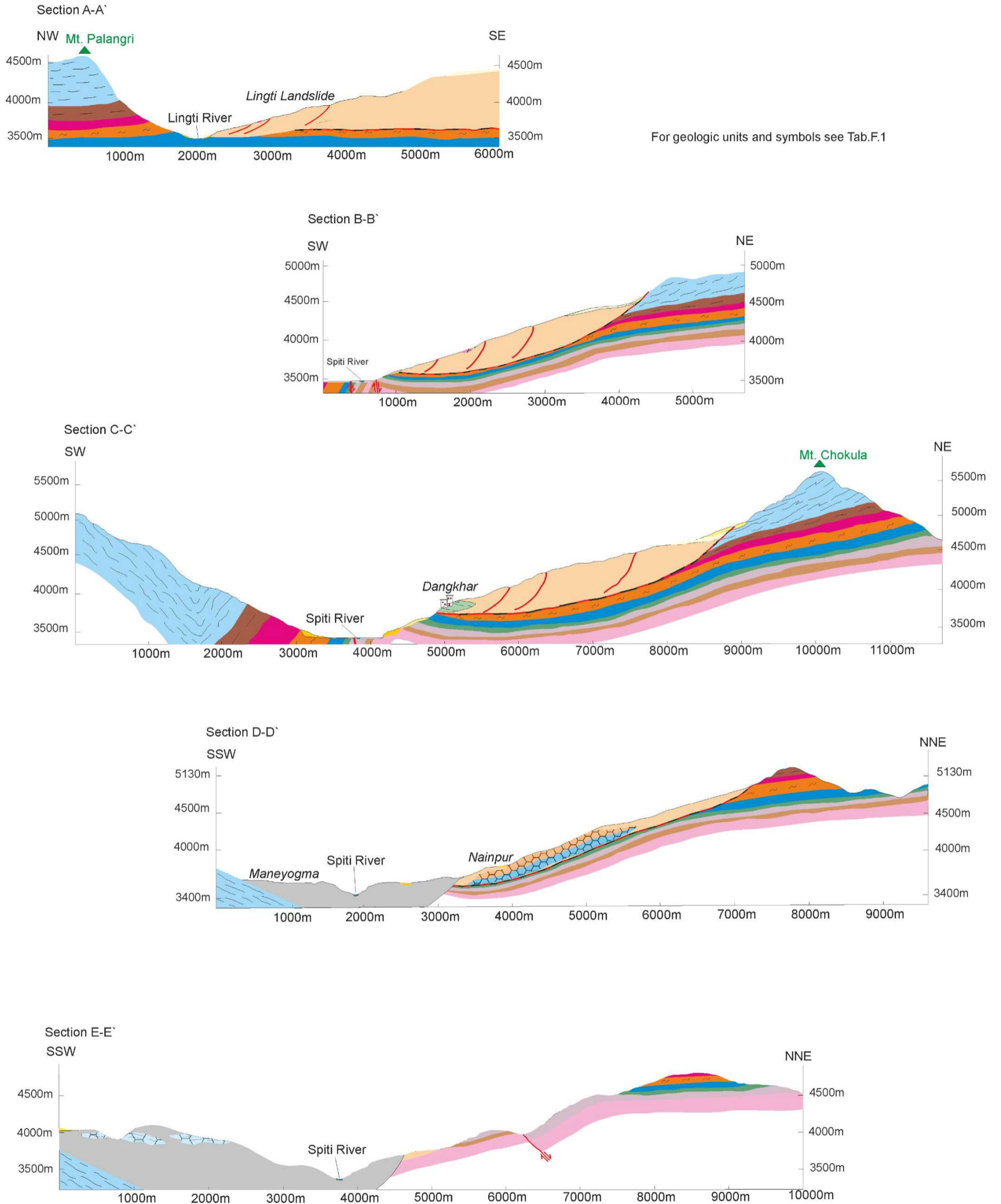
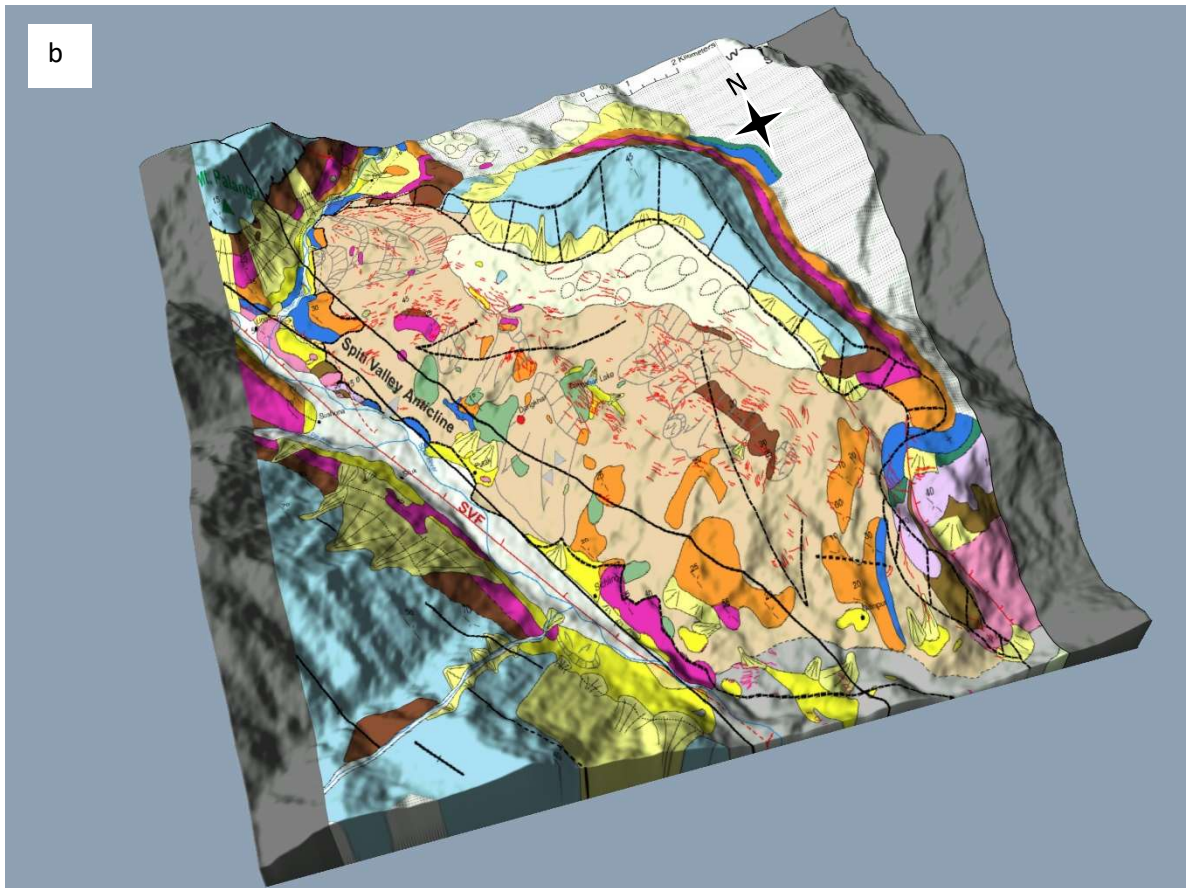
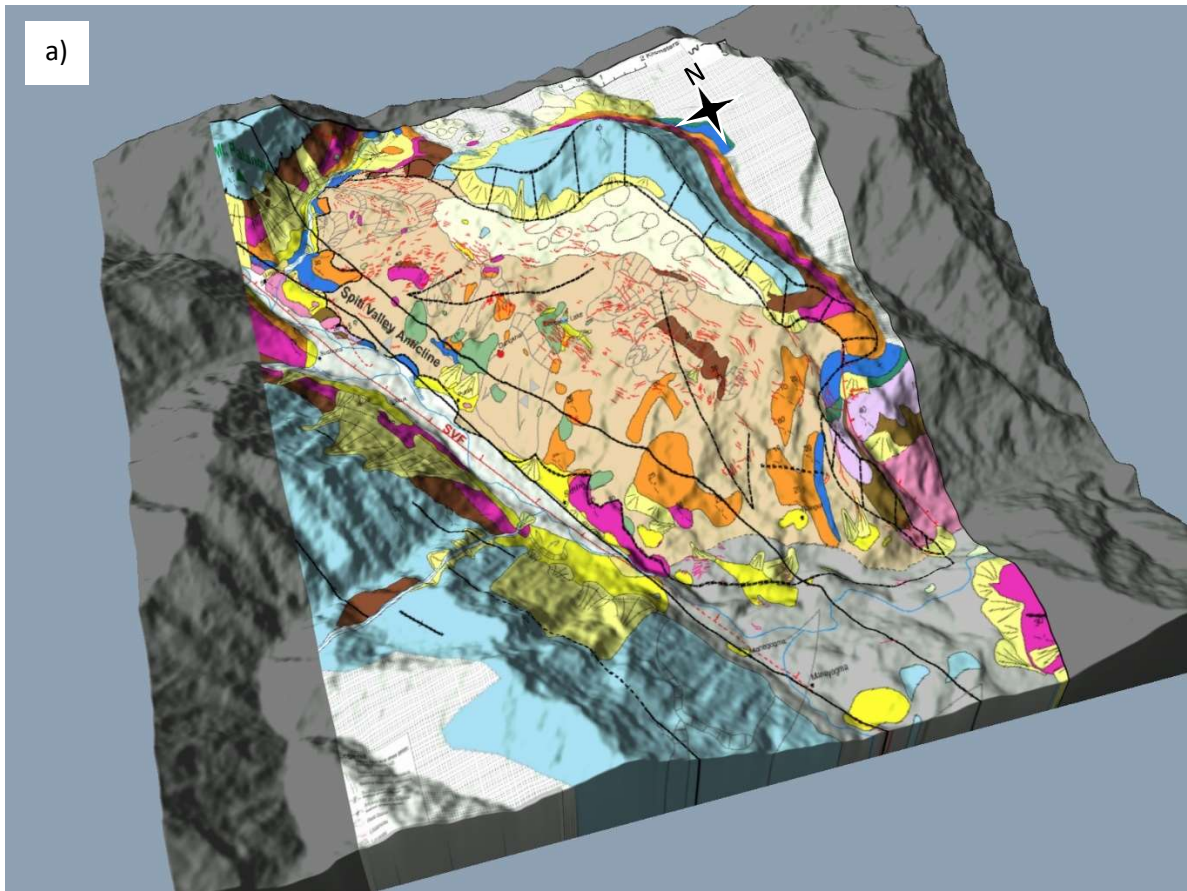
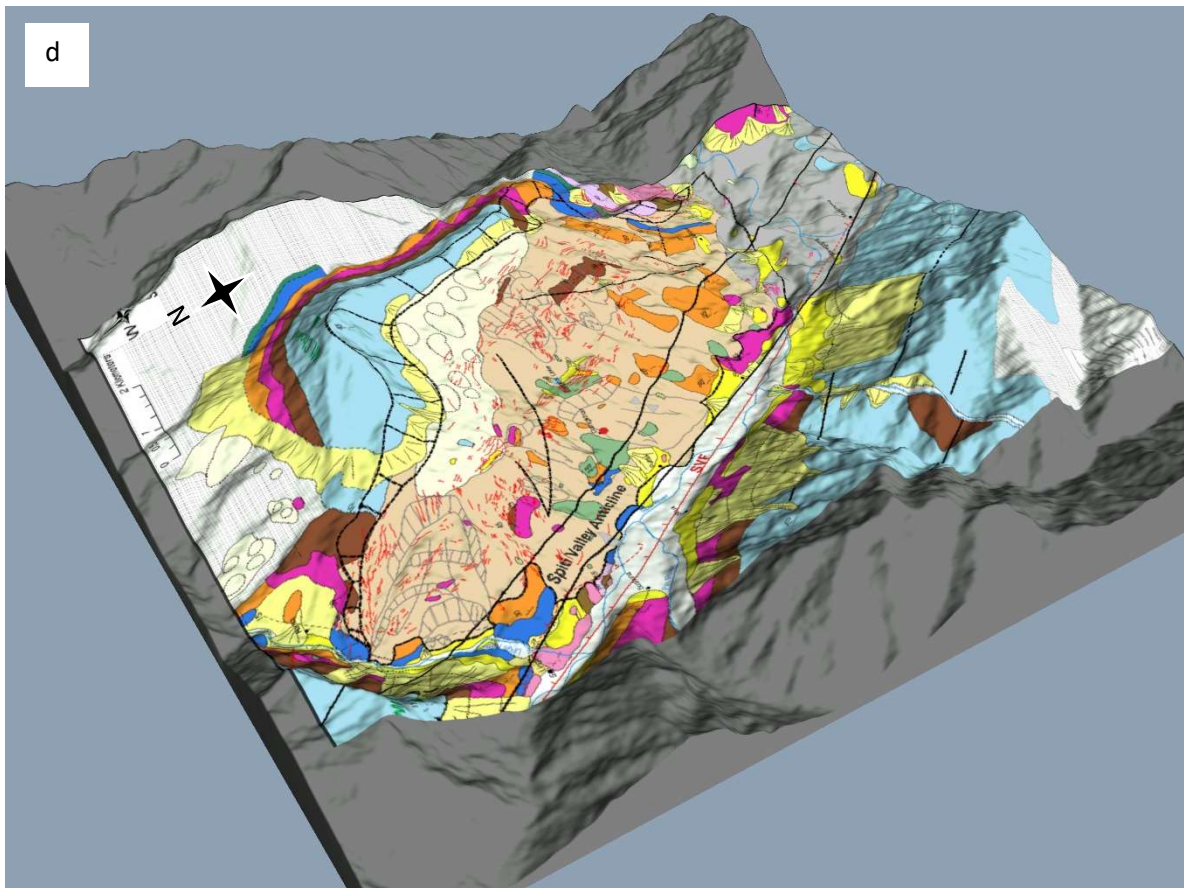
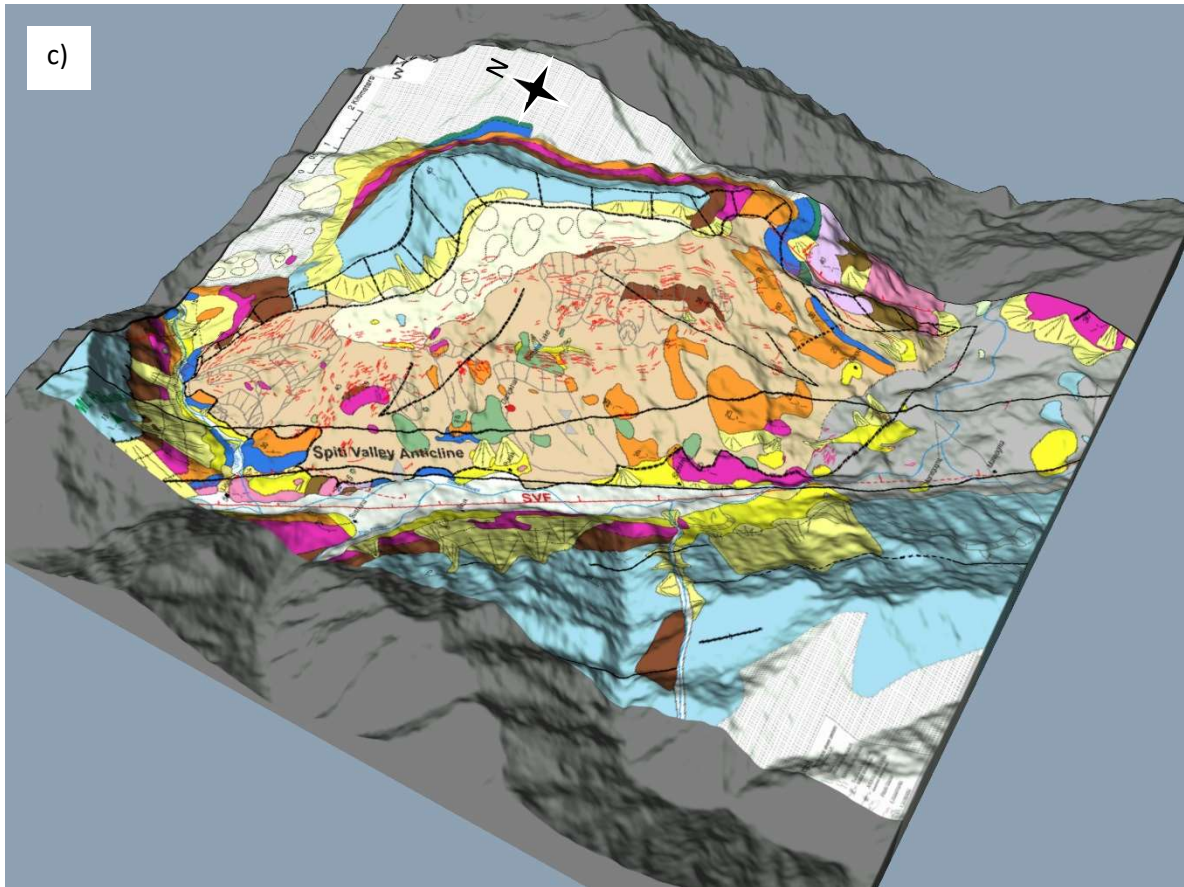


Fig.F.2 Geologic cross sections

F.4 – 3D geologic map views of the study area





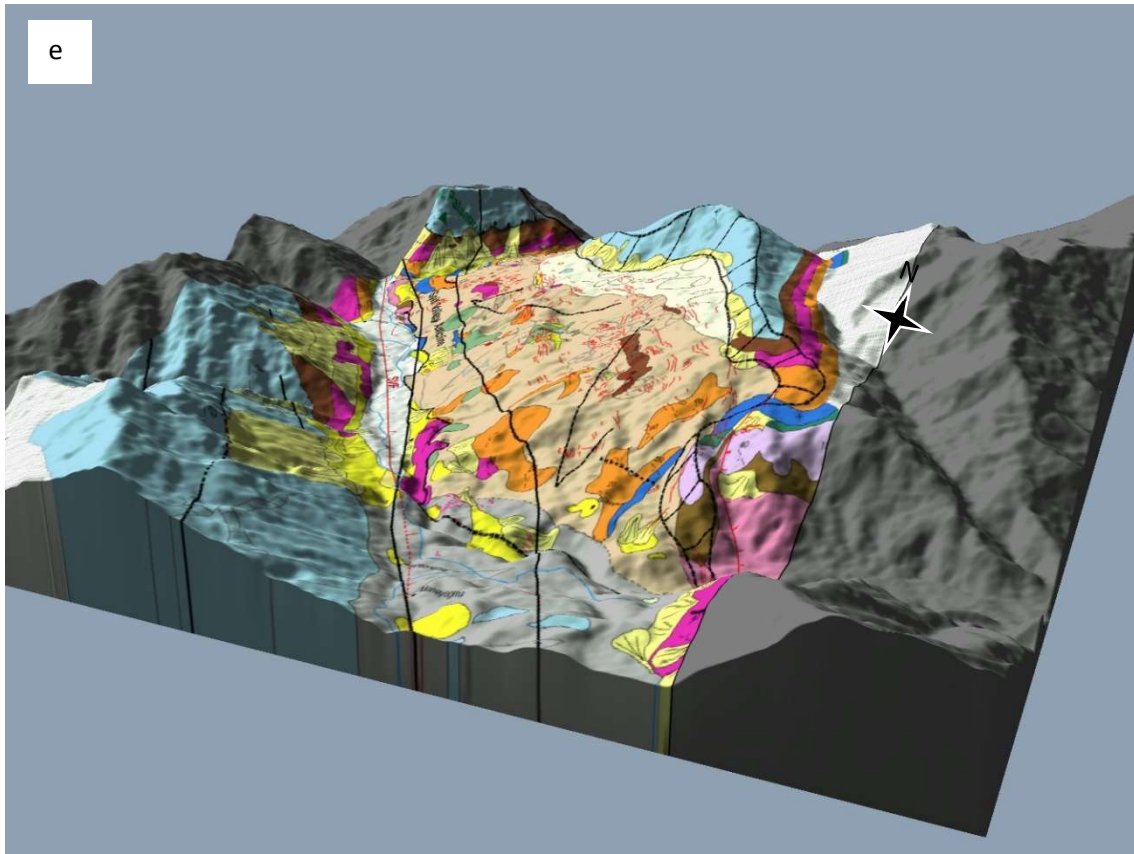


Fig.G.1 a-e 3D perspective views of the study area.
Block dimensions approximately 20 x 20 k

Appendix G – Geomorphologic map

G.1 Geomorphologic map of the Dangkhar Landslide

